University of Bath

PHD

Manipulation and Use of Sound Waves for Engineering Applications

Bucciarelli, Fabrizio

Award date:
2020

Awarding institution:
University of Bath

Link to publication

Alternative formats
If you require this document in an alternative format, please contact:
openaccess@bath.ac.uk

Copyright of this thesis rests with the author. Access is subject to the above licence, if given. If no licence is specified above, original content in this thesis is licensed under the terms of the Creative Commons Attribution-NonCommercial 4.0 International (CC BY-NC-ND 4.0) Licence (https://creativecommons.org/licenses/by-nc-nd/4.0/). Any third-party copyright material present remains the property of its respective owner(s) and is licensed under its existing terms.

Take down policy
If you consider content within Bath's Research Portal to be in breach of UK law, please contact: openaccess@bath.ac.uk with the details. Your claim will be investigated and, where appropriate, the item will be removed from public view as soon as possible.

Download date: 04. May. 2023

Manipulation and Use of Sound Waves for Engineering Applications

Fabrizio Bucciarelli

Department of Mechanical Engineering

University of Bath

Thesis submitted for the degree of
Doctor of Philosophy

May 2020

Copyright

Attention is drawn to the fact that copyright of this thesis rests with the author. A copy of this thesis has been supplied on condition that anyone who consults it is understood to recognise that its copyright rests with the author and that they must not copy it or use material from it except as permitted by law or with the consent of the author.

To my family

Learn from yesterday, live for today, hope for tomorrow.
The important thing is not stop questioning.

Albert Einstein (1879 – 1955), Physicist & Nobel Laureate

Acknowledgements

First of all, I would like to express my gratitude to Prof. Michele Meo who has been my mentor during the journey. He has always supported me with his professional experience and life teachings. I am thankful to have had Prof. Meo as a guide throughout my PhD and I am firmly convinced that he will be always a reference point in the future.

I turn my heartfelt thanks to my traveller fellow Mario with who I started this amazing experience at University of Bath, sharing houses, daily routine, hard time and memorable time. I will also never forget the amazing time spend with Salvatore. Thanks to both of You guys, this experience would definitely not be the same without you.

Many thanks to the good friends and colleagues that I met during these years: Dr. Onorio Iervolino, Dr. Fulvio Pinto, Dr. Francesco Ciampa, Dr. Gian-Piero Malfense Fierro, Dr. Dmitri Ginzburg, Stefano Cuomo, Marco Boccaccio, Francesco Flora, Francesco Rizzo, Mario Rapisarda, Christos Andreades and Harry Chu.

Thanks to Yanexy, who came into my life like a hurricane bringing her happiness Latino and her joy of living.

Lastly, but not least, I am grateful to my extraordinary family, my parents Giancarlo e Luisa, and my relatives Chiara e Giovanni for their constant support during my time abroad. We learnt that the absence and distance are not easy to manage, but if I am going to achieve such important milestone it is only because of You. So my biggest thanks goes to You.

Abstract

Over the last decade, the sound wave manipulation has become a focal point for many engineering applications, such as negative refraction, subwavelength imaging, cloaking and one-way transmittance. Only recently the sound wave manipulation has been deeply investigated to achieve full sound absorption because of the growing interest in noise mitigation and cancellation. However, the achieving of such challenging results is usually constrained by the general properties of naturally available materials, and this is the main reason for the emergence of engineered structures and metamaterials. In this thesis, the sound wave manipulation has been studied and applied in two main fields: material properties evaluation and perfect sound absorption. In the first case, a new approach based on the impedance tube test rig is proposed to evaluate not only the acoustic properties but also the elastic properties of the tested material. The proposed method results an innovative non-destructive approach to evaluate the out-of-plane elastic modulus for composite and porous materials.
Moreover the sound manipulation due to the sound wave and resonator structures interaction has been investigated with the main challenging purpose of low frequencies sound absorption using subwavelength structure. Therefore, in the following chapters of the thesis the developed new metamaterials are based respectively on Microperforated panel (MPP), elastic membrane, Graphene Oxide (GO) and Honeycomb structures. The sound absorption performances were studied through numerical and analytical models which helps to understand the absorption mechanism for each proposed metamaterial. Prototypes were manufactured for

each of proposed metamaterial unit cells and their absorption performances experimental tested using an impedance tube test rig. The results demonstrated how the proposed metamaterials represents subwavelength and tuneable devices which allows almost perfect and broadband absorption at low frequencies.

Contents

List of Figures

Chapter 1. Introduction

Chapter 2. Literature Review

Chapter 4 Design and Manufacturing of an Impedance Tube test rig for Acoustic Properties Measurements

Chapter 5 Non-destructive method based on acoustic measurement for elastic properties evaluation of anisotropic materials

Chapter 7 Metamaterial based on Membrane-type resonator for low frequencies sound absorption

Chapter 8 Sub-Wavelength Metamaterial for perfect broadband sound absorption

Chapter 1

Introduction

1.1. Sound Wave Manipulations and Sound Absorber

Considering a sound wave propagating in a general environment, the amount of energy associated to this wave can be described as a combination of the incident, reflected, absorbed and transmitted contributions, where the incident energy is always conserved between the three modes: Reflection, Absorption and Transmission [92]. These modes are usually quantified in terms of three coefficients which are respectively: Reflection Coefficient (***R***), the Absorption Coefficient (***α***) and the Transmission Loss (***TL***).

The major aspect of acoustic engineering nowadays is how to manipulate these modes, which affect the way the sound propagates, in order to achieve noise assessment and reduction.

Many research works are focused on each single manipulation mode. The sound wave striking a material/structure can be transmitted, absorbed and reflected

(***Figure 1.1***), and the amount of energy going into transmission, absorption and reflection depends on material/structure characteristics [10]. For instance, the Transmission mode across the material/structure is regularly considered a key parameter in the acoustic and noise reduction problems. However, material/structures which are characterized by low transmission, they will usually present high reflection.

Within the main purpose of reducing the overall sound energy, the recent research projects are focused in a material/structures designed with the aim of absorbing the incident sound energy and dissipating it via other mechanisms [94].

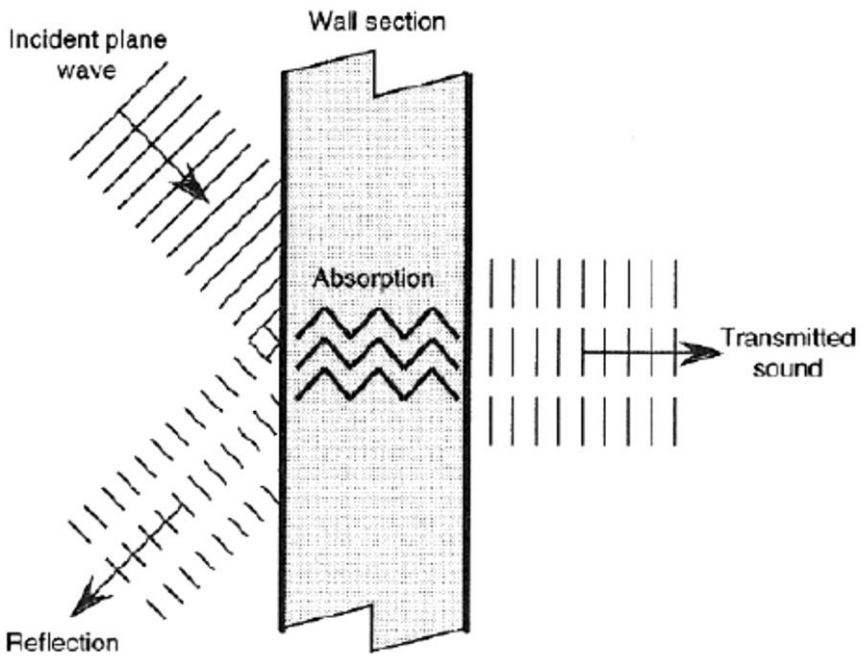

Figure 1.1. Sound wave energy contributions [93]

Three main actors play a key role in sound absorption and energy dissipation: *Viscous Dissipation*, *Thermal Dissipation* and *Impedance mismatch*.

One example is the porous absorbers which are currently used in a wide range of engineering applications. When the sound wave propagates through a network of interconnected holes, the energy will be dissipated. This is primarily due to the viscous dissipation in the vicinity of hole's wall where the non-slip boundary

condition can induce friction in the sub-millimetre boundary layer [10-95]. As well as viscous effect, there will be losses due to the thermal conduction [10-95]. However, this approach to manipulation the sound wave appears to be weak, in terms of absorption performances at low frequencies, this is because the sound dissipation is a quadratic function of frequency [95]. Because of the sound is associated with small air displacement, the relation between the generalized flux (e.g. flow rate, heat flux) and the generalized force (e.g. pressure, temperature) is linearly proportional. Therefore, since the dissipation power is represented by the product between the force and the flux and the dissipative force varies linearly as a function of the rate (e.g. dynamic friction varies linearly as a function of the relative velocity), then the sound dissipation is a quadratic function of the frequency. Moreover, the minimum thickness required for effective sound absorption is usually one order of magnitude smaller than the wavelength which makes the porous absorber inadequate due to the thickness exceeding size constrains [95-96].

Another important parameter which controls the sound wave manipulation in terms of absorption is the impedance matching. In fact, if the impedance of the absorber material/structure matches with the impedance of the air, then the reflection is minimum while the absorption into the material/structure is optimal. This opens a new branch of acoustic absorbers, which include the Micro-Perforated Panel Absorber (MPP) and the Resonator Absorbers where an air back cavity is designed the match the impedance of the air coupled with the concept of resonance. In this case the concept of resonance of single degree of freedom system is used to improve the impedance matching and increase the energy dissipation.

However, with this approach, a single frequency associated with the resonance frequency can be absorbed and even if the concept of resonance can help to increase the absorption at low frequencies, most of the resonator absorber are limited in terms of size according the quarter of wavelength [97].

To overcome these limitations and try to find a solution to the challenging problem of broadband absorption at low frequencies, the concept of Acoustic Metamaterials (AMMs) becomes of particularly interest bringing new prospective to this challenge.

The concept of Metamaterial was firstly introduced in electromagnetics to indicate new materials engineered to have properties not found naturally, which are typically arranged in repeating unit cell with proper designed geometry. However, in terms of manufacturing, the metamaterials in electromagnetics filed are particularly difficult to achieve because the characteristic size of the unit cell need to be smaller than the wavelength [98]. Moving this concept into the acoustic filed, because of the longer wavelength compared with the electromagnetic one, impressive sub-wavelength structure can be designed to manipulate the sound absorption.

The Acoustic Metamaterials are useful in manipulating acoustic waves that are governed by the Newton's law of motion, the fluid continuity equation and the thermodynamic equation of state [99]. For example, the acoustic wave equation in a homogeneous medium absent of a source is given by

$$\nabla^2 P - \frac{\rho}{K}\frac{\partial^2 P}{\partial t^2} = 0 \tag{1.1}$$

with P is pressure and ρ and k are the constitutive parameters, respectively the mass density and the bulk modulus.

The acoustic metamaterials are designed in aim of achieving a negative effective modulus and/or negative effective density which can be used to manipulated the sound wave [100] and optimized the material performances as summarized in ***Figure 1.2***.

The unusual values of negative effective density and negative modulus are strictly related to optimal absorption. The phase speed is expressed as the square root of the ration between the effective modulus and the effective density

$$c = \sqrt{\frac{K}{\rho}} \tag{1.2}$$

So, if either the modulus or density are negative, the phase velocity results an imaginary quantity corresponding in an exponential decay of the wave propagation. On the other way, when both the quantities are negative, the phase speed is real value which means wave propagation, but the energy and phase velocity are in

opposite direction. Then high absorption properties can be achieved when negative modulus and/or negative density arise.

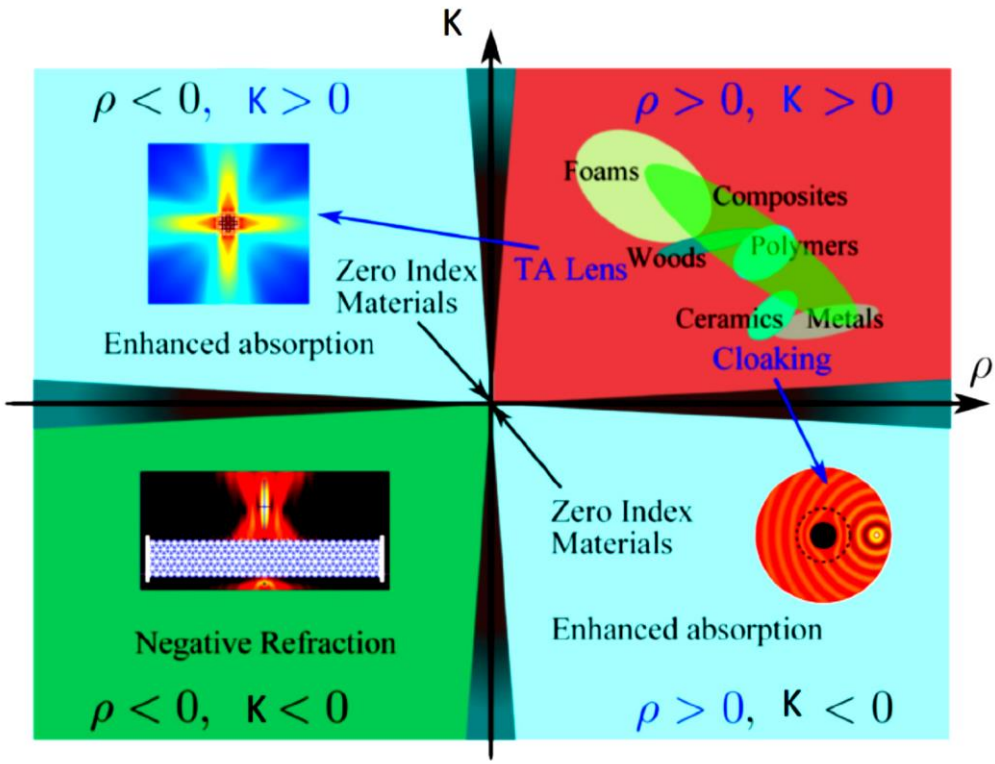

Figure 1.2. The material design space for acoustic metamaterials with example applications [101]

Negative effective mass and modulus can be achieved by very different mechanisms, which leaded the researchers to investigate deeply this topic proposing acoustic metamaterials characterized by these unusual properties based on different physical mechanisms.

Examples of negative modulus are all the acoustic metamaterials based on the Helmholtz resonator or in general cavity resonators, where the cavity acts as a dynamic volume source yielding a positive expansion as response to the applied pressure. The considerable limitation of this approach is the size of the chamber, especially for low frequency application, where typically an order of magnitude greater than the wavelength of the propagating wave need to be guaranteed.

On the other hand, negative effective density is normally shown in acoustic metamaterials membrane-type or mass-spring resonators which show an out of phase time harmonic motion of a moving mass. These metamaterials lead to effective total absorption in the sub-wavelength regime with respect the low frequency absorption. However, a broadband absorption results quite difficult to be achieved.

1.2. Sound Absorption and Noise Reduction in NVH applications

NVH (Noise, Vibration and Harshness) is becoming such a critical focus in the automotive industry since one of the highest priority is the vehicle cabin experience. When considering NVH in automotive field, the engineers are looking for the source of noise and vibration, and it refers to the entire range of perception from the initial hearing to feeling it. So, noise mitigation is not just about making vehicles quitter for more relaxing ride, but also about enhancing the infotainment experience.

There are many potential sources of NVH in automotive vehicles which can be placed in different categories: constant, periodic and random sources. Constant sources are road and wind noise, which are the results of aerodynamic fields around the vehicle. While these may vary with external factors such as speed, surface etc, they remain constant all the time the vehicle is moving. Periodic sources are those that occur from engine and transmission while random sources could be from sub-system such as pumps, or tires-roads interaction.

In conclusion the vehicle interior noise is a combination of engine noise, road noise, aerodynamic noise, intake noise and noise from components [107-108].

In particular the engine noise will be a combination of combustion noise and mechanical noise and usually is concentrated between 1- 4 KHz. The road noise includes the interior noise resulting from the contact between the tyres and the road,

being transmitted to the interior by both airborne and structure-borne paths. The road noise is mainly a low-frequency noise problem in a frequency range below 1KHz. In particular the structure-borne noise is localized below 500Hz while direct airborne noise paths from the tyre through the vehicle structure is above 500Hz which is often confused with wind noise.

Regarding the aerodynamic noise, it is a significant source of interior noise for many vehicles travelling at higher speeds. It is easily confused with road noise, being generally broadband in nature but with strong low frequency bias. A component of interior noise is also demanded to the brake system, including brake squeal with frequency components well above 1 KHz and brake moan with frequency component around 100Hz. In conclusion, the vehicle interior noise is concentrated in a frequency range between 100-4000 Hz.

If the aerodynamic noise can be controlled by proper design the vehicles profiles in order to optimize the aerodynamic interaction of the vehicles itself with the fluid, all the other interior noise components need to be mitigated using different solutions.

Nowadays the commonly used solution for noise mitigation and reduction in the vehicles cabin are the porous absorbing materials. However sound absorbing materials make a contribution to controlling the level of higher frequency noise in vehicle interiors. Their usefulness in controlling low frequency sound components, usually below 500Hz, is limited as the thickness of absorbing material required would be bulky and add too much weight to the vehicle. In fact, the efficiency of the porous material in sound absorption is proportional to the thickness of material itself and as reported in Figure 1.3, normally a global thickness of 100mm is required to absorb sound component around 500Hz, which represent a strong limitation in terms of engineering application. Usually the porous material thickness for NVH solution falls in a range between 5-50mm. Figure 1.4 shows the recent results in the terms of absorption properties of different acoustic porous materials with different thickness currently used in the automotive industry [109]. The tested materials are: sample1 - Basalt Wool (5mm), sample2 - Basalt Wool (15mm) , sample3 - Thetacell (10mm), sample4 - Thetafiber (10mm), sample5 - Polyester

(40mm), sample6 - Polyester (5mm). It is clear how these materials are quite efficient at high frequencies, however even with considerable thickness (40mm) their absorption properties degenerate considerable for frequencies lower than 1500Hz.

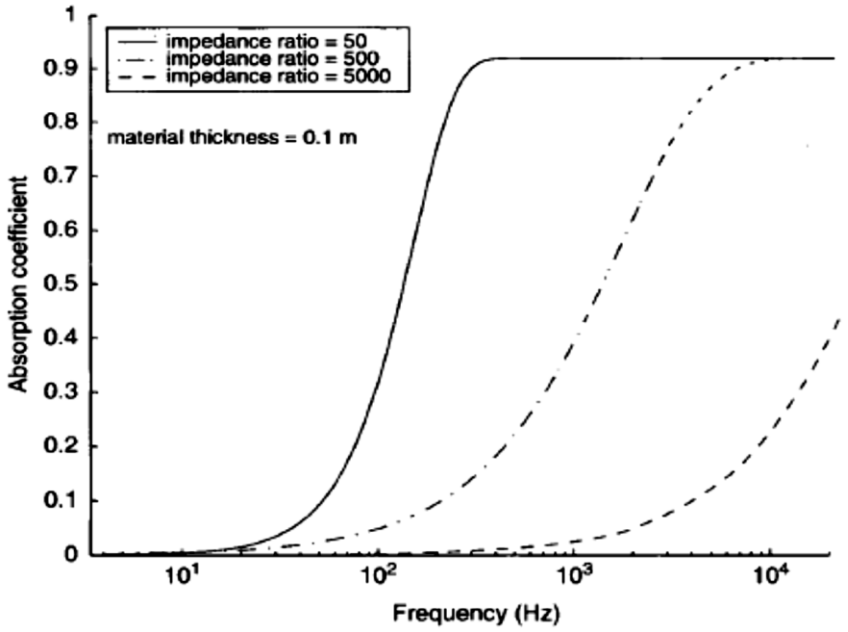

Figure 1.3 Typical absorption characteristic of porous material of 100mm thickness for different characteristic impedance [108].

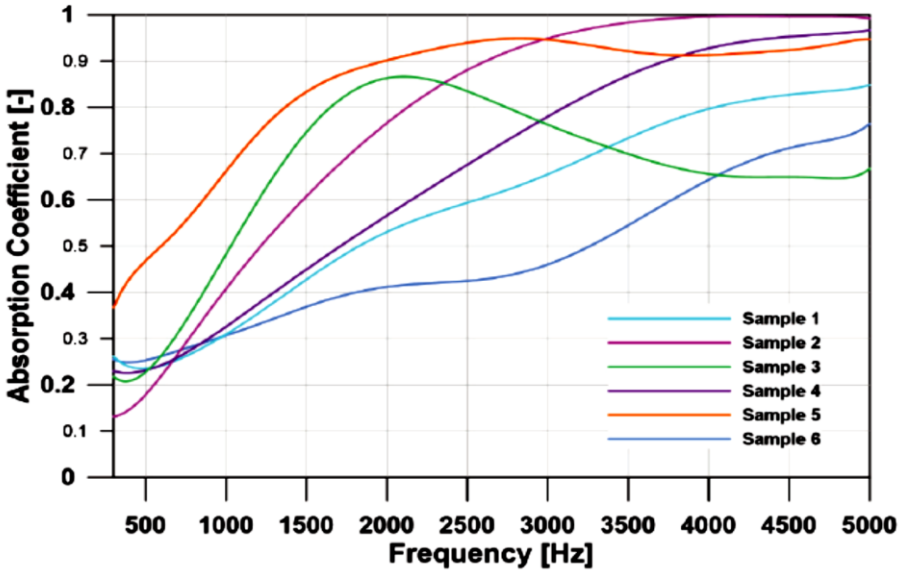

Figure 1.4 Sound absorption for acoustic porous materials in automotive application [109]

1.3. Objectives and overview

The principal aim of the present research work is to investigate the sound wave propagation/interaction with materials/structures in order to develop applicable solutions in the acoustic engineering field.
In particular the presented research is focused on two main macro-areas of interest:

- Material properties characterization
- Acoustic metamaterial for sound absorption

The first macro-area covers the vital need to evaluate the material properties and in particular the elastic properties of specific material types which have had a progressive growth in last years like composite materials and foams.
The traditional and common engineering methods for the material characterization are generally: tensile testing, compression testing and three points bending testing. These tests are suitable for isotropic materials since, as a tensile test can provide the elastic properties characterization only in one direction which is the direction of tension. This could be a limitation for anisotropic materials where, considering composite materials as an example, the out-of-plane Young's Modulus becomes challenging as these structures are usually thin in the out-of-plane direction. Moreover, these tests represent destructive test, as well as instrumental indentation test that infers from an indentation size and depth the Young's modulus.
There are then some non-destructive tests for material characterization purpose as the Resonant Frequency Test which estimates the Young's Modulus starting from the resonant frequencies obtained in the test. However, this approach is generally appropriated for thin film material and in any case allows the in-plane elastic properties.
The possibility to develop a non-destructive approach for the out-of-plane Young's modulus evaluation have been investigated and a new acoustic impedance-based method, applicable to composite materials and foam, is presented. The proposed method is based on the acoustic impedance measurement using an impedance tube approach. The impedance tube allows to generate a plane wave which will

propagate in the tube and interact with the tested sample. A standing wave is then generated in the tube as a consequence of the incident wave upon and reflected one from the test material. Because of the standing wave condition, measuring the pressure level in two sections of the tube, the reflection coefficient and then the acoustic impedance could be measured applying a Transfer Function Approach.
The reflection coefficient will be related to the acoustic impedance of the air, and at the same time to the acoustic impedance of the tested material. Since an incident plane wave will excited the longitudinal propagation wave into the material, then the acoustic impedance will be a function of the material density, and the longitudinal speed of sound. Moreover, the longitudinal speed of sound, under the assumption that the lateral dimension of the tested sample is smaller than the incident wavelength, is dictated by the elastic properties of the material.
So, manipulating the sound wave propagation and playing with the wave/material interaction in terms of sound reflection, the elastic properties, in particular the out-of-plane one, of anisotropic material can be measured in a non-destructive way.

The second macro area investigates the sound wave manipulation and the sound wave/structure interaction to develop new acoustic absorber structures and new acoustic metamaterials to be used in NVH applications.
As introduced in the previous paragraph, the vehicles interior noise mitigation/reduction problems are mainly covered using pours absorber materials.
However, the sound absorption performances of common acoustic foam used in the automotive industry are strictly related to the thickness of the material. The vehicle internal noise is the result of a sum of different noise sources which leads to a quite broadband noise spectrum. While the interior noise spectrum is in a frequency range between 100 to 4000 Hz, the porous absorbers nowadays installed on the vehicles are useless to absorbing frequencies below 1000 Hz with reasonable thickness (30-40mm). Moreover, 100mm thickness of material is required to achieve sound absorption at 500Hz which is a strong limitation because of the engineering constrains (weigh, size, etc).
.

Different solutions have been proposed to achieve sound absorption at low frequency such as resonator absorbers and recently the acoustic metamaterials.

The resonator absorbers, including Microperforated Panels (MPP), Helmholtz's resonators, etc. are characterized by the same limitation of the porous absorbers: their applicability at low frequencies is directly proportional to the thickness. Moreover, most of the resonator absorbers behave as single degree of freedom system and the absorption properties are related to the single resonance frequency. They cannot generate a broadband sound absorption. Regarding the acoustic metamaterial and in particular the membrane-type metamaterials, they are normally subwavelength absorbers which means they can achieve sound absorption for low frequencies (below 500 Hz) with reasonable small thickness (20-30mm). However, also the membrane-type acoustic metamaterials as for the resonator absorbers, they behave as single degree of freedom system and the absorption profile is characterized by a single narrow absorption peak.

In the present research work we investigate, and we proposed innovative solutions for vehicle interior noise absorption which overcome the limitations associated to the currently used porous absorbers. The aim is to achieve broadband sound absorption in a low frequency range (< 1KHz) minimizing the size of the absorber (ideally the thickness < 100mm).

Three different subwavelength passive absorber prototypes are presented.

The first proposed prototype is a multiplayers micro-perforated absorber which is capable of guaranteeing 90% of sound absorption in a frequency range of 300-2000Hz with a global thickness of 100mm. The performances in terms of absorption level and frequency range are related to the design parameters. An analytical model based on an equivalent electro-acoustical model is presented and used to investigate the effect of such parameters which are of paramount importance to optimize the design. In fact, the proposed prototype can be tuned to guarantee broadband absorption in the required frequency range.

The second prototype is based on the membrane-type acoustic metamaterial approach. The common membrane-type metamaterials behave as single degree of freedom which leads to a single absorption peaks. We proposed a new membrane-

type metamaterial which is forced to behave as multi degree of freedom system. Multiple resonances arise in the considered frequency range associated to the mutual interaction between the structural dynamic response and acoustic dynamic response of the resonator. The absorption profile will be then characterized by multiple peaks with a global broadband absorption at low frequencies.

The proposed prototype is a subwavelength acoustic resonator including a thin elastic plate and an enclosed air cavity which allows the sound absorption in a frequency range of 250-400Hz with a global thickness of 23mm. The absorption mechanism is associated to the hybrid resonances which occur when high order structural modes of the elastic plate are coupled with the acoustic modes of the cavity. A numerical model has been also proposed and validated with experimental measurement which will be deeply discussed in the following chapters.

In the third prototype we combined the concept of multi degree of freedom membrane-type metamaterials with the material properties of Graphene Oxide (GO). The prototype consists on GO micro foil embedded in a honeycomb core with a second GO micro foil as external skin. The single unit cell includes the GO foil, acting as membrane, and the honeycomb unit cell acting as resonating acoustic chamber. The single unit cell behaves as multi degree of freedom membrane-type metamaterial generating multiple resonance frequencies in the frequency range of interest. Moreover, the GO shows high damping properties which make wider the single resonance peaks. The resonance peaks start then to collapse to each other because of the high GO damping, leading to flat broadband sound absorption. Because the prototype need be suitable for NVH application not just the absorption properties but also the strength properties of the device need to be guaranteed. An equivalent configuration is then presented when the GO foil external skin is replaced by an MPP external skin. We demonstrate how optimizing the design of the MPP external skin, we can achieve the same absorption performance of the original configuration but with a considerable increment of the device strength.

The proposed subwavelength prototype achieves perfect sound absorption between 300Hz and 2500Hz with 70mm thickness or between 400Hz and 2500Hz with 50mm thickness. To study the absorption properties of the prototype an analytical

model is proposed based on the solution of the modal-acoustic problem. The impedance of the unit membrane-type cell can then be estimated and combined with the equivalent acoustic circuit analysis results in order to take into account the effect of the MPP external skin.
All the proposed prototypes have been manufactured and tested in an impedance tube test rig to evaluate the sound absorption properties.

1.4. Outline of the Thesis

The outline of the thesis is the following.

Chapter 2: a detailed literature review is presented, where a number of research works are reported in order to define the state of art of the passive absorber devices used for sound absorption. We focus in particular on the resonator absorbers grouped in two main categorises: Micro-Perforated Panel Absorber and Acoustic Metamaterials. Regarding the Acoustic Metamaterials only the Membrane-type, Plate-Type and Helmholtz-type resonators are taken into account.

Chapter 3: the basic concepts of acoustics are provided. Stating from the Continuity and Equilibrium equations, the sound wave propagation equation is derived. Concepts of how the sound wave equation can be implemented in a FE formulation are described. Moreover, the sound wave equation is used to derive the equivalent electro-acoustically formulation.

Chapter 4: the hardware and software design of an impedance tube test rig is described. The presented impedance tube test rig was designed, machined and assembled to support all the experimental measurements needed in this research work.

The main topics of the thesis will be exposed in a number of published papers. Each publication will be introduced by a brief description in which the motivation, the summary and the results of the single paper will be summarised.

Chapter 5: a new non-destructive method for the out-of-plane elastic properties evaluation is presented based on the acoustic impedance measurement through the Transfer Function approach. The method is suitable for anisotropic material as composite materials and foams.

Chapter 6: a multilayer micro-perforated absorber suitable for broadband sound absorption at low frequencies is presented. An optimization analytical process is also discussed based on equivalent electric-acoustical circuit analysis to demonstrate how the proposed absorber can be tuned with respect of the required frequency range.

Chapter 7: a new multi degree of freedom membrane-type metamaterial for broadband sound absorption at low frequencies is proposed. The absorption mechanism is leaded by hybrid resonances coming out from acoustic-structural resonances interaction. A numerical model is also presented to investigate and explain the absorption mechanism behind the proposed metamaterial.

Chapter 8: a new subwavelength resonator metamaterial for perfect absorption at low frequency is proposed. The metamaterial, based on embedded Graphene Oxide in honeycomb core, behaves as multi-degree of freedom resonator system with multi hybrid structural-acoustic resonances. Prototypes are manufactured and tested in an impedance tube test rig to evaluate the absorption performances. Analytical model is also presented to explain the absorption mechanism.

Chapter 2

Literature Review

2.1 Micro-Perforated Panel (MPP) Absorber

The Micro-Perforated Panel Absorber (MPP Absorber) is probably one of the most common Resonant Absorber, which can be considered a particular case of Helmholtz resonator. Considering sub-millimetre perforations, where the hole diameter is comparable with the boundary layer thickness, the losses will occur due to viscous boundary layers effects in the perforations [10].

The MPP Absorber structure usually consists of a micro-perforated sheet with an air-cavity behind, which represents a neat device because the physic of the system is associated to the resonance of a single degree of freedom mass-spring-damper system. The vibrating mass is the mass of air into the perforations while the spring is provided by the air enclosed in the cavity and the losses are provided by the boundary layer effect. So, the acoustic MPP absorber can provide a single narrow absorption peak at the resonance frequency.

The concept of MMP absorber was developed by Maa [13] who established the theoretical basis and the design principle of MPP absorber and proposed to describe the absorber using an equivalent electric circuit.

Maa proposed a model constructed from a thin perforated sheet of thickness t_h, with a certain perforation ration p, and a main hole diameter d. The perforated sheet was backed by an air cavity of depth D [14-15]. The theoretical model begins by considering the sound wave propagation within single short cylindrical tube. If the length of the tube is small compared with the wavelength, then starting from the equation of aerial motion, which describe the sound wave propagation into the tube, the specific acoustic impedance of the tube is given by [15]:

$$Z_1(\omega) = \frac{\Delta P}{u} = j\omega\rho_0 t_h \left[1 - \frac{2}{x_v\sqrt{-j}} \frac{J_1\left(x_v\sqrt{-j}\right)}{J_0\left(x\sqrt{-j}\right)}\right]^{-1} \tag{2.1}$$

where J_0 , J_1 are the Bessel function of the first kind and zero and first order respectively, $r_0 = d/2$ the radius of the orifice, ρ_0 is the air density. The term $x_v(\omega) = r_0\sqrt{\omega\rho_0/\eta}$, with η the air coefficient of viscosity, provides the losses through the tube as it is proportional to the ratio of the radius to the thickness viscous boundary layer. Maa [14] details an asymptotic solution of equation (2.1) for the typical values of $x(\omega)$ $(1 < x(\omega) < 10)$

$$Z_1(\omega) = \frac{32\eta t_h}{d^2}\sqrt{1 + \frac{{x_v}^2(\omega)}{32}} + j\omega\rho_0 t\left(1 + \frac{1}{\sqrt{9 + \frac{{x_v}^2(\omega)}{2}}}\right) \tag{2.2}$$

To get the specific impedance of the perforated panel, equation (2.2) can be applied to the holes of the MPP and divided by the perforation ration, which is defined as the ratio between the perforated areas over the area of the panel.

The real and imaginary part of the specific impedance assume the physical meaning respectively of acoustic resistance (R_1), representing the energy radiation and the viscous loses of the acoustic wave propagating through the perforations, and acoustic reactance (M_1), refers the mass of the air moving inside the perforation. In order to take into account the resistance due to air flow friction on the surface of the panel when the flow is forced to pass through the micro holes, and the mass reactance due the piston sound radiation at both ends, Maa uses the formulation of Morse and Ingard [16-17].

The specific impedance of the MPP can be then written as

$$Z_{MPP}(\omega) = \frac{Z_1(\omega)}{p\rho_0 c} = R_1(\omega) - i\omega M_1(\omega) \tag{2.3}$$

The normal incident absorption coefficient of a traditional single MMP absorber is derived by the well-known formula

$$\alpha(\omega) = \frac{4Re[Z_{tot}(\omega)]}{(1 + Re[Z_{tot}(\omega)])^2 + Im[Z_{tot}(\omega)]^2} \tag{2.4}$$

Where the $Z_{tot}(\omega)$ is the specific acoustic impedance of the MPP absorber defined as the sum of the MMP specific impedance and the acoustic impedance associated to the mass of air behind the panel which is a function of the depth *D* and can be estimated by

$$Z_{tot}(\omega) = Z_{MPP}(\omega) - jcot\left(\frac{\omega D}{c}\right) \tag{2.5}$$

From equation (2.4) is clear how the absorption level and the working frequency range associated to the MMP absorber is effectively influenced by the geometrical parameters of the performed panel [18-19-20]. ***Figure 2.1*** and ***Figure 2.2*** show the effect of the hole diameter and the perforation ratio on the absorption peak.

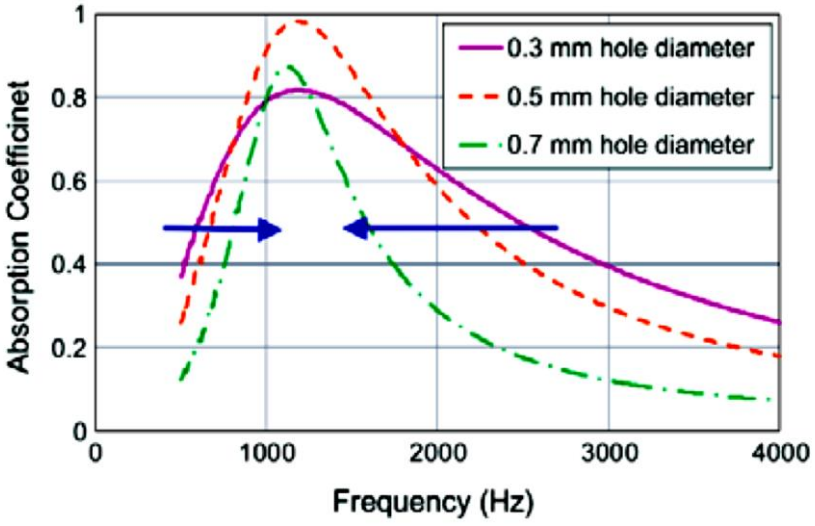

Figure 2.1. Effect of hole diameter on the MPP absorber sound absorption coefficient [18]

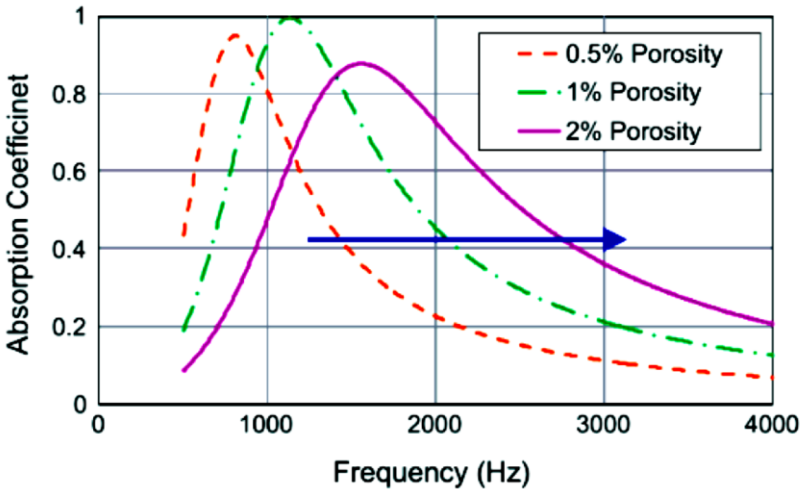

Figure 2.2. Effect of Perforation ratio on the MPP absorber sound absorption coefficient [18]

The single absorption peak associated to the MPP absorber represents a strong limitation which reduce the range of applications. So many researchers worked to improve the sound absorption capability of the absorber to broaden its bandwidth. The most common approach to achieve a broadband absorption is fully or partially full the enclose cavity of the resonator with porous material [21-22-23].

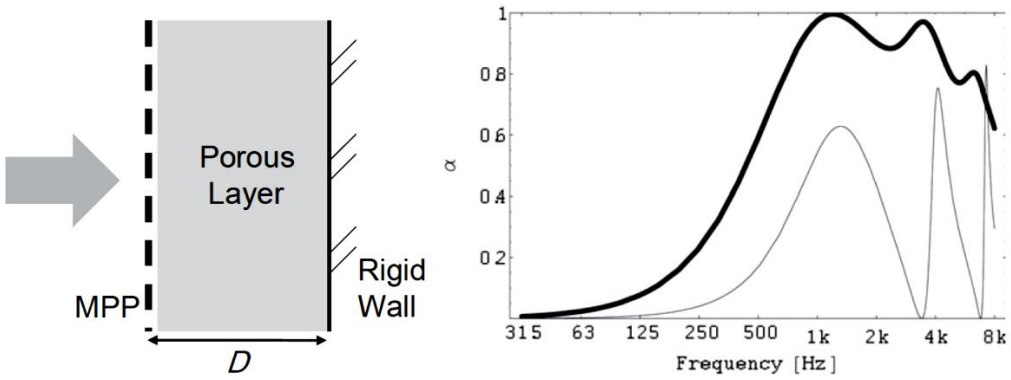

Figure 2. 3. Comparison between air backed MPP (thin line) and porous layer backed MPP (thick line). The MPP geometrical parameters are: hole diameter d=0.3mm, thickness t=0.3, perforation ratio p=5%, cavity depth D=50mm [23]

The dimension of the air cavity backed to the MPP plays a key role in the absorption properties. Since the mass of the air into the enclose cavity assumes the physical meaning of stiffening in a common single degree of freedom mass-spring system, increasing the volume of the backed chamber will shift the absorption peak of the

absorber at lower frequencies; in other words the backed chamber can be designed to match the required goal [24].

In this way, Wang et al [25] studied the effects of irregular-shaped cavity on the absorption performances. Taking into account the acoustic cavity modes, defined by equation (2.6), they demonstrated how considering a rectangular cavity, only the (0,n) acoustic modes are coupled with the MPP, so the absorption is associated to the 'piston motion' of the MPP-cavity system. Replacing the rectangular cavity with a non-uniform one (trapezoidal cavity), then all the (m-n) are involved which can produce more spectral peaks and increase the absorption properties ***Figure 2. 4***.

$$\varphi_{m,n}(x,y) = cos\left(\frac{m\pi x}{L_a}\right) cos\left(\frac{m\pi y}{L_b}\right) \tag{2.6}$$

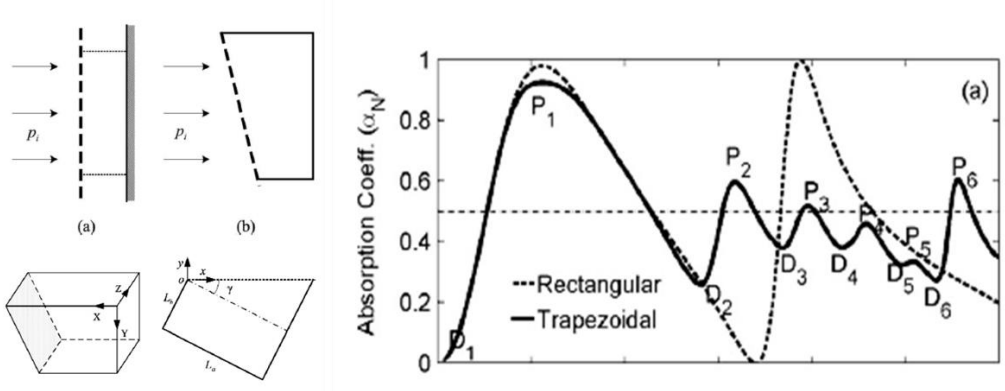

Figure 2. 4. Comparison between the absorption coefficient of MPP absorber with rectangular and trapezoidal air-backed cavity [25]

The absorption bandwidth can be considerable improved considering also multiple depths [27-28-29] of the air cavity or introducing one or more chamber partitions [26]. For instance, Wang and Huang [27] proposed multiple MPP absorbers with different cavity depths shown in ***Figure 2.5***. In this because of the non-uniform depth of the cavities, the single component MPP absorber get to resonance at difference frequencies. These strong local resonances account for the sound absorption while the supplementary sound absorption by the non-resonating MPP absorbers is trivial for the resonance performance. In the absorption mechanism, the out-phase air motion between the resonating and the non-resonating MMP

component is also involved changing the effective acoustic reactance of the MPP patch covering the resonating cavity, which shift the resonance frequency respect to the uniform cavity depths.

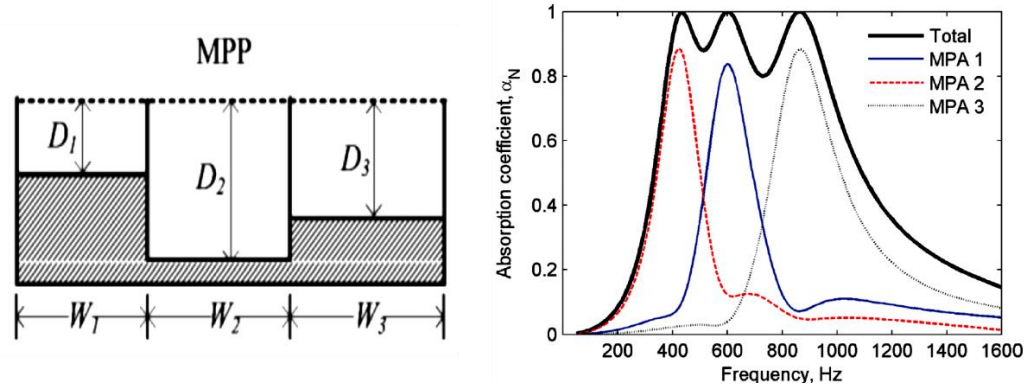

Figure 2.5. Absorption coefficient of MPP absorber with different cavity depths and the contribution of the single MPP component [27]

The parallel arrangement of MPP absorber is not the only solution which provides broadband sound absorption. The frequency absorption frequency can still be broadened with different arrangements of MPP layers.

Based on the wave theory and the Helmholtz-Kirchhoff formulation, Sakagami et. al [30-31] demonstrated how a double-leaf micro perforated panel series arrangement is effective for designing a wide-band absorption. As the single MPP leaf case, the properties in terms of wideband absorber can be considerable increased considering the hybrid double-layer microperforated panel/porous system [32] which can provide more than 90% of absorption in a frequency band ranging from 500 up to 14000 Hz (***Figure 2.6***).

Based on the equivalent electrical circuit model, Qian et al [33] tried to combine the double-leaf MMP with multiple cavity with different depths, obtaining high absorption over broad frequency band as reported in ***Figure 2.7***.

As stated above, for single or multi-leaf MPP absorber, the absorption performances are strictly related to the main structure parameters. Many authors studied then inhomogeneous MMP absorber with not constant structure parameters with the main goal to generate broadband absorption at low frequencies. In this way, example of parallel and series arrangements of MPP absorbers with different hole

diameters, or different perforation ratio can be found in literature [34-35]. All these research works are based on the assumption that the broadband absorption of inhomogeneous MPP absorber can be achieved optimising the structure parameters design (hole diameters, perforation ratio etc.) of each single MMP in order to move the single resonance close to each other. Since the parameters involved in the absorption mechanism are so many, in the last years many researcher published parametric analysis on the inhomogeneous MPP absorbers in order to better understand the effect on the structure parameters on the absorption [35-36-37].

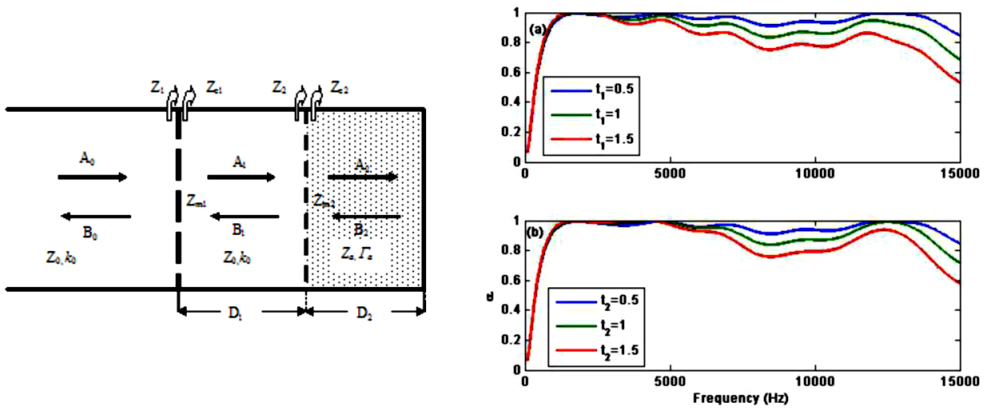

Figure 2.6. Absorption curves of a DL-MPP/P absorber with parameters (d1, p1, D1, d2, p2, D2, R1, V , β, γ) = (0.5 mm, 30%,1.9 cm, 0.5 mm, 30%, 5 cm, 21000 rayl/m, 0 m/s, 0, 0) with (a) t1 (in mm) variable and t2 = 0.5 mm, and (b) t2 (in mm) variable and t1 = 0.5 mm [32]

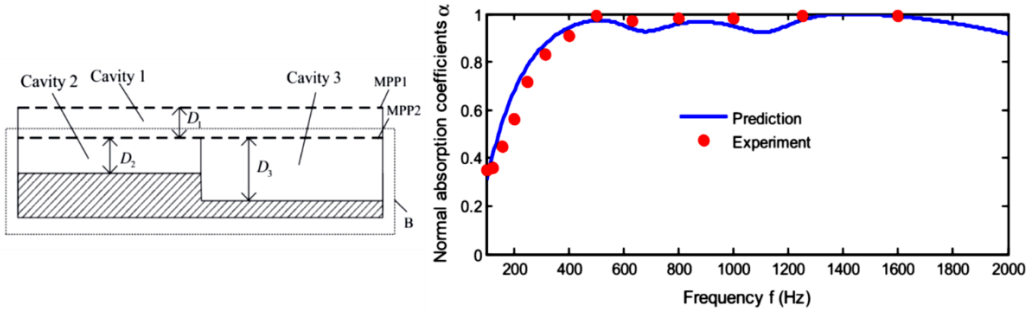

Figure 2.7. Absorption coefficient for a prototype with the following properties: D1,2,3=10mm,16mm,40mm; d1,2=0.13mm,0.15mm; t1,2=0.5mm,0. 5mm [33]

All the studies cited above considered the MMP as a rigid panel.

Lee et al [38] firstly taken into the account the flexibility of the perforated panel. In his mode, Lee studied the coupling effects of the micro-perforation, the flexible

panel vibration and the acoustic cavity modes. The dynamic response of the MPP was described using the differential governing equation of the plate, while the acoustic filed in terms of pressure and particles velocity was described by the homogenous wave equations. This model leads to the conclusion that the absorption peaks due to the panel vibration effect can widen the absorption bandwidth of MPP absorber.

In this case, as in the previous ones, it has been proven that the effective sound absorption at low frequencies is often limited except for considerable cavity depth. In order to cover this limitation, the researcher started to combine the concept of permeable/impermeable membrane [39-40-41-42], which provide better absorption at lower frequencies for the same cavity depth, with the MPP concept.

Hybrid MPP and PM (permeable membrane) with parallel or series arrangements started to be studied.

Sakagami [43], for instance, proposed a sound absorption structure with an MPP and a permeable membrane with a rigid-back wall and air cavities in between. Two main configurations were investigated: MPP on the illuminated side and PM on the illuminated side. The effect of MPP and PM combination for the first configuration is clear in ***Figure 2. 8*** where the absorption coefficient of the MPP-PM absorber is compared with the equivalent MPP-MPP absorber: the PM contributes to make the peak higher and efficient absorption. Comparing the MPP-MP structure with the equivalent MPP-MPP structure, we can say that the width of the absorption frequency range is almost the same, regarding the absorption peaks the MP increase the performance of the absorption.

The effect on sound absorption, when the MP is placed on the illuminated side is shown in ***Figure 2.9***. The PM-MPP structure shows porous-like absorption behaviour but comparing the absorption performances with a single MP absorber with the same air gap and the double MPP absorber, is clear how the use of MPP is almost useless when the PM is on the illuminated side.

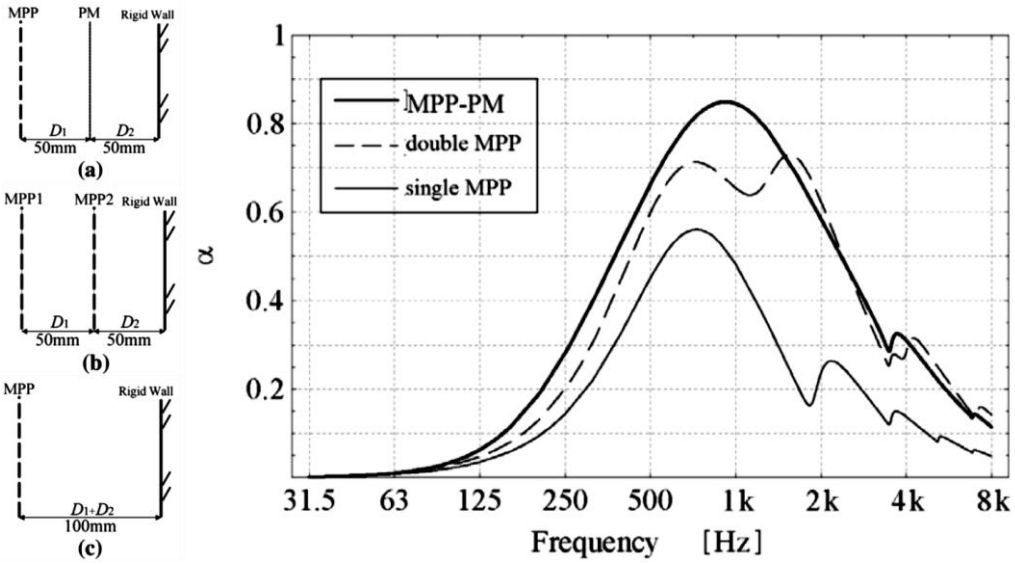

Figure 2. 8. Absorption coefficient of MPP-PM structure in comparison with single MPP absorbers: D1 =D2=50mm, t=0.3mm, d=0.3mm, p=1% [43].

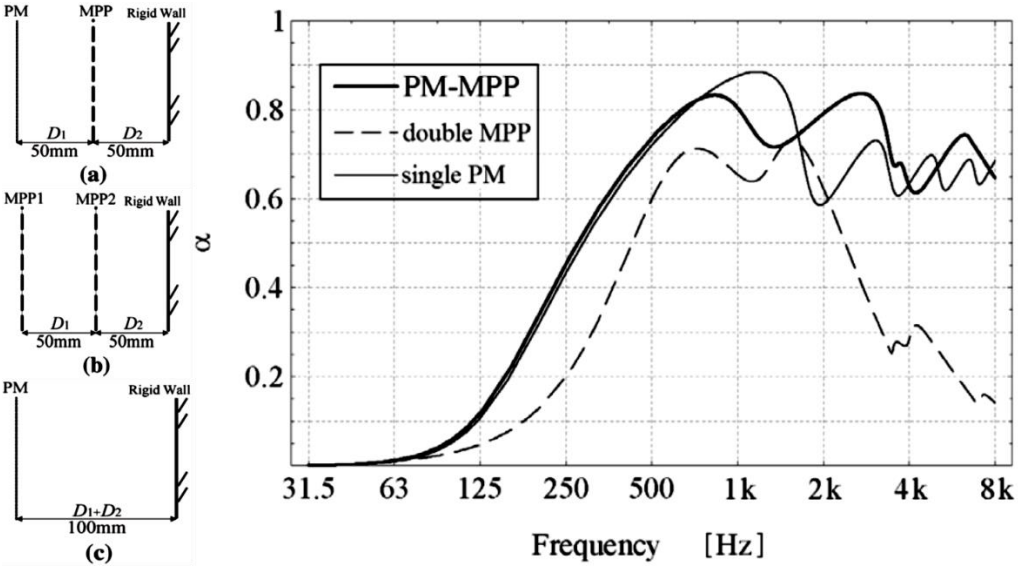

Figure 2.9. Absorption coefficient of MP-MPP structure in comparison with double MPP absorber and single MP absorber: D1 =D2=50mm[43]

Gai et al. in their studies [44-45] tried to combine in parallel arrangements, the MPP resonators with membrane cell. Following experimental results obtained from impedance tube measurement, they investigated the effect of the membrane cell size of the membrane cells. As shown in ***Figure 2.10***, the MPP with membrane

cells can provide more absorption than the single MPP absorber, and optimizing the size of the membrane cell, a wide sound absorption bandwidth and higher sound absorption peaks can be achieved.

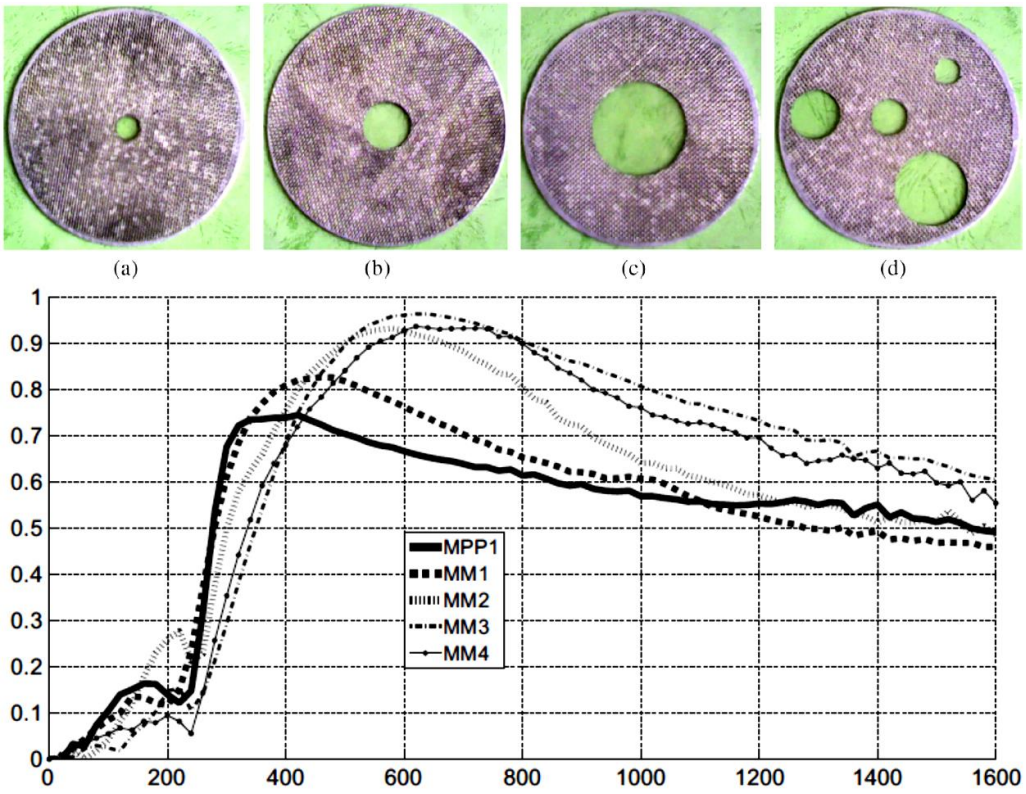

Figure 2.10. Experimental absorption curve of the single-leaf MPP (MPP1), the single-leaf MPP with 10 mm diameter membrane (MM1), 20 mm (MM2), 40 mm (MM3) and four membrane cells (MM4) [44].

The MPP absorbers are usually made of thin limb material, so they need to be reinforced in order to be effectively applicable. Many research projects suggested to use a honeycomb structure attached behind an MPP, showing that the honeycomb into the back cavity of the MPP absorber increases not only the sternness of the absorber but also the acoustic performance in terms of sound absorption particularly at low frequencies [43-46-47-48]. Different numerical model has been also developed and proposed, based on the Maa model [46] or on the Helmholtz—Kirchhoff integral approach [48]. These studies show how the honeycomb in the air cavity has an effect to increase the absorption peak associate to the absorber and at the same tie to broaden the absorption frequency range shifting at lower frequency.

2.2 Acoustic Metamaterial

2.2.1 Membrane and plate – type metamaterials

Acoustic Metamaterials (AMMs) membrane and plate – type is a general light-weight solution, which is particularly important in the prospective of low frequencies noise reduction and control [49]. This AMMs type have found applications in low-frequencies sound attenuation [50-51-52], cloaking [53], angular filtering [54] and many others. In this work, we will focus our attention to the membrane and plate – type AMMs for sound absorbing.

The membrane-plate type AMMs are usually devices which exhibit negative effective density when excited by acoustic wave, as a result of the restoring force in the membrane/plate generating an out of phase oscillation. This behaviour enables the use of sub-wavelength structures for low frequency absorption, therefore defying the conventional mass-density law [55].

The governing motion equation for a membrane under acoustic excitation can expressed as follow

$$T\nabla^2 w(x,y,t) - \rho_0 h \frac{\partial^2 w(x,y,t)}{\partial^2 t} = -P(x,y,t) \qquad (2.7)$$

where T is the uniform tension per unit length applied to the membrane, p is the external pressure, h is thickness of the membrane and ρ_0 is the air density. For a thin membrane equation (2.7) is still true, but the response is intrinsically dictated by the plate stiffness ($D_p = Eh^3/12(1-\upsilon^2)$, with E the Young's modulus, and υ the Poisson's ratio) instead the membrane tension.

Solving equation (2.7) the effective density can be estimated from the out of plane displacement and the normal acceleration of the membrane. Moreover for a membrane-type AMMs, the effective density has been shown to follow the Drude form and could be written as [49-50]

$$\rho_{eff} = \rho' \left(1 - \frac{\omega_c^2}{\omega^2}\right) \tag{2.8}$$

where ρ' is the averaged density of the air loaded with the membrane/plate and ω_c is the first resonance frequency of the membrane/plate. From equation (2.8) and ***Figure 2. 11*** is clear how the effective density is zero at the first resonance frequency, while is negative at frequency below of ω_c. With the frequency range below the first natural frequency, the normal acceleration of the membrane has been found to be out of plane with respect to the external incoming sound excitation.

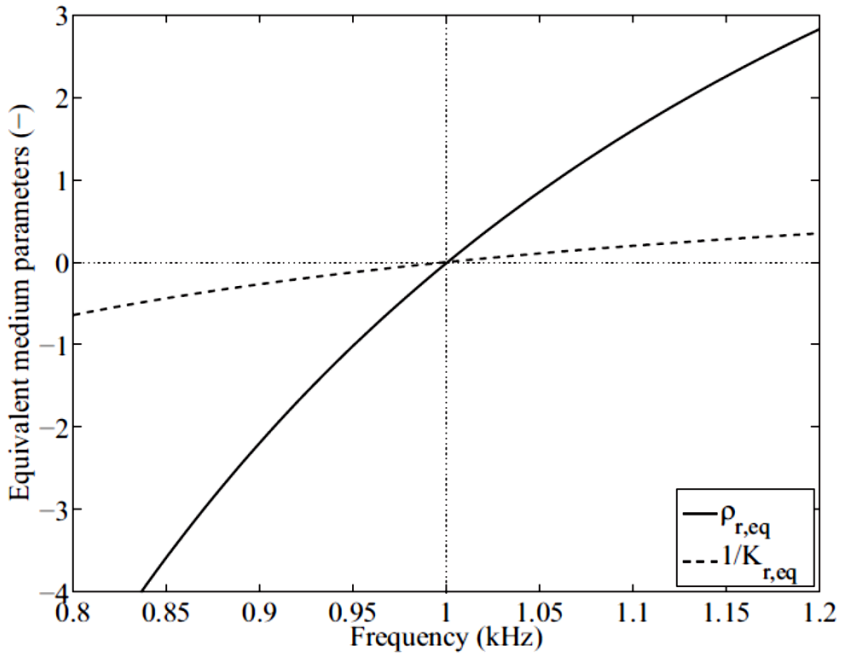

Figure 2. 11. Normal effective density of clamped plate-type AMM [56]

Following this approach Shen [57] and Huang [49] outlined for a membrane, negative density would occur over a wide broadband below the first resonant frequency of the membrane, known as the cutoff-frequency. The same negative density behaviour was observed by Lee et al. [50], who proposed an array of pre-stretched membrane placed in series with a certain separation distance in a waveguide, and the Drude-form (equation 2.8) was theoretically derived.

Yao et al. [52] used a mass-spring model to explain the negative density below the cutoff- frequency and the numerical model has been validate measuring the

transmission loss of the structure shown in ***Figure 2. 12***. The structure is a periodic system, where two aluminium blocks, together with a connecting sheet, realized the mass *m.* The aluminium blocks are connected to a fixed aluminium block by two spring (G_s); while the single cell of the periodic system is connected to each other by springs (K_s). Yao et al. [52] started from the equilibrium equation of a spring-mass system (equation (2.9)) to estimate the dispersion relation of the system (equation (2.10)).

$$m\frac{d^2w_n}{dt^2} = K_s(w_{n-1} - w_n) - K_s(w - w_{n+1}) - 2G_s w_n \tag{2.9}$$

$$\left(m - \frac{2G_s}{\omega^2}\right)\omega^2 = 4K_s sin^2\frac{qa}{2} \tag{2.10}$$

where q is the Bloch wave vector and a is the spacing apart between the unit cell. Comparing equation (2.10) with dispersion relation of a simple mass-spring lattice model, Yao [52] defined the effective mass of the system

$$m_{eff} = m\left(1 - \frac{\omega_0^2}{\omega^2}\right) \quad with \quad \omega_0 = \sqrt{\frac{2G_s}{m}} \tag{2.11}$$

The measured and estimated transmission loss with the effective mass are plotted in ***Figure 2. 13***. It is seen that negative effective mass occurs below the cut-off frequency and the transmission loss drops below such frequencies which demonstrates the existence of negative mass.

In 2010 Lee [58] used the previous array of pre-stretched membrane presented in [50] with branch opening (side holes) to demonstrated how double negative, density and bulk modulus, can be achieved using membrane-type metamaterials. The proposed structure combines the effect of negative effective density (equation 2.8) provided by the membrane and the negative bulk modulus (equation 2.12) provided by the side holes to define a frequency gap. In fact, according with equation 2.12, below the cut-off frequency ω_{SH} it has a negative bulk modulus, while above ω_{SH} the modulus is positive.

$$K_{eff} = K\left(1 - \frac{\omega_{SH}^2}{\omega^2}\right)^{-1} \tag{2.12}$$

The consequent transmission loss is plotted in ***Figure 2.14***. There is a frequency gap in the range of frequency between $\omega_{SH} < \omega < \omega_c$, and for the frequencies below and above this gap the medium is transparent. It was observed how the phase velocity is negative under the cut-off frequency of the branch opening (ω_{SH}) [61]. The capability of the branch opening to introduce negative bulk modulus in these kind of metamaterial, is studied in many other research jobs [59,60]. Samples were fabricated, tested and the measured acoustic properties compared with the results provided by the analytical model proposed. The physics behind such double negativity can be summarized as follow. The phase velocity is found to be negative under the cut-off frequency of the branch opening (ω_{SH}), and a reversed Doppler effect can be observed [66]. Above the membrane resonance frequency (ω_c) is double positive, while for the frequencies in-between the cut-off frequency and the resonance frequency, such metamaterials show only negative density.

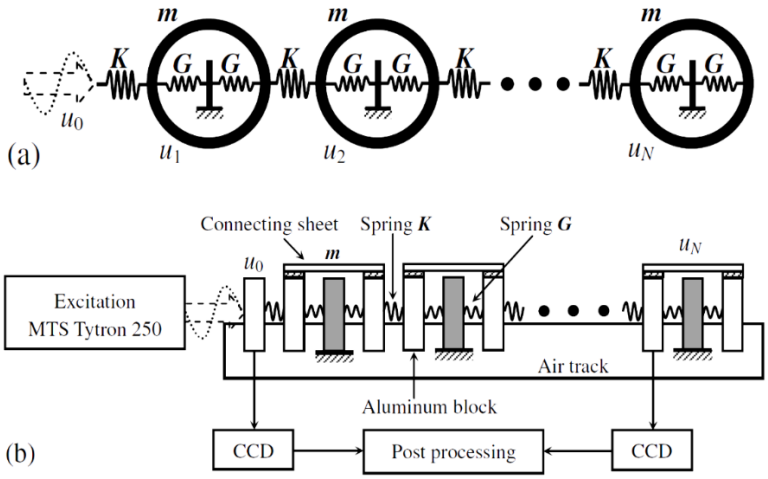

Figure 2. 12. Finite mass-spring system (a); experimental realization for such system (b) [52]. The displacement u_n refer to the displacement w_n in equation 2.9

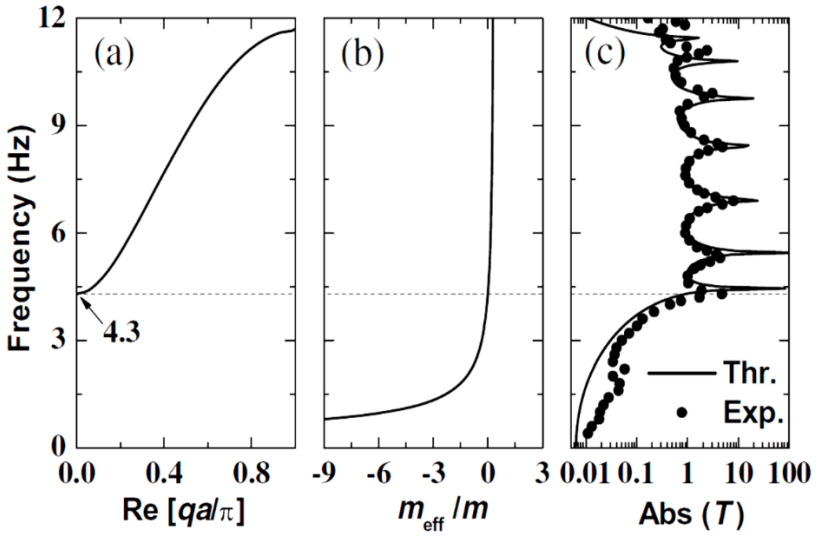

Figure 2. 13. (a) Dispersion curve from equation (2.10), (b) normalized effective mass from equation (2.11), (c) experimental and theoretical transmittances for a seven-period system [52]

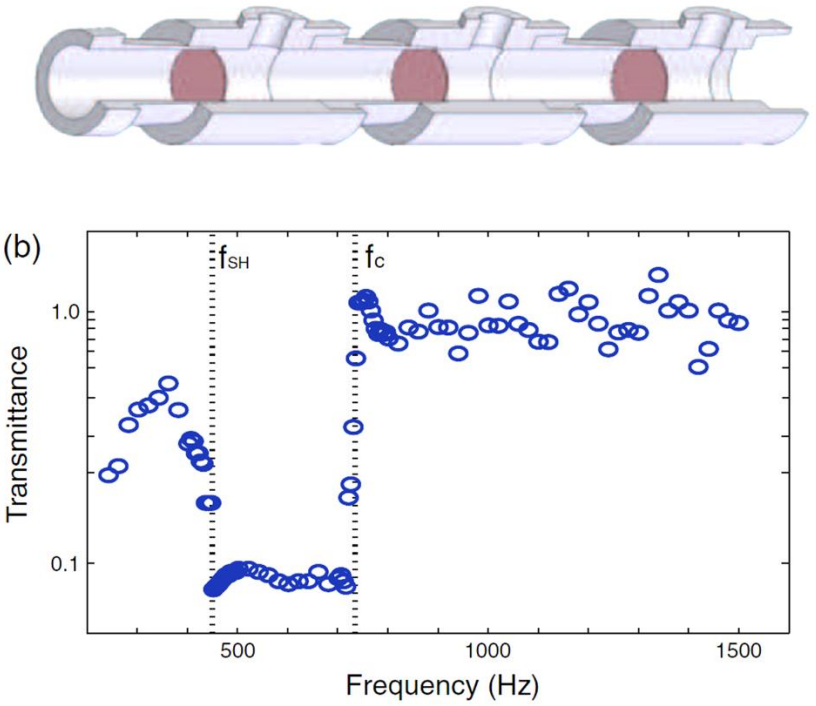

Figure 2.14. (a) composite structure consisting of interspaced membranes with side holes; (b) Transmission loss for the proposed structure [58]

2.2.2 Membrane and plate – type metamaterials with attached masses

Yang et al. [62] were the first to investigate the capability of this new group of metamaterials. In their first research work, they proposed an experimental realization and theoretical understanding of a membrane-type metamaterial with different masses attached, which can break the mass density law of sound attenuation in a wide frequency range. The acoustic properties of such construction are associated to the dynamic response of the stretched membrane. Because of the weak elastic modulus of the membrane, different low frequency oscillation pattern can be excited even within a small and finite sample with fixed boundary conditions. The oscillation, which actually represents the eigenmodes of the membrane can be tuned by placing small masse at the centre of the membrane achieving near-total sound reflection in the frequency range in-between the eigenmodes. Analysing the transmission loss (***Figure 2.15***), two considerable peaks and one dip in between are clearly identified. If the peaks are related to the eigenmodes of the membrane, the dip is due by the anti-resonance. In particular the high transmission loss associate to the peaks, are due to the large average displacement of the membrane when the eigenmodes are excited. On the other hands at the transmission dip, the measured displacement is minimum inducing a minimum in the transmission loss but a maximum sound reflection. Yang [62] demonstrated how the low transmission loss break the mass law.

The near total reflection between two eigenmodes (where the averaged displacement of the membrane is zero) not guarantee an effective bandwidth results. To overcome this limitation, which is common in most of the membrane-type unit cell metamaterial, Yang et al [63] extended their research to a membrane-type metamaterial panel which included an elastic thin membrane pre-stressed and fixed by a rigid plastic grid and one or more masses attached at the centre of each grid. Considering planar array of unit cell, the global acoustic behaviour of the array is not dissimilar compare with the single unit cells, because the rigid grid isolates the vibration of the unit cell from the others. Stacking multiple panels together, it shows

substantial increasing on the acoustic performance of the metamaterial. In particular stacking two or more identical panels, it is equivalent to increasing the global thickness of the material which leads to an increasing of the transmission loss amplitude. On the other hand, stacked multiple panels tuned on different dip frequencies, leads to great benefices in terms of broadband behaviour [63-64]. In this case, the global acoustic properties will be the results of the superposition of the single spectrum without interference between the individual layers. For example, Yang [63] proposed a multilayer panel which provide broadband shields between 50-1000 Hz with a Transmission Loss over 40dB (***Figure 2.16***).

This type of membrane-type structure was numerically investigated performing parametric analysis on single unit cell in order to better understand the effect on the acoustic properties of the attached mass or the pre-stressed induced to the membrane [65]. Increasing the mass, an increasing of the transmission loss peak magnitude was observed, while the peak frequency shifted at lower frequencies. While increasing the membrane pre-tension, the transmission loss peak will shift at higher frequency with an increasing of the peak amplitude (***Figure 2.17***). The same group [66] demonstrated also, how changing the shape and the distribution of the attached mass on the membrane, it leads to a slightly broadening of the transmission loss peaks and an amplitude arising.

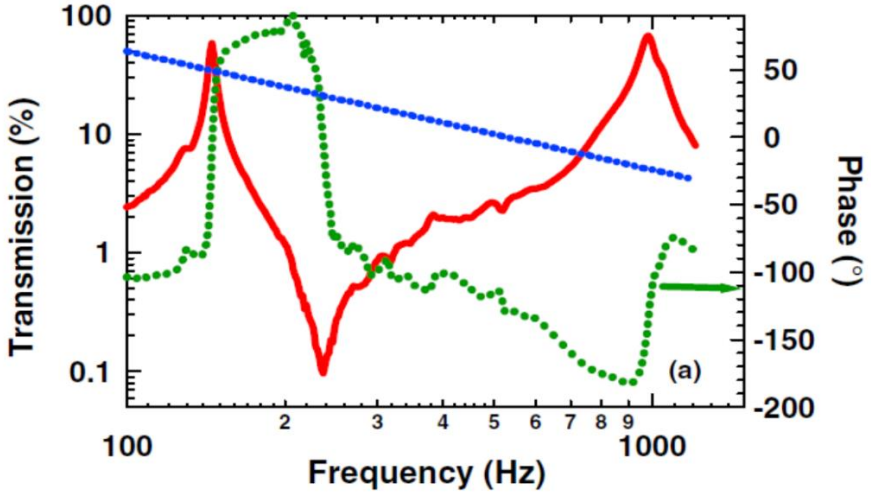

Figure 2.15. Transmission loss amplitude (red line) and phase (green line) of the membrane-type resonator with mass. The blue line is the transmission loss amplitude according with mass density law [62].

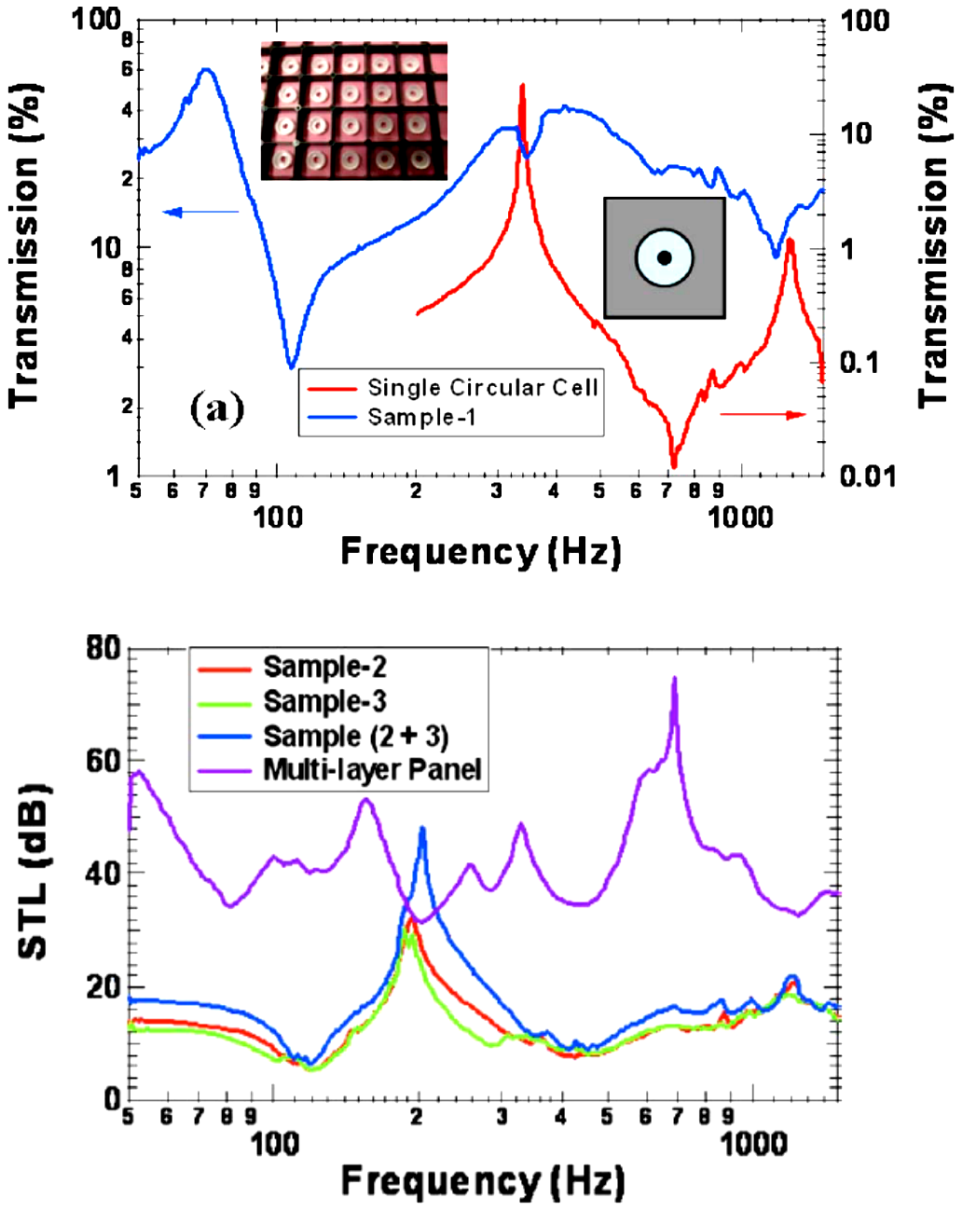

Figure 2.16. (Upper) Transmission spectra of single unit cell (red line) and array (blue line). (Lower) Transmission loss of two single layer samples (red and green line), two sample stacked together (blue line) and four single layer stacked together (purple line) [63]

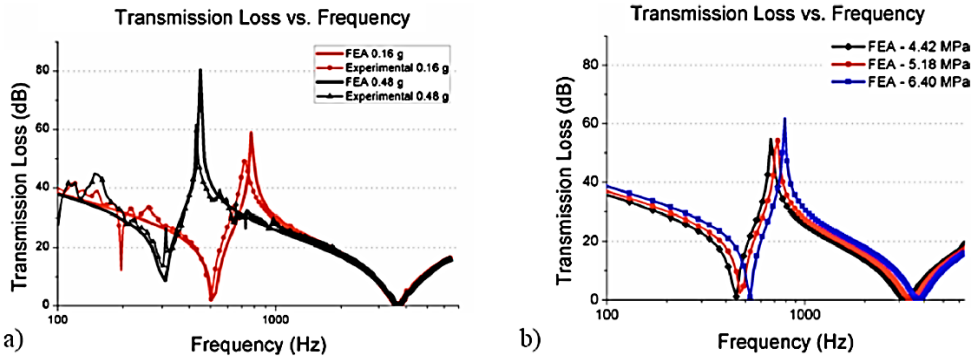

Figure 2.17. Transmission loss pf membrane-type unit cell with attached mass: (a) mass variation, (b) pre-tension variation [65]

In some of the already discussed research work [62-66] the acoustic properties in terms of transmission loss of the membrane-type unit cell was numerically investigated using Finite Element approach and Finite Element Model, with consequent high computational effort. Zhang et al. [67] then proposed an analytical model analysing both the dynamic response of the unit cell, in terms of eigenvalues and eigenvectors, and the acoustic properties in terms of transmission loss. In this analytical model the bending stiffness of the membrane is assumed to be negligible and the mass does not prevent the bending of the membrane. Moreover, the inertial force related the attached mass was treated as external concentrated force. As acoustic load, a plane sound wave was applied and the pressure on the membrane-air interface is linked assuming the normal velocity equal to the velocity of the membrane, so the differential equation of motion was presented in the form:

$$\rho_s \frac{\partial^2 w}{\partial t^2} + \rho_{mass} \tilde{h}(x, y, x_0, y_0, l_x, l_y) \frac{\partial^2 w}{\partial t^2} + 2\rho_0 c \frac{\partial w}{\partial t} - T\nabla^2 w = 2Ae^{j\omega t} \tag{2.13}$$

where ρ_{mass}, l_x, l_y are the width, the length and the density per unit area of the mass, while ρ_s L_x, L_y are the density per unit area and the dimensions of the membrane. x_0, y_0 is the corner of the mass closest to the origin of the reference system. $\tilde{h}(x, y, x_0, y_0, l_x, l_y)$ represents a combination of four Heaveside functions. w is normal displacement of the membrane; T is the pre-tension applied on the membrane and A is the amplitude of incident pressure. Solving equation (2.13)

using the mode superposition and integrating on all the membrane, a matrix formulation was written

$$-\omega^2\{[M]+[Q]\}\{q\}+j\omega[C]\{q\}+[K]\{q\}=2A\{H\} \tag{2.14}$$

where $[M]$ is the mass matrix, $[Q]$ is the inertia matrix, $[C]$ and $[K]$ the damping and stiffness matrix and $\{q\}$ is the vector of generalized coordinates. Solving equation 2.14 in terms of q the normal displacement of the membrane was calculated and the sound amplitude transmission coefficient expressed as

$$t_p=\left|\frac{j2\rho_0 c\omega}{L_x L_y}\{H\}^T\frac{1}{-\omega^2\{[M]+[Q]\}+j\omega[C]+[K]}\{H\}\right| \tag{2.15}$$

where $\{H\}$ include the membrane mode shapes.

Based on the approach, Tian et al [68] extended this analytical model to a circular membrane with an attached ring. Also in this case the inertial forces due to the mass were considered as an external force applied on the membrane. They demonstrated also the relation between the ring size/mass with the resonance. Increasing the inner diameter of the ring but keeping constant the weight, the resonance will shift at higher frequencies. The same effect is achieved by decreasing the weight of the ring. As a results of superposition effect, multiple rings with different internal radius generate multiple resonances.

In 2012 Mei et al. [69] used the concept of membrane-type metamaterial for low frequency sound attenuation and proposed a so called "Dark Acoustic Metamaterial" which could yield almost 100% acoustic absorption at low frequency. The proposed metamaterial consists of fixed pre-stressed membrane decorated with two semi-circular iron plate backed with an airgap with an aluminium reflector. They demonstrated how at the resonance frequencies of the unit cell, the acoustic energy associated to the incoming sound wave is converted in elastic energy through the flapping of the platelets. In fact considering the biharmonic equation of elastic membrane, then the corresponding elastic curvature energy per unit are is given by [70, 71]

$$\Omega = \frac{1}{2} D_p \left[\left(\frac{\partial^2 w}{\partial x^2} \right)^2 + \left(\frac{\partial^2 w}{\partial y^2} \right)^2 + 2\upsilon \frac{\partial^2 w}{\partial x^2} \frac{\partial^2 w}{\partial y^2} + 2(1-\upsilon) \left(\frac{\partial^2 w}{\partial x \partial y} \right)^2 \right] \quad (2.16)$$

where D_p is the flexural rigidity of the membrane ($D_p = Eh^3(1-\upsilon^2)/12$), E is the Young Modulus, υ is the Poisson ration of the membrane, while w is the out of plane displacement of the membrane. Since the Elastic Energy is a function of the second order spatial derivatives of the out of plane displacement, a very large value of Ω is generated around the platelet because of the discontinuity of the first order derivatives of w. Moreover, the Potential Elastic Energy will be also high around such discontinuity since the second order derivative is quadratic. As the local dissipation is proportional to the product of the elastic energy with the dissipation coefficient, when the flapping modes of the platelet are excited, the displacement discontinuity will induce an increment of the elastic energy which lead to a substantial absorption around these flapping resonance frequencies. Mei, then defined a relation between the elastic energy and the absorption coefficient using the Poynting's theorem for elastic wave [72]

$$\alpha = \frac{2\omega^2 \left(\frac{\chi_0}{E} \right) \int U dv}{\frac{P^2 S}{\rho_0 c}} \quad (2.17)$$

where U is the elastic energy, S is the membrane's area, P, ρ_0, c are respectively the pressure amplitude, the density and the sound speed of the incoming sound wave. χ_0 defines the imaginary part of the membrane elastic modulus ($Im(E) = \omega\chi_0$ [69]) and was obtained experimental by fitting the absorption coefficient.

The proposed unit cell shown three absorption peaks located at 172Hz, 340Hz and 813Hz related to the flapping modes of the platelet plotted in ***Figure 2.18***. But because the high curvature energy and elastic energy were confined around the attached mass, in order to achieve a broadband absorption, the same research group [69] proposed a multiplayer absorption panel considering a unit cell with multiple semi-circular platelet, measuring a broadband high absorption in the frequency

range of 200-1000Hz. ***Figure 2.19*** shows the proposed multilayer panel with the relative absorption coefficient experimental measured.

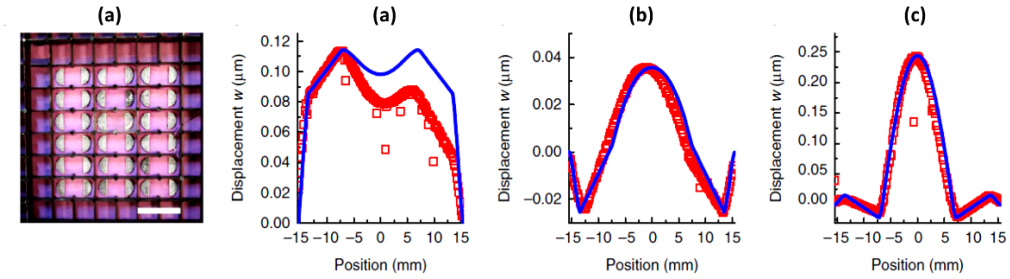

Figure 2.18. (a) Array of unit cell. (b) Out of plane displacement of the unit cell mid-plane at the absorption peak frequencies: 172Hz, 340Hz and 813Hz [69]

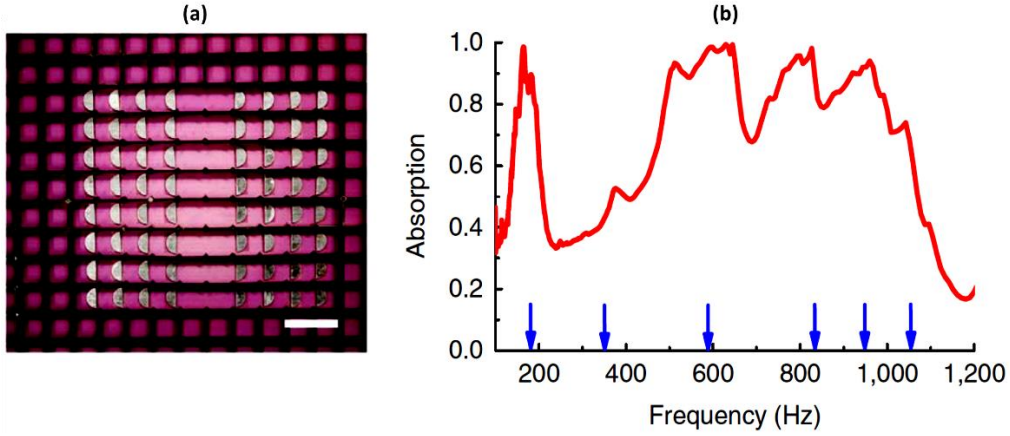

Figure 2.19. (a) Multi-layers panel with tweaked unit cell. (b) experimental measured absorption coefficient; the blue narrows show the absorption peaks predicted by the FE simulation [69]

A theoretical model of this kind of "Dark Acoustic Metamaterial" unit cell was proposed by Chen et al. [73, 74] who developed a coupled vibro-acoustic model to predict the absorption coefficient of the unit cell. First of all the eigenfrequencies and eigenmodes of the unit cell were calculated including the initial tension effect of the membrane on the effective bending stiffness ($D_p^* = D_p + (\sigma_0 h^3/12)$, with D_p the bending membrane stiffness and σ_0 the initial stress). The effect of the platelets was taken into account defining a force loading in at each *i*th collocation points from the *s*th attached mass along the *s*th inner boundaries. Finally, the absorption coefficient was calculated solving the coupled vibro-acoustic

integrodifferential equation (2.18) assuming a complex Young modulus to take into account the damping effects in the forced vibration.

$$\begin{aligned} & D_p^* \nabla^4 w - T\nabla^2 w - \omega^2 \rho_s w + 2i\omega\rho_0 c\langle w\rangle \\ & \qquad - 2\omega^2\rho_0 \int_0^{L_x}\int_0^{L_y} G(w - \langle w\rangle)dx^*dy^* \\ & \qquad = 2P_I + \sum_{s=1}^{S}\sum_{i=1}^{I_s} F_i\delta(x - X_i)\delta(y - Y_i) \end{aligned} \tag{2.18}$$

where G is the Green function, $S = \sqrt{(x-x^*)^2 + (y-y^*)^2 + (z-z^*)^2}$, δ is the Dirac delta, F_i is the force loading at the *i*th collocation point from the *s*th attached mass, ⟨ ⟩ denotes the average of the parameter, Lx and Ly are the membrane dimension and P_I is the incident amplitude sound plane wave.

Solving equation 2.18, using the modal superposition method, the out of plane velocity of the membrane can be calculated which is used to define the pressure field around the unit cell and estimate the absorption coefficient. The developed vibroacoustic plate model was validated comparing the results in terms of transmission and reflection with the results from FE analysis and in terms of absorption with the experimental results reported by Mei [69] (***Figure 2.20***).

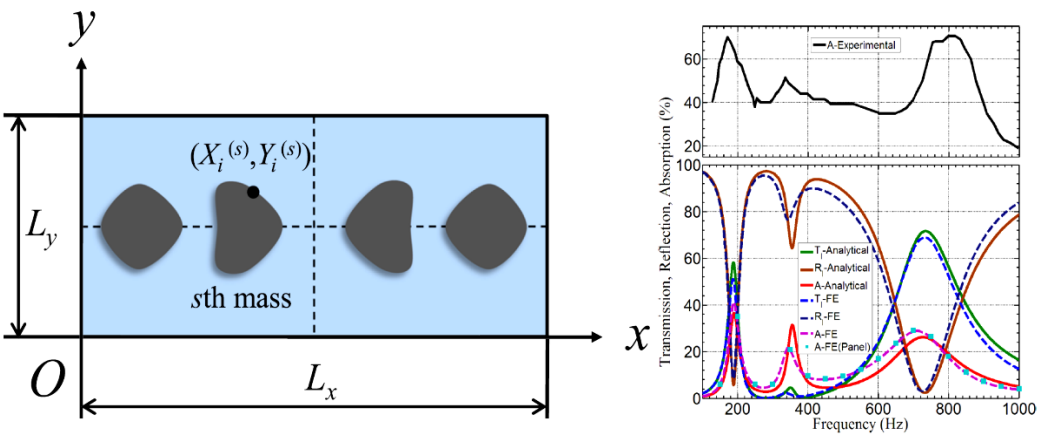

Figure 2.20. (Left side) Analytical Model geometry. (Right side) comparison of transmission, reflection and absorption coefficient of the membrane unit cell with two semicircular masses between analytical, FE and experimental data [73]

In the same year, Ma et al. [75] proposed a new decorated membrane-type metamaterial which provide total absorption at certain tenable frequency. The concept behind this metamaterial is the "hybrid resonance" which defines the unit cell of metamaterial impedance-matched to the airborne sound proving 100% of sound absorption. The unit cell comprised the table a circular membrane mounted over a solid surface with sealed gas in between and a circular attached mass in the centre. The membrane with the attached mass shows two eigenmodes characterized respectively by the oscillation of the central mass and the oscillation of the surrounding membrane with the mass being stationary (***Figure 2. 21***). However, these resonances can be "hybridizing" by placing the membrane close to a hard-reflective surface and a sealed gas in between. In other words, the sealed gas and the reflective surface will add an extra impedance in series with membrane impedance ($Z_{tot} = Z_M + Z'$) which leads to an hybrid resonance (***Figure 2. 21***), due to the coupling of the piston-like component of the membrane and the transmitted and reflected pressure components. At that frequency the imaginary part of the total impedance of the unit cell (Z_{tot}) is demonstrated to be zero, which means that it is possible to achieve perfect matching with the impedance of the air. Another example of membrane-type metamaterial decorated by attached masses was proposed by Yang te al. [76] who introduce the concept of "degenerate resonant frequency" achieving total absorption a such frequency. The unit combined a monopole (symmetric) and a dipole (anti-symmetric) resonators tuned to resonate at the same frequency, the so called "degenerate frequency". Similar to the hybrid resonance, the proposed degenerate absorption unit makes the average impedance of the two resonators to be impedance-matched with the background medium. The absorber unit cell includes a single stretched membrane with attached mass in the centre for dipolar resonance in series with a pair of coupled stretched membrane with attached mass for monopolar resonance, achieving 98% of absorption at the degenerate frequency.

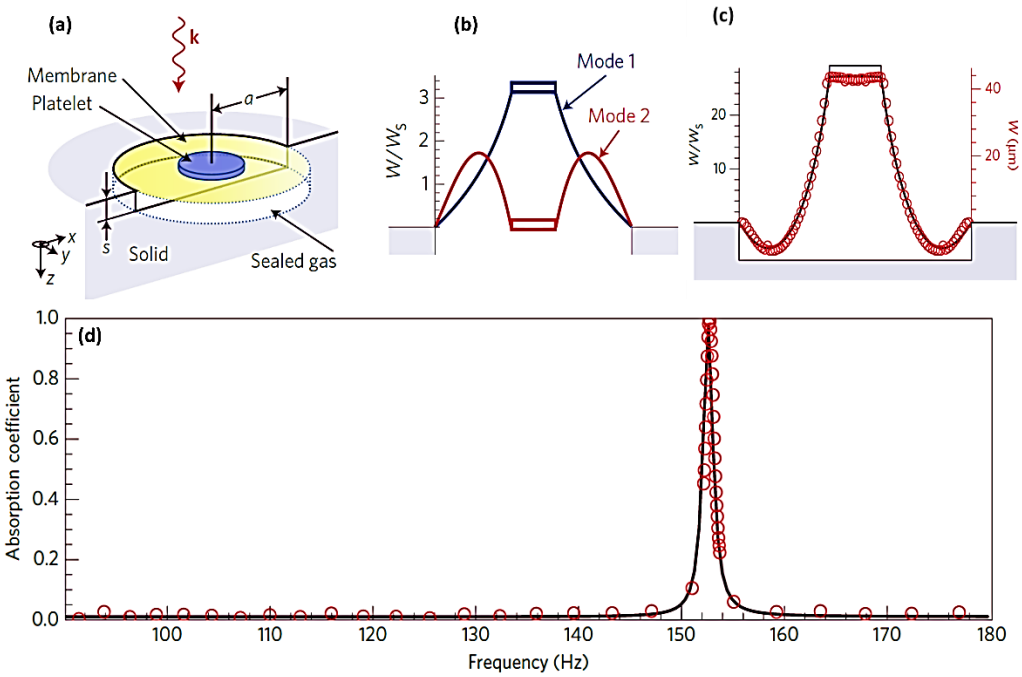

Figure 2. 21. (a) Unit cell geometry. (b) Cross section eigenvectors of unit cell at two resonance frequencies. (c) Normal displacement at the hybrid resonant absorption peak. (d) Absorption coefficient of proposed unit cell with the peak at the hybrid resonance. [75]

Most of the decorated membrane-type metamaterial provide only negative density effect, however Yang et al [77] in 2013 presented a new decorated membrane –type metamaterials which induces double negative density and bulk effect in a single resonating structure, in a relative broadband frequency range. The proposed unit cell comprises two identical circular membrane decorated with two circular platelets with the masses attached to the membrane centre. The membranes are fixed to a rigid cylindrical side wall (***Figure 2.22***). They demonstrated how combining together monopolar and dipolar resonances on the same unit cell, it leads to a double negative effect. Considering the first three eigenmodes, the out of plane displacement field shows a membranes in-phase motion carrying the ring in a translational motion for the first mode, a membrane out-phase motion and the ring is motionless for the second mode, out-phase motion between the ring and the platelets and in-phase motion of the membranes for the third mode. The first and the third modes (symmetric) represent dipolar resonance and since the total mass of

the platelets and the ring is the dominant parameter for tuning the resonance frequency, they provide a mass-like resonance [78]. However, the second mode (antisymmetric) represents monopolar resonance where the bulk in terms of transverse membrane dimension and the membrane separation played a key role in the frequency tuning. It provides a bulk-modulus like resonance [78]. The three main eigenfrequencies divide the spectrum in two main passband: the first one in-between the first dipolar and the monopolar resonances which is a double-positive band and the second one in-between the monopolar and the second dipolar resonance which is a double-negative band. In terms of acoustic properties, they demonstrated also how the real part of the dynamic mass density crosses zero at the two dipolar frequencies and as consequence, the effective impedance of the unit cell matches with the background air generating two transmission peaks accompanied by reflection minima [77] (***Figure 2.22***).

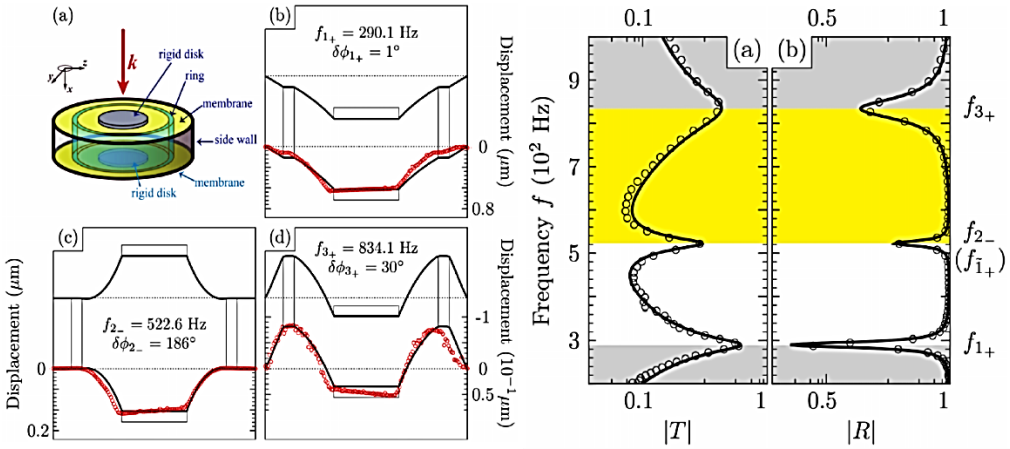

Figure 2.22. Left: (a) Schematic drawing of the unit cell. (b-d) out of plane displacement field for the dipolar resonances. (c) out of plane displacement for the monopolar resonance. Right: Transmission and Reflection coefficient for the unit cell

2.2.3 Helmholtz Resonator – type metamaterial

At low frequencies the interaction between the viscous air medium and the absorber structures are usually very weak because of the slow fluctuation of the sound wave which leads to an inefficient sound energy dissipation effect.

In general, considering common sound absorbing materials (acoustic foam, Helmholtz resonator, etc.), to increase the absorption performances at low frequencies two main approaches can be considered: increase the wave path more than one quarter of wavelength [13-79-80-81] or field intensifying such as Helmholtz chambers with thickness greater than one fourth of wavelength [16-82-83]. In other words, the strong limitation of the common absorber for the low – frequency absorption is the size of the resonator itself.

The Helmholtz resonator – type metamaterials go beyond the size limitation of the common absorber achieving low – frequency sound absorption.

In 2014, Caiet al. [84] used the concept of "space-coiling" [85] to propose an absorber panel containing coplanar long tubes or coplanar Helmholtz resonant chamber (***Figure 2.23***). The quarter-wavelength cavity of a Helmholtz resonator is bent into 2D coplanar tubes and embedded in a thin panel. The result is an absorber panel which achieve 100% of absorption at design frequency with a considerable thickness reduction compared with the equivalent Helmholtz size but keeping constant its wave dissipation performances.

The non-dimensional impedance of panel with embedded tubes can be expressed

$$\frac{Z_{in}}{Z_0} = \frac{(\rho_0 C)^{0.5}}{Z_0}\left[-i\frac{cot(kL_t)}{\tau}\right] \tag{2.19}$$

where Z_0 is the characteristic impedance of air, $\tau = N\pi r_t^2$ (N number of embedded tubes, r_t tube radius) which is an indication of the porosity, L_t is the length of the tube, k is the effective propagation constant and the effective density ρ and the compressibility C are constitutional wave variables and can be calculated from visco-thermal acoustic theory [86]. Condition for full absorption is the matching between the impedance of the panel and the characteristic impedance of the air,

so $\frac{Z_{in}}{Z_0} = 1$. When the radius of the tube is big enough (millimetre scale), then the term $\frac{(\rho C)^{0.5}}{Z_0}$ is close to one. Moreover, for small porosity (τ) the *cot* must approach to zero which leads to the condition $kL_t = \pi/2$ and as a consequence $L_t \approx \lambda/4$ which is one quarter of the wavelength.

In particular the proposed panel guarantees full sound absorption at 250 Hz with a global panel thickness of 13.3mm.

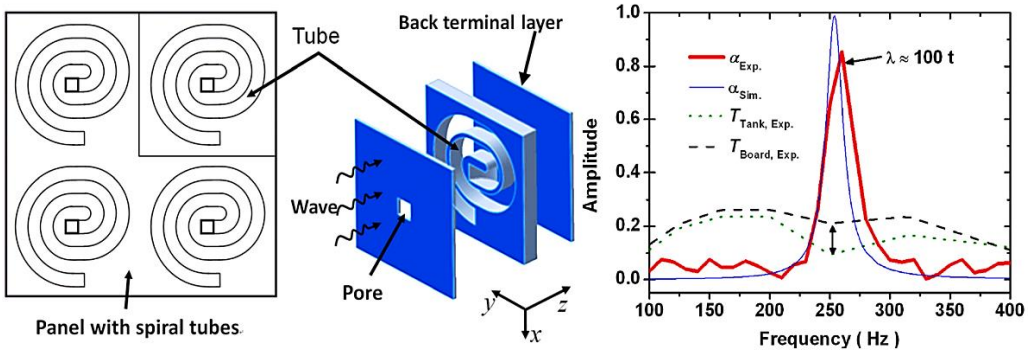

Figure 2.23. Left: Sketch of sound absorption panel with arrays of embedded co-planar tubes. Right: Example of absorption coefficient for the proposed panel [84]

The same approach of coiling up space to achieve full absorption by increasing the sound path is considered by Li [87] who proposed an acoustic metasurface with sub wavelength thickness with 100% sound absorption at 125Hz. He studied the energy dissipation phenomena associated to the full absorption using a common normalized impedance model [13, 14, 15] writing the normalized acoustic impedance ($Z = Rs + jM_s$) as the sum of its real part (acoustic resistance) and its imaginary part (acoustic reactance). He demonstrated how coiling up a quarter-wave resonator in a plane perpendicular to the incident plane wave the full absorption is related to resonance phenomena of the structure (acoustic reactance equal to 0) and the impedance matching with the impedance of air (acoustic resistance equal to 1) (***Figure 2.24***).

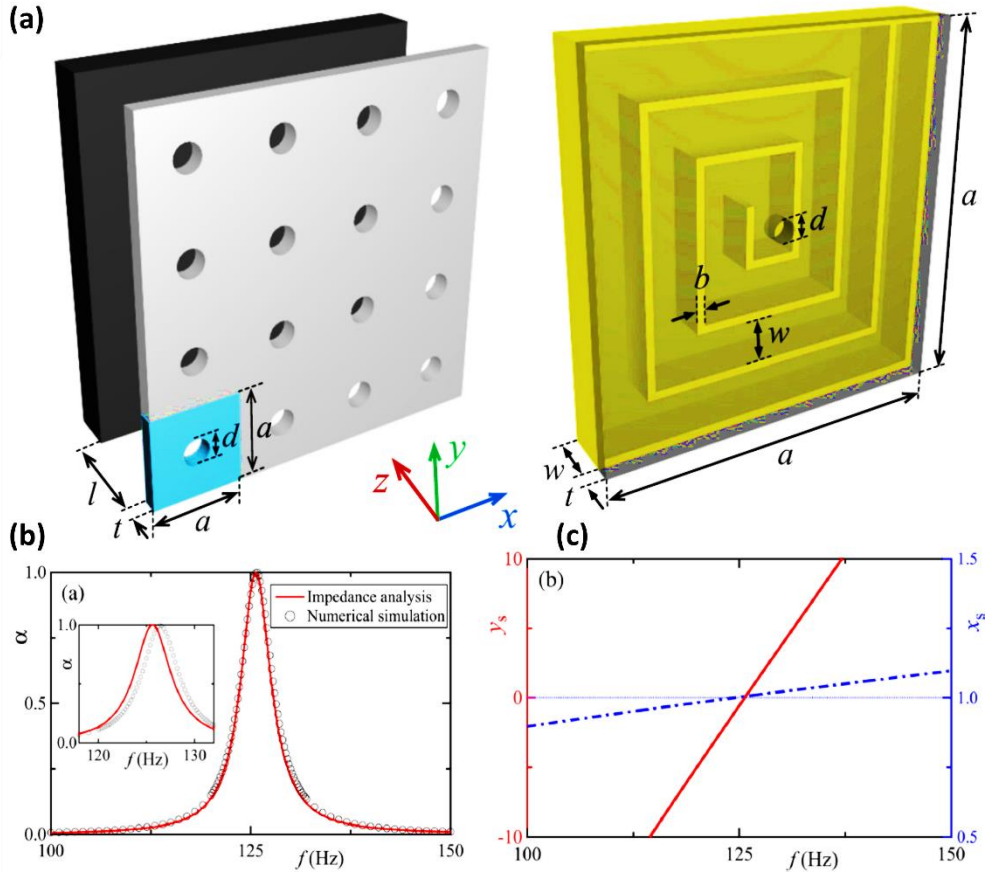

Figure 2.24. (a) Acoustic metasurface. (b) Sound absorption for d = 3.3mm, t = 0.2mm, a = 100mm, w=12 mm, and b¼1 mm. (c) Plot of the normalized acoustic reactance (ys) and acoustic reactance (xs) [87].

These resonator metamaterials provide a single narrow absorption peaks.

Different broadband sound absorbing structures have been proposed.

Inspired by the space coiling, Chen et al [88] demonstrated how a series of two axially coupled tube coiled in a plane is able to absorb low frequency sound energy with broader frequency bandwidth (***Figure 2.25***). They proposed a numerical model where the surface impedance of the unit cell is expressed

$$Z_{in} = \frac{Z_2}{\phi_2} \tag{2.20}$$

where ϕ_2 is the porosity of the unit cell and the impedance of the tube 2 is expressed as

$$Z_2 = Z_1^c \frac{Z_1^c - jZ_{11}\,cot(k_2L_2)}{Z_{11} - jZ_1^c cot\,(k_2L_2)} \tag{2.21}$$

where $Z_{11} = Z_1/\phi_1$ and $\phi_1 = A_1/A_2$ with A_1 and A_2 being the cross-sectional areas of tube 1 and tube 2 respectively. $Z_1 = -jZ_1^c \cot(k_1L_1)$ is the acoustic impedance at the two tubes connection while $Z_1^c = \sqrt{\rho_{eq1}E_{eq1}}$ is the characteristic impedance of tube 1, where ρ_{eq1}, E_{eq1} are respectively the effective density and effective bulk modulus of air in the hollow tube [86-89]. $k_{1,2}$ represent the effective propagation constant of tube 1 and 2 while $L_{1,2}$ are their lengths.

The numerical model suggests that, also in this case, the full absorption requires the impedance match condition between the unit cell and the air which occurs at the resonance frequency of each tube. The proposed unit cell shown two full absorption peaks close enough in frequency to generate a broadband absorption (***Figure 2.25***).

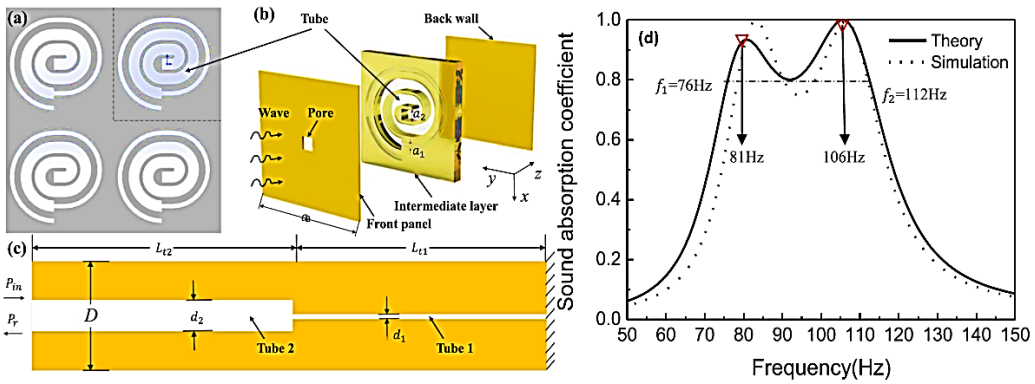

Figure 2.25. (a) Sketch of the sound absorbing panel with designed unit cell; (b) Make-up of the unit cell; (c) Schematic of two straight axially coupled tubes in series in analysis. (d) Absorption coefficient for panel thickness of 117.1mm, diameters of tube 1 and 2 of 3mm and 12mm and tube lengths of 857.5mm and 860mm [88].

Always with a view to achieve a broadband absorption, new structures based on parallel resonators installation was proposed by Groby et al. [90]. Here a multiple-peaks absorption into the frequency range of 500Hz-3000Hz is achieved by a periodic parallel arrangement of quarter-length tube resonator (Helmholtz-type) with a global thickness 13-17 times thinner than the acoustic wavelength. The

perfect absorption of the structure is demonstrated to be caused by critical coupling between those subwavelength resonators.

Full broadband absorption can be also achieved considering an array of airgap in between two adjacent sawteeth in series with different heights and each airgap characterized by a resonance at λ/4. The results is a triangular shape device proposed by Jiang et al. [91] with total absorption in a frequency range 612Hz – 10000Hz (***Figure 2.26***). They theoretical demonstrated that, considering the impedance transfer equation (equation 2.21), for gap heights equal to multiple of quarter of the wavelength ($h = (2m-1)\frac{\lambda}{4}$) the acoustic impedance of the open end of the airgap is zero which means that the sound wave can radiate into the gap without any restriction, leading to a trapping effect. The proposed device has a limitation in terms of size because show a maximum gab height of 140mm and a total length of 370mm.

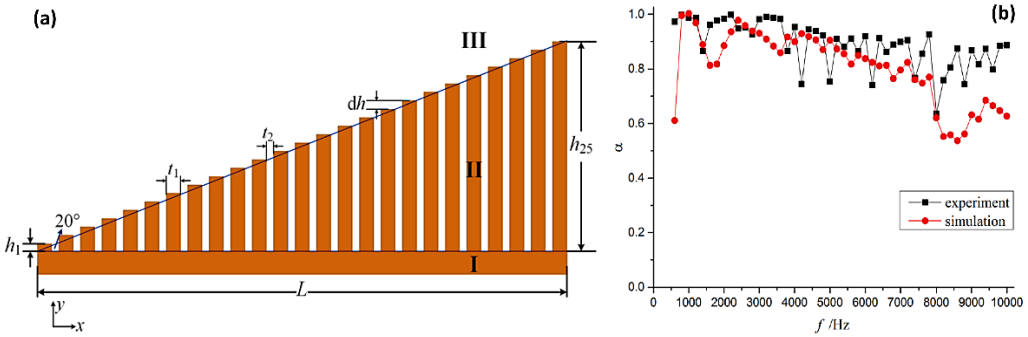

Figure 2.26. (a) Sketch of full broadband absorbing device. (b) Absorption coefficient

2.3 Limitations of Resonator Absorbers for NVH applications

As introduced in the previous chapter, the main object of this research work is to propose new solutions for automotive NVH applications. Two main design parameters need to be taken into account: frequency working range and thickness of the structure. The frequency working range is related to noise spectrum generated by different noise sources into the vehicle cabin, while the thickness is limited by

engineering constrains such as size and weight. Usually the interior vehicle noise spectrum is between 100Hz to 4000Hz. Porous absorber materials are currently used for vehicle noise mitigation. However, for porous absorbers, the minimum thickness is usually one order of magnitude smaller than the wavelength to guarantee considerable sound absorption, which makes such solution not suitable for sound absorption at frequencies lower than 1000 Hz because the required thickness will be greater than 100mm.

In the previous paragraph we discussed about the status of art of the resonator absorbers in order to define alternatively solution applicable for sound absorption at low frequency (<1000 Hz) keeping subwavelength sizing.

First of all, we discussed about Microperforated Panel (MPP) absorbers.

The MPP absorbers can discretised as single degree of freedom (SDOF) mass-spring system where the absorption properties are related to the resonance phenomena. In particular the mass properties are related to the mass of air into the perforation and the stiffness properties are related to mass of air into the resonator chamber. The absorption profile for the MPP absorbers is characterized by one absorption peak related to single resonance frequency (Figure 2.1 – 2.2.). Moreover, the resonance frequency is inversely proportional to the stiffness properties, which means that low frequency absorption can be achieved increasing the size (thickness) of the resonator chamber.

The limitation in terms thickness is solved introducing the membrane-type metamaterials which are sub-wavelength absorber applicable for frequency range lower than 500Hz. However, broadband sound absorption cannot be achieved by the unit cell of such materials. In fact, as for the MPP absorber, the membrane-type metamaterials behave as SDOF mass-spring system where the mass properties are related to the vibrating membrane mass, and the stiffness properties are related to the mass of air into the resonator chamber. As a consequence, the absorption profile is characterized by a single narrow absorption peak.

In conclusion, refereeing to the target application, in this research work we proposed new subwavelength sound absorbers suitable for broadband sound absorption at low frequency (<1000 Hz).

2.4 List of Symbols

Symbol	Description
α	Absorption Coefficient
R	Reflection Coefficient
TL	Transmission Loss
P	Pressure
u	Particle velocity
w	Displacement
t	Time
x,y	Geometrical coordinates
ω	Frequency variable
k	wavenumber
ρ	Material Density
ρ_s	Membrane density per unit of area
ρ_{mass}	Platelet density per unit of area
K	Bulk Modulus
E	Elastic Modulus
υ	Poisson Ratio
ρ_0	Density of air
K_s, G_s	Stiffness of spring
m	Mass
c	Speed of sound in air
η	Coefficient of viscosity
Z_n	Acoustic Impedance
R_n	Acoustic Resistance
M_n	Acoustic Reactance
J_n	Bessel Functions
G	Bessel Function
$\tilde{h}$	Combination of four Heaveside functions
p	Perforation Ratio
t_h	MPP thickness panel
d	MPP perforation diameter
x_v	Loss coefficient through MPP perforation
T	Pre-Tension membrane
h	Membrane thickness
D_p	Membrane flexural rigidity
φ_{mn}	Acoustic mode shapes
L_x , L_y	Membrane dimensions
l_x , l_y	Platelet dimensions
$[M],[C],[K]$	Mass, Damping, Stiffness Matrix
Ω	Membrane Curvature Energy
S	Membrane Surface
X_0	Imaginary part of membrane elastic modulus

Chapter 3

Theoretical Background: Fundamentals of Acoustic

3.1 Sound Wave Equations

The fluid motion can be described by using the Equation of Continuity, which relates the motion of the fluid to its compression or dilatation, and the Equilibrium Equation which relates internal and inertial forces of the fluid according to the Newton's second law.

Assuming the propagation of small linear perturbances in a compressible medium, then the continuity and equilibrium equation can be linearized.

The continuity equation describes the conservative transport of mass and it results from the fact that the total net influx into an infinitesimal box of volume must be equal to the rate which the mass increase in the volume:

$$\frac{\partial \rho}{\partial t} + \nabla(\rho v) = 0 \tag{3.1}$$

where ρ is the density properties and v the particle velocity.

The Equilibrium equation may be derived by the Navier-Stokes equations of fluid momentum

$$\rho \frac{\partial v}{\partial t} + \nabla P + \rho v \nabla v = 0 \tag{3.2}$$

where P is the pressure variable.

As anticipated, we can assume that the fluctuation in the fluid dynamic quantities are so small that their products can be neglected. This means that we can write quantities as the sum of a mean part and a small fluctuation

$$\rho = \rho_0 + \rho'(t) \tag{3.3}$$

$$v = v'(t) \tag{3.4}$$

$$P = P_0 + P'(t) \tag{3.5}$$

where the subscript 0 indicates the mean value and a prime symbol a fluctuation.

Under such assumption and neglecting the second order terms, which are the products of small quantities, we can rewrite the continuity and equilibrium equations as

$$\frac{\partial \rho'}{\partial t} + \rho_0 \nabla v' = 0 \tag{3.6}$$

$$\rho_0 \frac{\partial v'}{\partial t} + \nabla P' = 0 \tag{3.7}$$

which are known as the linearized Euler equations.

If we combine the equation 3.6 and equation 3.7

$$\frac{\partial}{\partial t}\left(\frac{\partial \rho'}{\partial t} + \rho_0 \nabla v'\right) - \nabla\left(\rho_0 \frac{\partial v'}{\partial t} + \nabla P'\right) = \frac{\partial^2 \rho'}{\partial t^2} - \nabla^2 P' \tag{3.8}$$

In order to express equation (3.2) in terms of pressure and eliminate the density, we need to introduce equations of status for the fluid

$$P = P_0 + \frac{\partial P}{\partial \rho}\Big|_{\rho=\rho_0} (\rho - \rho_0) + \frac{1}{2}\frac{\partial^2}{\partial \rho^2}\Big|_{\rho=\rho_0} (\rho - \rho_0)^2 + \cdots \quad (3.9)$$

Linearizing the pressure-density relationship identified by equation (3.9), we can express the pressure fluctuation

$$P' = P - P_0 \approx \frac{\partial P}{\partial \rho}\Big|_{\rho=\rho_0} (\rho - \rho_0) = c^2 \rho' \quad (3.10)$$

where we defined $c^2 = \frac{\partial P}{\partial \rho}\Big|_{\rho=\rho_0}$.

Substituting equation (3.10) in the equation (3.8), we can finally define the sound wave equation

$$\nabla^2 P - \frac{1}{c^2}\frac{\partial^2 P}{\partial t^2} = 0 \quad (3.11)$$

where *c* is the speed at which small disturbance propagates through a fluid, and we can identify as the speed of sound for the common application of the linearized sound wave equation. In particular for inviscid isotropic elastic fluid the pressure depends on the volume dilatation ($tr\varepsilon$)

$$\frac{\partial P}{\partial t} = -K\, tr\frac{\partial \varepsilon}{\partial t} = -K\, \nabla v \quad (3.12)$$

where K is the bulk modulus. Taking into account the linearized continuity equation (equation (3.6))

$$\frac{\partial P}{\partial t} = \frac{K}{\rho_0}\frac{\partial \rho'}{\partial t} \quad (3.13)$$

Which means that the speed of sound depends on the elastic and the inertia properties of the media

$$c = \sqrt{\frac{\partial P}{\partial \rho'}} = \sqrt{\frac{K}{\rho_0}} \quad (3.14)$$

3.2 FE implementation of sound wave equation

In the previous paragraph the sound wave equation is derived from the linearized formulation of continuity equation and equilibrium (or momentum) equation.

The wave equation (equation (3.11)) is developed from equations (3.6) and (3.7) for regions of space not containing any source of acoustic energy. If an internal source is presented, then the acoustic equations need to be modified to take into account the generated acoustic disturbance.

Assuming the fluid is compressible, which means the density changes due to pressure variations, an internal acoustic source and no mean flow of the fluid, the continuity and equilibrium equation can be expressed

$$\frac{\partial \rho}{\partial t} + \nabla(\rho v) = Q \tag{3.15}$$

$$\rho \frac{\partial v}{\partial t} + \nabla P + \rho v \nabla v = F_e \tag{3.16}$$

where *Q* is the mass source, *Fe* is an externally applied force that most likely results in a momentum exchange across an interface or the oscillation of a rigid body and the gravitational force are ignored.

Combining equation (3.14) and (3.15), the inhomogeneous sound wave can be written

$$\nabla \cdot \left(\frac{1}{\rho_0} \nabla p\right) - \frac{1}{\rho_0 c^2} \frac{\partial^2 P}{\partial t^2} + \nabla \cdot \left[\frac{4\mu}{3\rho_0} \nabla \left(\frac{1}{\rho_0 c^2} \frac{\partial P}{\partial t}\right)\right] = -\frac{\partial}{\partial t}\left(\frac{Q}{\rho_0}\right) + \nabla \cdot \left[\frac{4\mu}{3\rho_0} \nabla \left(\frac{Q}{\rho_0}\right)\right] \tag{3.17}$$

where c is the speed of sound (as derived in equation (3.14)), *K* is the bulk modulus, μ is the dynamic viscosity and Q the mass source.

Since the viscous dissipation has been taken into account using the Stokes hypothesis, the wave equation is referred to as the lossy wave equation for propagation of sound in fluids.

Assuming the pressure varying harmonically in time, the inhomogeneous sound wave equation can be reduced as

$$\nabla \cdot \left(\frac{1}{\rho_0}\nabla p\right) - \frac{\omega^2}{\rho_0 c^2} P + j\omega \nabla \cdot \left[\frac{4\mu}{3\rho_0}\nabla\left(\frac{1}{\rho_0 c^2} P\right)\right] = -j\omega\left(\frac{Q}{\rho_0}\right) + \nabla \cdot \left[\frac{4\mu}{3\rho_0}\nabla\left(\frac{Q}{\rho_0}\right)\right] \qquad (3.18)$$

with ω angular frequency.

The finite element formulation is obtained by testing wave equation (equation (3.19)) using the Galerkin procedure [102]. Equation (3.19) is multiplied by testing function w and integrated over the volume of the domain [103] which yields the following:

$$\iiint_{\Omega_f} \frac{1}{\rho_0 c^2} w \frac{\partial^2 p}{\partial t^2} dv + \iiint_{\Omega_f} \nabla\left(\frac{4\mu}{3\rho_0^2 c^2}\nabla\frac{\partial p}{\partial t}\right) dv + \iiint_{\Omega_f} \nabla w \cdot \left(\frac{1}{\rho_0}\nabla p\right) dv +$$

$$- \oiint_{\Gamma_f} w\left(\frac{1}{\rho_0} + \frac{4\mu}{3\rho_0^2 c^2}\frac{\partial}{\partial t}\right)\hat{n} \cdot \nabla p ds + \oiint_{\Gamma_f} w \frac{4\mu}{3\rho_0^2}\hat{n} \cdot \nabla Q ds = \qquad (3.19)$$

$$= \iiint_{\Omega_f} w \frac{1}{\rho_0}\frac{\partial Q}{\partial t} dv + \iiint_{\Omega_f} \nabla w \cdot \left(\frac{4\mu}{3\rho_0^2}\nabla Q\right) dv$$

where dv is the volume differential of acoustic domain (Ω_f), ds is the surface differential of acoustic domain boundary (Γ_f) and $\hat{n}$ is the normal unit vector to the boundary.

From the momentum equation, the normal acceleration of the fluid, expressed in terms of the normal displacement, is given

$$\frac{\partial v_{n,f}}{\partial t} = \hat{n} \cdot \frac{\partial v}{\partial t} = \hat{n} \cdot \frac{\partial^2 u_f}{\partial t^2} = -\left(\frac{1}{\rho_0} + \frac{4\mu}{3\rho_0^2 c^2}\frac{\partial}{\partial t}\right)\hat{n} \cdot \nabla p + \frac{4\mu}{3\rho_0^2}\hat{n} \cdot \nabla Q \qquad (3.20)$$

where u_f is the displacement of fluid particle.

Substituting equation (3.20) into equation (3.19) yields the acoustic wave equation (3.18) and can be expressed as follows:

$$\iiint_{\Omega_f} \frac{1}{\rho_0 c^2} w \frac{\partial^2 p}{\partial t^2} dv + \iiint_{\Omega_f} \nabla w \cdot \left(\frac{4\mu}{3\rho_0^2 c^2}\nabla\frac{\partial p}{\partial t}\right) dv + \iiint_{\Omega_f} \nabla w \cdot \left(\frac{1}{\rho_0}\nabla p\right) dv +$$

$$+ \oiint_{\Gamma_f} w\hat{n} \cdot \frac{\partial^2 u_f}{\partial t^2} ds = \iiint_{\Omega_f} w \frac{1}{\rho_0}\frac{\partial Q}{\partial t} dv + \iiint_{\Omega_f} \nabla w \cdot \left(\frac{4\mu}{3\rho_0^2}\nabla Q\right) dv \qquad (3.21)$$

The finite element approximating shape functions for the spatial variation of the pressure and displacement components are given by:

$$P = \{N\}^T\{p\} \tag{3.22}$$

$$u = \{N'\}^T\{u\} \tag{3.23}$$

with $\{N\}$ is the element shape function for pressure, $\{N'\}$ is the element shape function for displacement and $\{p\}$, $\{u\}$ are the nodal pressure and displacements vectors.

Using such formulation into the equation (3.22), the finite element statement of the wave (equation (3.19)) is expressed in matrix notation as following:

$$\left[M_f\right]\{\ddot{p}\} + \left[C_f\right]\{\dot{p}\} + \left[K_f\right]\{p\} + \bar{\rho}_0[R]^T\{\ddot{u}\} = \left\{f_f\right\} \tag{3.24}$$

Where

$\left[M_f\right] = \bar{\rho}_0 \iiint_{\Omega_f} \frac{1}{\rho_0 c^2}\{N\}\{N\}^T dv$ is the acoustic fluid mass matrix

$\left[C_f\right] = \bar{\rho}_0 \iiint_{\Omega_f} \frac{4\mu}{\rho_0^2 c^2}[\nabla N]^T[\nabla N] dv$ is the acoustic fluid damping matrix

$\left[K_f\right] = \bar{\rho}_0 \iiint_{\Omega_f} \frac{1}{\rho_0}[\nabla N]^T[\nabla N] dv$ is the fluid stiffness matrix

$[R]^T = \oiint_{\Omega_f}\{N\}\{n\}^T\{N'\}^T ds$ is the acoustic fluid boundary matrix

$\left[f_f\right] = \bar{\rho}_0 \iiint_{\Omega_f} \frac{1}{\rho_0 c^2}\{N\}\{N\}^T dv\{\dot{q}\} + \bar{\rho}_0 \iiint_{\Omega_f} \frac{4\mu}{\rho_0^2 c^2}[\nabla N]^T[\nabla N] dv\{q\}$ is the acoustic fluid load, with $\bar{\rho}_0$ the acoustic fluid mass density constant.

The discretized sound wave equation expressed in matrix formulation in equation (3.24) can be easily combined with the discretized structural motion equation to define fluid-structural problems.

3.3 Sound Wave Equations and Equivalent Electro-Acoustical Analysis

The concept of equivalent electro-acoustical analysis is introduced by Maa [13-14-15] in order to describe the absorption properties of the microperforated resonator in terms of acoustic impedance.

The microperforated panel can be studied starting from the wave propagation into the single perforation which is a small tube. The air inside each tube can be studied as the sum of large number of thin coaxial cylindrical layers, and each layer moves along the axial direction under the restriction of its inertia and viscous force proportional to the radial gradient of velocity [104]. So, assuming the pressure difference between the two ends of the tube (ΔP) as force acting on the system, the momentum equation applied to the small tube in polar coordinates can be written

$$\rho_0 \frac{\partial v}{\partial t} - \frac{\eta}{r_1}\frac{\partial}{\partial r_1}\left(r_1 \frac{\partial v}{\partial r_1}\right) = \frac{\Delta P}{t_h} \tag{3.25}$$

where ρ_0 is the air density, η is the dynamic viscosity constant of air, v is the axial particle velocity of the air in the tube, t_h is the length of the tube (and the MPP thickness) and r_1 is the radius vector which is zero on the internal wall of the perforation and maximum in the axis.

Assuming a sinusoidal particle motion, equation (3.25) can be rewritten

$$\left(\frac{\partial^2}{\partial r_1^2} + \frac{1}{r_1}\frac{\partial}{\partial r_1} + k^2\right) v = \frac{\Delta P}{\eta t_h} \tag{3.26}$$

where $k^2 = -\frac{j\omega\rho_0}{\mu}$

Assuming as boundary condition, zero velocity on the tube wall ($r_1 = r_0$), the solution of equation (3.26) can be expressed by the Bessel function of first kind and zero order (J_0) and first kind and first order (J_1)

$$\bar{v} = \frac{2}{r_0^2}\int_0^{r_0} v r_1 dr_1 = -\frac{\Delta P}{\mu k^2 t_h}\left[1 - \frac{2}{kr_0}\frac{J_1(kr_0)}{J_0(kr_0)}\right] \tag{3.27}$$

where $\bar{v}$ is the average velocity into the tube.

The specific acoustic impedance is defined as the ration between the pressure filed and the velocity. Combining equation (3.27) which defines the average velocity in the small tube, and the difference of pressure at two ends of the tube, the characteristic impedance can be expressed as

$$Z_1 = \frac{\Delta P}{\bar{v}} = j\omega\rho_0 t_h \left[1 - \frac{2}{x\sqrt{-j}} \frac{J_1\left(x\sqrt{-j}\right)}{J_0\left(x\sqrt{-j}\right)}\right]^{-1} \tag{3.27}$$

where $x = \sqrt{\frac{\rho_0 \omega}{\eta}}$ is proportional to the thickness of the viscous boundary layer ($\sqrt{2\mu/\omega}$, with μ the kinematic viscosity constant of the air).

At this point Maa [13] gave an approximation of equation (3.27) based on the Zwikker and Kosten formulas [105] for tube of diameter *d*, which is supposed to be very narrow and relative wide (*x<1* and *x>10*). Such Hypothesis lead to two different solution of (3.27)

$$x < 1 \rightarrow \frac{4}{3} j\omega\rho_0 t_h + 32\frac{\rho_0 \mu t_h}{d^2} \tag{3.28}$$

$$x > 10 \rightarrow j\omega\rho_0 t_h + \frac{4\rho_0 \mu t_h}{d}\sqrt{\frac{\omega}{2\mu}}(1+j) \tag{3.29}$$

Combining equation (3.28) and (3.29), we can define a characteristic acoustic impedance equation suitable for small value of *x* (equation (3.28)) and big value of *x* (equation (3.29))

$$Z_1 = \frac{32\rho_0 \mu t_h}{d^2}\sqrt{1 + \frac{x^2}{32}} + j\omega\rho_0 t_h \left(1 + \frac{1}{\sqrt{9 + \frac{x^2}{2}}}\right) \tag{3.30}$$

Equation (3.30) defines a complex quantity where the real part represents the equivalent acoustic resistance (R_1) while the imaginary part represents the equivalent acoustic reactance (M_1).

However, correction factors need to be applied to acoustic resistance and acoustic reactance in order to take into account the fact that the length of the perforation (i.e. the thickness of the MMP) is not large compared with the diameter of the perforation itself. Regarding the acoustic reactance, the sound radiation from both the tube ends makes the effective length of the tube increased by *0.85d* [106]. Regarding the acoustic resistance, it will increase of $2\sqrt{2\omega\rho_0\eta}$ if both of the tube is ended in infinite baffles [16]. The increment is related to the fact that the resistance is produce by friction loss due to the air moves along the baffles when the air flows into and out of the tube.

The acoustic impedance can be then expressed

$$R_1(\omega) = \frac{32\eta t}{p\rho_0 c d^2}\left(\sqrt{1+\frac{x(\omega)^2}{32}}+\frac{\sqrt{2}}{8}x\frac{d}{t}\right) \tag{3.31}$$

$$M_1(\omega) = \frac{t}{pc}\left(1+\frac{1}{\sqrt{9+\frac{x(\omega)^2}{2}}}+0.85\frac{d}{t}\right) \tag{3.32}$$

$$Z_{MPP}(\omega) = R_1(\omega) - i\omega M_1(\omega) \tag{3.33}$$

This approach allows to study the acoustic characteristics from an equivalence between the electric properties and the acoustic properties i.e. resistance, reactance, impedance, and it will be used in the next chapters of this thesis to investigate the absorption performances of MPP absorbers.

3.4 List of Symbols

The symbols and their explanation used in Chapter 3 for the mathematical notation are reported below:

Symbol	Description
ρ	Density Function
ρ'	Density Fluctuation
ρ_0	Density of air
v	Velocity Function
v'	Velocity Fluctuation
P	Pressure Function
P'	Pressure Fluctuation
c	Speed of sound in air
t	Time Function
ω	Angular Frequency
K	Bulk Modulus
Q	Acoustic Mass Source
μ	Dynamic Viscosity
Ω_f	Acoustic Domain
Γ_f	Acoustic Domain Boundary
u	Displacement Function
w	Weighting Function
N	Element Shape Function
M_f, C_f, K_f	Acoustic Mass, Damping and Stiffness Matrices
R	Acoustic Field Boundary Matrix
f_f	Acoustic Load Function
r_1	Tube Radius Vector
t_h	Length of tube – thickness of MPP
J_0 , J_1	Bessel Functions
x	Viscous Boundary layer Function
d	Tube Diameter
Z_1	Acoustic Impedance
R_1	Acoustic Resistance
M_1	Acoustic Reactance

Chapter 4

Design and manufacturing of an Impedance Tube test rig for Acoustic Properties Measurements

4.1 Introduction

The impedance tube is the most commonly used test rig of measuring the acoustic properties such as the acoustic impedance, the normal absorption coefficient and the normal transmission lost coefficient of tested sample. The apparatus, the measurement approach and the post processing of data are standardized in ASTM E-1050[1] and ASTM E-2611 [2].

The test apparatus includes a tube with a sound source in one end and the tested sample mounted at the other end, and eventually a second tube downstream the sample. A plane standing wave is generated into the tube using a broadband acoustic signal [11-12] generated from the acoustic source and travelling into the tube. The acoustic pressure level of the travelling plane wave is measured along different stations upstream and downstream the sample.

The Transfer Function Method [3-4-9] is then use to estimate the acoustic properties of the tested sample. This method is based on the decomposition of the stationary sound wave pattern into the tube in its forward and backward travelling components (incident, reflected and transmitted sound wave components). This is achieved measuring the sound pressure level on different microphone locations, running the transfer functions between the acquired signals and examining their relative amplitude and phase. Two different approaches, based on the main transfer function method, will be applied to estimate respectively the normal sound absorption coefficient and the transmission lost coefficient as explained in the following chapters.

The transfer function method is implemented in Matlab environment. A LabView interface was programmed to control the test rig in terms of input-output acquisitions and linked with the Matlab code for the measured data post processing.

From the Labview user-interface, the user can select all the parameter to manage the sound wave generator and the acquisition parameters.

In the *Waveform generator* subsection (***Figure***), the general test parameters for the test can be defined. Different signals including burst random noise and sine sweep having a uniform spectral density across the frequency range, can be setup in *Waveform Type*. *Amplitude* allows to define the amplitude peak-to-peak of the pre-selected signals, while the *Requested Frequency* sets the sampling rate for the generated output signals.

In the *Oscilloscope* subsection the input/output signals can be managed. The *Sample Rate* is the sampling rate of the captured signal, while the *Sample per Channel* is the buffer size. Amplification on the received signals can be applied in *Gain* section.

In *Waveform* subsection (***Figure 4.2***) the input sound wave parameters can be set up and the geometry parameters of the impedance tube test rig can be defined for the acoustic properties evaluation in the post-processing. Mic1Pos and Mic2Pos are the microphone location coordinate respect to the specimen surface. The working frequency range of the impedance tube test rig is identified by *Lf* (lower frequency

limit) and *Hf* (higher frequency limit). The sweep signal, the signal length in time domain is declared in *Sweep Time.* A tail where the signal is imposed to be zero can be added at the beginning and the end of the signal. The time length of the tail is defined in *Time of Tail. Low* and *High Frequency* are the output frequency range. In order to remove the noise on the input signals and increase the accuracy of the acoustic properties estimation, a cutting percentage can be applied in *Cut Signal*, which allows to cut the beginning of the sending signal to remove input noise in the system. In the *Burst Signal Info* short signal with a number of frequencies (*No.Freq*) between the *Low* and *High Frequency* with a number of cycles per frequency (*No.Cycles*) can be defined.

When the geometry parameters of the tube, the frequency working range are set and the input signal defined, the sound input wave will be generated from the speaker. The complex pressure at active microphones will be measured and passed to the Matlab subroutine where the acoustic properties will be calculated. In particular the reflection coefficient, the normal absorption coefficient and the normal transmission loss coefficient will be shown in the in the Labview user-interface.

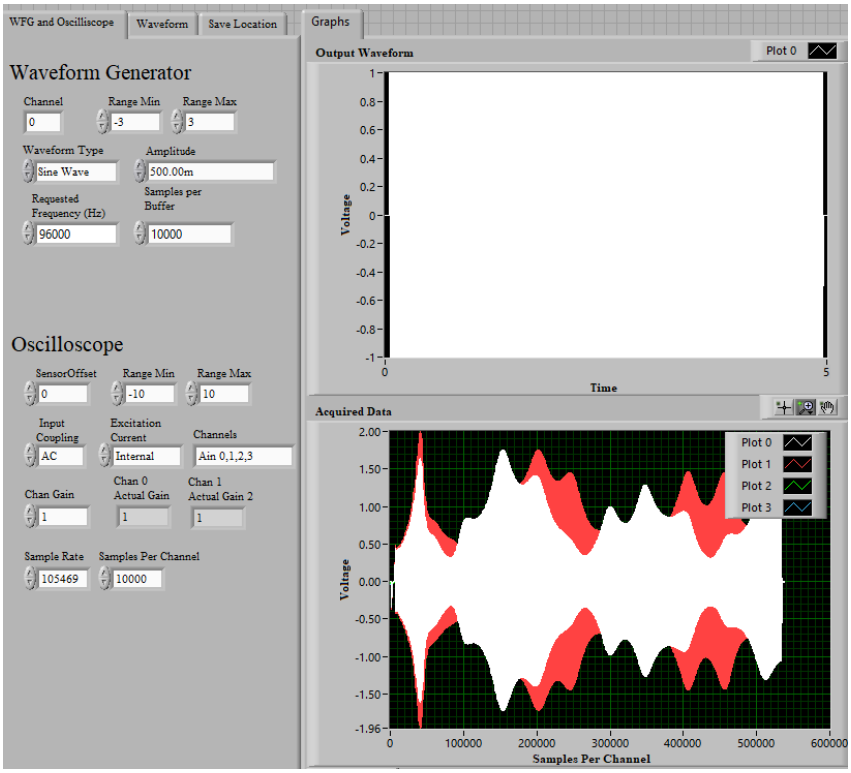

Figure 4.1. Impedance Tube LabView user interface: Wave Generator and Oscilloscope subsection

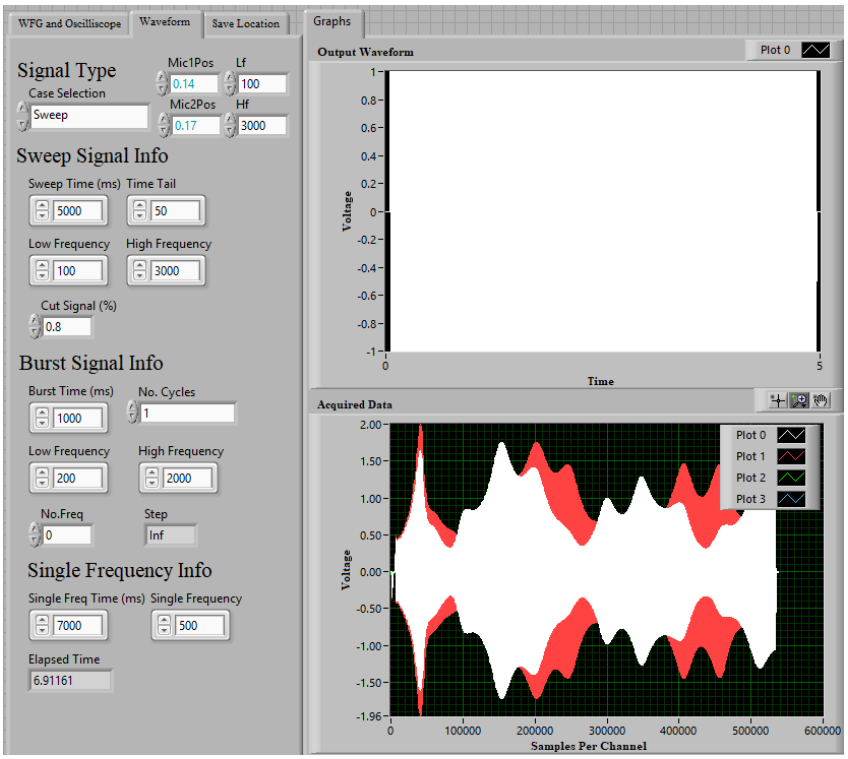

Figure 4.2. Impedance Tube LabView user interface: Waveform subsection

4.2 Impedance Tube Design

According with the ASTM standard E 1050 – E 2611 [1-2], two and four microphones impedance tube has been designed, machined and installed in the NDT Lab of Mechanical Engineering Department.

The apparatus is essentially a tube with a constant cross section and 6mm wall thickness. In order to minimize the sound losses through the wall, a high acoustic impedance material is chosen for the tube (Aluminium). Moreover, the inner surface of the tube was carefully machined to guarantee straight, smooth and nonporous surface in order to maintain low sound attenuation and avoid potentially sound reflections which compromise the plane standing wave into the tube.

The geometrical design of the tube is strictly related to the operational frequency range of the tube itself. In particular two main geometrical parameters of the tube are function of the lower and upper working frequency: tube diameter (*d*) and the microphones spacing (*s*).

The tube diameter is inversely proportional to the upper frequency limit, while the microphones spacing is inversely proportional to the lower frequency limit.

When the required operational frequency range of the tube is set, the inner diameter of tube can be estimated

$$d < \frac{Kc}{f_u} \tag{4.1}$$

where f_u is the upper working frequency, c is the speed of sound in the tube and K is a geometrical scale factor which takes into account the cross section shape (K=0.586 for cylindrical tube and K=0.5 for rectangular tube).

An essential parameter for the measurement accuracy is the microphone spacing.

In particular, increasing the microphone spacing the measurement accuracy is increased. The minimum value of the microphone distance is defined by the lower frequency of the prescribed frequency range. The spacing should be greater than 5% of the specified lower limiting frequency wavelength

$$s < 0.05\frac{c}{f_l} \tag{4.2}$$

Moreover, considering the Transfer Function Method for the data post processing and acoustic properties evaluation, the reflection coefficient cannot be determined using this method for such frequency where the microphone spacing is a multiple of half wavelength of the sound [3]. Assuming f_u as the upper limiting frequency of the impedance tube, the microphone spacing must be less than the lower half wavelength in order to avoid this singularity in the reflection estimation. To be conservative the actual microphone spacing has been designed to be the 80% of that limit value

$$s > 0.4\frac{c}{f_u} \tag{4.3}$$

The impedance tube apparatus includes a sound source at one end location of the tube and the tested sample at the other end location. The distance between the sound source and the closer microphone (x) and the distance between the incident surface of the sample and the closer microphone (l) must be designed.

The applicability of the transfer function method is associated to the initial hypothesis of plane standing wave into the impedance tube. The sound source could generate non-plane waves. In order to guarantee a completed develop of a plane waves before the wavefront reach the firs measuring location, the first microphone should be placed distance enough from the sound source. Since the non-plane waves usually subside at a distance equivalent to three tube diameters, the distance between the sound source and the closer microphone can be define

$$x > 3d \tag{4.4}$$

Regarding the distance between the incident surface of the sample and the closer microphone, it depends on the characteristic of the sample surface, and in any case, it needs to be kept smaller as much as possible to minimize the signal-noise ratio. This distance must be designed to guarantee plane wave condition of the reflected wave in the second measuring location. Considering flat and smooth surface of the

sample, the result of the interaction between the incident plane wave and the sample will be a plane wave. In this case, the distance between the sample and closer microphone can be minimized within half of the tube diameter. If the sample is characterized by nonhomogeneous surface, non-plane reflected waves could be generated after the incident wave interaction with the sample. In order to suppress the effect of higher-order modes and keep a plane wave condition, one tube diameter is the minimum distance. The worse is represented by asymmetrical and nonhomogeneous surface. Since the higher order modes will decay exponentially as they propagate along the tube, and the asymmetry on the surface will generate strong non plane reflected waves, the closer microphone should be placed at least two tube diameter from the sample surface. In order to cover all the possible conditions in terms of surface sample, the distance between the sample and closer microphone is designed to be

$$l > 2d \tag{4.5}$$

As explained before in this paragraph, the operating frequency range where plane standing wave is guaranteed and the transfer function method applicable, is strictly related to the microphone positions. In order to extend as much as possible the frequency range, multiple microphone stations are included in the designed apparatus. In particular, a third microphone is included to cover the need for accurate low frequency measurements. As shown in ***Figure 4.3***, two different configurations can be set for the present apparatus which allow covering two overlapped frequency range [85-700] Hz and [250-3000] Hz.

The possible impedance tube configurations with the relative geometrical design parameters are summarized in Table 1 and Table 2.

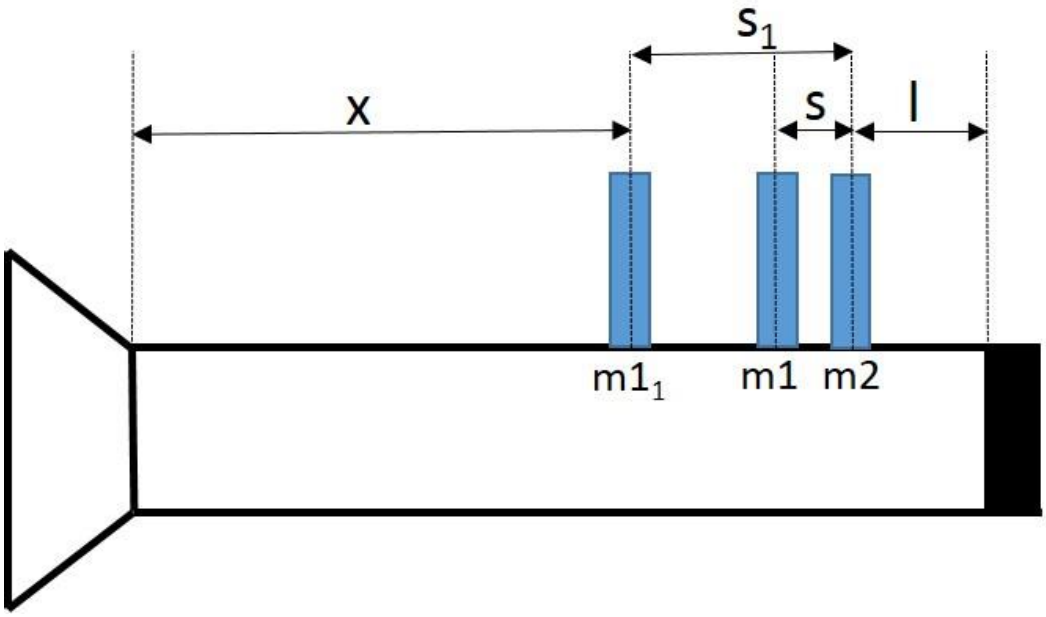

Figure 4.3. Geometrical design parameters for the Impedance Tube

Frequency Range	250-3000 [Hz]
d	50.8 [mm]
l	140 [mm]
x	160 [mm]
s	30 [mm]

Table 1. High frequency Impedance Tube configuration

Frequency Range	85-700 [Hz]
d	50.8 [mm]
l	140 [mm]
x	160 [mm]
s1	200 [mm]

Table 2. Low frequency Impedance Tube configuration

Two different tube assembly conditions can be considered to measure the sound absorption coefficient and the sound transmission loss respectively.

Two microphones configuration can be used to measure the sound absorption coefficient. In this case, two microphones are placed upstream the tested sample according with the design requirements shown in this paragraph. Since the standing wave pattern into the tube must be decomposed into forward-backward upstream travelling components and forward-backward downstream travelling components, four microphones configuration is required to measure the sound transmission loss. In this case the apparatus is a set of two symmetric tubes respectively upstream and downstream respect to the sample with two microphones placed upstream and two microphones downstream. The upstream-downstream microphone locations are symmetrical respect to the sample and defined by the equations (4.2 - 4.5) (***Figure 4.4***).

The drawing s for the two impedance tube configurations are reported in in *Appendix A1*.

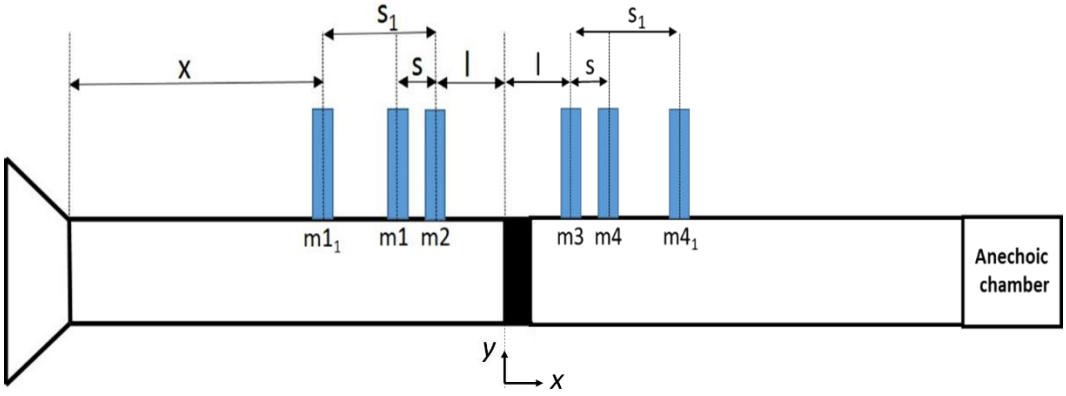

Figure 4.4. Geometrical design parameter for the Impedance Tube for Sound Transmission Loss measurement

Regarding the termination, two different approaches are considered for the two and four microphones configurations.

A moving piston configuration is used for the two microphones configuration. In this case, the tube termination includes a moving piston with a high reflection aluminium head of 35mm thickness (*Appendix A2*). The piston head is tightly fixed

to the internal wall of the tube termination in order to minimise the sound losses and provide a sound-reflective termination.
Different tube termination is used for the four microphones configuration. In this case an anechoic termination is designed to minimise the reflection of the sound wave back down the tube. Anechoic condition has been guaranteed installing a pyramidal shaped section about 300 mm long of high absorption acoustic foam.

4.3 Transfer Function Method

The Transfer Function Method introduced for the first time by Chung and Blaser [3 - 4] is based on the broadband stationary sound signal decomposition into the its incident, reflected and transmitted component using the transfer function relation between the sound pressure at different locations along the impedance tube. This sound wave decomposition leads to the sound reflection coefficient, sound absorption coefficient and transmission loss coefficient.

The Transfer Function approach is applicable to both the rig configurations: Two Microphones configuration and Four Microphones configuration. However, because in this research work we focus on the Absorption/Reflection properties of materials/structures, only Two Microphones configuration is taken into account. More information regarding the applicability of the Transfer Function method to the Four Microphones configuration are included in *Appendix A3*.

4.3.1 Transfer Function Method: Two Microphones configuration

Considering the two microphones configuration and assuming $p_1(t)$ and $p_2(t)$ the acoustic pressure at the microphone locations, each pressure can be decomposed in its incident and reflected contribution:

$$p_1(t) = p_{1i}(t) + p_{1r}(t) \tag{4.6}$$

$$p_2(t) = p_{2i}(t) + p_{2r}(t) \tag{4.7}$$

The pressure components can be expressed in terms of the impulsive responses:

$$p_{1r}(t) = \int_0^\infty r_1(\tau) p_{1i}(t-\tau) d\tau \tag{4.8}$$

$$p_{2r}(t) = \int_0^\infty r_2(\tau) p_{2i}(t-\tau) d\tau \tag{4.9}$$

$$p_{2i}(t) = \int_0^\infty h_i(\tau) p_{1i}(t-\tau) d\tau \tag{4.10}$$

$$p_{2r}(t) = \int_0^\infty h_r(\tau) p_{1r}(t-\tau) d\tau \tag{4.11}$$

$$p_2(t) = \int_0^\infty h_{12}(\tau) p_1(t-\tau) d\tau \tag{3.12}$$

Where *r1* and r2 are the impulsive responses corresponding to the reflected wave evaluated at the microphone locations, while h_i and h_r are the impulsive responses corresponding to the incident and reflected waves evaluated between the two microphone locations. Finally, h_{12} is the impulsive response relative to the combined incident and reflected waves evaluated between the microphone locations.

The complex reflection coefficient is defined as the ratio between the amount of sound wave energy reflected back and the incident one. So, combining the equation (4.6 - 4.12) we can write the complex reflection coefficient in terms of the auto-spectral density of the incident pressure $S_{1i\,1i}(f)$ and the reflected pressure $S_{1i\,1r}(f)$ at the first microphone location:

$$R_1(f) = \frac{S_{1i\,1r}(f)}{S_{1i\,1i}(f)} = \frac{\int_0^\infty [h_{12}(\tau) - h_i(\tau)]\, e^{-j2\pi/\tau} d\tau}{[h_r(\tau) - h_{12}(\tau)] e^{-j2\pi/\tau} d\tau} \tag{4.13}$$

Using equation (4.13), we can see how the complex reflection coefficient is the Fourier transform of the impulsive response of the reflected wave evaluated at the first microphone location

$$R_1(f) = \frac{S_{1i\,1r}(f)}{S_{1i\,1i}(f)} = \int_0^{\infty} r_1(\tau) e^{-j2\pi/\tau} d\tau \tag{4.14}$$

Similarly, using the equation (4.10 - 4.12), we can write the acoustic transfer functions corresponding to the impulsive responses h_i, h_r and h_{12} which are the acoustic transfer function of the incident and reflected sound waves between the microphone locations and the combined incident-reflected sound waves acoustic transfer function respectively:

$$H_i(f) = \frac{S_{1i\,2i}(f)}{S_{1i\,1i}(f)} = \int_0^{\infty} h_i(\tau) e^{-j2\pi/\tau} d\tau \tag{4.15}$$

$$H_r(f) = \frac{S_{1r\,2r}(f)}{S_{1r\,1r}(f)} = \int_0^{\infty} h_r(\tau) e^{-j2\pi/\tau} d\tau \tag{4.16}$$

$$H_{12}(f) = \frac{S_{12}(f)}{S_{11}(f)} = \int_0^{\infty} h_{12}(\tau) e^{-j2\pi/\tau} d\tau \tag{4.17}$$

Combining the previous equations, the complex reflection coefficient can be expressed in term of Fourier transform

$$R_1(f) = \frac{H_{12}(f) - H_i(f)}{H_r(f) - H_{12}(f)} \tag{4.18}$$

Equation (3.14) defines the acoustic reflection coefficient at the first microphone location. However, a relation between the complex reflection coefficients at two microphone stations can be defined combining the equations (4.8 - 4.11)

$$\frac{R_1(f)}{R_2(f)} = \frac{H_i(f)}{H_r(f)} \tag{4.19}$$

Now, assuming a plane wave condition into the tube and neglecting losses at the tube wall, the transfer function of the incident and reflected sound wave can be expressed:

$$H_i(f) = e^{-jks} \tag{4.20}$$

$$H_r(f) = e^{jks} \tag{4.21}$$

where *k* is the wave number and s is two microphones spacing.

Under the no losses through the tube wall, the magnitude of the complex reflection coefficient is independent of the measurement location, however a singularity in the reflection coefficient can be identified when $H_r - H_{12} = 0$, for which R_1 becomes indeterminate. According with equations (4.20) and (4.21), this condition occurs when

$$ks = m\pi \quad or \quad s = m\frac{\lambda}{2}, m = 1,2,3 \ldots \tag{4.22}$$

Equation (4.22) define a constrain on the microphone spacing. In fact, for integer multiple of the half wavelength of the sound wave, the complex reflection coefficient is indeterminate. This constrain needs to be taken into account in the impedance tube design, and in order to avoid these points of singularity, the microphone spacing must be designed according to equation (4.3).

In order to evaluate the acoustic properties of the tested sample, the complex reflection coefficient must be evaluated on the sample surface. Applying equation (4.15) between the first microphone station and the sample surface and defining *l* the distance between the second microphone station and the sample surface (***Figure 4.3***)

$$\frac{R_1(f)}{R(f)} = \frac{H_i'(f)}{H_r'(f)} \tag{4.23}$$

where

$$H_i' = e^{-jk(l+s)} \tag{4.24}$$

$$H_r' = e^{jk(l+s)} \tag{4.25}$$

So, the complex reflection coefficient at the sample surface can be defined

$$R(f) = R_1(f)e^{j2k(l+s)} = \frac{H_{12} - e^{-jks}}{e^{jks} - H_{12}} e^{j2k(l+s)} \tag{4.26}$$

When the reflection coefficient is estimated, the normal incident sound absorption coefficient can be determined. The sound absorption coefficient represents the amount of sound energy absorbed by the sample which is defined as the difference between the incident sound energy and reflected one, respect to the incident sound energy. So, using the definition of the complex reflection coefficient, the normal incident sound absorption coefficient can be expressed

$$\alpha(f) = 1 - |R(f)|^2 \tag{4.27}$$

The normal acoustic specific impedance of tested sample can be estimated by the complex reflection coefficient. Considering the fluid-structure interface, and assuming a plane and normal incident sound wave, the complex reflection coefficient can be expressed in terms of the characteristic impedance of the fluid (Z_0) and the characteristic impedance of the solid (Z) [5-6-7]

$$R(f) = \frac{Z(f) - Z_0}{Z(f) + Z_0} \tag{4.28}$$

The specific acoustic impedance can be rewritten as

$$z(f) = \frac{Z(f)}{Z_0} = \frac{1 + R(f)}{1 - R(f)} \tag{4.29}$$

where the characteristic impedance of the fluid (air in this case) is expressed as the product of the fluid density and the speed of sound in the fluid $Z_0 = \rho c$.

The specific impedance is a complex quantity where the real part and the imaginary part assume a meaning of specific acoustic resistance and specific acoustic reactance respectively. The specific acoustic resistance is involved in the sound energy dissipation through internal friction of a medium transmitting, reflecting or

absorbing sound wave, while the specific acoustic reactance concerns the effect of inertia and elasticity of a medium transmitting, reflecting or absorbing sound wave.

4.3 Assessment of error in the Impedance Tube test rig

The acoustic properties evaluation through the transfer function method, using an impedance tube test rig, could be affected by several factors which may introduce errors on the acoustic properties estimation.

The Transfer Function Method is based on the measurement of the transfer function (H_{12}) between two microphones placed on two stations along the tube. According with equation (4.26), the acoustic properties can be estimated starting from the input data: transfer function (H_{12}), the microphone spacing (s) and the distance between the second microphone and the tested sample (l). The resulting errors in acoustic properties evaluation will be then affected by the errors in the input data and by the sensitivity of the calculation formulas to the errors in the input data.

Regarding the transfer function (H_{12}) estimation, two types of error are possible: bias and random errors. The bias errors are mainly related to the inadequate spectral resolution. Boden and Abom [110] provided the limits in terms of spectral resolution to keep the errors on the transfer function small. In particular, the bias errors extreme values for the not highly termination ($R\sim0$) and for high reflective ($R\sim1$) terminations are defined by the following expressions:

$$\varepsilon_b = \left(\frac{800\pi^2\Delta f^2 l^2}{3c^2}\right)1.5 \tag{4.30}$$

$$\varepsilon_b = \left(\frac{800\pi^2\Delta f^2 l^2}{3c^2}\right)9900 \tag{4.31}$$

Regarding the proposed impedance tube test rig, where the distance l is 0.14m, assuming an acceptable bias error on 1% in amplitude on the transfer function estimation, equations (4.30) and (4.31) lead to spectral resolution of 39 Hz and

0.48Hz. In order to keep the bias error smaller than 1% the frequency resolution in the test set was set to 0.3Hz.

Moreover, because of the transfer function method for the post-processing of the data is a complex ratio between the complex pressure measured by the two microphones, another source of error could be the mismatch in amplitude and phase which will affect the measurement and the estimation of the acoustic properties in particular at low frequencies. Therefore, a calibration approach to compensate this measurement mismatches, due to not microphones calibration and sound wave attenuation, is proposed in this research work and deeply explained in Chapter 5. As shown in Figure 5.12 the calibration approach allows to keep the error on estimation of the acoustic properties at low frequencies smaller than 1%.

As anticipated, other input data as microphone spacing (*s)* and the microphone distance from the tested sample (*l*) could introduce error on the acoustic property evaluation. The error on such input data measurement can be normally quantified in ∓5mm. Following we report a numerical investigation where the influence of error related to *s* and *l* on the acoustic property evaluation is quantified applying perturbations on the input data of equation (4.26).

Assuming the geometrical parameters for proposed impedance tube, defined in Table 1, perturbation on the microphone spacing (*s*) is applied and the effect on the reflection coefficient and on the absorption coefficient are plotted on *Figure 4.5* and *Figure 4.6* respectively. Assuming the error on the input data *s* quantified in ∓5mm, the error propagated in the measured absorption and reflection coefficient will be respectively of 0.3% and 2.5%.

Figure 4.7 and *Figure 4.8* show the error associated to the measured absorption and reflection coefficient when a perturbation is applied on the input data *l.* In this case, an error on the input data of ∓5mm, it will introduce an error on the absorption and reflection coefficient less than 0.5%.

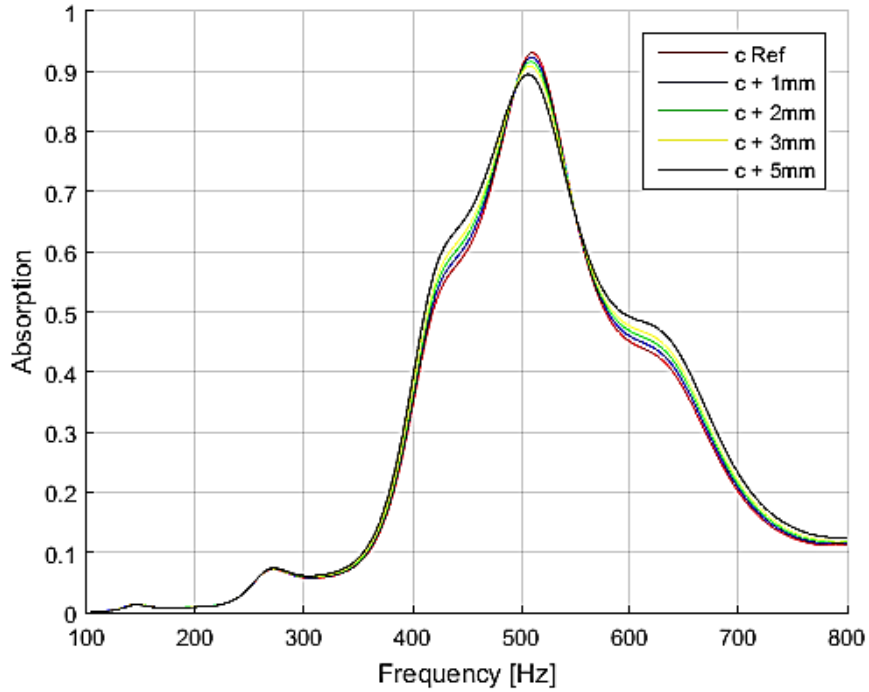

Figure 4.5. Error on the absorption coefficient induced by perturbation on the *s* input data

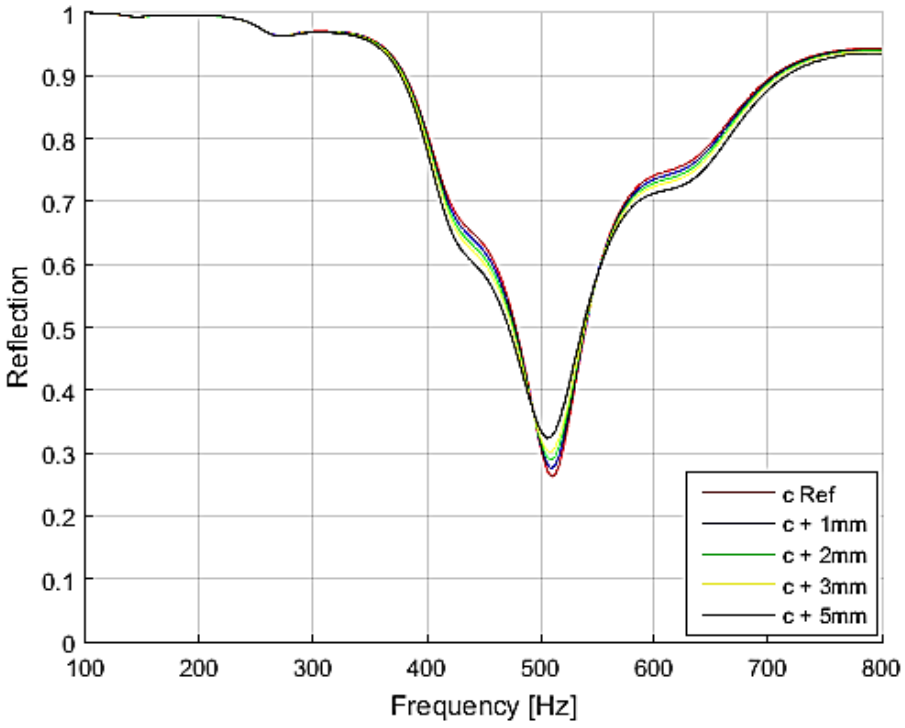

Figure 4.6. Error on the reflection coefficient induced by perturbation on the s input data

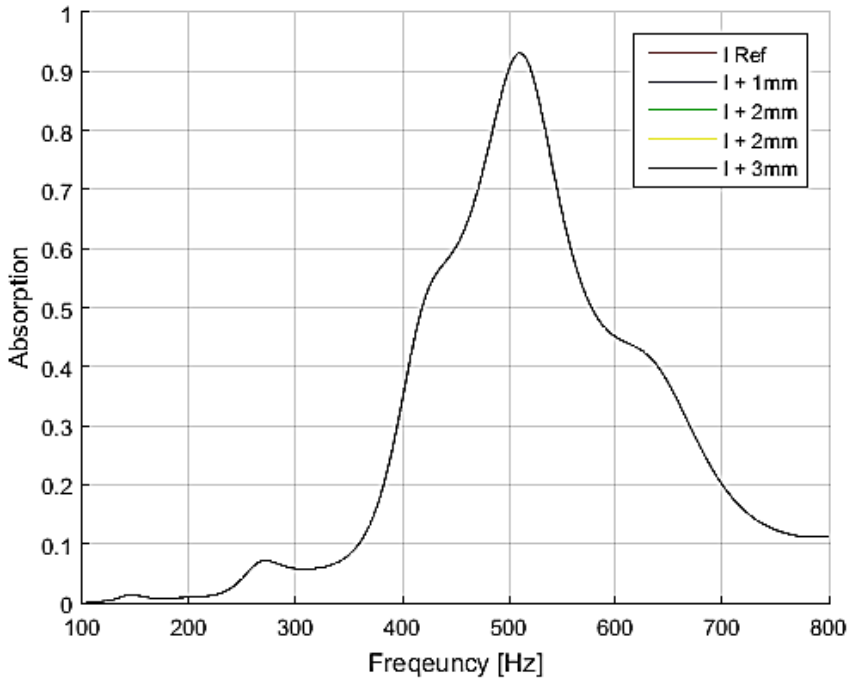

Figure 4.*7*. Error on the absorption coefficient induced by perturbation on the *l* input data

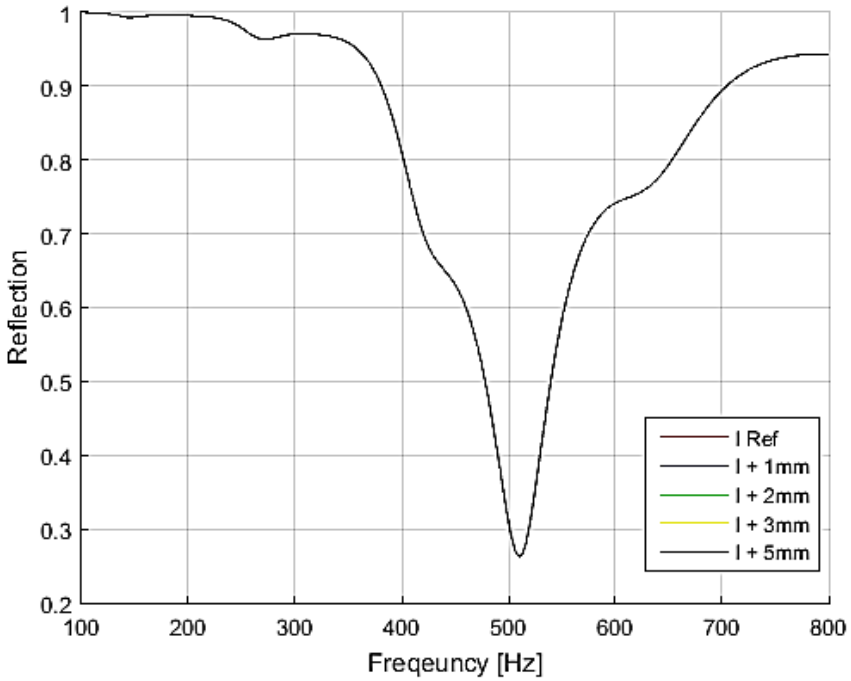

Figure 4.*8*. Error on the reflection coefficient induced by perturbation on the *l* input data

4.4 List of Symbols

The symbols and their explanation used in Chapter 4 for the mathematical notation are reported below:

Symbol	Description
d	Internal diameter of the Impedance Tube
K	Geometrical Scale Factor for cylindrical or square cross section
f_u	Upper frequency limit
f_l	Lower frequency limit
s	Microphone Spacing
x	Distance between sound source and 1st Mic location
l	Distance between sample and 2nd Mic location
p_1 , p_2	Complex Pressure measured at Mics locations
p_i , p_r	Incident and Reflected component of pressure
t	Time variable
r_1 , r_2	Impulsive response of reflected component at Mic locations
h_1 , h_2	Impulsive response of incident component at Mic locations
h_{12}	Impulsive response of combined incident and reflected component at Mic locations
S_{1i1i}	Auto Spectral Density of incident pressure at Mic1
S_{1i1r}	Auto Spectral Density of reflected pressure at Mic1
S_{1i2i}	Auto Spectral Density of incident pressure at Mic2
S_{1i2r}	Auto Spectral Density of reflected pressure at Mic2
H_i	Acoustic Transfer Function of incident pressure component
H_r	Acoustic Transfer Function of reflected pressure component
H_i`	Acoustic Transfer Function of incident pressure component at sample incident surface
H_r`	Acoustic Transfer Function of reflected pressure component at sample incident surface
H_{12}	Acoustic Transfer Function of combined incident-reflected component
R_1	Reflection Coefficient at Mic1 location
R_2	Reflection Coefficient at Mic2 location
R	Reflection Coefficient at sample incident surface
k	Wave number
α	Absorption Coefficient
Z	Characteristic Acoustic Impedance of sample
Z_0	Characteristic Acoustic Impedance of air

Chapter 5

Non-destructive method based on acoustic measurement for elastic properties evaluation of anisotropic materials

Advancement of material technology has expanded the number of materials which find application in several engineering fields. Composites materials, 3D printed materials, biological materials represent an example of innovative and advanced materials where structures can be both anisotropic heterogeneous making it difficult to assess the material characterization with the traditional engineering methods.

The need to characterize this material, in particular in terms of their elastic properties, become then crucial.

However traditional methods as tensile testing or instrumental indentation [2 - 3] are not suited for identify the out-of-plane elastic modulus of anisotropic materials because of manufacturing process limitations. Further compounding the issue is the destructive condition of the methods.

Alternative techniques based on ultrasound have been developed for non-acoustic properties and Young's Modulus measurement [11-12-13]. However, even if these techniques represent a non-destructive approach, the scattering of the longitudinal

waves, especially for porous materials, makes it difficult to identify the back wall echo and thus accurately determine the Young's Modulus.

In this research work, the authors proposed a new non-destructive approach for the out-of-plane elastic modulus evaluation that is applicable to a wide range of materials which provides advantages.

The proposed approach is based on the reflection coefficient measurement of the tested material which is function of the acoustic impedance of air and the acoustic impedance of the material. An impedance tube is used as test rig and starting from pressure measurements, the Transfer Function Method is applied to estimate the reflection coefficient due to the interaction between the incident sound wave and tested material. The plane standing wave condition guaranteed by the impedance tube makes true the assumption that the sound wave/material interaction is substantially referred to the longitudinal wave. Since the propagation velocity for the longitudinal wave is related to the elastic properties of the material, and the acoustic impedance is directly proportional to such velocity, the out-of-plane Young's modulus can be then estimated starting from acoustic impedance measurement. A proper test rig calibration is applied to minimize any mismatch in amplitude and phase of the acoustic pressure responses which could affect the measurements.

The feasibility of this method is demonstrated in numerical way developing a coupled acoustic-structure FE model based on RVE approach.

The FE model was implemented in Ansys Workbench 18.1 environment (student license). Different element types were used to model the structural part (tested material) and the acoustic one (acoustic bodies).The structural parts of the FE model, including matrix and reinforcing fibre for composite material, is meshed using higher order 3-D 20-node solid element (SOLID186) that exhibits quadratic displacement behaviour. The element is defined by 20 nodes having three translational degrees of freedom per node. The element supports plasticity, hyperelasticity, creep, stress stiffening, large deflection, and large strain capabilities. It also has mixed formulation capability for simulating deformations of nearly incompressible elastoplastic materials, and fully incompressible

hyperelastic materials. SOLID186 elements are well suited to modelling irregular meshes. The acoustic bodies are then meshed using 3D 20-nodes FLUID220 type element which exhibits quadratic pressure behaviour and it is suitable fluid-structure interaction problems.

The structural element size is chosen to accurately describe the geometry of the reinforcing fibres. Figure 5.1 shows a mesh convergence analysis for the structural element where the equivalent stress and the equivalent strain are the reference results. According with mesh convergence analysis 0.1μm is used as element size.

Also for the acoustic body, the mesh should be fine enough to capture the acoustic mode shapes and guarantee a plane wave condition. So a minimum of 12 elements per wavelenght are required along the propagation wave direction. A mesh convergence analysis is performed for the maximum frequenxy required and the average pressure in the acoustic body profile as a function of the number of elements along the wave propagation direction is reported in Figure 5.2. According with Figure 5.2 60 element are used in the propagation direction to mesh the acoustic body (element size 4μm).

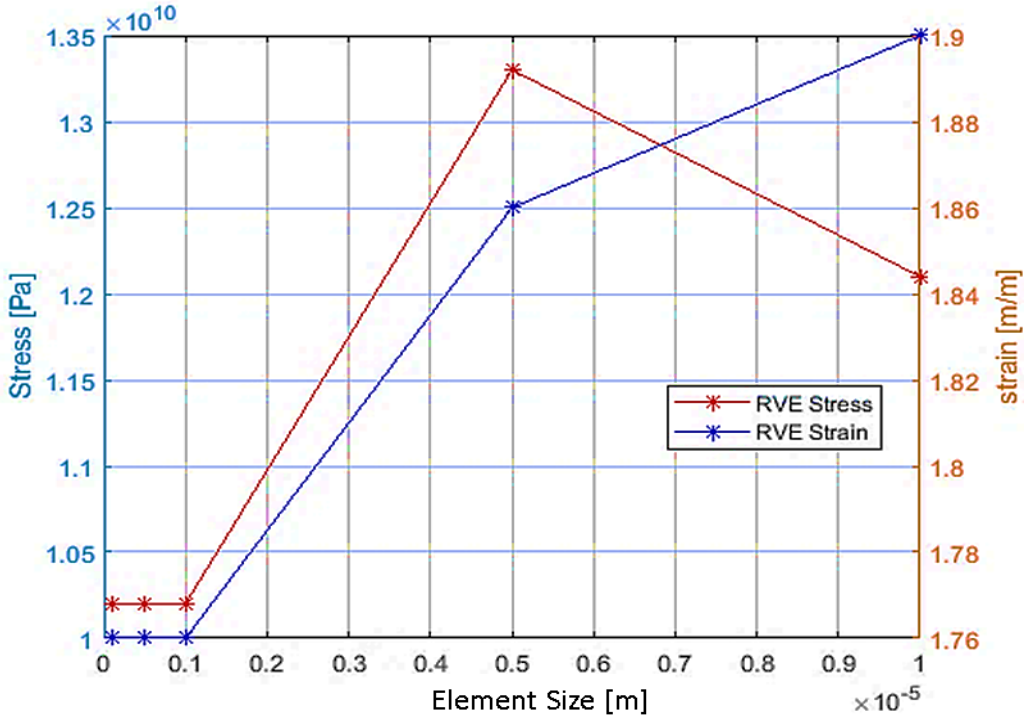

Figure 5.1 Structural element mesh convergence analysis

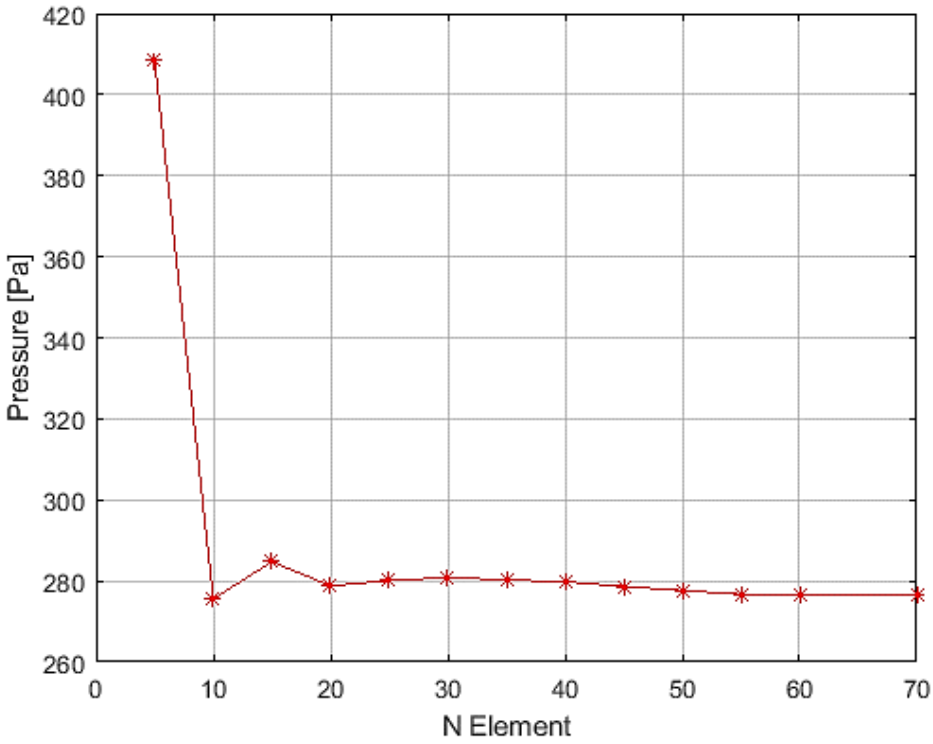

Figure 5.2. Acoustic element mesh convergence analysis

Then, an experimental measurement campaign is performed on different materials as foams and epoxy-carbon fibre composite and vynilester-glass fibre composite, applying the proposed method to extract the out-of-plane Young's Modulus. The measured properties are in good agreement with the values obtained by the standard methods as tensile tests and ultrasound time of flight measurements.

In particular the proposed approach can be applied for those materials, as porous materials, where the ultrasound approach cannot be applied, giving results within the 2% of error with respect to tensile testing results. For the first time, it was shown that using sound waves the out-of-plane elastic properties can be evaluated within the 3% of error of the longitudinal speed measurement and the 10% for the elastic modulus with respect to the ultrasonic testing.

5.1 List of Symbols

The symbols and their explanation used in Chapter 5 for the mathematical notation are reported below:

Symbol	Description
d	Impedance Tube internal diameter
K	Geometrical Scale Factor for cylindrical or square cross section
f_u	Upper frequency limit
f_l	Lower frequency limit
s	Microphone spacing
p_1 , p_2	Complex Pressure at Mic locations
P_i , P_r	Incident and Reflected complex pressure
$\widehat{P}_i$, $\widehat{P}_r$	Amplitude of incident and reflected pressure
H_i	Acoustic Transfer Function of incident pressure component
H_r	Acoustic Transfer Function of reflected pressure component
H_{12}	Acoustic Transfer Function of combined incident-reflected component
x	Coordinate along the tube
R	Reflection coefficient
H_c	Calibration Factor
k_0	Complex wave number (k real part, k`` imaginary part)
c	Speed of sound in air
θ_i, θ_L , θ_s	Propagation Angle of Incident, Longitudinal and Shear Wave
Z_1 , Z_L , Z_s	Characteristic Impedance of fluid, longitudinal wave and shear wave
Z_2	Characteristic Impedance of tested material
V_1 ,V_L , V_s	Sound propagation speed for fluid, longitudinal wave and shear wave
ρ_1 , ρ_1	Density of fluid and material
C_{Ls}	Longitudinal sound speed in the material
E	Elastic Modulus of the material
t	Time variable

x_i	Global level coordinates
y_i	Micro level coordinates
u_i^{η}	Exact value of the field variables
u_i	Macroscopic value of field variables
ε_{ij}	Microstructural strain tensor
$\bar{\varepsilon}_{ij}$	Macroscopic strain tensor
ε_{ij}^{*}	Fluctuating Microstructural strain tensor
η	Ratio between microstructure size to the total size of the analysis region
V_{RVE}	Volume of RVE
Ω	Total of macroscopic and microscopic domain
D_{ijkl}	Stiffness Tensor
M_{ijkl}	Tensor to relate the RVE variables to the averaged ones
σ_3 , ε_3	Stress and Strain in out of plain direction
ρ	Density of air
v	Particles velocity vector
Q	Acoustic Sound Source
p	Pressure
b	Body Force
S	Viscous Stress Tensor
$[M_s]$, $[C_s]$, $[K_s]$	Structural Mass, Damping and Stiffness Matrix
Ω_f	Acoustic Domain
Γ_f	Boundary of Acoustic Domain
$\{p\}$, $\{u\}$	Nodal pressure and Nodal displacement vectors
$[M_f]$, $[C_f]$, $[K_f]$	Acoustic Mass, Damping and Stiffness Matrix
$[R]^T$	Acoustic boundary matrix
$\{f_s\}$	Structural load vector
$\{f_f\}$	Acoustic load vector

5.2 Journal Paper Reference Details

The research work presented in this chapter is part of published journal paper which the reference details are as follow:

"A non-destructive method for evaluation of the out of plane elastic modulus of porous and composite materials"

Authors:

Fabrizio Bucciarelli - Department of Mechanical Engineering, University of Bath, Bath, UK.

Gain Piero Malfiense Fierro - Department of Mechanical Engineering, University of Bath, Bath, UK.

Mauro Zarrelli – Institute of Polymers, Composite and Biomaterials, Naples, ITA.

Michele Meo - Department of Mechanical Engineering, University of Bath, Bath, UK.

Corresponding Authors: Michele Meo – m.meo@bath.ac.uk

Journal: Applied Composite Materials volume 26, pages871–896(2019) - DOI: 10.1007/s10443-018-9754-5

The Statement of Authorship From and the paper a reported next.

This declaration concerns the article entitled:	
A non-destructive method for evaluation of out of plane elastic modulus of porous and composite materials	
Publication status (tick one)	
Draft manuscript	
Submitted	
In review	

Accepted	
Published	✓

Candidate's contribution to the paper (detailed, and also given as a percentage).	
The candidate contributed to/ considerably contributed to/predominantly executed the…	
Formulation of ideas:	80% The ideas to increase the capability of an impedance tube test rig, commonly used for the material acoustic characterization, in order to develop a non-destructive method for elastic properties evaluation of anisotropic material.
Design of methodology:	90% I defined and performed the analytical and numerical modelling for the proposed non-destructive approach
Experimental work:	60% I performed the experimental measurement campaign to validate the numerical/analytical model and prove the feasibility of the proposed approach. Dr Fierro helped me to set up the test rig for the experimental test campaign. Dr. Zarrelli provided the tested samples.
Presentation of data in journal format:	90% I decided structure, wrote all draft, prepared all figures. Prof. Meo provided feedback on drafts and helped with submission, responses to reviews and publication process.

Statement from Candidate			
This paper reports on original research I conducted during the period of my Higher Degree by Research candidature.			
Signed		**Date**	05/01/2020

A non-destructive method for evaluation of the out of plane elastic modulus of porous and composite materials

F. Bucciarelli[1], G.P. Malfense Fierro[1], M. Zarrelli[2], M. Meo[1]*

[1] Department of Mechanical Engineering, University of Bath, Bath, UK

[2] Institute of Polymers, Composites and Biomaterials, Naples, Italy

* corresponding author: m.meo@bath.ac.uk

Keywords: Elastic Modulus, Sound Waves, Impedance, RVE

Abstract

This paper presents an effective and reliable non-destructive method to measure the Young Modulus of porous and out of plane Young Modulus of composite materials using sound waves. First, a Finite Element Model based on Representative Volume Element (RVE) is developed to demonstrate how the elastic properties of composite material can be estimated by acoustic measurements using an impedance tube test rig. Second, the results of the experimental measurement campaign was carried out to validate the proposed method. In particular, two soft elastic foams with different density, an epoxy-carbon fibre composite and vynilester-glass fibre composite were tested. In the proposed method, a two-microphone impedance tube setup was used where the measured acoustic pressures at two upstream locations allowed the estimation of the reflection coefficient and the acoustic impedance of the tested materials. Since the acoustic impedance can be expressed as a function of the longitudinal speed of sound (assuming a plane standing wave excitation), the elastic modulus can be estimated which is associated with the speed of sound. The elastic modulus measured using the proposed method were in good agreement with the values obtained by the standard methods such as tensile tests and ultrasound time of flight measurements. The proposed method would allow in an accurate and fast

manner the non-destructive evaluation of Young Modulus of porous materials and for the first time the proposed approach is applied successfully to the measurement of out of plane Young modulus of composite materials.

1 Introduction

The rapid assessment of the elastic properties of materials has never been more prevalent than today, due to the acceleration in material development. Advancement of material technology has expanded the number of materials and applications for which these materials can be used. In particular, carbon fibre reinforced polymers (CFRP) have given way to a wide variety of complex materials with material characteristics that vary according to use. For example, CFRP applications range from a very specific highly technology environments (aerospace, Formula 1 and nuclear) to mass market applications (sport equipment, automotive and energy applications). At the same time the advent of commercial 3D printing has added a wide variety of materials that can be customised for a specific use, with highly varying material properties. A further area of interest is the characterisation of biological material where structures can be both anisotropic and heterogeneous making it difficult to assess these materials with traditional engineering methods. The speed and rate of material development has also been enhanced due to ever increasing automation. Thus, it is vital to evaluate the material properties (Elasticity, Yield, Hardness, etc.) of these components before they are used in the field.

The focus of this paper is to provide an alternative method for the measurement of the out-of-plane Young's Modulus (Elastic Modulus - *E*). The Young's Modulus of a material defines the relationship between stress and strain and provides a direct measure of material stiffness. A number of techniques have been used for the determination of the Young's Modulus, using both destructive and non-destructive testing procedures. These methods include: resonant frequency (in-plane) [1], instrumental indentation [2 - 3], traditional engineering methods (tensile tests) and ultrasound techniques [4].

Resonant frequency testing has focused on the evaluation of the Young's Modulus with regard to thin film materials (in recent times), which generally focus on the calculation of the Young's modulus of a micro-lever using the value of resonant frequencies obtained in prior experiments, although requiring both a numerical modal analysis as well as evaluation of experimental results. While instrumental indentation is a destructive method that infers from an indentations size and depth the Young's Modulus.

Traditional engineering methods are very common, highly controlled testing techniques, which generally focus on tensile, compression and three-point bending tests. These tests are highly suited for isotropic materials, as a tensile test can only provide one Young's modulus (in the direction of tension) but determination of the out-of-plane Young's Modulus becomes very difficult when investigating anisotropic materials. For example composite materials; as these structures are relatively thin in the out-of-plane direction, further compounding the issue is the manufacturing process which requires individual plies (+/-0.25mm per ply) to be placed on top of one another in the out-of-plane direction, thus requiring an enormous number of plies to be placed to meet the requirements for a tensile test in the out-of-plane direction.

Ultrasound methods provide various advantages over the previously mentioned techniques as smaller specimens can be used with less complicated geometries than mechanical testing methods [5]. Furthermore, the tests are non-destructive, thus more than one elastic constant can be evaluated per specimen. These methods often rely on the determination of the speed of sound through the specimen from which the elastic properties can be obtained [6].

This paper proposes a novel impedance-based method to determine the out-of-plane Young's Modulus of anisotropic materials. The method is based on the evaluation of the acoustic impedance (Z) of a material with the use of a two-microphones impedance tube. Impedance tubes are generally used for characterisation of sound absorbing materials, such as wool or polymers, used within building and transport applications.

An impedance tube is a simple apparatus that allows for a plane wave to be generated and propagate down a pipe, this acoustic wave then reflects off test materials. The phase interference between the waves in the pipe, which are incident upon and reflected from the test sample result in the formation of a standing wave pattern in the pipe. Under conditions of no absorption, the incident and reflected waves have the same amplitude resulting in nodes of zero pressure and antinodes with double the pressure. Whereas, if there is absorption by the test sample, the incident and reflected waves have different amplitudes and the nodes do not have zero pressure. The pressure amplitudes at nodes and antinodes can be measured with microphone probes. These measurements can be used to calculate a materials reflection coefficient (R), its absorption coefficient (α), and its impedance (Z) [7 - 8].

One of the most common ways to determine the acoustic impedance of materials is with ultrasound, where the impedance is directly related to the longitudinal speed of sound through the material. Recently various authors have developed alternative techniques based on ultrasound in order to determine: the acoustic impedance [9 - 10], non-acoustic properties of materials [11] and the Young's Modulus [12 - 13]. One of the issues with ultrasound testing of impedance and Young's Modulus testing is its ability to evaluate materials with high structural damping or porosity. Acoustic impedance and Young's Modulus analysis testing requires the accurate determination of the speed of sound through a known thickness. Porous materials result in the scattering of the longitudinal wave which makes it difficult to identify the back-wall echo and thus accurately determine the impedance or Young's Modulus of these types of materials (foams, rubber etc.).

The proposed method provides a solution that is applicable to a wide range of materials from soft foams to hard composite materials, and thus provides an advantage over traditional techniques such as ultrasound for the determination of the out-of-plane Young's Modulus.

The paper is organized in four sections. The first section of the paper describes the principles and basic assumptions of the proposed method. The method is then numerically validated in the second section. A coupled structural-acoustic FE

model is developed including a RVE model of composite material as the tested sample for which the elastic properties are well-know from the literature. The proposed method is applied to the simulation data in a further post-processing step, where the elastic modulus is estimated and compared with the expected one. An experimental measurement campaign on different materials is then reported in the last section of the paper. The experimental setup and the samples used in the experimental campaign are presented. Results evaluated with the proposed method for the tested materials are finally discussed and compared with those given by standard method (tensile testing and ultrasound time of flight).

2 Elastic Modulus Estimation Method

The proposed method is based on the two-microphones impedance tube because a plane standing wave condition is required. Starting from the acoustic pressure measurements in two different locations through the pipe, the Transfer Function Method is applied to estimate the reflection coefficient and acoustic impedance. It is demonstrated how the acoustic impedance can be related to elastic properties of the material including the propagation speed of sound.

2.1 Impedance Tube

According with the ASTM E 1050 [33], a two microphone impedance tube is expressed as a one-dimensional wave guide, with a sound source at one end and the acoustic load (typically the test sample) placed at the other end which guarantees a plane standing wave into the duct . In order to maintain plane wave propagation into the duct, the characteristic dimension of the tubes cross section satisfy the following condition:

$$d < \frac{K\,c}{f_u} \tag{2.1}$$

where K is a geometrical parameter associated to the cross-section shape (0.5 for rectangular or square cross section), c the speed of sound and f_u the upper frequency

limit. In order for a plane wave to fully develop before reaching the pressure acquisition points within the tube a minimum of 3*d* must be allowed between sound source and the nearest pressure acquisition point. The acquisition points spacing was prescribed to be less than 80% of shortest half wavelength of interest

$$s < 0.4\frac{c}{f_u} \tag{2.2}$$

2.2 Transfer Function Method

The Transfer Function Method for acoustic properties measurements was proposed in 1980 by Chung and Blaser [36 - 37]. The theory behind this method involve the decomposition of a standing wave into its incident and reflected components using a simple transfer-function relation between the acoustic pressures measured in two different locations as shown in Figure 5.3.

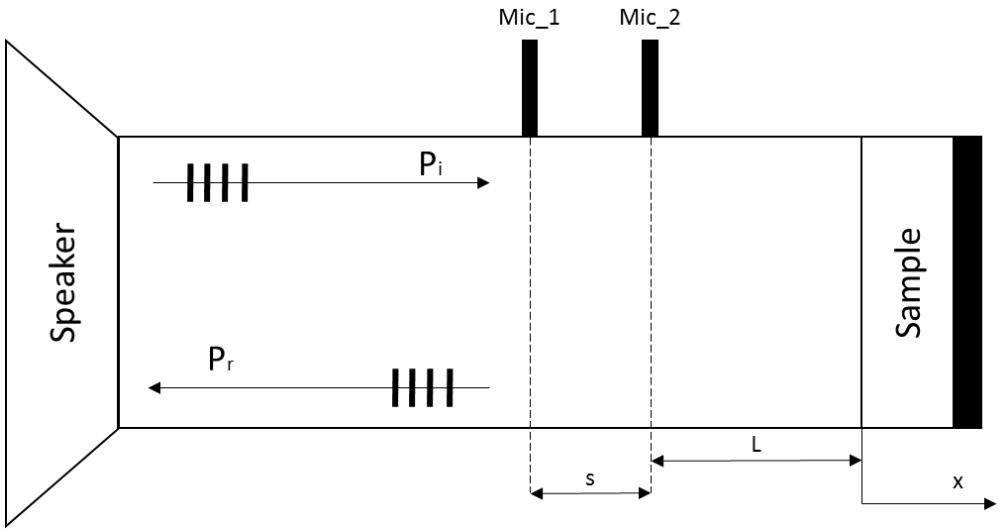

Figure 5.3. Impedance Tube configuration with two microphones and a rigid back wall.

According with Figure 5.3, the complex sound pressure at the microphone positions can be calculated

$$p_1 = \hat{P}_i e^{(-jk_0 x_1)} + \hat{P}_r e^{(jk_0 x_1)} \quad (2.3)$$

$$p_2 = \hat{P}_i e^{(jk_0 x_2)} + \hat{P}_r e^{(-jk_0 x_2)} \quad (2.4)$$

where $\hat{P}_i$ $\hat{P}_r$ are the amplitude of the incident and reflecting wave respectively, k_0 the wave number in air and x_1 and x_2 are the microphones coordinates according with the considered reference system.

The reflection coefficient (R) can be expressed through the transfer function (H_{12}) between the complex pressures at two microphone positions and the transfer function of the incident (H_i) and reflecting waves (H_r):

$$R = \frac{H_{12} - H_i}{H_r - H_{12}} e^{(2jk_0(L+s))} \quad (2.5)$$

Where s is the microphone spacing and L is the distance between the sample and the closed microphones. Moreover, the transfer function of the incident and reflecting wave at the two microphone positions can be expressed as:

$$H_i = \frac{P_i(x_2)}{P_i(x_1)} = \frac{\hat{P}_i e^{(-jk_0 x_2)}}{\hat{P}_i e^{(-jk_0 x_1)}} = e^{(jk_0 s)} \quad (2.6)$$

$$H_r = \frac{P_r(x_2)}{P_r(x_1)} = \frac{\hat{P}_r e^{(jk_0 x_2)}}{\hat{P}_r e^{(jk_0 x_1)}} = e^{-(jk_0 s)} \quad (2.7)$$

where P_i and P_r are the complex pressures of the incident and reflecting waves.

2.3 Impedance Tube Calibration

Considering that, the Transfer Function Method for the post-processing of data is a complex ratio between the acoustic pressure responses measured by the two microphones system, any mismatch on the amplitude and phase will affect the accuracy of the measurements. Therefore, a correction factor was be defined. So, at the first step of the calibration procedure the mics are placed in a rigid plate located at the end of the tube. In this case they were exposed to the same sound pressure

and phase, so the ratio of the fast Fourier transforms of the two time signals for the two microphones represent a correction factor (Hc) for the amplitude and phase mismatches

$$H_c = \frac{fft(p_2)}{fft(p_1)} \tag{2.8}$$

which will be applied to the complex measured transfer function between the sound pressures measured by the microphones placed in the standard position (Figure 5.3)

$$H_{12} = \frac{\widehat{H}_{12}}{H_c} \tag{2.9}$$

where $\widehat{H}_{12} = fft(\hat{p}_{mic1})/fft(\hat{p}_{mic2})$ is the uncorrected (measured) transfer function.

Moreover, the thermal viscous losses, which induce attenuation on the propagating incident and reflected waves within the tube are not negligible [33]. In order to take into account tube attenuation, a complex wave number must be introduced where the imaginary part represent the attenuation constant

$$k_0 = k - jk'' \tag{2.10}$$

If the real part is linearly dependent on the frequency and inversely proportional to the speed of sound ($k = 2\pi f/c$), the imaginary part is not a priori known, except to empirical relationship [33 - 34].

Therefore, the attenuation constant can be measured [34].

Considering an acoustically rigid and high reflection material sample and measuring the transfer function (corrected for the amplitude and phase mismatches), the equation (2.5) can be solved assuming a reflection coefficient (R) of 1 and including a complex wave number

$$H_{12} = \frac{e^{-jk_0L} + e^{jk_0L}}{e^{-jk_0(L+s)} + e^{jk_0(L+s)}} = \frac{cos[(k - jk'')L]}{cos[(k - jk'')(L + s)]} \tag{2.11}$$

Equation (2.11) can be solved numerically for k'' by means of a Newton-Raphson iteration scheme and assuming an initial guess the empirical value

$$k_0'' = \frac{A\sqrt{f}}{c\,d} \tag{2.12}$$

where *d* is the tube diameter and *A* is a constant (A = 0.0194 [35]).

When the imaginary part is estimated, the complex wavenumber can be included into the equation (2.5) for the experimental data post-processing.

2.4 Elastic Modulus Estimation

In this section the proposed method is presented starting from the sound wave propagation at the interface of two different media.

Consider the air-solid interaction shown in Figure 5.4, with a plane incident sound wave. Due to the difference in acoustic properties between two media, the energy associated to the incident wave will be in part reflected and in part transmitted at the interface.

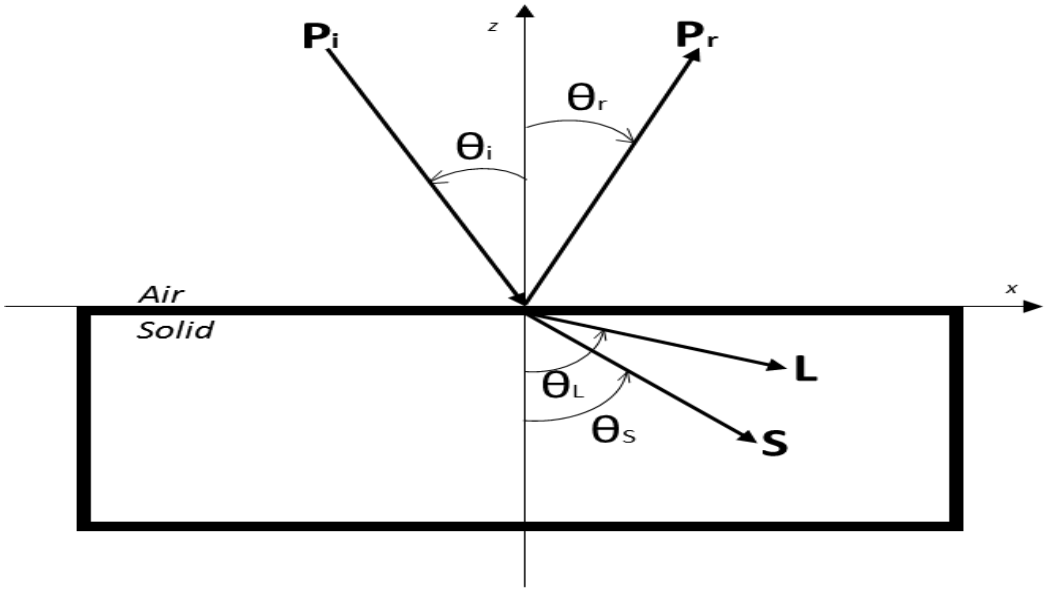

Figure 5. 4. System of reflection-transmission at air-solid interaction.

At the interface three boundary conditions must be satisfied. First, the particle velocity normal to the bounding surface and the pressure variation must be

continuous. Continuity of normal stress must be guaranteed and finally zero tangential stress is required since the fluid cannot support viscous stress (assuming an ideal non-viscous liquid). These boundary conditions can be written in term of velocity potentials, which can be expressed as plane wave solutions to the wave equation [14 - 15] and solved in terms of reflection and transmission coefficients. In particular, the reflection coefficient can be written as

$$R(\theta) = \frac{Z_L cos^2 2\theta_S + Z_S sin^2 2\theta_S - Z_1}{Z_L cos^2 2\theta_S + Z_S sin^2 2\theta_S + Z_1} \tag{2.13}$$

where θ_S is the angle of the propagating shear waves.

Since in a solid the wave propagation is associated to longitudinal and shear waves, Z_L and Z_S represent the longitudinal and shear characteristic impedance respectively, while Z_1 is the characteristic impedance of the fluid

$$Z_1 = \frac{\rho_1 V_1}{cos\theta_i}, Z_L = \frac{\rho_2 V_L}{cos\theta_L}, Z_S = \frac{\rho_2 V_S}{cos\theta_S} \tag{2.14}$$

So the characteristic impedance is a function of the density (ρ_1 density of fluid - ρ_2 density of solid media) and the relative propagation velocity (V_1 speed of sound in the fluid, V_L speed of propagating longitudinal waves, V_S speed of propagating shear waves).

Because of longitudinal and shear wave are involved, an effective impedance (Z_{eff}) can be defined

$$Z_{eff} = Z_L cos^2(2\theta_s) + Z_S sin^2(2\theta_s) \tag{2.15}$$

so that the reflection coefficient becomes

$$R(\theta) = \frac{Z_{eff} - Z_1}{Z_{eff} + Z_1} \tag{2.16}$$

The geometrical laws of reflection of sound waves are the same as those that apply to light waves unless the length of the sound waves is not comparable with the linear dimensions of the reflecting objects [16]. As the wavelength is small relative to the dimension of the reflectors, the Snell's law can be applied

$$\frac{sin\theta_i}{V_i} = \frac{sin\theta_S}{V_S} \tag{2.17}$$

In the particular case of plane and normal incident waves, the incidence angle is zero ($\theta_i = 0$), so according with equation (2.17) results in reflection and transmission angles of zero and only longitudinal waves are transmitted into the media, so from equation (2.16) the reflection coefficient can be simplified as follows:

$$R = \frac{Z_2 - Z_1}{Z_2 + Z_1} \tag{2.18}$$

where Z_1 is the characteristic impedance of fluid ($Z_1 = \rho_f C_f$, with C_f speed of sound in the fluid) and Z_2 is characteristic impedance of solid ($Z_2 = \rho_s C_{Ls}$) which is a function of the longitudinal sound speed in the solid.

The speed of sound describes the speed of sound waves passing through an elastic medium and varies with the medium employed as well as with the properties of the medium, in particular it is closely related to the stiffness of the material. When considering solid materials, there is non-zero stiffness both for volumetric and shear deformations. Hence, in a solid it is possible to generate sound waves with different velocities dependent on the deformation mode. When the lateral dimension (thickness) of the medium is much smaller than the incident wavelength the speed of sound can be expressed by the relation

$$C_{Ls} = \sqrt{\frac{E}{\rho}} \tag{2.19}$$

Considering a normal incident plane wave, as we demonstrated only longitudinal waves will pass through the solid, so the speed of sound in equation (2.19) represents the longitudinal speed of sound. Moreover, the Elastic Modulus included in equation (2.19) represents the out of plane component of elastic properties of the material (E_3).

Now combining the equations (2.18) and (2.19) and assuming the acoustic impedance under plane incident wave condition ($Z_2 = \rho_s C_{Ls}$), the Elastic Modulus of material can be expressed as:

$$E = \frac{1}{\rho_s}\frac{(1+R)^2}{(1-R)^2}Z_1 \tag{2.20}$$

In conclusion the elastic modulus of the material can be estimated using acoustic measurement. Starting from the sound pressure measurements in two different position through an impedance tube and applying the transfer function method the acoustic impedance and the reflection coefficient can be measured and the elastic modulus can be estimated then through the equation (2.20).

3 Numerical Simulation

In order to validate the proposed method, a numerical model, based on the Representative Volume Element (RVE), was developed. An RVE model of composite material for which the elastic properties were known from literature, was developed and included in the FE simulation.

First a coupled acoustic-structural harmonic analysis was considered in order to simulate the impedance tube test rig. The simulation data in terms of sound pressures acquired during the simulation was used as input data and the elastic modulus was estimated by the proposed method and compared with the expected one.

Moreover, a static structural analysis was implemented using the same RVE model in order to simulate a standard tensile testing and estimate the elastic modulus according with the Hooke's law. The results were then compared with the expected one and with the elastic modulus extracted by the proposed method

3.1 Representative Volume Element (RVE)

The Representative Volume Element (RVE) [17-20] is a powerful and commonly used approach for numerical modelling and elastic behaviour analysis of composite materials and general periodic structures [21 - 24]. Different RVE models have been developed, but in this work the Homogenization Theory was

taken into account which was shown to give more accurate estimates of effective stiffness for periodic composite material [21].

The homogenization theory is based on two assumptions. The fields vary on multiple scales due to the existence of microstructure, and the microstructure is assumed spatially periodic. Starting from such assumption the field variables are approximated by an asymptotic

$$u_i^{\eta}(x_i, y_i) = u_{0i}(x_i, y_i) + \eta u_{1i}(x_i, y_i) + \eta^2 u_{2i}(x_i, y_i) + \cdots \tag{3.1}$$

where u_i^{η} is the exact value of the field variable, u_{0i} is the macroscopic or average value of the field variable, u_{1i}, u_{2i}, etc. are perturbations in the field variables due to the microstructure, x_i are the global level coordinates, y_i are the micro level coordinates, and η the ratio of the microstructure size to the total size of the analysis region. In the elasticity theory u_{0i} would be the continuum level displacements while u_{1i} would be the microstructural displacements. The relation between the macro and micro coordinate can be expressed

$$y_i = \frac{x_i}{\eta} \tag{3.2}$$

Applying the derivatives with respect to xi to the expansion of the displacement (equation (3.1)) and neglecting the higher order terms of the weak form of equilibrium equations governing the mechanical behaviour of composite material, the small deformation strain tensor can be written as

$$\varepsilon_{ij}(u) = \bar{\varepsilon}_{ij} + \varepsilon_{ij}^{*} \tag{3.3}$$

where

$$\bar{\varepsilon}_{ij}(u) = \frac{1}{2}\left[\frac{\partial u_{0i}}{\partial x_j} + \frac{\partial u_{0j}}{\partial x_i}\right] \quad and \quad \varepsilon_{ij}^{*}(u) = \frac{1}{2}\left[\frac{\partial u_{1i}}{\partial y_j} + \frac{\partial u_{1j}}{\partial y_i}\right] \tag{3.4}$$

ε_{ij} is the microstructural strain tensor, $\bar{\varepsilon}_{ij}$ is the macroscopic strain tensor and ε_{ij}^{*} is the fluctuating microstructural strain tensor which is assumed to vary periodically. In the same way, the virtual strain tensor can be expressed

$$\varepsilon_{ij}(v) = \varepsilon_{ij}^{0} + \varepsilon_{ij}^{1} \tag{3.5}$$

where

$$\varepsilon_{ij}^{0}(v) = \frac{1}{2}\left[\frac{\partial v_{0i}}{\partial x_j} + \frac{\partial v_{0j}}{\partial x_i}\right] \quad and \quad \varepsilon_{ij}^{1}(v) = \frac{1}{2}\left[\frac{\partial v_{1i}}{\partial y_j} + \frac{\partial v_{1j}}{\partial y_i}\right] \tag{3.6}$$

Assuming the virtual displacement varying only on microscopic level and is constant on the macroscopic level ($\varepsilon_{ij}^{0}(v)$=0), and assuming η goes to zero in the limit, then the standard weak form of equilibrium equation can be written as

$$\int_{\Omega} \frac{1}{V_{RVE}} \int_{V_{RVE}} D_{ijkl}\left(\varepsilon_{ij}^{1}(v)\right)\left(\bar{\varepsilon}_{kl}(u) + \varepsilon_{kl}^{*}(u)\right) dV_{RVE} d\Omega = 0 \tag{3.7}$$

where Ω is the total of macroscopic and microscopic domain of composite material, V_{RVE} is the volume of RVE and D_{ijkl} is the stiffness tensor. Equation (3.7) is satisfied if the integral over RVE is zero, so the equilibrium equations may be written

$$\int_{V_{RVE}} D_{ijkl}\varepsilon_{ij}^{1}(v)\varepsilon_{kl}^{*}(u)\, dV_{RVE} = -\int_{V_{RVE}} D_{ijkl}\varepsilon_{ij}^{1}(v)\bar{\varepsilon}_{kl}(u)\, dV_{RVE} \tag{3.8}$$

For linear problem in 3-dimensions, $\bar{\varepsilon}_{kl}(u)$, which is unknown apriori, can be written as a linear combination of unit strains as following

$$\bar{\varepsilon}_{pm}^{11} = -\begin{bmatrix}1 & 0 & 0\\ 0 & 0 & 0\\ 0 & 0 & 0\end{bmatrix}, \quad \bar{\varepsilon}_{pm}^{12} = -\begin{bmatrix}0 & 1 & 0\\ 0 & 0 & 0\\ 0 & 0 & 0\end{bmatrix}, \quad \bar{\varepsilon}_{pm}^{13} = -\begin{bmatrix}0 & 0 & 1\\ 0 & 0 & 0\\ 0 & 0 & 0\end{bmatrix}$$

$$\bar{\varepsilon}_{pm}^{21} = -\begin{bmatrix}0 & 0 & 0\\ 1 & 0 & 0\\ 0 & 0 & 0\end{bmatrix}, \quad \bar{\varepsilon}_{pm}^{22} = -\begin{bmatrix}0 & 0 & 0\\ 0 & 1 & 0\\ 0 & 0 & 0\end{bmatrix}, \quad \bar{\varepsilon}_{pm}^{23} = -\begin{bmatrix}0 & 0 & 0\\ 0 & 0 & 1\\ 0 & 0 & 0\end{bmatrix} \tag{3.9}$$

$$\bar{\varepsilon}_{pm}^{31} = -\begin{bmatrix}0 & 0 & 0\\ 0 & 0 & 0\\ 1 & 0 & 0\end{bmatrix}, \quad \bar{\varepsilon}_{pm}^{32} = -\begin{bmatrix}0 & 0 & 0\\ 0 & 0 & 0\\ 0 & 1 & 0\end{bmatrix}, \quad \bar{\varepsilon}_{pm}^{33} = -\begin{bmatrix}0 & 0 & 0\\ 0 & 0 & 0\\ 0 & 0 & 1\end{bmatrix}$$

Applying the symmetry of strain states and substituting the unit strains on the right-hand side of equation (3.8), the stress tensor can be derived as

$$\sigma_{ij}^{*kl} = D_{ijpm}\bar{\varepsilon}_{pm}^{kl} \tag{3.10}$$

A set of six auxiliary problems have to be solved for ε_{kl}^{*kl} in equation (3.8) using equation (3.10)

$$\int_{V_{RVE}} D_{ijkl}\varepsilon_{ij}^{1}(v)\varepsilon_{pm}^{*kl}(u)\, dV_{RVE} = \int_{V_{RVE}} \varepsilon_{ij}^{1}(v)\sigma_{ij}^{*kl}\, dV_{RVE} \tag{3.11}$$

To ensure periodicity of the strain field ε_{pm}^{*kl} in equation (3.8) the value of ε_{ij}^{*} for any arbitrary $\bar{\varepsilon}_{kl}$ can be written as

$$\varepsilon_{ij} = -\varepsilon_{ij}^{*kl}\bar{\varepsilon}_{kl} \tag{3.12}$$

So the relation between local RVE strain and the average strain can be written

$$\varepsilon_{ij} = M_{ijkl}\bar{\varepsilon}_{kl} \qquad with \qquad M_{ijkl} = \frac{1}{2}\left(\delta_{ik}\delta_{il} + \delta_{il}\delta_{jk}\right) - \varepsilon_{ij}^{*kl} \tag{3.13}$$

Finally the effective stiffness tensor which relates average stress and average strain can be estimated from M_{ijkl} by writing the Hooke's law at microscopic level and then integrating over the volume of RVE and divide by the volume of RVE

$$\overline{D}_{ijkl} = \frac{1}{|V_{RVE}|}\int_{V_{RVE}} D_{ijpm}M_{pmkl}dV_{RVE} \tag{3.14}$$

3.2 Static Structural Analysis

A static structural analysis was used to extract a preliminary indication of the elastic modulus of the sample. Considering an RVE approach, and assuming the material to behave as a linear elastic solid, a constant axial loading and fixed support boundary conditions was applied on the sample (Fig.5.5). The two ends of the RVE along the transverse direction are marked as a fixed area and load area respectively. A displacement boundary condition was prescribed at the fixed area (ux = uy = uz = 0), while a force was applied as the loading condition to the load area. The applied load is confined in the elastic range, so measuring the stress induced by the loading

conditions and the relative strain status, the Hooke's law can provide an estimation about the elastic modulus of the sample:

$$E_3 = \frac{\sigma_3}{\varepsilon_3} \tag{3.15}$$

Where σ_3 and ε_3 are the tensile stress and strain respectively along the loading direction.

In order to obtain the averaged stress-strain results for a certain prescribed load and boundary conditions, periodic boundary condition [25 - 29] need to be applied on the RVE. The periodic boundary conditions were implemented by creating identical mesh on opposite faces of RVE to ensure the same coordinates are tangential to the face.

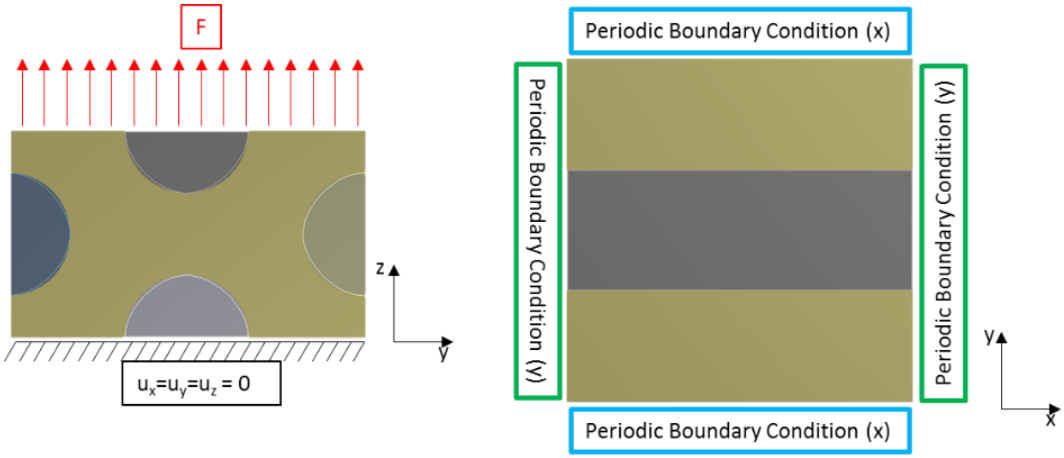

Figure 5.5. Loading and boundary condition applied on Representative Volume Element for the static structural analysis

3.3 Coupled Acoustic-Structural Analysis

Then a coupled acoustic structural analysis was carried to simulate in-silico the impedance tube measurements and verify the proposed approach numerically. In acoustic fluid-structural interaction (FSI) problems, the structural dynamic equation (equation *(3.16))* must be considered along with the Navier-Stokes equations of fluid momentum (equation (3.17)) and the flow continuity equation (equation (3.18).

$$[M]\{\ddot{u}(t)\} + [C]\{\dot{u}(t)\} + [K]\{u(t)\} = \{f(t)\} \tag{3.16}$$

$$\rho\frac{dv}{dt} = -\nabla p + \nabla \cdot S + \rho b \tag{3.17}$$

$$\frac{\partial \rho}{\partial t} = -\nabla \cdot (\rho v) + Q \tag{3.18}$$

Where ρ is the density, v is the velocity vector, Q is mass source, S is the viscous stress tensor, p the pressure, b is the body force and $[M], [C], [K]$ are the mass, damping, stiffness matrices respectively. Combining the Navier-Stokes and the continuity equations, the acoustic wave equation can be written as

$$\nabla \cdot \left(\frac{1}{\rho_0}\nabla p\right) - \frac{1}{\rho_0 c^2}\frac{\partial^2 p}{\partial t^2} + \nabla \cdot \left[\frac{4\mu}{3\rho_0}\nabla\left(\frac{1}{\rho_0 c^2}\frac{\partial p}{\partial t}\right)\right] = -\frac{\partial}{\partial t}\left(\frac{Q}{\rho_0}\right) + \nabla \cdot \left[\frac{4\mu}{3\rho_0}\nabla\left(\frac{Q}{\rho_0}\right)\right] \tag{3.19}$$

where μ is the dynamic viscosity and ρ_0 is the mean fluid density.

The discretized structural equation (equation (3.16)) and the acoustic wave equation (equation (3.20)) must be considered simultaneously at the FSI interface. So, it is convenient writing the equation in a matrix form. The finite element formulation is obtained by testing wave equation (equation (3.19)) using the Galerkin procedure [30]. Equation (3.19) is multiplied by testing function w and integrated over the volume of the domain [31] which yields the following:

$$\iiint_{\Omega_f} \frac{1}{\rho_0 c^2} w \frac{\partial^2 p}{\partial t^2} dv + \iiint_{\Omega_f} \nabla\left(\frac{4\mu}{3\rho_0^2 c^2}\nabla\frac{\partial p}{\partial t}\right) dv + \iiint_{\Omega_f} \nabla w \cdot \left(\frac{1}{\rho_0}\nabla p\right) dv +$$

$$-\oiint_{\Gamma_f} w\left(\frac{1}{\rho_0} + \frac{4\mu}{3\rho_0^2 c^2}\frac{\partial}{\partial t}\right)\hat{n} \cdot \nabla p ds + \oiint_{\Gamma_f} w\frac{4\mu}{3\rho_0^2}\hat{n} \cdot \nabla Q ds = \tag{3.20}$$

$$= \iiint_{\Omega_f} w\frac{1}{\rho_0}\frac{\partial Q}{\partial t} dv + \iiint_{\Omega_f} \nabla w \cdot \left(\frac{4\mu}{3\rho_0^2}\nabla Q\right) dv$$

where dv is the volume differential of acoustic domain (Ω_f), ds is the surface differential of acoustic domain boundary (Γ_f) and $\hat{n}$ is the normal unit vector to the boundary.

From the equation of momentum conservation, the normal acceleration of the fluid, expressed in terms of the normal displacement, is given

$$\frac{\partial v_{n,f}}{\partial t} = \hat{n} \cdot \frac{\partial v}{\partial t} = \hat{n} \cdot \frac{\partial^2 u_f}{\partial t^2} = -\left(\frac{1}{\rho_0} + \frac{4\mu}{3\rho_0^2 c^2}\frac{\partial}{\partial t}\right)\hat{n} \cdot \nabla p + \frac{4\mu}{3\rho_0^2}\hat{n} \cdot \nabla Q \qquad (3.21)$$

Substituting equation (3.21) into equation (3.20) yields the acoustic wave equation (3.19) and can be expressed as follows:

$$\begin{aligned} &\iiint_{\Omega_f} \frac{1}{\rho_0 c^2} w \frac{\partial^2 p}{\partial t^2} dv + \iiint_{\Omega_f} \nabla w \cdot \left(\frac{4\mu}{3\rho_0^2 c^2} \nabla \frac{\partial p}{\partial t}\right) dv + \iiint_{\Omega_f} \nabla w \cdot \left(\frac{1}{\rho_0} \nabla p\right) dv + \\ &+ \oiint_{\Gamma_f} w \hat{n} \cdot \frac{\partial^2 u_f}{\partial t^2} ds = \iiint_{\Omega_f} w \frac{1}{\rho_0} \frac{\partial Q}{\partial t} dv + \iiint_{\Omega_f} \nabla w \cdot \left(\frac{4\mu}{3\rho_0^2} \nabla Q\right) dv \end{aligned} \qquad (3.22)$$

The finite element approximating shape functions for the spatial variation of the pressure and displacement components are given by:

$$P = \{N\}^T \{p\} \qquad (3.23)$$

$$u = \{N'\}^T \{u\} \qquad (3.24)$$

with $\{N\}$ is the element shape function for pressure, $\{N'\}$ is the element shape function for displacement and $\{p\}$, $\{u\}$ are the nodal pressure and displacements vectors.

Using such formulation into the equation (3.22), the finite element statement of the wave (equation (3.19)) is expressed in matrix notation as following:

$$\left[M_f\right]\{\ddot{p}\} + \left[C_f\right]\{\dot{p}\} + \left[K_f\right]\{p\} + \bar{\rho}_0 [R]^T \{\ddot{u}\} = \left\{f_f\right\} \qquad (3.25)$$

Where

$\left[M_f\right] = \bar{\rho}_0 \iiint_{\Omega_f} \frac{1}{\rho_0 c^2} \{N\}\{N\}^T dv$ is the acoustic fluid mass matrix

$[C_f] = \bar{\rho}_0 \iiint_{\Omega_f} \frac{4\mu}{\rho_0^2 c^2} [\nabla N]^T [\nabla N] dv$ is the acoustic fluid damping matrix

$[K_f] = \bar{\rho}_0 \iiint_{\Omega_f} \frac{1}{\rho_0} [\nabla N]^T [\nabla N] dv$ is the fluid stiffness matrix

$[R]^T = \oiint_{\Omega_f} \{N\}\{n\}^T \{N'\}^T ds$ is the acoustic fluid boundary matrix

$[f_f] = \bar{\rho}_0 \iiint_{\Omega_f} \frac{1}{\rho_0 c^2} \{N\}\{N\}^T dv\{\dot{q}\} + \bar{\rho}_0 \iiint_{\Omega_f} \frac{4\mu}{\rho_0^2 c^2} [\nabla N]^T [\nabla N] dv\{q\}$ is the acoustic fluid load, with $\bar{\rho}_0$ the acoustic fluid mass density constant.

So the acoustic and structural matrices are coupled for fluid-structure interaction.

$$\begin{bmatrix} M_s & 0 \\ \bar{\rho}_0 R^T & M_f \end{bmatrix} \begin{Bmatrix} \ddot{u} \\ \ddot{p} \end{Bmatrix} + \begin{bmatrix} C_s & 0 \\ 0 & C_f \end{bmatrix} \begin{Bmatrix} \dot{u} \\ \dot{p} \end{Bmatrix} + \begin{bmatrix} K_s & -R \\ 0 & K_f \end{bmatrix} \begin{Bmatrix} u \\ p \end{Bmatrix} = \begin{Bmatrix} f_s \\ f_f \end{Bmatrix} \quad (3.26)$$

where the subscript "s" and "f" represent the structural and fluid parts respectively.

3.4 Numerical Simulation Results

In order to validate the numerical models two different materials were considered of which the mechanical properties are well known [32]: a thermoplastic polymer (Polypropylene) and a unidirectional carbon-epoxy composite. For the polypropylene isotropic mechanical properties were considered. Regarding the composite, the matrix was considered to be isotropic, while the anisotropic material parameters for the fiber been applied [17]. The material properties are summarized in Table 3.1 and Table 3.2.

Fiber	**E_{f1} [GPa]**	**$E_{f2} = E_{f3}$ [GPa]**	**ν_{f12}**	**G_{f12} [GPa]**	**G_{f13} [GPa]**	**G_{f23} [GPa]**
T300	230	27.5	0.2	75	75	7
Matrix	**E_m [GPa]**			**ν_m**		
Epoxy 914	4.0			0.35		
Composite	**E_1 [GPa]**	**$E_2 = E_3$ [GPa]**	**ν_{12}**	**ν_{23}**	**G_{12} [GPa]**	
T300/914	136	11	0.28	0.4	5.5	

Table 3.2. Material properties for composite T300/914

Polypropylene	E [GPa]	ν	G [GPa]
	1.4	0.36	0.4

Table 3.3. Material properties for Polypropylene

A RVE with a cross section of 0.014-0.009mm was built. For the epoxy-carbon composite, the carbon fibers were included. In particular a RVE with a hexagonal distribution of fiber was modelled. The fibers presented a diameter of 7.0 μm and a fiber volume fraction of 0.6 (Fig.5.6). Symmetric and periodic boundary conditions in y and x coordinates, according with the local reference system of Fig.5.6 must be applied in order to guaranty the periodicity of the microstructural strain tensor (ε_{ij}^{*}).

Regarding the static-structural analysis, a unidirectional tension loading was applied in z direction to estimate the out of plane (E_3) elastic modulus. The mesh was fine enough to accurately represent the geometry of the reinforced fibers. Under the prescribed loading condition, the maximum tensile stress on the RVE and the relative strain status in the z direction were used to estimate the out of plane elastic modulus according to Hooke's law (equation (3.15)). The simulation result in terms of tensional stress (σ_3) and strain (ε_3) for both materials are shown in Fig.5.7 and Fig.5.8.

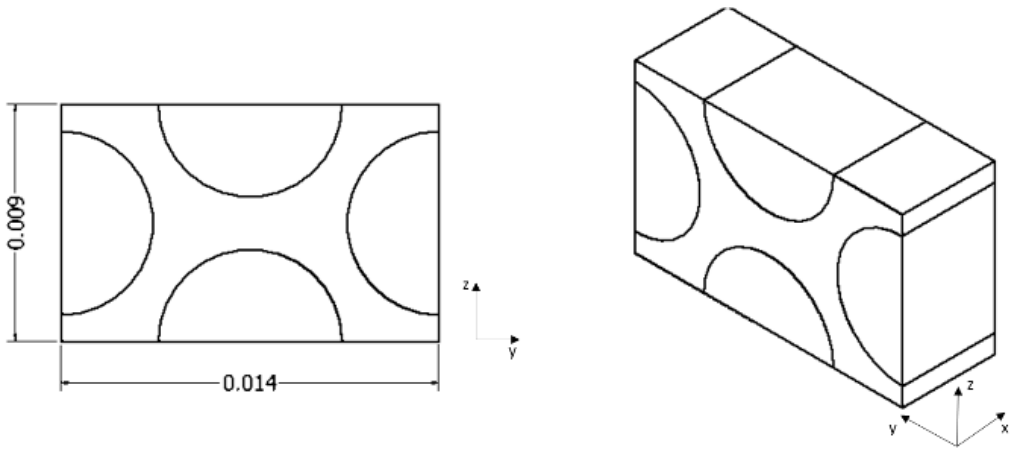

Figure 5.6. RVE model of unidirectional carbon-epoxy composite

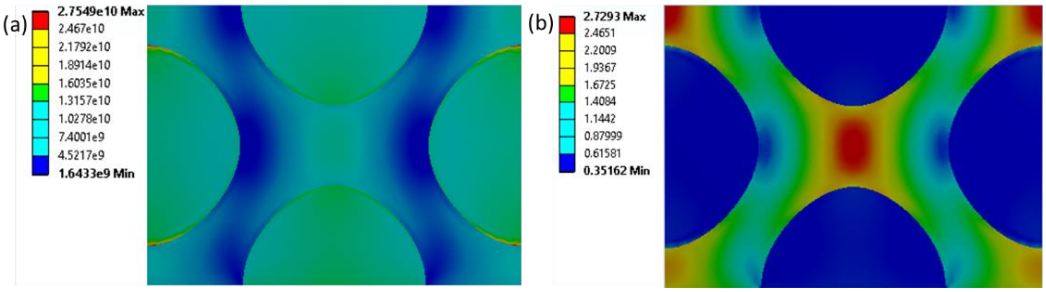

Figure 5.7. Simulation results in terms of equivalent tensile stress σ_3 and equivalent strain ε_3 for the carbon-epoxy RVE

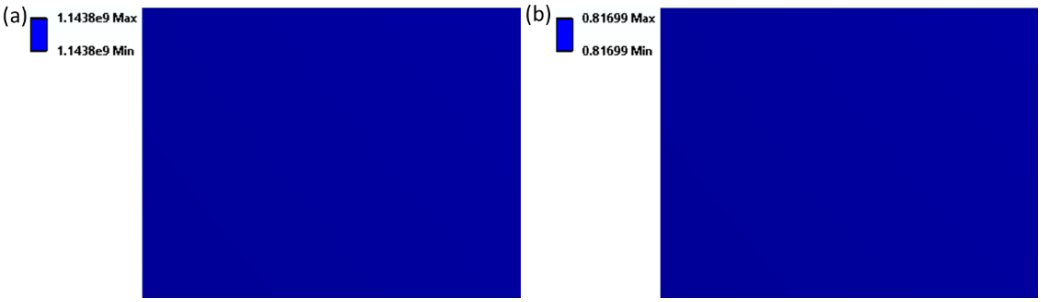

Figure 5.8. Simulation results in terms of equivalent tensile stress σ_3 and equivalent strain ε_3 for the Polypropylene RVE

Regarding the coupled acoustic-structural analysis the implemented FE model is shown in Fig.5.9**.** The fluid volume into the tube was modelled as an acoustic body. Radiation boundary conditions were used at the input plane of the fluid domain, therefore acoustic waves normal to the boundary will be absorbed and not reflected into the acoustic domain. The acoustic load was applied in the same input plane and modelled using an acoustic mass source. On the other end of the acoustic body, the previous described RVEs were placed as samples and fluid-structure boundary conditions were applied. In order to avoid any translation of the sample a fixed support boundary conditions was applied on the external surface of the test sample. Finally, a coupled acoustic-structural harmonic analysis was set up to measure the pressure profile in two different planes into the fluid volume, according with constrains of equation (2.1) and equation (2.2).

Starting from the acquired pressure time histories during the simulation, the reflection coefficient of the RVE can be extracted following the transfer function method, and then the acoustic impedance of the RVE can be estimated (Fig.5.10 and Fig.5.11) and the proposed method was applied in the post-processing of data to estimate the elastic modulus.

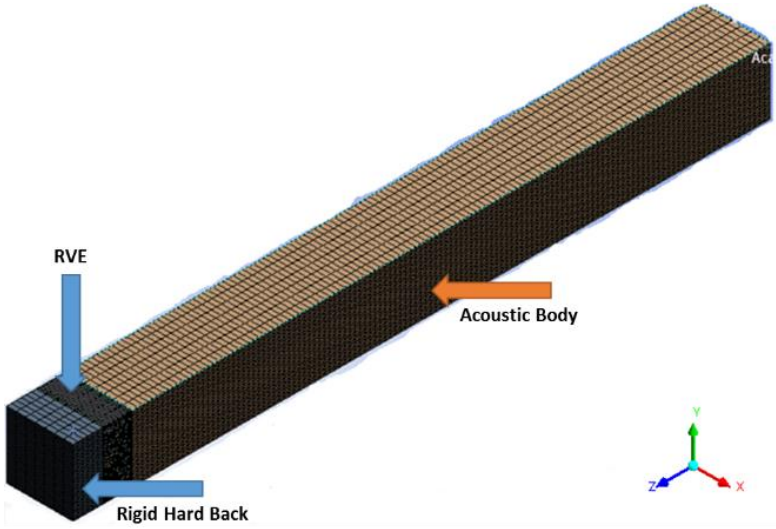

Figure 5.9. Couple acoustic-structural FE model

The results in terms of elastic modulus estimated by the proposed method and the tensile testing simulation compared with the elastic properties declared by the materials datasheet are reported in Table 3.3.

	Datasheet	**Static-Structural Analysis**		
Material	**E_3 [GPa]**	**σ_3 [GPa]**	**ε_3**	**E_3 [GPa]**
Carbon –Epoxy	11.0	2.755e10	2.729	10.1
Polypropylene	1.4	1.144e9	0.817	1.4

	Datasheet	**Acoustic-Structural Analysis**		
Material	**E_3 [GPa]**	**Z [Pa s/m]**	**C_L [m/s]**	**E_3 [GPa]**
Carbon –Epoxy	11.0	3.897e6	2706	10.5
Polypropylene	1.4	1.153e6	1178	1.36

Table 3.3 Simulation results for the carbon-epoxy and polypropylene RVE, compared with the elastic properties declared by the data sheet.

The results obtained from the numerical simulation both static-structural and acoustic-structural analysis are in good agreement with the elastic properties declared by the datasheet of the relative materials. The proposed approach produced good results for isotropic (polypropylene) and orthotropic (epoxy-carbon composite) materials. The results from the acoustic-structural analysis match the results obtained with the static-structural model which simulate the standard tensile tests, commonly used for the elastic characterization of materials. Therefore, it was shown that using a standard impedance tube test rig both material acoustic characterization and elastic property evaluation of materials can be achieved.

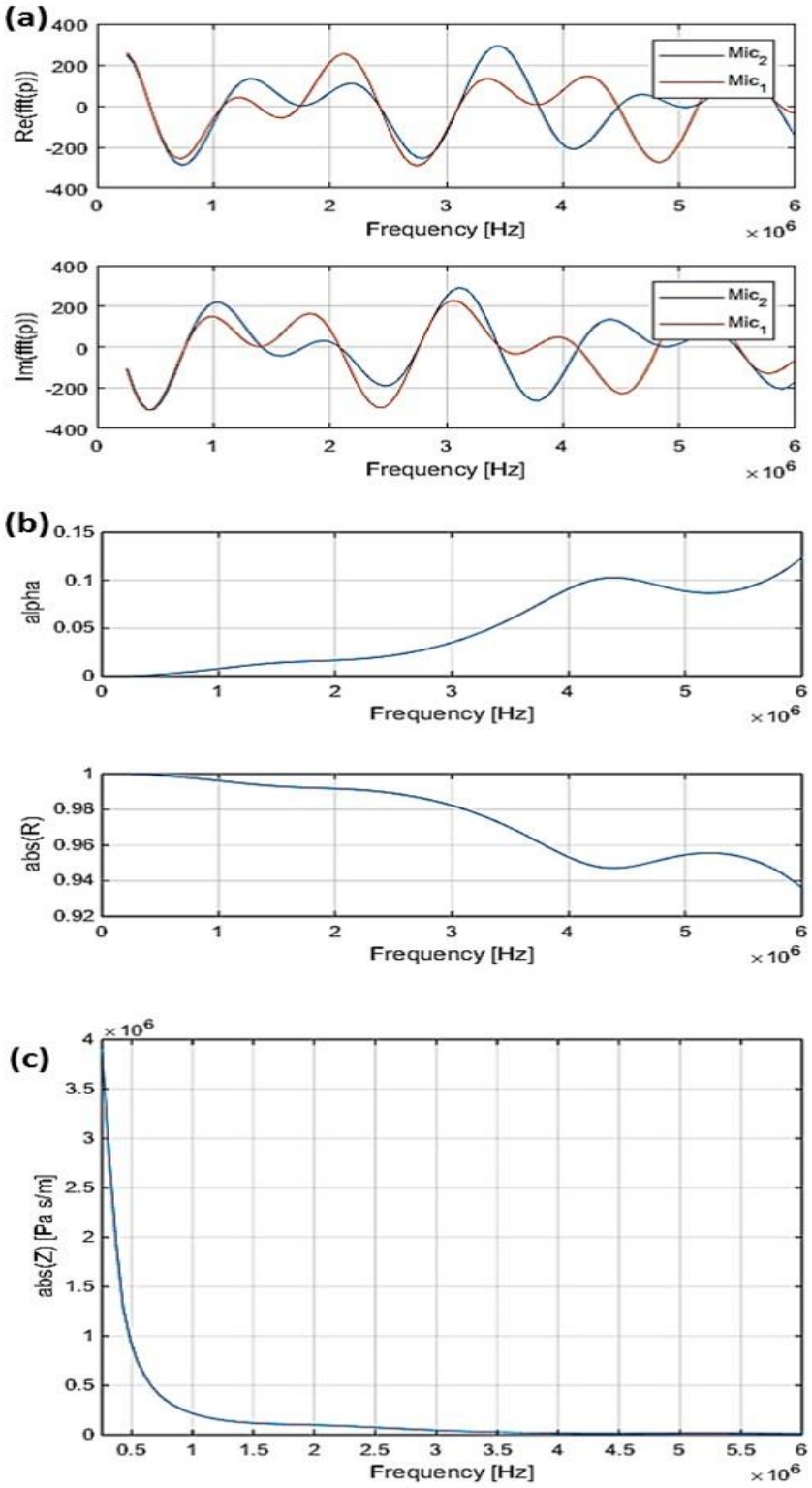

Figure 5.10. Acoustic-structural simulation results for carbon-epoxy RVE in terms of fft of pressure time histories at two different acquisition points, Absorption and Reflection Coefficients and Acoustic impedance

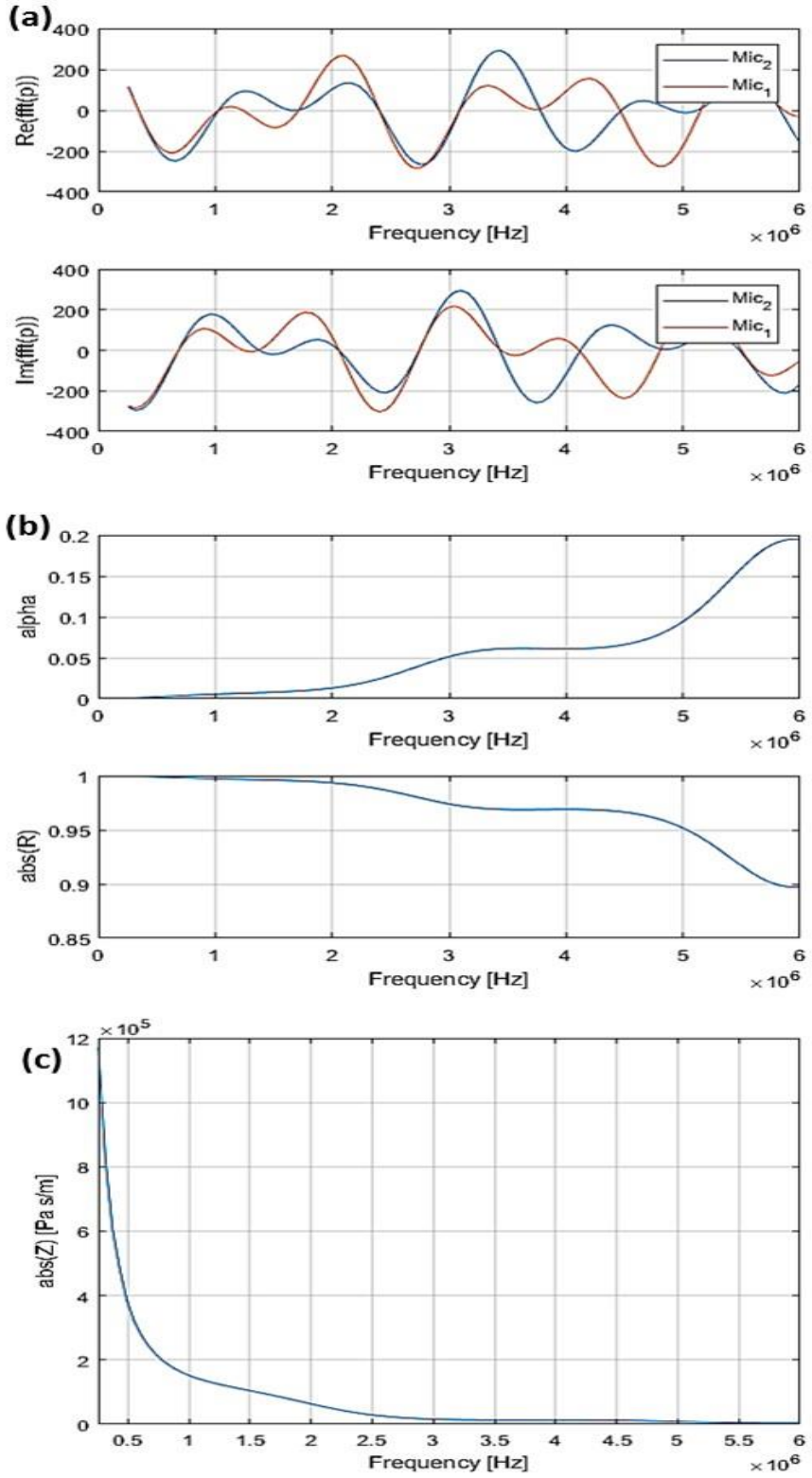

Figure 5.11. Acoustic-structural simulation results for polypropylene RVE in terms of fft of pressure time histories at two different acquisition points, Absorption and Reflection Coefficients and Acoustic impedance

4 Experimental Measurement Campaign

Here the results of an experimental measurement campaign are reported.
Different materials were tested, and the proposed method was used to estimate the elastic modulus. In particular, two types of materials (foam and composite) were used to demonstrate the ability of the method to evaluate the Young's Modulus of soft porous isotropic materials and out of plane Young's Modulus of hard complex anisotropic materials.
The estimated elastic modulus was compared with those measured by standard testing methods. Regarding the composite samples the ultrasound time of flight (according with ASTM E 494 [39]) was used while for the foam sample, where such method produces inaccurate results because of the scattering of the longitudinal wave through the holes, a tensile test was used (according with ASTM D 3574 [38]).

4.1 Experimental Setup

Four samples were tested in the present measurement campaign.
The tested materials include two acoustic soft foams with different densities (Foam 1 ($\rho = 20\ kg/m^3$) – Foam 2 ($\rho = 25\ kg/m^3$)), and two composites. The composite materials consist of epoxy resin (HexFlow RTM 6) reinforced by carbon fibre (HexForce Carbon Fabrics G1157) (sample 1) and Vynilester reinforced by glass fibre (sample 2).
The test rig used in the present work was the standard two microphones impedance tube described in the ASTM standard [33]. Such equipment is normally used for the measurement of the acoustic properties of porous and fibre materials.
When testing elastic properties of thermoplastic, polymer or composite materials within the test rig, there is potential for critical errors to occur. These errors are generally related to the phase and amplitude mismatch between the microphone measurements and attenuation of the tube walls associated to viscous thermal losses. In this case, these materials behave as acoustically rigid and the reflection

coefficient is normally greater than 0.98-0.99, thus limiting the accuracy of the measurement. As the elastic properties are a function of the longitudinal propagation speed in the material, which is strictly related to the reflection coefficient, the measurement of such coefficient must as accurate as possible.

A calibration procedure was applied to take into account the phase mismatch and the viscous thermal losses at the walls of the tube in order to increase the accuracy of the experimental measurements.

Cylindrical samples with a diameter of 50.8mm were tested in an aluminium impedance tube with an internal diameter of 50.8mm, so the experimental results are confined to the working frequency range (250 – 3800 Hz). A loudspeaker at one end of the tube was used to generate a broadband signal; in particular the samples were excited by a 3s sine-sweep in the considered working frequency range. In addition, the amplitude-phase mismatch of the microphone measurements and the thermal-viscous losses were compensated according with the following proposed calibration procedure.Fig.5.12 shows the calibration effect on the measured reflection coefficient. The effect of using no correction data is to underestimate the reflection coefficient which lead to a under estimation of the acoustic impedance. At low frequencies the uncalibrated reflection coefficient estimation error was over 3%, a critical error for high reflective materials such as composites and polymeric materials.

The sample placing into the tube were done carefully in order to fit the sample itself with the internal wall of the tube. Any relative moving of the sample with the tube and any leakage must be avoid. The downstream section of the tube consisted of a hard-back termination attached to the downstream surface of the sample.

The two upstream measurement position were spaced of 30mm, the second microphone position were separated by a 140mm from the incident surface of the sample and the first microphone position were placed 330mm from the speaker in order to guarantee the completely development of the standing plane wave into the tube.

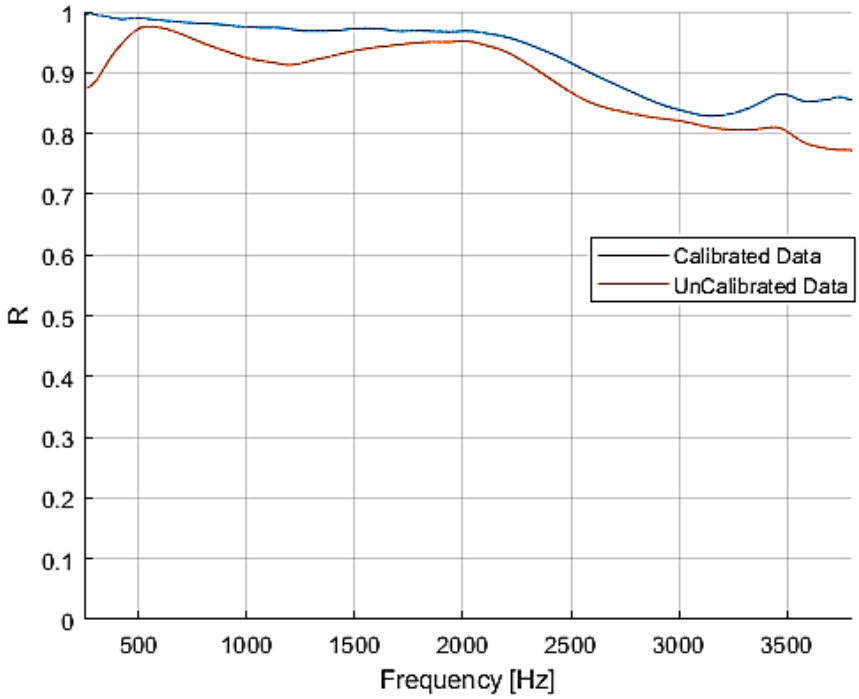

Figure 5.12. Effect of the calibration effect on the measured Reflection coefficient of composite material

Regarding the tensile testing carried out on the foam samples (Foam 1 and Foam 2) a dog bone shaped sample was used (refer to Fig.5.13) with the material elastic modulus determined from measured stress-strain curves.

For the ultrasound time of flight measurements an ultrasonic pulse was sent which propagates through the sample with a certain longitudinal sound speed. Measuring the time between the front wall and back wall echo of the samples, the time of flight was estimated. Moreover, since the sample thickness is known, the longitudinal sound wave into the material can be calculated and used to evaluate the elastic modulus of the tested sample.

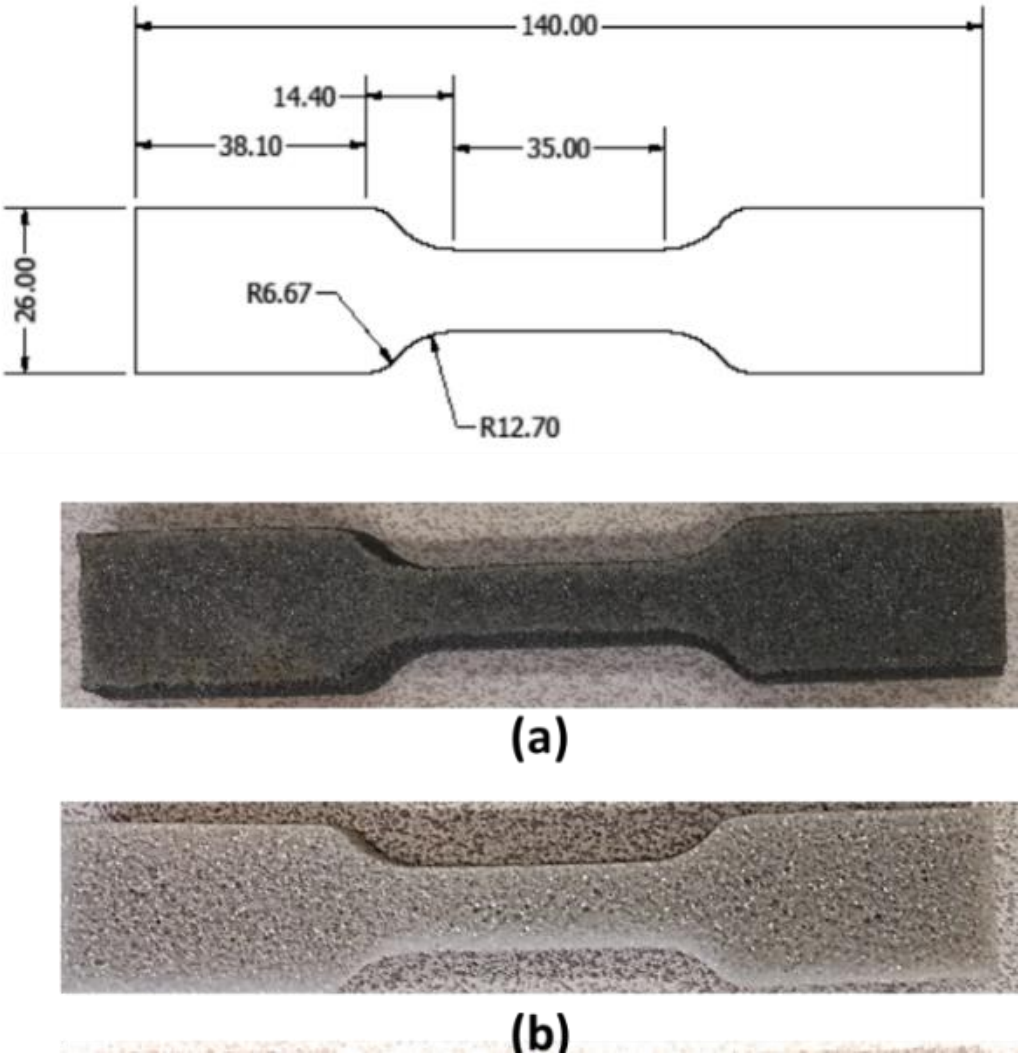

Figure 5.13. Dog bone shape samples for tensile testing for the Foam 1 sample and Foam 2 sample

4.2 Experimental Results

Since the considered test rig is designed to guarantee a plane standing wave, the hypothesis of normal incident at the fluid-sample interface is fulfilled and longitudinal sound wave will propagate into the sample, thus estimation of the out of plane elastic properties is possible.

The calibrated sound pressures measured at two microphone positions were used to estimate the reflection coefficient and the acoustic impedance of the samples using the Transfer Function Method.

To reduce the effect of errors related to mounting the samples, material variability and the uncertainty of experimental measurements, five different measurements were performed for each sample. The results were consistent in terms of the reflection coefficient and elastic modulus. Moreover, since the tests were performed under plane wave conditions and only longitudinal waves propagate through the sample, the out of plane elastic properties are a function of the fibre volume fraction and not a function of fibre orientation.

The measured reflection coefficient and the relative acoustic impedance for the tested materials are shown in Fig.5.14, Fig.5.15, Fig.5.16, Fig.5.17.

Moreover in Fig.5.18 is shown the stress-strain curves measured during the tensile testing on the foam sample (Foam 1 and Foam 2).

Finally, the initial pulse and the back-wall echo measured for both composite samples (Sample 1 and Sample 2) are shown in Fig.5.19.

In Table 4.1 the elastic properties of the tested samples were estimated with the proposed method and compared with the relative elastic properties estimated with the commonly used methods.

Sample	Proposed Method		Time of Flight		Tensile Testing
	C_L [m/s]	E [Pa]	C_L [m/s]	E [Pa]	E [Pa]
Foam 1		0.11e6			0.12e6
Foam 2		0.049e6			0.05e6
Epoxy-Carbon	2748	10.18e9	2860	11.7e9	
Vynilester–Glass	2275	8.01e9	2353	8.56e9	

Table 4.1. Elastic properties of tested materials evaluated using the proposed method and compared with the results obtained through the commonly used methods

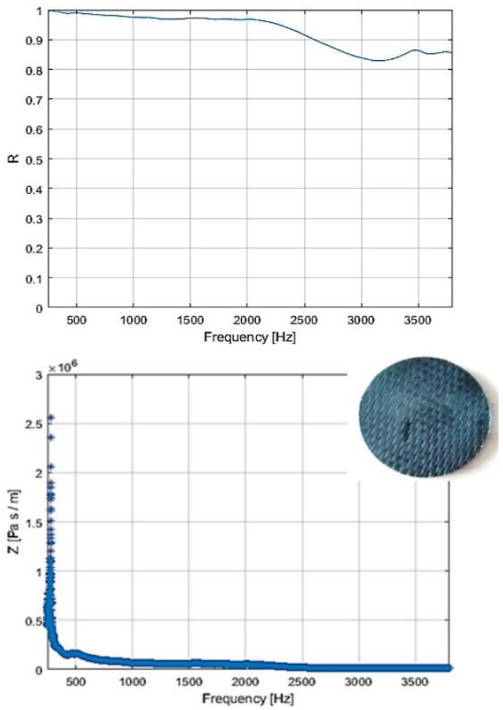

Figure 5.14. Measured reflection coefficient and acoustic impedance for Sample 1 (Epoxy-Carbon fiber composite)

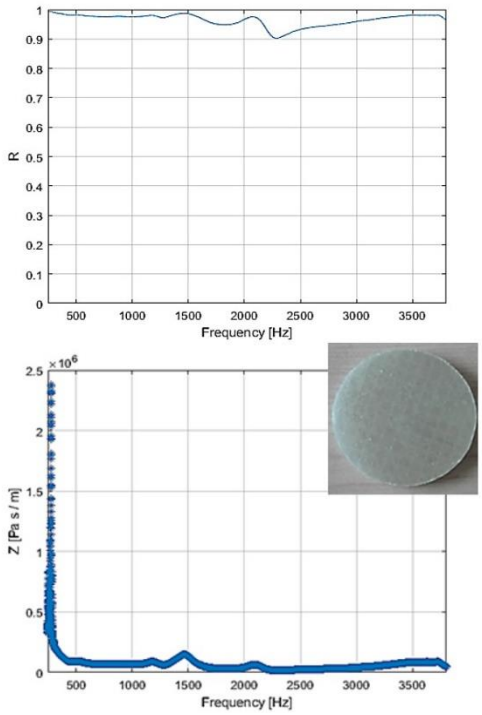

Figure 5.15. Measured reflection coefficient and acoustic impedance for Sample 2 (Vynilester-Glass fiber composite)

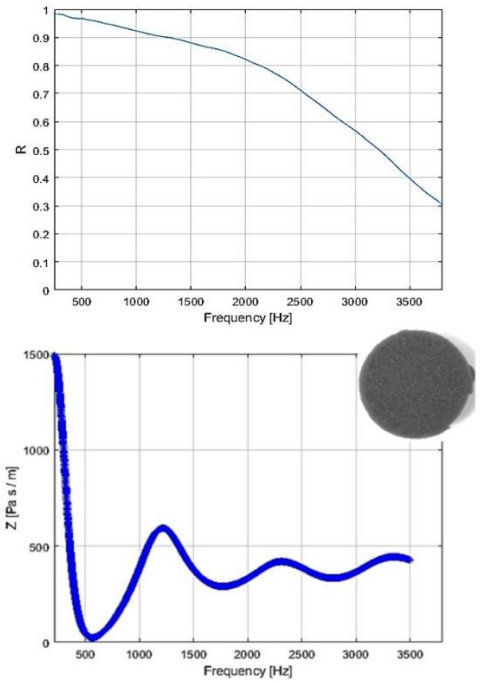

Figure 5.16. Measured reflection coefficient and acoustic impedance soft acoustic Foam 1 (ρ = 20 kg/m3)

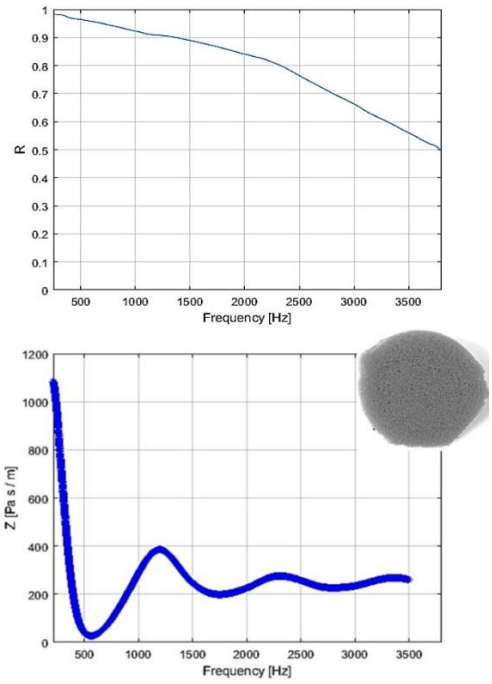

Figure 5.17. Measured reflection coefficient and acoustic impedance soft acoustic Foam 2 (ρ = 25 kg/m^3)

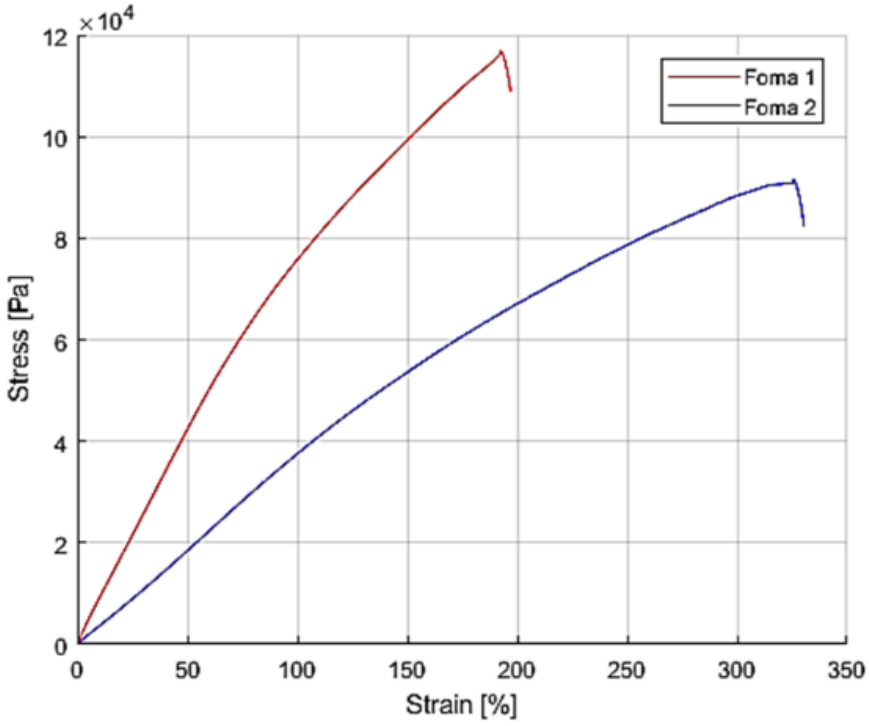

Figure 5.18. Stress-Strain curves for the tested acoustic soft foam

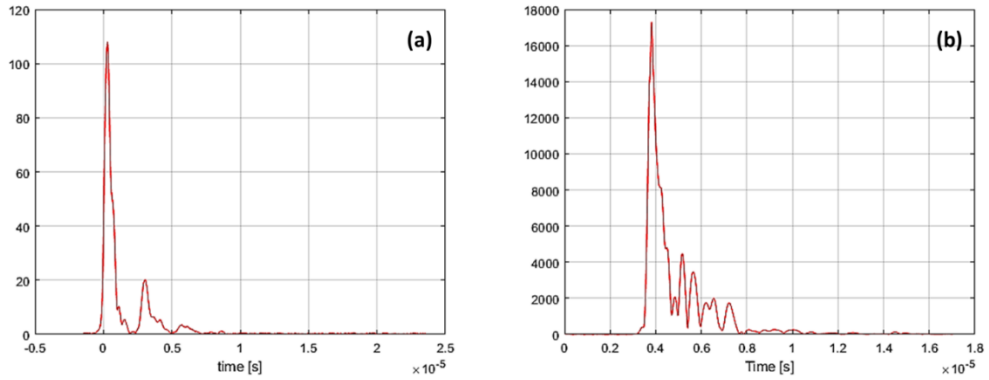

Figure 5.19. Initial pulse and the back-wall echo for the Sample 1 (Epoxy-carbon fibre and Sample 2 (vynilester-glass sample)

Considering the acoustic soft foam, the results in terms of elastic modulus estimated with the proposed method match with the elastic properties estimated by tensile tests with errors of under 8% for the Foam 1 and under 2% for Foam 2. It is clear that, the random distribution of porosity within the foam, allows for it to be considered isotropic.

When composite materials were tested, the results are always in good agreement with the results obtained with the time of flight approach both in terms of longitudinal sound speed and elastic modulus, but in this case the measurement uncertainties lead to error of 12% and 6% on the elastic modulus and 4% and 3% on the longitudinal speed respectively for the epoxy-carbon composite and vynilester-glass composite. In this case the mismatch of the results is associated with thermal-viscous losses through the impedance tube and to the amplitude-phase mismatch of the microphones. Reduced reflection coefficient accuracy occurs with highly reflective materials leading to a reduction in the accuracy of the estimated elastic properties (as explained in the previous section).

5 Conclusions

This paper proposes a method for the estimation of the elastic properties of porous, polymeric and composite materials using sound wave by measuring the reflection coefficient and the acoustic impedance in an impedance tube. The procedure described is based on the Transfer Function Method that derives information about the materials reflection coefficient. Under such hypothesis, the reflection coefficient is a function of the longitudinal speed of sound, of the acoustic impedance and as a consequence and the elastic properties of the material. A procedure was proposed to reduce the errors and the uncertainties on the measurements for high acoustic reflective materials such as composite or polymeric materials. The method was first tested in-silico using representative volume element and then experimentally verified.

The proposed approach would allow for the estimation of the elastic modulus for materials where ultrasound time of flight cannot be applied, for example porous materials. An error of only 2% is achieved when comparing the elastic modulus results with those obtained by destructive test (tensile testing).

For the first time, it was shown that using sound waves the elastic properties of composite materials can be evaluated where no standard test is available. In this case, the measured elastic modulus represents the out of plane elastic modulus (E_3) and measurement errors were around 3% for the longitudinal speed of sound and 10% for the elastic modulus with respect to ultrasonic testing.

The proposed methods is a reliable, effective and quick non-destructive method for the Elastic Modulus evaluation providing clear advantage over traditional techniques such as standard destructive methods or ultrasound time of flight measurements

REFERENCES

1. Petersen, K. E., "*Silicon as a mechanical material"*, Proceedings of the IEEE **70**, pp. 420-457, 1982.
2. Oliver, W. C. and Pharr, G. M., "*Measurement of hardness and elastic modulus by instrumented indentation: Advances in understanding and refinements to methodology*", Journal of materials research 19, pp. 3-20 , 2004.
3. Oliver, W. C. and Pharr, G. M., "*An improved technique for determining hardness and elastic modulus using load and displacement sensing indentation experiments"*, Journal of materials research 7, pp. 1564-1583 (1992).
4. Lang, S. B., "*Ultrasonic method for measuring elastic coefficients of bone and results on fresh and dried bovine bones"*, IEEE Transactions on Biomedical Engineering, pp. 101-105, 1970.
5. Ashman, R., Cowin, S., Van Buskirk, W. and Rice, J., "*A continuous wave technique for the measurement of the elastic properties of cortical bone"*, Journal of biomechanics 17, pp. 349-361, 1984.
6. Rho, J. Y., Ashman, R. B. and Turner, C. H., "*Young's modulus of trabecular and cortical bone material: ultrasonic and microtensile measurements"*, Journal of biomechanics 26, pp. 111-119, 1993.
7. Jones, M. G. and Stiede, P. E., "*Comparison of methods for determining specific acoustic impedance"*, The Journal of the Acoustical Society of America 101, pp. 2694-2704 , 1997.
8. Dalmont, J.-P., "*Acoustic impedance measurement, Part I: A review"*, Journal of Sound and Vibration 243, pp. 427-439, 2001.
9. Kumar, A., Kumar, B. and Kumar, Y., "*A novel method to determine the acoustic impedance of membrane material"*, Ultrasonics 35, pp. 53-56, 1997.
10. Song, B. H. and Bolton, J. S., "*A transfer-matrix approach for estimating the characteristic impedance and wave numbers of limp and rigid porous materials"*, The Journal of the Acoustical Society of America 107, pp. 1131-1152, 2000.
11. Doutres, O., Salissou, Y., Atalla, N. and Panneton, R., "*Evaluation of the acoustic and non-acoustic properties of sound absorbing materials using a three-microphone impedance tube"*, Applied Acoustics 71, pp. 506-509, 2010.
12. Buchaillot, L., Farnault, E., Hoummady, M. and Fujita, H., "*Silicon nitride thin films Young's modulus determination by an optical non destructive method"*, Japanese Journal of Applied Physics 36, pp. L794, 1997.

13. França, D. and Blouin, A., "*All-optical measurement of in-plane and out-of-plane Young's modulus and Poisson's ratio in silicon wafers by means of vibration modes"*, Measurement Science and Technology 15, pp. 859, 2004.
14. J. David, N. Cheeke, *"Fundamentals and Applications of Ultrasonic Wave",* CRC PRESS, 2002.
15. A. B. Wood, *"A Textbook of Sound",* G. BELL AND SONS LTD, 1964.
16. D.T. Blackstock, *"Fundamentals of Physical Acoustics", JOHN WILEY & SONS, 2000.*
17. W. Sun, Z. Guan, Z. Li, M. Zhang, Y. Huang, "*Compressive failure analysis of unidirectional carbon/epoxy composite based on micro-mechanical models*", CHINESE JOURNAL of AERONAUTICS, 2017.
18. X.L. Chen, Y.J. Liu, "*Square representative volume elements for evaluating the effective material properties of carbon nanotube-based composite*", COMPUTATIONAL MATERIALS SCIENCE 29 1-11, 2004.
19. G.M. Odegard, *"Costitutive modelling of piezoelectric polymer composite"*, ACTA MATERIALIA 52 5315-5330, 2004.
20. S. Kari, H. Berger, R. Rodriguez-Ramos, U. Gabbert, *"Computational evaluation of effective material properties of composite reinforced by randomly distributed spherical particles",* COMPOSITE STRUCTURES 77 223-231, 2007.
21. S. J. Hollister, N. Kikuchi, *"A comparison of homogenization and standard mechanics analysis for periodic porous composites",* COMPUTATIONAL MECHANICS 10 73-95, 1992.
22. L. Iorga, Y. Pan, A. Pelegri, *"Numerical characterization of material elastic properties for random fiber composites",* J. MECH. MATER. STRUCT 3 1279-1298, 2008.
23. C. Pelissou, J. Baccou, Y. Monerie, F. Perales, *"Determination of the size of the representative volume element for random Quasi-brittle composite",* J. SOLIDS STRUCT 46 2842-2855, 2009.
24. K. P. Babu, P.M. Mohite, C.S. Upadhyay, *"Development of an RVE and its stiffness predictions based on mathematical homogenization theory for short fiber composites",* INTERNATIONAL JOURNAL OF SOLIDS AND STRUCTURES 130-131 80-104, 2018.
25. Z. Xia, Y. Zhang, F. Ellyin, *"A unified periodical boundary conditions for representative volume elements of composites and applications",* INTERNATIONAL JOURNALS OF SOLIDS and STRUCTURES 40 1907-1921, 2003.]
26. R.J.M. Smit, W.A.M. Brekelmans, H.E.H. Meijer, *"Prediction of the mechanical behaviour of nonlinear heterogeneous system by multi-level finite element modelling",* COMPUTER METHODS IN APPLIED MECHANICS AND ENGINEERING 155 181-192, 1998.

27. J. Segurado, J. Llorca, *"A numerical approximation to the elastic properties of sphere-reinforced composites",* JOURNAL OF THE MECHANICS AND PHYSICS OF SOLID 50 2107-2121, 2002.
28. C. Huet, *"Application of variational concepts to size effects in elastic heterogeneous bodies"*, J. MECH. PHYS. SOLIDS 8 812-841, 1990.
29. S. Hazanov, C. Huet, *"Order relationships for boundary condition effects in heterogeneous bodies smaller than the representative volume"*, J. MECH. PHYS. SOLIDS 42 1995-2011, 1994.
30. K. J. Bathe, *"Finite Element Procedures",* PRENTICE-HALL, 1996.
31. O. C. Zienkiewicz. R. E. Newton. *"Coupled Vibrations of a Structure Submerged in a Compressible Fluid"*, PROCEDINGS OF THE SYMPOSIUM ON FINITE ELEMENT TECHNIQUES, 1969.
32. PD. Soden, MJ. Hinton, AS. Kaddour, *"Lamina Properties. Lay-up configurations and loading conditions for a range of fibre-reinforced composite laminates"*, COMP SCI TECHNOL 58(7) 1011-1022, 1998.
33. ASTM 1050, *"Standard Test Method for Impedance and Absorption of Acoustical Materials using a Tube, two microphones and a digital frequency analysis system",* ASTM INTERNATIONAL, 2012.
34. J. Han, D.W. Herrin, A. F. Seybert, *"Accurate measurement of small absorption coefficient",* SAE INTERNATIONAL, 01-2224, 2007.
35. ISO 10534-2/2, *"Acoustic-Determination of sound absorption coefficient and impedance in impedance tubes – Part 2: Transfer-function method".*
36. J.Y. Chung, D.A. Blaser, *"Transfer function method of measuring in-duct acoustic properties. I. Theory",* The Journal of the Acoustical Society of America, 68, 907, 1980.
37. J.Y. Chung, D.A. Blaser, *"Transfer function method of measuring in-duct acoustic properties. II. Experiment",* The Journal of the Acoustical Society of America, 68, 914, 1980.
38. ASTM D 3574, *"Standard Test Method for Flexible Cellular Materials – Slab, Bonded, and Molded Urethane Foams "*, ASTM INTERNATIONAL, 2012.
39. ASTM E 494, *"Standard Practice for Measuring Ultrasonic Velocity in Materials",* ASTM INTERNATIONAL, 2012.

Chapter 6

Micro-Perforated Panel for passive sound absorption solutions

Microperforated panel absorbers are applied in several acoustic engineering applications representing one of the most promising alternatives to porous absorbing materials for noise reduction. Those devices are of particular interest because of their easy commercial realization and their simple physics which allows accurate predictions of acoustic behaviour.

The Microperforated panel absorbers can be seen as particular case of Helmholtz resonator, where the perforation is smaller than the incident sound wave wavelength. In that case, the sound absorption mechanism is due both to the resonance phenomena and the losses occur due to viscous boundary layer effects in the perforations [1-5].

However, the limitations with these absorbers is getting broadband absorption at low frequencies. The MPP absorber behaves as single degree of freedom mass-spring system, with the mass properties related to mass of air into the perforation and the stiffness properties related to the mass of air in the acoustic cavity. So, as it relies on devise resonance, the sound absorption is normally limited to a narrow peak at the resonance frequency [18,43] (Figure 2.1). The resonance frequency is also inversely proportional to the stiffness properties of the device. The

applicability then of MPP absorber a low frequency is associated to big acoustic cavity. In order to increase the broadening absorption properties of MPP absorber, the enclose acoustic cavity can be fully or partially full of porous absorber [32] (Figure 2.3, Figure 2.6). There is an evidence advantage in terms broadening, but the absorption efficiency is still confined above 1kHz since the thickness of the porous materials required to achieve sound absorption is one order of magnitude smaller than the wavelength. To cover this limitation, the researchers start to combine the concept of permeable/impermeable membrane [39,40,41,42], which provide a better absorption at lower frequencies for the same cavity depth, with the MPP. Also in this case it is possible achieve broadening absorption but the frequency working range of the absorber is still above 800 Hz and the global absorption level is always lower than 90% (Figure 2.11).

This research work will cover the challenges in the design of subwavelength resonant structures to extend the absorption bandwidth below 1kHz.

A prototype of multilayers microperforated panel absorber is presented which guarantees a sound absorption level over 90% in a low frequency range between 300Hz to 2000Hz. In the multilayer absorbers, each single layer absorber is characterized by one resonance frequency coupled with viscous/thermal loss through the perforation. So, the result of adding more absorber in series is the resonances coupling which leads to broadband absorption. Also, considering a considerable high perforation ratio, the mass of the equivalent dynamic system is higher, and the resonances are shifted at lower frequencies as consequence.

Starting from the electro-acoustical equivalent circuit analysis proposed by Maa [3-4-5], an analytical model based on the acoustic impedance series/parallel is developed to describe the acoustic performance of the absorber. Then parametric analysis is run to investigate the effect of the design parameters, such as perforation ratio, perforation diameter, panel thickness and, cavity depth on the absorbing properties. The optimised set of design parameters coming out from analytical analysis are used to design and machine different multilayers absorber configuration which are tested experimentally in an impedance tube test rig. The experimental results are in perfect match with the predicted numerical ones.

In the last part of the work, the effect of the perforation geometry is also experimental investigated keeping constant all the other parameters. We demonstrated how, keeping constant the perforation ratio, the shape and the number of the holes can be designed without any significant changes in the absorption characteristics of the resonator.

6.1 List of Symbols

The symbols and their explanation used in Chapter 6 for the mathematical notation are reported below:

Symbol	Description
α	Absorption Coefficient
R	Complex Reflection Coefficient
H	Transfer Function between two microphones
k	Wavenumber
s	Microphones spacing
l	Sample-Microphone distance
ω	Angular frequency
K	Geometrical scale factor associated to the impedance tube
f_u	Upper limit frequency for the impedance tube
f_l	Lower limit frequency for the impedance tube
d_t	Impedance tube diameter
Z_{TOT}	Acoustic Impedance of absorber
Z_{MPP}	Acoustic Impedance of panel
Z	Impedance of Airgap
R_1	Acoustic Resistance of Panel
M_1	Acoustic Reactance of Panel
M_2	Bulk mass Reactance
m	Surface Density of Panel
p	Perforation Ratio
d	Diameter of Orifice
r_0	Radius of Orifice
t	Panel Thickness
D	Airgap Length
L	Length of slot
b	Width of slot
Ar	Slot Aspect Ratio
n_s	Number of slots

Δp	Pressure difference applied to the ends of micro-tubes
u	Particle velocity
r_1	Radius vector in cylindrical coordinates
J_0	Bessel function of first kind and zero order
J_1	Bessel function of first kind and first order
c	Speed of sound in air
ρ_0	Density of air
η	Air coefficient of viscosity

6.2 Journal Paper Reference Details

The research work presented in this chapter is part of published journal paper which the reference details are as follow:

"A multilayer Micro-Perforated Panel prototype for broadband sound absorption at low frequencies"

Authors:

Fabrizio Bucciarelli - Department of Mechanical Engineering, University of Bath, Bath, UK.

Gain Piero Malfiense Fierro - Department of Mechanical Engineering, University of Bath, Bath, UK.

Michele Meo - Department of Mechanical Engineering, University of Bath, Bath, UK.

Corresponding Authors: Michele Meo – m.meo@bath.ac.uk

Journal: Applied Acoustics, Volume 146, pages 134-144,(2019) - DOI: 10.1016/j.apacoust.2018.11.014

The Statement of Authorship From and the paper a reported next.

This declaration concerns the article entitled:	
A multilayer Micro-Perforated Panel prototype for broadband sound absorption at low frequencies	
Publication status (tick one)	
Draft manuscript	
Submitted	
In review	
Accepted	
Published	✓
Candidate's contribution to the paper (detailed, and also given as a percentage).	
The candidate contributed to/ considerably contributed to/predominantly executed the…	
Formulation of ideas:	80% I formulate the idea discussing it with my supervisor.
Design of methodology:	100% I developed and implemented the analytical model and performed all the parametric analysis for the optimization
Experimental work:	80% Dr. G.P. Malfense Fierro helped me with the prototype manufacturing while I performed all the experimental measurement campaign.
Presentation of data in journal format:	80% I wrote the paper and followed the review process. Prof. Meo supported me during the submission and the review process
Statement from Candidate	

This paper reports on original research I conducted during the period of my Higher Degree by Research candidature.			
Signed		**Date**	05/01/2020

A multilayer Micro-Perforated Panel prototype for broadband sound absorption at low frequencies

F. Bucciarelli[1], G.P. Malfense Fierro[1], M. MEO[3,a]

[1] Department of Mechanical Engineering, University of Bath, Bath, UK

[a] m.meo@bath.ac.uk

Abstract

Microperforated panel (MPP) absorbers are one of the most promising alternatives to porous sound absorbing materials. However, these structures cannot achieve high and broadband absorption at low frequencies. To be effective, once defined the material properties the geometrical parameters of the absorber need to be optimized to match the prescribed absorption level. This paper presents a multiple layer MPP absorber with a high sound absorption coefficient and broadband absorption at low frequencies. An electro-acoustical equivalent circuit model was used for a parametric analysis to study the relationships between the absorption mechanism and the absorbers geometrical parameters in the proposed multilayer MPP. A prototype of this absorber was machined and tested in an impedance tube test ring and the experimental acoustical properties in terms of absorption coefficient were extracted using the transfer function method. It was demonstrated that the five-layer MPP absorber was capable of guaranteeing a high absorption (constantly over 90%) in a frequency range from 400 to 2000 Hz. The results indicate that the proposed multilayer MPP absorber provides a good alternative for sound absorption applications.

Symbol	Description
α	Absorption Coefficient
R	Complex Reflection Coefficient
H	Transfer Function between two microphones
k	Wavenumber
s	Microphones spacing
l	Sample-Microphone distance
ω	Angular frequency
K	Geometrical scale factor associated to the impedance tube
f_u	Upper limit frequency for the impedance tube
f_l	Lower limit frequency for the impedance tube
d_t	Impedance tube diameter
Z_{TOT}	Acoustic Impedance of absorber
Z_{MPP}	Acoustic Impedance of panel
Z	Impedance of Airgap
R_1	Acoustic Resistance of Panel
M_1	Acoustic Reactance of Panel
M_2	Bulk mass Reactance
m	Surface Density of Panel
p	Perforation Ratio
d	Diameter of Orifice
r_0	Radius of Orifice
t	Panel Thickness
D	Airgap Length
L	Length of slot
b	Width of slot
Ar	Slot Aspect Ratio
n_s	Number of slot
Δp	Pressure difference applied to the ends of micro-tubes
u	Particle velocity
r_1	Radius vector in cylindrical coordinates
J_0	Bessel function of first kind and zero order
J_1	Bessel function of first kind and first order
c	Speed of sound in air
ρ_0	Density of air
η	Air coefficient of viscosity

1 Introduction

Microperforated panel (MPP) absorber has been recognised as the next generation of fiber-free sound absorbing material [1-2]. Maa [3-5] first proposed the concept of MPP absorber establishing its theoretical basis and design guidelines. Maa put forward the revolutionary idea that by reducing the perforation of the panel to sub-millimeter scale, sufficient resistance could be provide for high sound absorption without the use of fiber or porous material.

MPP absorber applications, improvements and theoretical developments have been extensively studied in order to improve the sound absorption performance by various constructions. Wang and Huang [6] presented a parallel arrangement of multiple MPP absorbers with different cavity depths. The acoustic properties of a prototype considering three cavities with different depth has been studied using a finite element approach and compared with experimental measurements. In the same field Guo [12] proposed a compound MPP sound absorber composed by an array of parallel-arranged MPP sub-absorber with different depth with better absorption performance when compared with single MPP absorbers. Lee [7] tried to combine the micro perforation effect with flexible vibration of a thin plate in order to widen the sound absorption frequency range. Lu [8] first introduced flexible tube bundles attached to the MPP and Zhang [9] then improved lower frequency sound absorption by attaching tree-like bundles to the perforations. Recently, starting with research done by Iwan [10], Li [11] discussed theoretically and experimentally how to design a low frequency perforated panel sound absorber with short extended tubes with limited thickness.

On the other hand, different research works tried to couple the MPP with honeycomb or membrane structures in order to increase the sound absorption performance. Pan [13] demonstrated that an improvement of the sound absorption is possible when one of the surface sheets of the honeycomb panel is microperforated. Sakagami [14] placed honeycomb structures within a cavity between plates of a double-leaf MPP. He demonstrated theoretically and

experimental that due to the effect of the honeycomb the peak frequency shifts to lower frequency and the peak value increases.

Sakagami [15-16] also proposed a sound absorption structure with an MPP and a permeable membrane with a rigid-back wall and air cavities in between; this resulted in an increase in the peak absorption and broadening of the absorption frequency range. Gai [17] demonstrated experimentally how a composite MPP sound absorber with membrane cells can provide more sound absorption than the single leaf MPP absorber and absorption gradually rises with the increase of the membrane area.

In this paper we theoretically and experimentally discuss how to design a broadband multilayer MPP absorber. An analytical design model is presented, and the parametric analysis results are discussed in order to study how the design parameters affect the acoustic properties of the multilayer MPP absorber. An optimized five layers MPP absorber prototype was designed, machined and tested. A flat broadband absorption (over 90%) can be achieved in a frequency range between 400 Hz to 2000Hz. At the same time an experimental investigation regarding the influence of the perforation shape on the sound absorption is exposed in this paper.

2 Electro-Acoustical Equivalent Circuit Analysis

Maa [3-5] proposed a MPP absorber formed by a single micro perforated layer and a rigid back wall with an air gap in-between.

Considering a single layer MPP the absorption coefficient is a function of the acoustic impedance of the panel itself and can be estimated [3]

$$\alpha(\omega) = \frac{4Re[Z_{tot}(\omega)]}{(1 + Re[Z_{tot}(\omega)])^2 + Im[Z_{tot}(\omega)]^2} \tag{2.1}$$

The MPP can be considered as a distribution of short tubes separated by distances larger than their diameters but smaller than the wavelength of the incident sound wave [5]. The propagation of sound wave in a tube can be described using the

equation of aerial motion which is valid for a short tube compared with the incident wavelength [19]

$$\rho_0 \dot{u} - \frac{\eta}{r_1}\frac{\partial}{\partial r_1}\left(r_1 \frac{\partial u}{\partial r_1}\right) = \frac{\Delta p}{t} \tag{2.2}$$

where $\rho_0$is the density of the air, η the air coefficient of viscosity, r_1 the radius vector of the cylindrical coordinate into the tube, *t* is the length of the tube which is equal to the panel thickness, Δp is pressure difference applied to the ends of the tube and u is the particle velocity. Equation (2.2) can be solved for the particle velocity, in particular the average particle velocity can be found over the tube cross section. So, the acoustic impedance of the orifice, expressed by the ration between the pressure difference and the average particle velocity can be calculated

$$Z_1(\omega) = \frac{\Delta p}{u} = j\omega\rho_0 t\left[1 - \frac{2}{x\sqrt{-j}}\frac{J_1\left(x\sqrt{-j}\right)}{J_0\left(x\sqrt{-j}\right)}\right]^{-1} \tag{2.3}$$

where $x(\omega) = r_0\sqrt{\omega\rho_0/\eta}$ and J_0 , J_1 are the Bessel function of the first kind and zero and first order respectively, r_0 the radius of the orifice. So, the orifice acoustic impedance is a function of x which is proportional to the ratio of the radius to the thickness of the viscous boundary layer $\left(\sqrt{2\eta/\omega\rho_0}\right)$. Maa provided an approximate formula [4] which can be applied for values of *x* between 1 and 10 that are the typical values associated with MPPs [4-5]

$$Z_1(\omega) = \frac{32\eta t}{d^2}\sqrt{1 + \frac{x^2(\omega)}{32}} + j\omega\rho_0 t\left(1 + \frac{1}{\sqrt{9 + \frac{x^2(\omega)}{2}}}\right) \tag{2.4}$$

$d = 2r_0$ being the diameter of the tube.

Under the hypothesis that the holes on the perforated panel are spaced more than a diameter from each other, the equation (2.4) can be applied to the holes of the MPP and the acoustic impedance of the MPP will be that of an orifice divided by the perforation ratio (defined as the ratio between the perforated area over the area of the panel)

$$Z_{MPP}(\omega) = \frac{Z_1}{p\rho_0 c} = R_1(\omega) - i\omega M_1(\omega) \tag{2.5}$$

$$R_1(\omega) = \frac{32\eta t}{p\rho_0 c d^2}\left(\sqrt{1 + \frac{x(\omega)^2}{32}} + \frac{\sqrt{2}}{8} x \frac{d}{t}\right) \tag{2.6}$$

$$M_1(\omega) = \frac{t}{pc}\left(1 + \frac{1}{\sqrt{9 + \frac{x(\omega)^2}{2}}} + 0.85\frac{d}{t}\right) \tag{2.7}$$

where p is the perforation ratio, c the sound speed and ω the angular frequency.

The impedance is a complex quantity where the real part, named acoustic resistance ($\boldsymbol{R_1}$) represent the energy radiation and the viscous loses of the acoustic wave propagating through the perforations. The imaginary part, named acoustic reactance ($\boldsymbol{M_1}$) refers the mass of the air moving inside the perforation.

The end terms in eq. (2.6) and (2.7) represent correction factors introduced by Morse and Ingard [18] which take into account respectively the resistance due to air flow friction on the surface of the panel when the flow is forced to pass through the micro holes, and the mass reactance due the piston sound radiation at both ends.

If the MMP panel is lightweight the acoustic properties of the MMP layer can be affected by the sound-induced vibration. However, in this paper, the panel will be assumed acoustically rigid.

The MPP represent the principal element in a MPP absorber which is formed, as introduced at the beginning of the chapter, by a single MPP, a rigid back wall with an air gap in between. Each coupled hole-air cavity can be considered as a Helmholtz resonator in order to achieve a single resonance peak in absorption characteristic.

It has been proven in different works [1-2-3-16-20] that MPP absorber can be equivalently described by an equivalent electric circuit, including the global impedance of the perforated panel ($Z_{MPP}(\omega)$) and the characteristic impedance associated to the mass of air behind the panel (Z) which is a function of the depth D and can be estimated by

$$Z(\omega) = i \cot(Dk(\omega)) \tag{2.8}$$

with k the wavenumber ($k = \omega/c$).

With the equivalent electric circuit analogy, the acoustic impedance, the pressure difference and velocity of the particles are associated with the electric impedance, the voltage and the electric current respectively. As shown in Figure 6.1 the global circuit impedance is the result of the series between the global impedance of the MPP with the impedance associated to the air behind it.

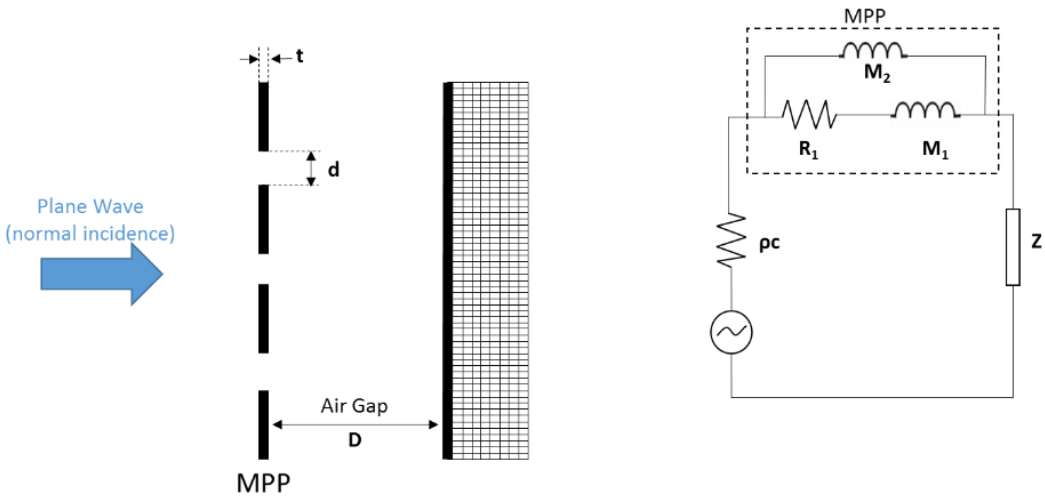

Figure 6.1: A single MPP absorber with the equivalent electro-acoustical circuit

Following the series and parallel laws for the electric circuits, the equivalent impedance of the equivalent circuit can be easily estimated

$$Z_{tot}(\omega) = \left(\frac{1}{R_1(\omega) - i\omega M_1(\omega)}\right)^{-1} + Z(\omega) \qquad (2.9)$$

Such calculated Z_{tot} represent exactly the acoustic impedance of the single MPP absorber, so can be used to estimate the absorption coefficient following the equation (2.1).

Following the same approach a multilayers MPP absorber is proposed which includes n MPP layers placed in parallel with different or constant geometrical parameters (t_i, d_i,p_i)separated by n air gap between them with variable or constant depth (D_i). For each micro-perforated layer equations (2.5 – 2.7) can still be applied, with equation (2.8) used for modelling the air impedance between them.

The multiple layer MPP system with the relative equivalent electro-acoustic circuit model is shown in Figure 6.2.

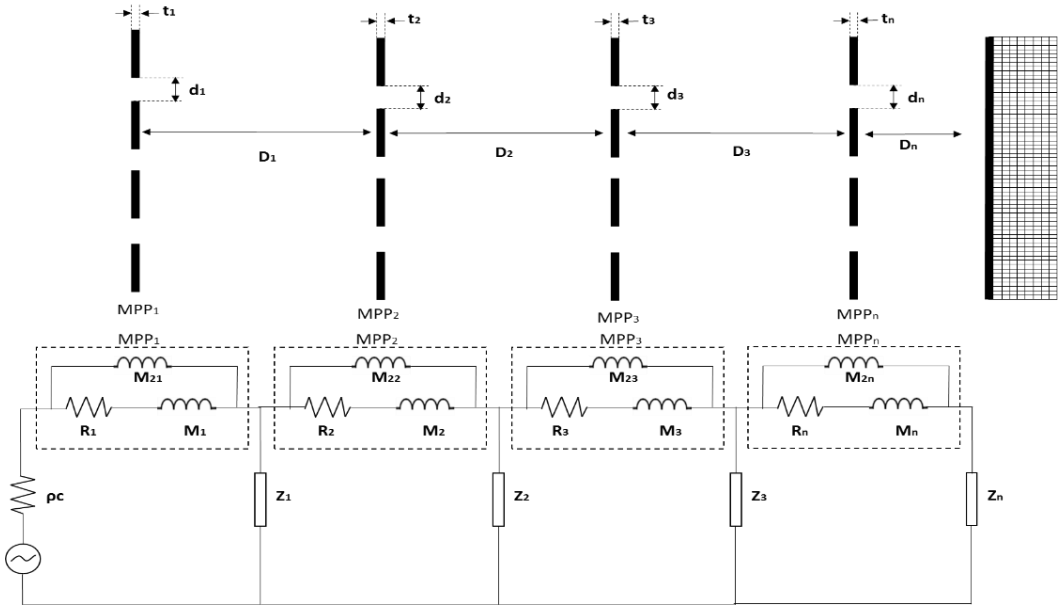

Figure 6.2: Multiple Layer MPP absorber and its electro-acoustical equivalent circuit model

First the acoustic impedance for each layer is estimated solving the parallel between the pre-estimated series and the bulk mass reactance

$$Z_{layer_j}(\omega) = \left(\frac{1}{R_j(\omega) - i\omega M_j(\omega)}\right)^{-1} \qquad j = 1, n \qquad (2.10)$$

The total acoustic impedance of the system is then estimated solving sequentially the series and parallels until the basic equivalent circuit is achieved

$$Z_{parallel_j} = \left(\frac{1}{Z_{n-j}} + \frac{1}{Z_{serie_j}}\right)^{-1} \qquad j = 1, n-1 \qquad (2.11)$$

$$Z_{serie_{j+1}} = Z_{layer_{n-j}}(\omega) + Z_{parallel_j} \qquad j = 1, n-1 \qquad (2.12)$$

using as starting point $Z_{serie_1} = Z_{layer_n} + Z_n$.

3 Parametric Analysis

A multilayer MPP absorber with substantial broadband frequency sound absorption cannot be achieved with a conventional type, but the efficiency in terms of amplitude and frequency range is strictly related to the geometrical design parameters. In order to determine the effects of the MPP parameters on the absorption coefficient an analytical model was developed, and a parametric analysis run. In the following analysis the number (n=6) and the material (Perspex: ρ=1180Kg/m^3) of the layers are kept constant. First the length of the backing space (D) was increased. Figure 6.3 shows the absorption coefficient considering different air gap lengths varying from 20 to 60 mm. The peaks shift to low frequencies as D increased but simultaneously the maximum absorption is guaranteed for a smaller frequency range. So, a better absorption at low frequencies can be achieved increasing the entity of the backing air space; in particular focusing on 100 Hz there is an increment of 44% on α (from 11% for an air gap of 20mm to 55% for an air gap of 60mm). For high values of D the absorption trend generally becomes smoother but the frequency range covered by an absorption higher than 90% reduces from [370-2200] Hz for D=20mm to [150-1180] Hz for D=60mm.

The effect of the layers thickness is significant, both in terms of absorption coefficient amplitude and the frequency range interested by the maximum absorption while the curve shape is quite constant (Figure 6.4). If the thickness is changed from 1 to 5 mm, the response curve shifts to lower frequencies with a simultaneous reduction in absorption level.

In Figure 6.5(a-b) the diameter of the perforations is changed first from 0.2 to 0.6 mm (a) and then from 0.6 to 1.2mm (b). The effect of the hole diameter on the absorption coefficient is not monotonic. An optimum value can be identify around 0.4-0.6 mm. The sound absorption performance deteriorates when the diameter becomes larger, so it is important to keep the diameter under 0.6mm to maintain a flat absorption trend over 90%. Increasing the diameter with respect to the optimum value, the trend of the absorption is not smooth and the resonance peaks associated to the single layers of the multiple MPP absorber are more evident. On the other

hand, by decreasing the dimension of the diameter the frequency range where the absorption is relevant can be increased but the absorption level at low frequencies reduces.

The perforation ratio of the MPP layers is changed from 1% to 6% (refer to Figure 6.6) with these changes not affecting the curve shape. Increasing *p* from 1% to 6% results in a significant gain in the sound absorption, with an increase of the maximum absorption from 70% to 100%. Although, there is a clear shift of the first peaks to higher frequencies, in particular moving the perforation ratio from 1% to 6% the peak shifts from 100 Hz to 400 Hz.

The effect of the number of the layers is studied in Figure 6.7. A substantial gain in terms of broadband absorption level at low frequencies can be achieved by adding layers in the MPP absorber. Each MPP layer with its relative air gap represents a Helmholtz resonator which may be discretized as a mass spring damper system. So, each of them will be characterized by a resonant frequency which is strictly related to the absorption peak. Adding perforated layer with a backing air gap, a coupling of resonance systems will be generated with a considerable gain in the absorption level. On the other hand, the single layer of the multiple layer absorber will behave as a single layer absorber but with a different air gap. For example as shown in Figure 6.7, the first absorption peak for a 6 layers MPP absorber is depicted at 400 Hz; the same frequency may be absorbed using a single layer with the same geometrical parameters but with an air gap length of 1.8mm which is the sum of the air gap length of the considered multiple layer absorber, thus the effect of the number of layers is indirectly related to the air gap length. The benefit associated to an increment of the number of layer is a result of the superposition of two different effects: the first one is the coupling of the resonance frequencies of each absorber, the second one is the effect of the local air gap between each layer and the following one, and the global air gap between the single layer and hard back.

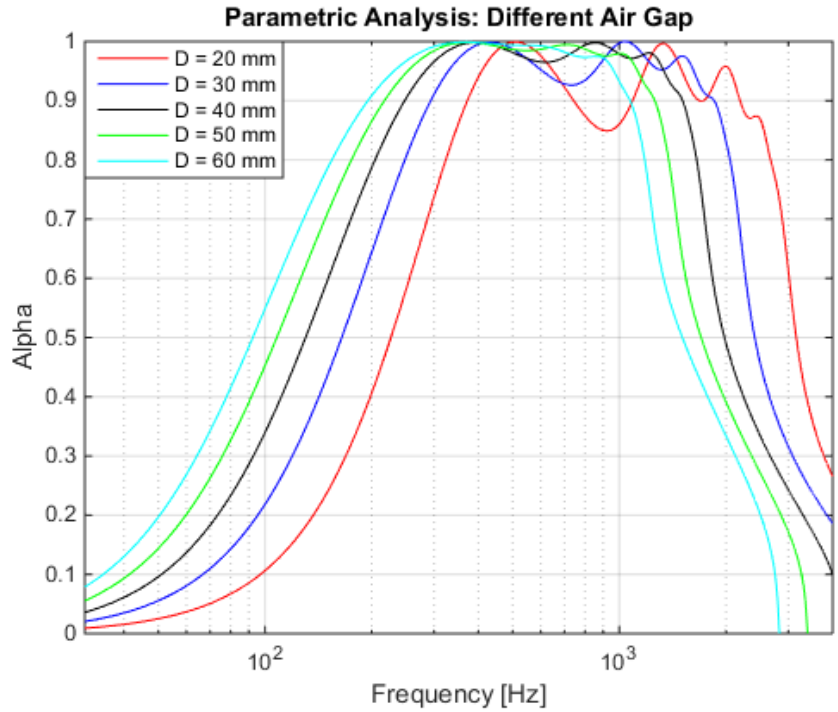

Figure 6.3: Absorption coefficient of a 6 layers MPP absorber with different backing cavities [p=6%; t=1.5mm; d=0.5mm]

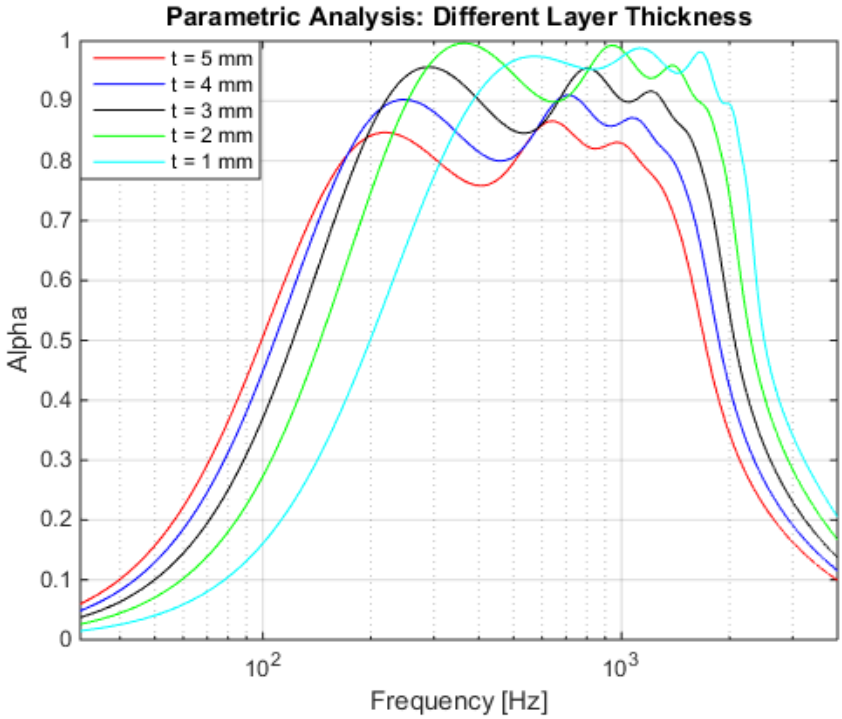

Figure 6. 4: Absorption coefficient of a 6 layers MPP absorber with different layer thickness [p=6%; D=30mm; d=0.5mm]

(a)

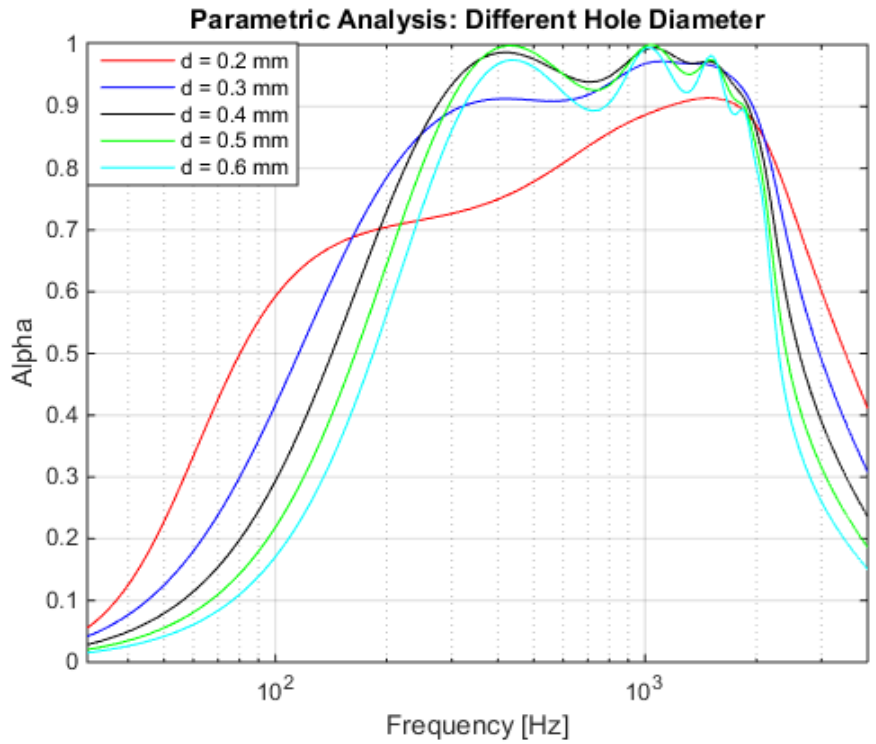

(b)

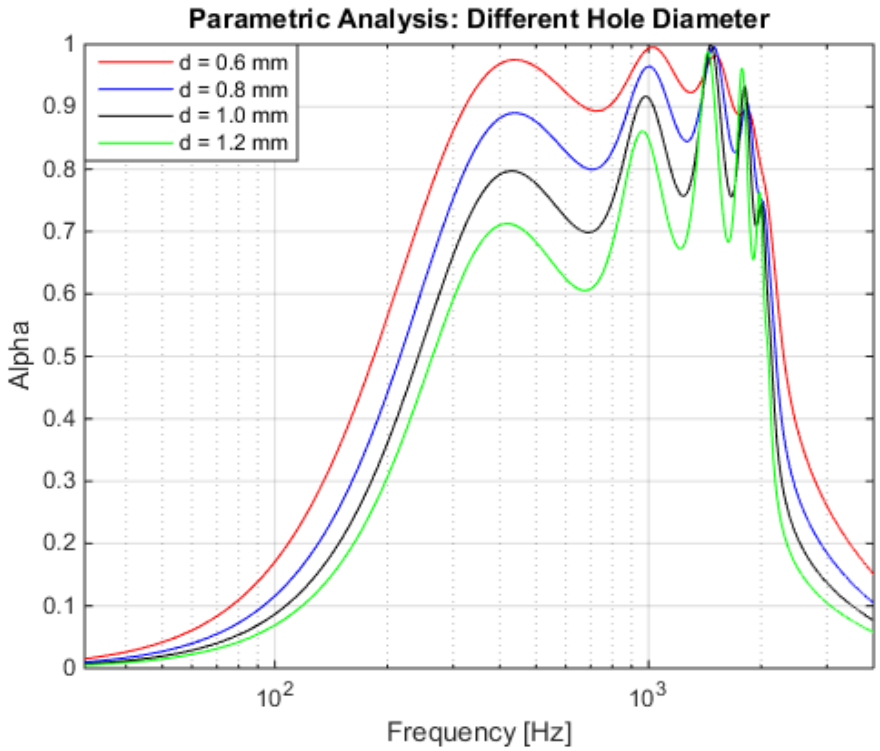

Figure 6.5: Absorption coefficient of a 6 layers MPP absorber with different hole diameters [p=6%; t=1.5mm; D=30mm]

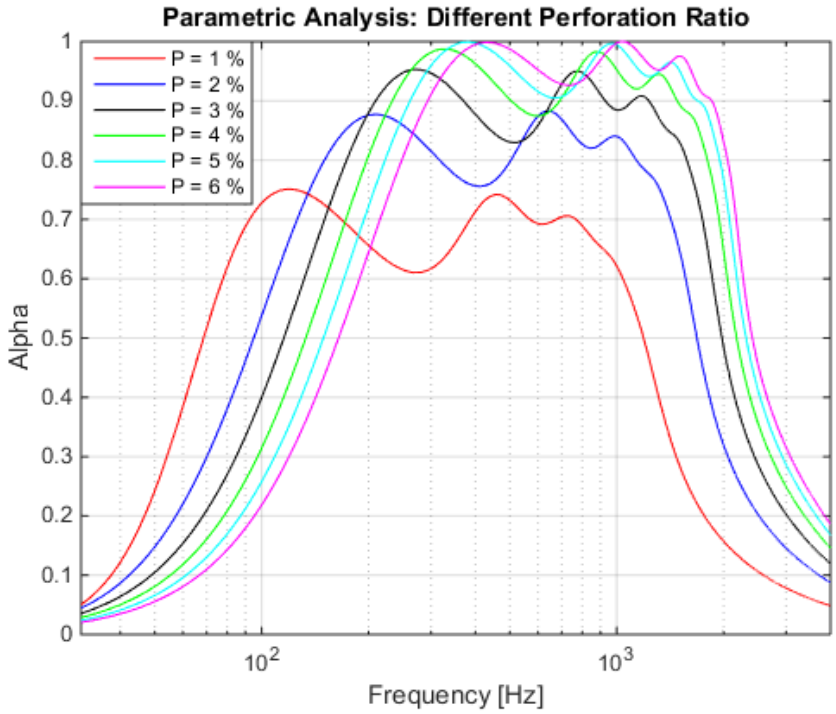

Figure 6.6: Absorption coefficient of a 6 layers MPP absorber with different perforation ratio [D=30mm; t=1.5mm; d=0.5mm]

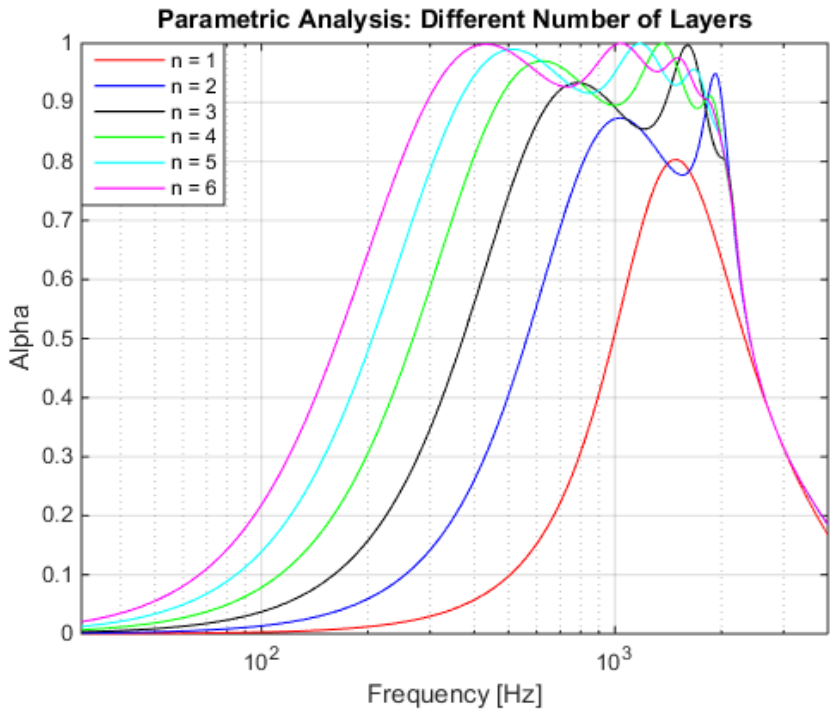

Figure 6.7: Absorption coefficient multi layers MPP absorber with different number of layers [D=30mm; t=1.5mm;d=0.5mm, p =6%]

4 Experimental Validation

Experimental studies were carried out in order to validate the analytical model of a multiple MPP absorber. The measurements of normal absorption coefficient have been conducted in a commonly used two microphones impedance tube with the sample placed at one end of the tube with a hard back surface, while the front end of the tube had a loud speaker to generate a broadband random signal into the tube (Figure 6.8). The test ring has been designed according to ASTM E-1050 [21] in order to guarantee a standing plane wave into the tube. In the present work a straight tube made of aluminium of 15mm thickness (so the tube wall can be assumed as acoustically rigid) with an internal diameter of 50.8mm has been considered, with experimental results limited to the working frequency range of the tube (300-3800Hz), in fact the working frequency range is a function of the tube dimensions. In particular, in order to maintain plane wave propagation, the upper frequency limit is defined as

$$f_u < \frac{Kc}{d_t} \tag{4.1}$$

where c is the speed of sound in the tube, d_t is the tube internal diameter and K is a geometrical scale factor and for a circular cross section $K=0.586$.

The lower frequency limit depends on the spacing of the microphones. In particular, the minimum microphone spacing may exceed one percent of the wavelength corresponding to the lower frequency of interest.

$$f_l > \frac{c}{100 s_{min}} \tag{4.2}$$

Two microphones have installed in the upstream part of the tube to sense the incident and reflected sound wave, thereby the obtaining both the reflection amplitude and phase. The maximum microphones spacing may be less than 80% of the shortest half wavelength of interest.

$$s_{max} > \frac{0.4c}{f_u} \tag{4.3}$$

Moreover, in order to maintain the greatest signal-noise ratio, the spacing between the sample and closest microphone should be greater than $2d_t$ in order to facilitate

the dissipation of higher order modes generated from any rough surface of the sample which decay exponentially as they propagate along the tube. A minimum distance of $3d_t$ between the sound source and the closest microphone is required to ensure that a plane wave develops before reaching the microphones and the sample. All the geometrical parameters of the test ring are shown in Table 4.1.

Frequency Range	300 – 3800 [Hz]
Tube Diameter	50.8 [mm]
Mic Spacing (s)	30 [mm]
Sample – Mic distance (l)	140 [mm]
Source – Sample distance	330 [mm]

Table 4.1: Test ring geometrical parameters.

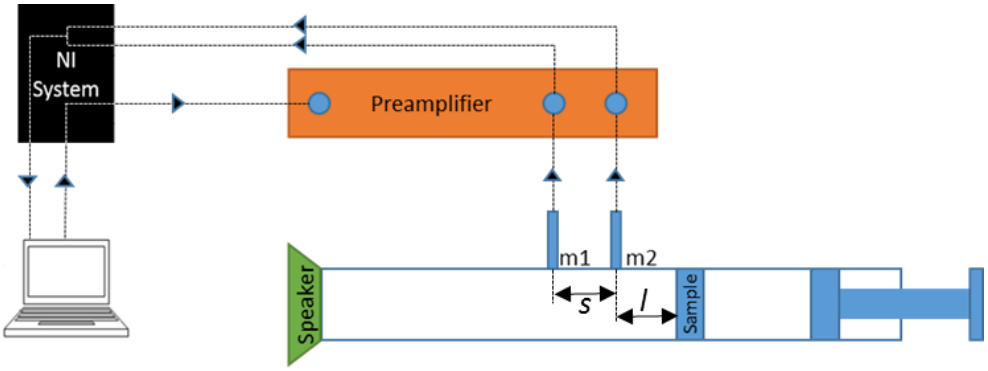

Figure 6.8: Impedance tube Test rig

The normal absorption coefficient has been estimated measuring the transfer function between the two microphones signals along with the microphone spacing, the distance between the incidence surface of the sample and the closest microphones (Transfer Function Method [21])

$$\alpha = 1 - |R|^2 \tag{4.4}$$

where R is the complex reflection coefficient measured on the sample incident surface

$$R = R_r + jR_i = \frac{H - e^{-jks}}{e^{jks} - H} e^{2jk(l+s)} \tag{4.5}$$

where *H* is the transfer function calculated from the complex ratio of the Fourier transform of the acoustic pressures at the microphones.

The normal absorption coefficient measured following equation (4.4) has been then compared with the result obtained from the numerical simulation.

The different configurations of tested prototype have been described in Table 4.2.

Two different materials for the perforated panels have been considered: Aluminium and Perspex in order to investigate the effect of the density on the sound absorption phenomena. The same geometrical parameters, panel thickness, hole dimeter, air gap length and number of layers have been considered for the aluminium prototype and the perspex one. As shown in Figure 6.9 (a)-(b) the density does not have any real affect on the absorption coefficient because the machined panel cannot be considered a lightweight structure and the effect of the bulk vibration is negligible; therefore, the panel may be assumed to be acoustically rigid.

Sample	**Material**	**n.**	**t (mm)**	**d (mm)**	**p (%)**	**D (mm)**
Sample_1	Aluminium (2700 kg/m^3)	1	1	1	1	30
Sample_2	Perspex (1180 kg/m^3)	1	1	1	1	30
Sample_3	Aluminium (2700 kg/m^3)	3	1	1	1	6
Sample_4	Perspex (1180 kg/m^3)	3	1	1	1	6
Sample_5	Perspex (1180 kg/m^3)	1	1.6	0.5	6	22
Sample_6	Perspex (1180 kg/m^3)	2	1.6	0.5	6	22
Sample_7	Perspex (1180 kg/m^3)	3	1.6	0.5	6	22
Sample_8	Perspex (1180 kg/m^3)	4	1.6	0.5	6	22
Sample_9	Perspex (1180 kg/m^3)	5	1.6	0.5	6	22
Sample_10	Perspex (1180 kg/m^3)	6	1.6	0.5	6	22

Table 4.2: Prototype configurations

The numerical model has been validated comparing the measured normal absorption coefficient with the numerical simulation for different configurations as shown in Figure 6.10 (a-f). The experimental results are in good agreement with the numeric simulation, so the information from the parametric analysis can be used to design an optimised multilayer MPP absorber focusing on broadband absorption at low frequencies.

In order to achieve high broadband absorption, especially at low frequencies, an optimised prototype of a multilayer MPP absorber has been designed by exploiting the results from the previous parametric analysis.

(a)

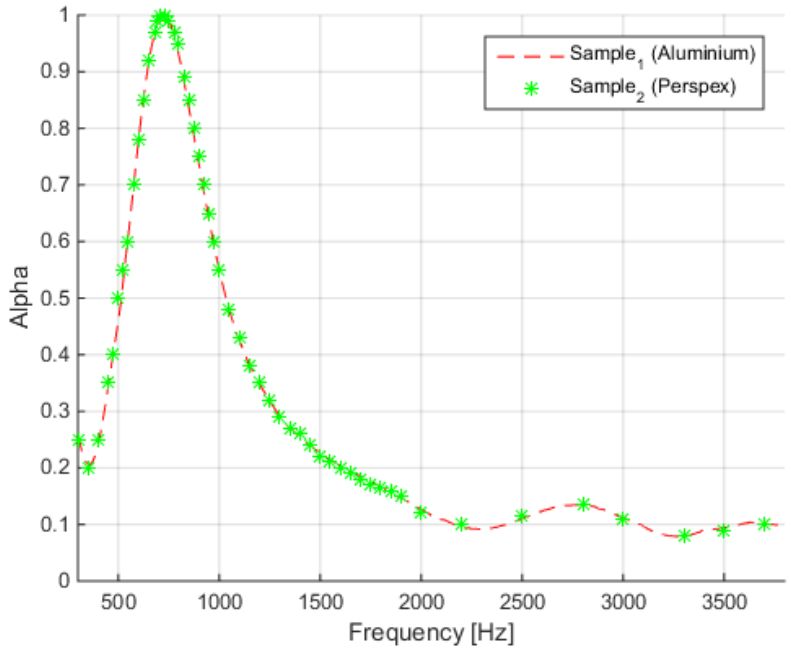

Figure 6.9 (a): Comparison between experimental absorption coefficients related to the Sample_1 (Aluminium) and Sample_2 (Perspex) [n=1; t=1mm; d=1mm; p=1%]

(b)

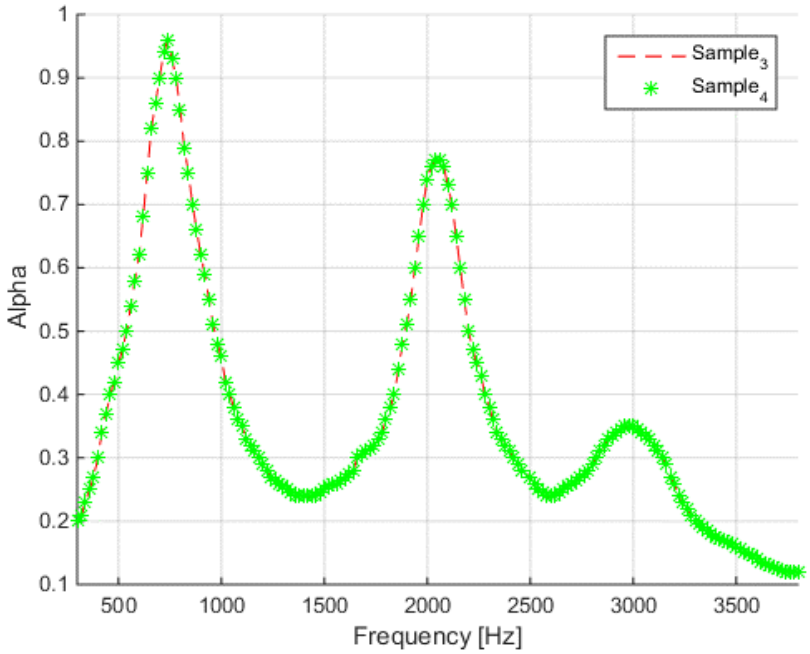

Figure 6.10 (b): Comparison between experimental absorption coefficients related to the Sample_3 (Aluminium) and Sample_4 (Perspex) [n=3; t=1mm; d=1mm; p=1%]

As shown in Figure 6.7, the frequency range covered by a high absorption level is a function of the number of the layers; so in order to achieve the maximum broadband absorption, 6 layers has been considered. By fixing the length of the absorption band, the air gap length between each layer can be optimised in order to achieve the lowest possible frequencies. In this way two factors must be taken into account. First of all, as shown in Figure 6.3, by increasing the air gap depth, lower absorption frequencies were achieved.

. On the other hand, the global size of the absorber is an important design parameter which could be minimised. However, for small depth values there is a decoupling between each resonator and the single resonant peaks which resulted in different and marked absorption peaks. So, a compromised between all those considerations is required to guarantee a smooth and flat broad band absorption at low frequencies. In this case an air gap length of 22mm has been considered. The geometrical parameters of the single layers, perforation ratio, hole diameters and layer thickness are strictly related. Chosen the appropriate thickness to raise the absorption level (Figure 6.4), the combination of perforation ratio and hole dimension needs to be optimized. In particular considering under millimetres thickness high perforation ratio is recommended to increase the absorption. Figure 6.5 shows that for a thickness of 1.5mm and a perforation ratio of 6%, the optimum hole dimeter is 0.5mm. For this value the absorption is maximised over a considerable broadband frequency range. Following this design approach, a 6 layer MPP absorber with a constant airgap length of 22mm between each panel and a hard back at the end (Configuration: Sample_10) has been machined and tested in an impedance tube test ring. Each Perspex layer has 1.6mm thickness, a perforation ratio of 6% with a hole diameter of 0.5mm taking into account that the perforation ratio is a function of the hole diameter square ($p = n\frac{d^2}{D_p^2}$ with D_p the diameter of the prototype) and the minimum holes spacing should be 1 times the hole diameter.

In Figure 6.10(f) the measured normal absorption coefficient is plotted (red line) and compared with the numerical results (blue line) for the 6-layer prototype. The experimental result is in good agreement with the numerical simulation. The

proposed prototype considerably increases sound absorption at low frequencies. A fairly constant absorption level all over 80% over the frequency range of 400-2500 Hz is guaranteed with a local absorption peaks of 99% around the frequencies 450Hz, 1200Hz, 1700Hz. As previously highlighted, each absorber (single perforated layer with the relative air gap) represents a resonant absorber which can be described as a mass vibrating against a spring. The mass is a plug of air in the opening of the perforated sheet and the spring is provided by air enclosed in the cavity. Moreover, the viscous losses within the small orifices can be used to increase absorption. Thus, the increase in sound absorption at low frequencies is correlated to the resonance phenomena of the absorbers coupled with the viscous losses through the holes. Each absorber is characterised by one natural frequency, so adding more absorber in series results in coupling of the resonances which give a broadband absorption. On the other hand, considering a considerable perforation ratio, the mass of the equivalent dynamic system will increase, because the natural frequency is inversely proportion to the mass and the resonances will move to lower frequencies.

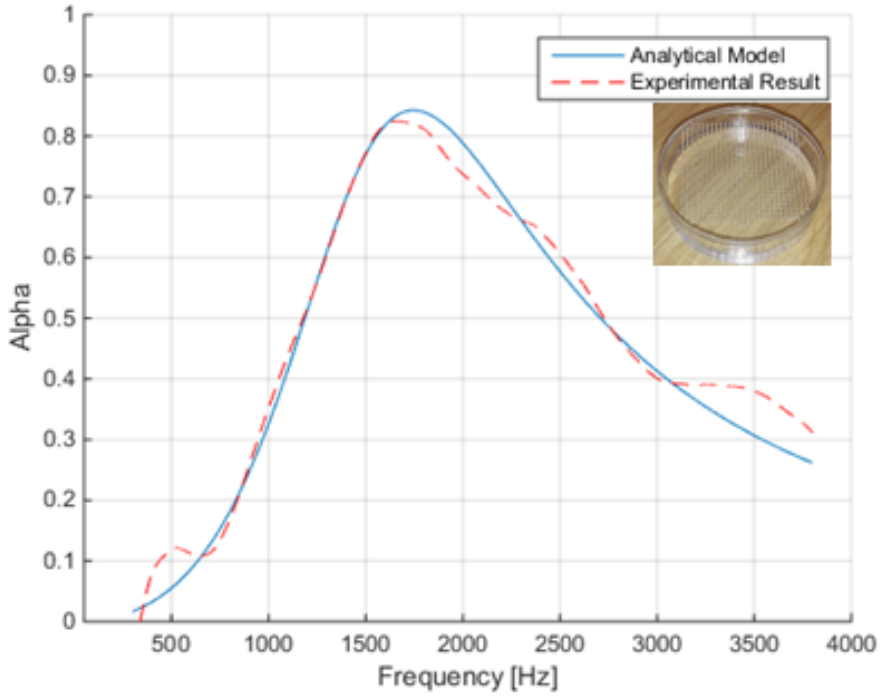

Figure 6.11 (a): Sample_5: 1 layer MPP absorber [t=1.6mm; d=0.5; p=6%; D=22mm]

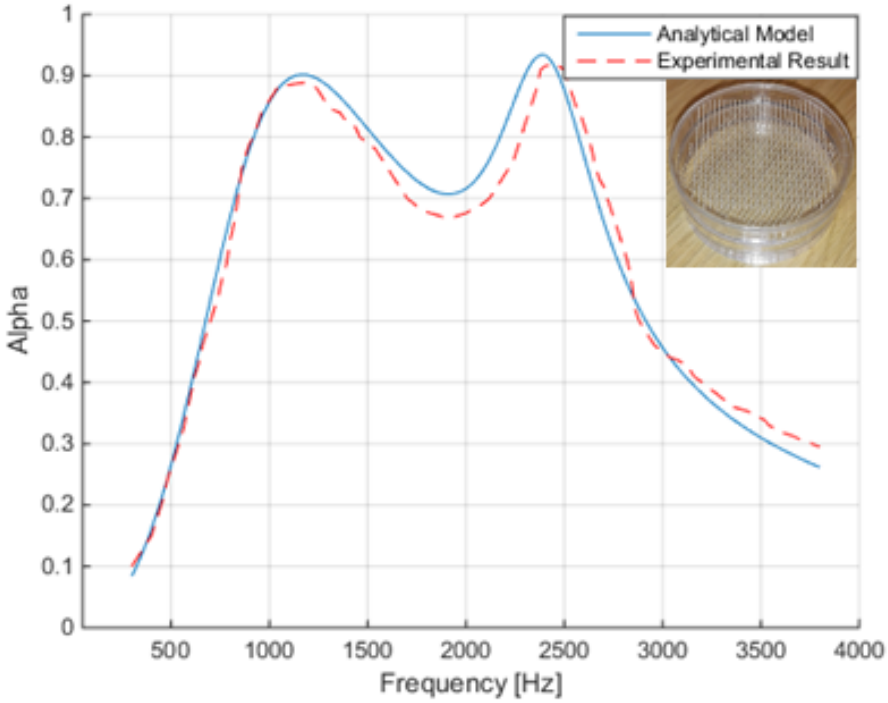

Figure 6.12 (b): Sample_6: 2 layers MPP absorber [t=1.6mm; d=0.5; p=6%; D=22mm]

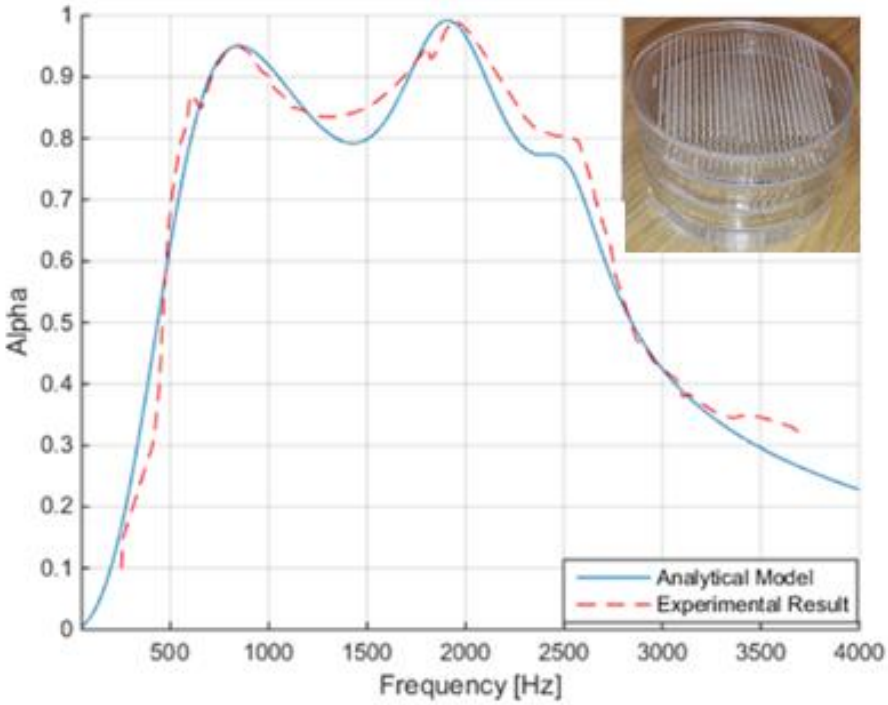

Figure 6.13 (c): Sample_7: 3 layers MPP absorber [t=1.6mm; d=0.5; p=6%; D=22mm]

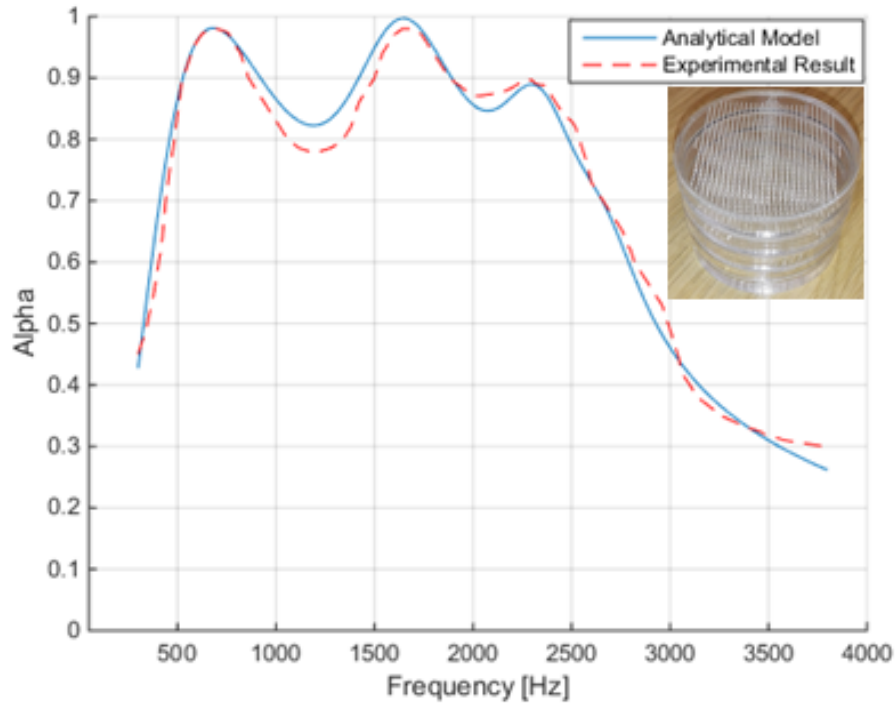

Figure 6.14 (d): Sample_8: 4 layers MPP absorber [t=1.6mm; d=0.5; p=6%; D=22mm]

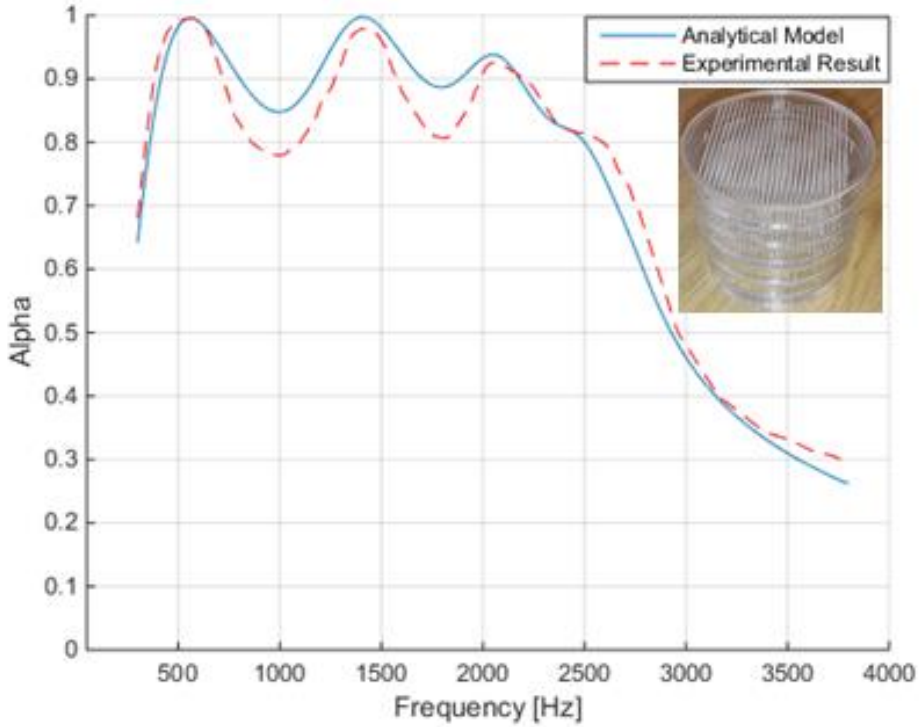

Figure 6.15 (e): Sample_9: 5 layers MPP absorber [t=1.6mm; d=0.5; p=6%; D=22mm]

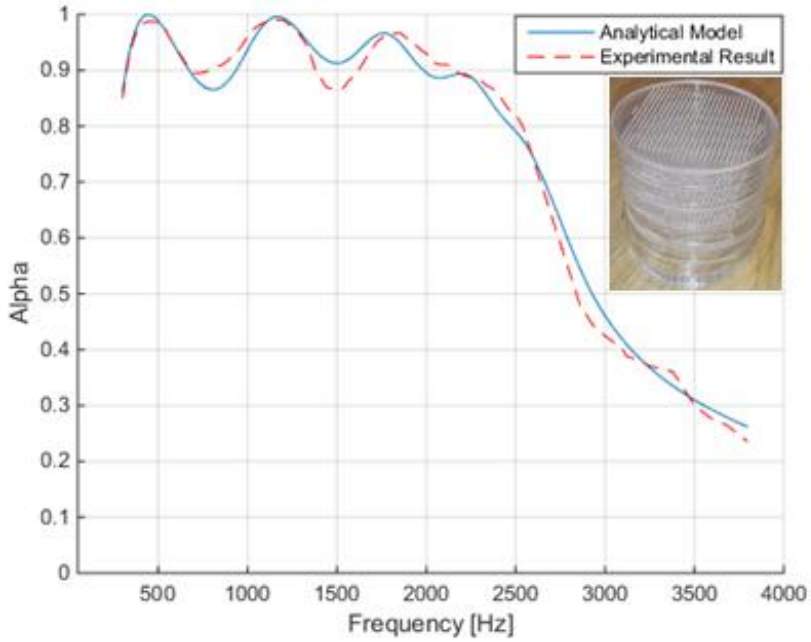

Figure 6.16 (f): Sample_10: 6 layers MPP absorber [t=1.6mm; d=0.5; p=6%; D=22mm]

The perforation ratio can be increased by; enlarging the dimension of the holes or reducing such dimension while adding more perforations on the sheet. Considering the second approach there will be a gain also in the absorption level because of the increment of the viscous loss through smaller holes.

Moreover, considering each absorber as a multiple Helmholtz resonators system, the resonance frequency of such system is inversely proportion to the volume of cavity. Coupling different resonators, the resonance will be a function not only of the relative cavity associated to the single layer but also of all sequential cavities. As a consequence, the sound absorption will increase at lower frequencies.

The proposed prototypes can reach almost a broadband absorption all over 80% at low frequencies where the relevant sound wavelength in air is always 7 times of magnitude larger than the prototype lengths and 10 times of magnitude larger the prototype diameters as reported in Table 4.3.

Sample	Wavelength	Prototype Length	Prototype Diameter
Sample_5	0.23 m	L = λ / 10	L = λ / 10
Sample_6	0.38 m	L = λ / 8	L = λ / 10
Sample_7	0.57 m	L = λ / 8	L = λ / 10
Sample_8	0.69 m	L = λ / 7	L = λ / 10
Sample_9	0.86 m	L = λ / 7	L = λ / 10
Sample_10	1.14 m	L = λ / 7	L = λ / 10

Table 4.3: Sub-wavelength dimensions of MPP Prototypes

In order to study the influence of the perforation geometry a second experimental measurement campaign was carried out. Micro slotted panels were taken into account and compared with the micro perforated panels in terms of sound absorption performance.

First of all the effect of the slots instead of holes has been studied. Keeping constant the perforation ratio, the layer thickness and the air gap length, the hole diameter in the perforated panel is assumed to be the same as the width (*b*) of the slits in the slotted panel; so the slits length (*L*) was changed to match the prescribed perforation ratio (Table 4.4)

Sample		Material	t (mm)	p (%)	b (mm)	L (mm)	d (mm)	D (mm)
Sample_A	MPP	Perspex	2.5	1			1	30
	MSP	Perspex	2.5	1	1	10		30
Sample_B	MPP	Perspex	1.6	6			0.5	30
	MSP	Perspex	1.6	6	0.5	20		30

Table 4.4: Design parameters for the tested micro perforated panels and micro slotted panels

As shown in Figure 6.11 (a) and (b) the experimental measurements verified that the shape of the orifices, holes or slots, does not really affect the shape of the absorption coefficient curve. But, taking into account the equal perforation ratio, using the MSP instead of the MPP absorber there is a slight reduction in sound absorption. As the resistance of the MSP is lower than the MPP, it has a lower contribution to absorption.

(a)Sample A

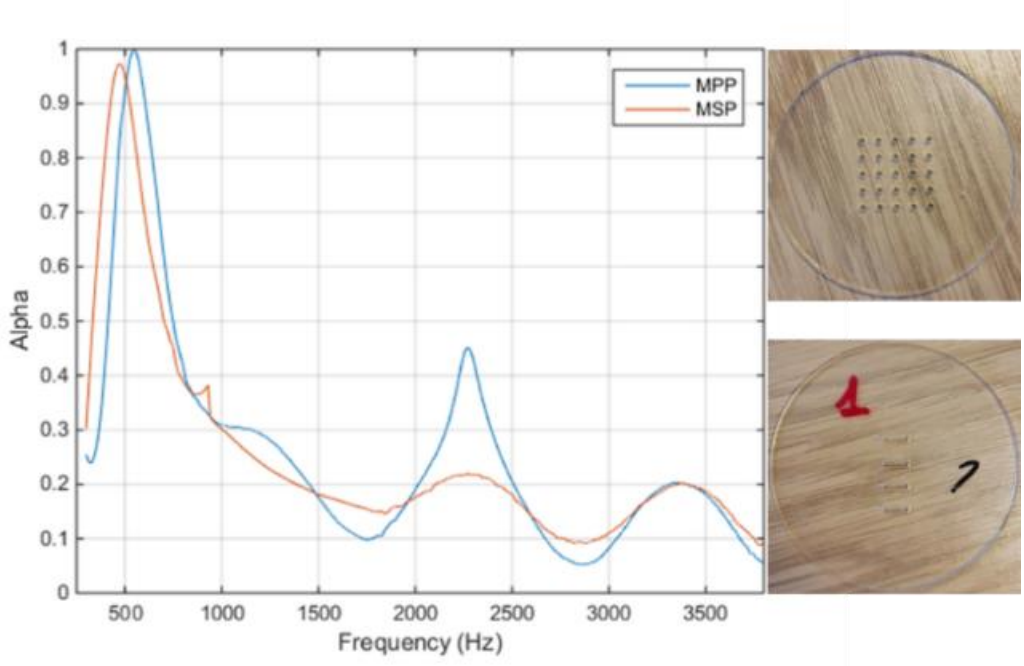

(b)Sample B

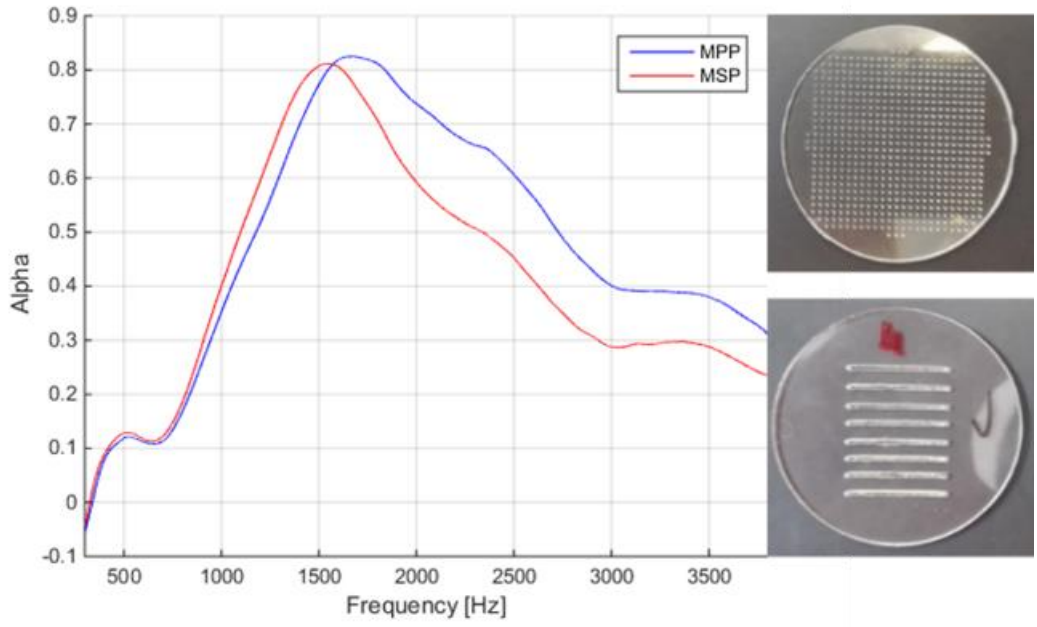

Figure 6.17 (a-b): Comparison between MPP absorber and MSP absorber

The effect of the aspect ratio and the number of slots on the absorption characteristics have been experimental investigated. In both cases the perforation ratio has been kept constant, while the dimensions and the number of the slots have been changed to match the required perforation ratio. The slot aspect ratio (Ar) can be defined as the ratio between the longer side of the slot to its shorter side ($Ar = L/b$). Three slotted panels with different slot dimensions (Table 4.5) have been compared (Figure 6.12), as well as slotted panels with the number of slots (n_s) adjusted between 2 to 4, refer to Table 4.6. The absorption coefficients are plotted in Figure 6.13. As shown in Figure 6.12 and Figure 6.13 the aspect ratio and the slot numbers don't have an important impact on the sound absorption properties for the micro slotted panels. So, if the perforation ratio is chosen as a design parameter and kept constant, the shape and the number of the slots can be designed without any significant changes in the MSP absorption characteristic.

Sample	**Material**	**t [mm]**	**p [%]**	**Ar**	**L [mm]**	**b [mm]**
MSP_1	Perspex	1.6	1	1.25	2.5	2.0
MSP_2	Perspex	1.6	1	5	5.0	1.0
MSP_3	Perspex	1.6	1	20	10.0	0.5

Table 4.5: MSP geometrical parameters with different slot aspect ratios

Sample	**Material**	**t [mm]**	**p [%]**	**Ar**	**n_s**	**L [mm]**	**b [mm]**
MSP_4	Perspex	1.6	1	40	2	20.0	0.5
MSP_5	Perspex	1.6	1	27	3	13.5	0.5
MSP_6	Perspex	1.6	1		4	10.0	0.5

Table 4.6: MSP geometrical parameters with different slot numbers on the sheet

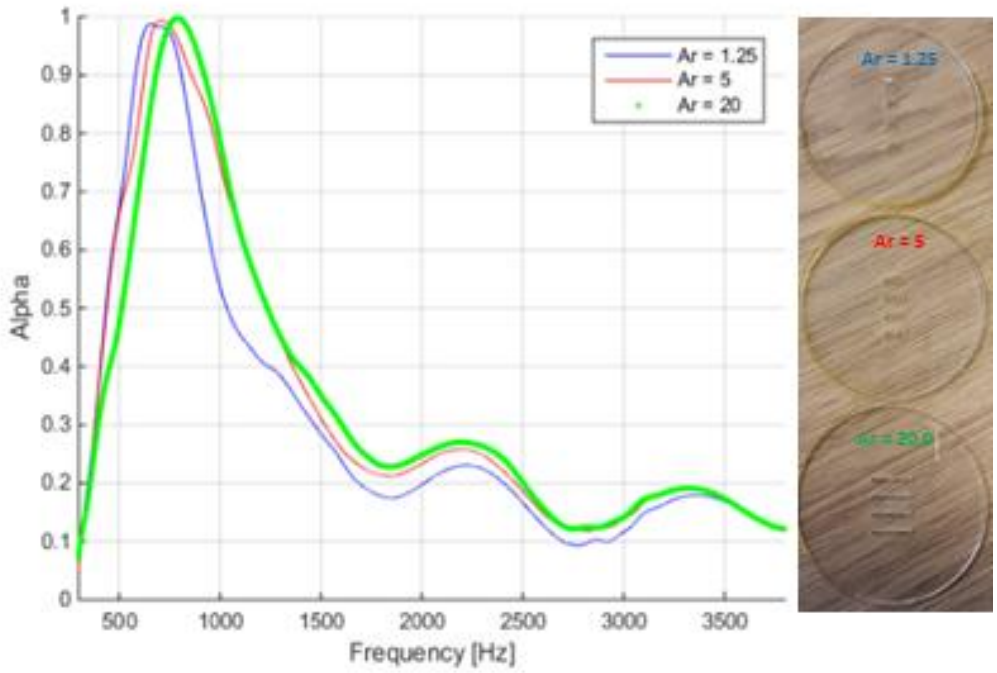

Figure 6.18: Absorption Coefficient for MSP with different aspect ratio [p = 1%, t = 1.6mm, D = 30mm, n_s =4]

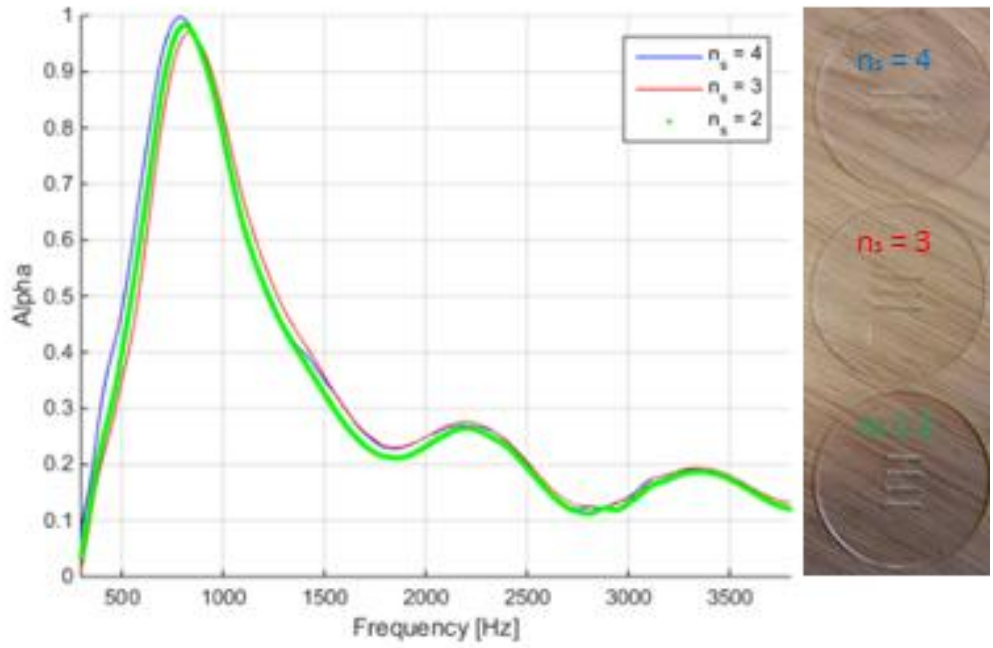

Figure 6.19: Absorption Coefficient for MSP with different slot number [p = 1%, t = 1.6mm, D = 30mm]

Multilayer MSPs have been tested in order to investigate the impact of the number of layers on the sound absorption (Figure 6.14). The geometrical parameters are constant through the layers, in particular each panel present a thickness of 1.6mm, perforation ratio of 6%, slot length of 30.5 mm, slot width of 0.5 mm and an air gap of 22mm. Each MSP has been designed to have the same geometrical parameters of the previous MPP, so in Figure 6.14(f) the absorption coefficients of 6 layers MPP and 6 layers MSP have been compared. The effect of the number of layers on the MSP is comparable with that of the MPP. A multilayer approach leads to a gain on the absorption level at low frequencies together with a broadband absorption proportional to the number of added layers. The absorption level is slightly less in the MSP. Considering a continuous slot instead of multiple micro holes dislocated all around the sheet, the viscous loss associate to the air passing through the perforations will be less, with consequent decreasing of the absorption level.

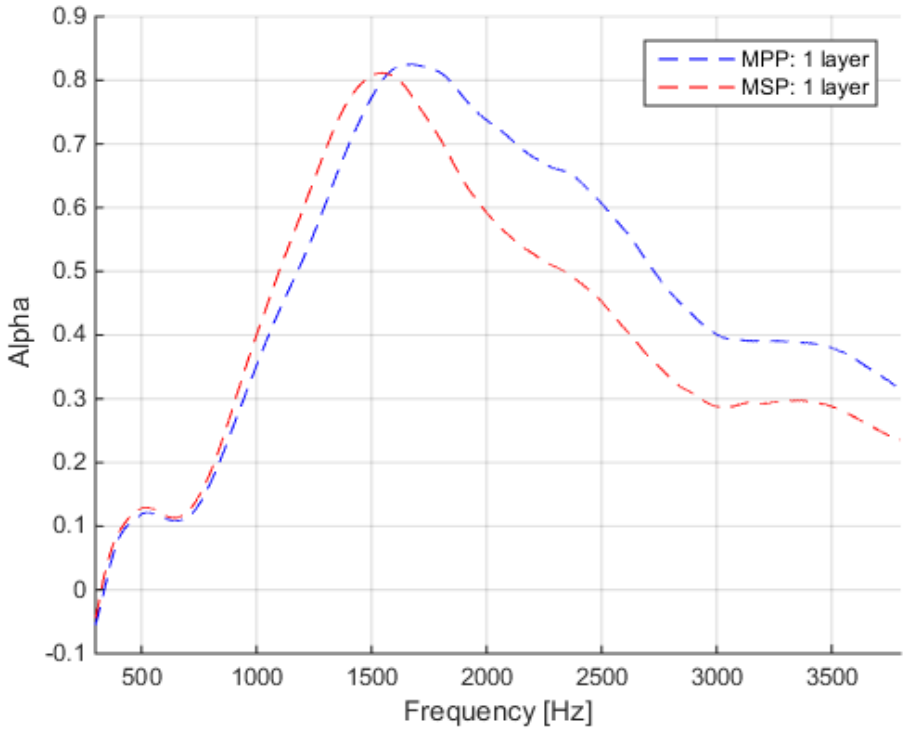

Figure 6.20 (a): comparison between measured absorption coefficients of multilayer MPP and multilayer MSP: 1 layers MSP-MPP [t=1.6mm; d=b=0.5; p=6%; D=22mm]

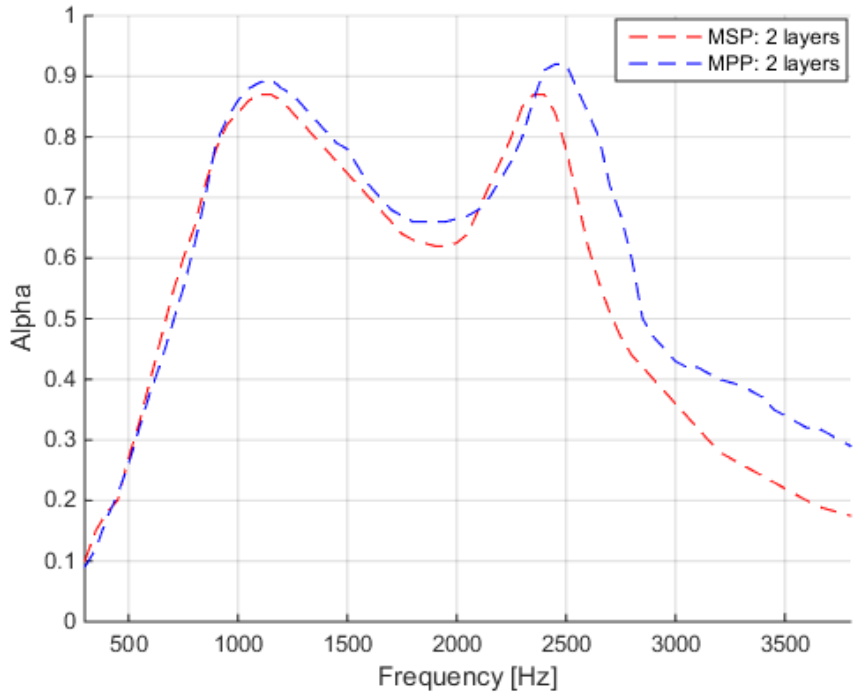

Figure 6.21 (b): comparison between measured absorption coefficients of multilayer MPP and multilayer MSP: 2 layers MSP-MPP [t=1.6mm; d=b=0.5; p=6%; D=22mm]

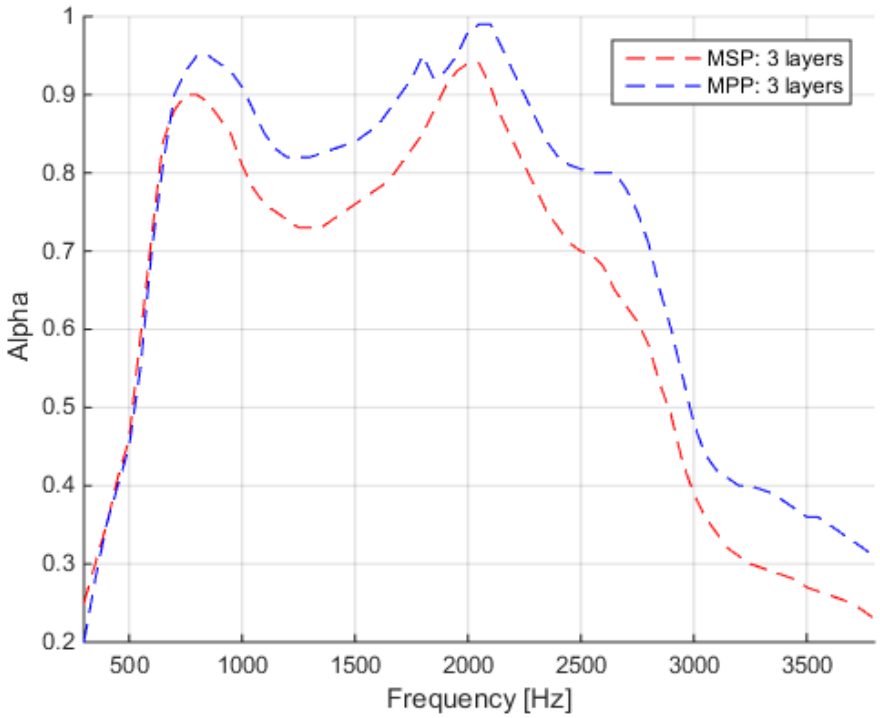

Figure 6.22 (c): comparison between measured absorption coefficients of multilayer MPP and multilayer MSP: 3 layers MSP-MPP [t=1.6mm; d=b=0.5; p=6%; D=22mm]

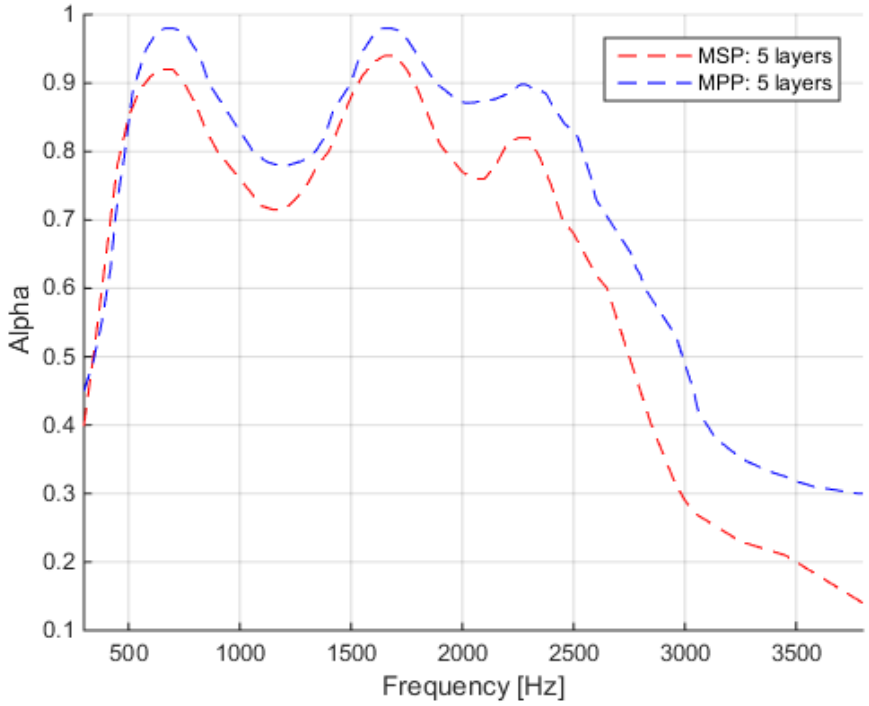

Figure 6.23 (d): comparison between measured absorption coefficients of multilayer MPP and multilayer MSP: 4 layers MSP-MPP [t=1.6mm; d=b=0.5; p=6%; D=22mm]

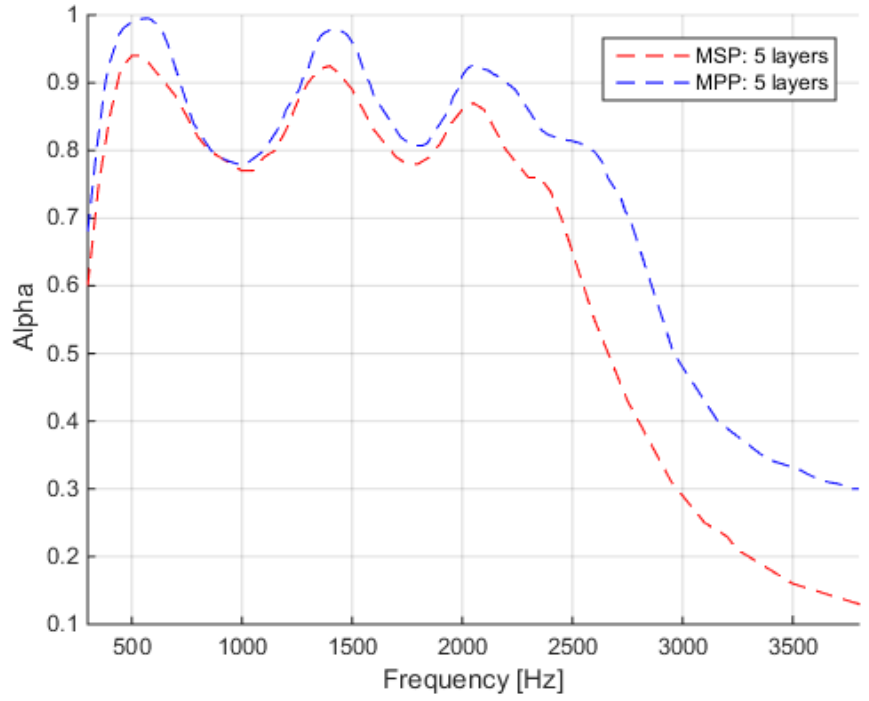

Figure 6.24 (e): comparison between measured absorption coefficients of multilayer MPP and multilayer MSP: 5 layers MSP-MPP [t=1.6mm; d=b=0.5; p=6%; D=22mm]

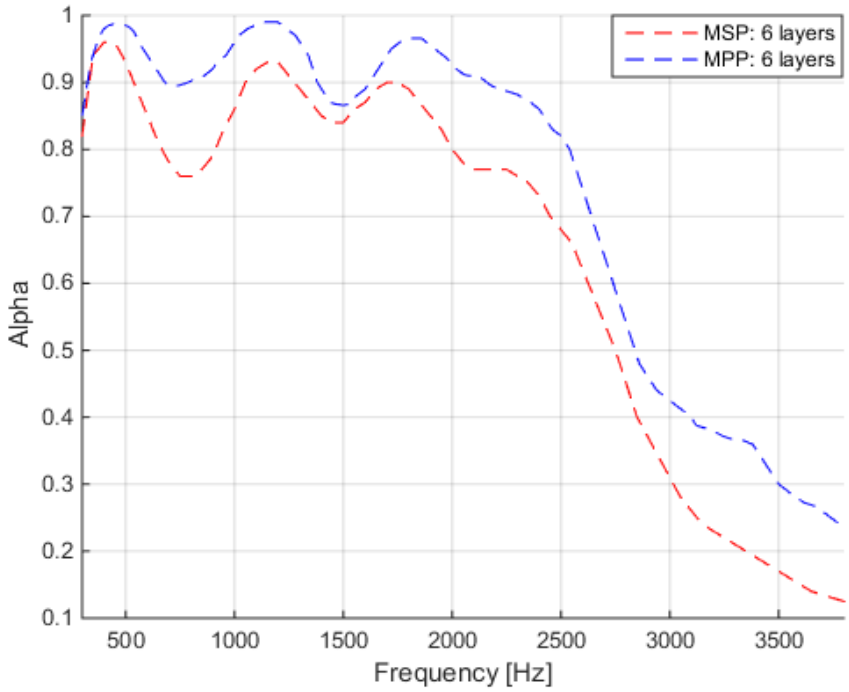

Figure 6.25 (f): comparison between measured absorption coefficients of multilayer MPP and multilayer MSP: 6 layers MSP-MPP [t=1.6mm; d=b=0.5; p=6%; D=22mm]

5 Conclusion

Looking for an efficient sound absorbing structure, a multiple layers MPP absorber was developed consisting of six plastic micro perforated panels placed in series with air gap in between and a rigid backed wall at the end. An analytical model to design a multiple MPP absorber was developed by optimising the number of layers, the perforation ratio, the diameter of the holes, the layer thickness and the air gap depth in order to guarantee a high and constant broadband absorption at low frequencies. The optimised prototype was manufactured and tested in an impedance tube test ring by measuring the absorption coefficient in a frequency range between 250-4000 Hz. The experimental results show how the prototype guarantees a constant high absorption in a frequency range between 400Hz to 2000Hz, with the absorption level over 90% in such frequency range. Moreover, the proposed prototypes represent a sub-wavelength absorbers because the wavelength in air at

low frequencies is 7 times of magnitude larger than the global length of the prototypes and 10 times of magnitude larger than the diameter of the prototypes.

REFERENCES

[1] K. Sakagami, M. Morimoto, W. Koike. “A numerical study of double-leaf microperforated panel absorbers”. Applied Acoustics, 67: 609-619 (2006).

[2] K. Sakagami, M. Morimoto, W. Yairi. “A note on the effect of vibration of a microperforated panel on its sound absorption characteristics”. Acoust Sci & Tech, 26:204-7 (2005).

[3] D.Y. Maa. “Theory and design of microperforated panel sound absorbing construction”. Sci Sin, 18:55-71 (1975).

[4] D.Y. Maa. “Microperforated panel wideband absorbers”. Noise Cont Eng Journal, 29: 77-84 (1987).

[5] D.Y. Maa. “Potential of microperforated panel absorber”. Journal Acoust Soc Am, 104: 2861-6 (1998).

[6] C. Wang, L.H. Huang. “On the acoustic properties of parallel arrangement of multiple micro-perforated panel absorbers with different cavity depths”. Journal Acoust. Soc. Am, Vol.130, No1, (2011).

[7] Y.Y.Lee, E.W.M.Lee. “Sound absorption of a finite flexible micro-perforated panel backed by an air cavity”. Journal Sound and Vibration, 208:227-243, (2005).

[8] Y. Lu, X. Li, J. Tian, W. Wei. “The perforated panel resonator with flexible tube bundle and its acoustical measurements”. Proceeding of Inter-Noise, (2001).

[9] Q. Zhang, Y. Lu, J. Yang, X. Wei. “Design and experiment study of the perforated panel resonance absorber with tree like tube bundles”. Noise and Vibration Control, 29:253:256, (2009).

[10] Y. Iwan. “New sound absorption improvement strategy for QRD element”. Proceeding of ICSV20, 7-11, (2013).

[11] D. Li, D. Chang, B. Liu, J. Tian. “A perforated panel sound absorber for low frequencies”. Proceeding of ICSV22, 12-16, (2015).

[12] W. Guo, H. Min. “A compound micro-perforated panel sound absorber with partitioned cavities of different depths”. IBPC, 78: 1617-1622, (2015).

[13] J. Pan, J. Guo, C. Ayres. “Improvement of Sound Absorption of Honeycomb panels”. Proceeding of Acoustics 2005.

[14] K. Sakagami, I. Yamashita, M. Yairi, M. Morimoto. “Effect of honeycomb on the absorption characteristics of double-leaf microperforated panel (MPP) space sound absorbers”. Noise Control Eng. J. 59.4:363 (2011).

[15] K. Sakahami, Y. Fukutani, M. Yari, M. Morimoto. “Sound absorption characteristics of double-leaf structure with an MPP and a permeable membrane”. Applied Acoustics, 76: 28-34, (2014).
[16] K. Sakahami, M. Morimoto, M. Yari. “A note on the relationship between the sound absorption by microperforated panels and panel/membrane type absorbers”. Applied Acoustics, 70: 1131-1136, (2009).
[17] X.L. Gai, X.H. Li, B. Zhang, T. Xing, J.J. Zhao, Z.H. Ma. “Experimental study on sound absorption performance of microperforated panel with membrane cell”. Applied Acoustics, 110: 241:247, (2016).
[18] P.M. Morse, U. Ingard. “Theoretical Acoustic”. McGraw-Hill, pp. 460-463, 1968.
[19] I. B. Crandall, “Theory of Vibration System and Sound”, Van Nostrand, 1926.
[20] K. Sakagami, K. Matsutani, M. Morimoto, “Sound absorption of a double-leaf micro-perforated panel with air-back cavity and a rigid-back wall: Detailed analysis with Helmholtz-Kirchoff integral formulation”, Applied Acoustics 71, 411-417, (2010).
[21] American Society for Testing and Materials, “ASTM E 1050-98, Standard test method for impedance and absorption of acoustical materials using a tube, two microphones and a digital frequency analysis system”, (1998).

Chapter 7

Metamaterial based on Membrane-Type resonator for low frequencies sound absorption

In the previous Chapter we proposed an acoustic absorber prototype based on multi-layers Microperforated (MPP) structure which shows almost perfect absorption in a wide frequency range from 300 Hz to 2000Hz. However, the broadening absorption at low frequency is strictly related to the resonant backed cavity depth and as a consequence to the global thickness of the absorber. In the specific case, the thickness for the proposed absorber is 100mm. Membrane-type metamaterials (MMA) have been recently introduced and deeply studied to achieve better absorption at lower frequency minimizing the global size of the absorber. Many research works have demonstrated how these devices represent a good subwavelength device for low frequencies sound absorption, however it is still struggling the broadening absorption. The basic membrane or plate type metamaterials consist of an elastic membrane/plate with an enclosed air cavity. As for the MPP absorbers, the MMA can be easily described in first instance as a single degree of freedom resonant system, where the mass effect is associated to the membrane/plate mass and the stiffness effect is related to the air mass into

the backed cavity. In other words, these devices behave as a piston, where at the resonance frequency the membrane/plate move in phase with the air cavity mass. As result, the sound absorption coefficient shows a single narrow peak at the resonance frequency. A particular configuration of membrane-type metamaterial has been proposed to generate multiple resonance frequencies in the considered frequency range. It consists of prestressed membrane with decorated plates [69,70,71,73,74]. The relative displacement between the membrane and plates generates multiple resonances frequencies which leads to multiple peaks in the absorption profile. However, these are really narrow peaks and quite far from each other in frequency. So, for example the unit cell can achieve low frequencies absorption at 170 Hz and 340 Hz, but it is a single frequency absorption. To achieve broadband sound absorption, array of multiple unit cells needs to be combined together, as suggested in Figure 2.18 and Figure 2.19. If the thickness of the unit cell is 28mm, when we consider an array of multiple unit cells, the global thickness increases to 56mm. Other membrane-type metamaterials have been proposed with decorated membranes which generate "hybrid resonance" [75] or "degenerate resonance" [76]. If they provide high sound absorption below 400Hz with a global thickness around 30mm, their absorption profile is still characterized by single narrow peak.

In this research work a membrane type metamaterial unit cell is proposed which allows to achieve broadband absorption in a low frequency range between 250Hz and 400Hz with a global thickness of 23mm.

We demonstrate how optimizing the geometrical parameters and the material properties of the membrane we can induce the membrane-type metamaterial absorber to behave not as single degree of freedom system, but as a multi degree of freedom system. Multiple resonance frequencies can be arisen due to the mutual interaction between the structural dynamic response of the membrane and acoustic dynamic response of the acoustic chamber. In fact, the vibration of plate will be perturbed by the fluid pressure loading and the acoustic field in the cavity will be influenced by the dynamic response of the plate.

In particular, out of plane displacement of the plate generates an acoustic volumetric force acting on the acoustic field and exciting the higher order acoustic modes in the chamber. On the other hand, the acoustic modes generate a non-uniform pressure distribution acting on the membrane. As result, the absorber doesn't behave as single degree of freedom system, as for the common membrane-type metamaterials, but as multi degree of freedom system.

In the published manuscript, a numerical model based on the fluid structural interaction is proposed to study the absorption mechanism behind the proposed metamaterial unit cell solving the coupled structural-acoustic dynamic equations.

The FE model was implemented in Ansys Workbench 18.1 environment (student license). Different element types were used to model the structural part (membrane) and the acoustic one (acoustic bodies). The structural parts of the FE model, which include the unit cell membrane, is meshed using higher order 3-D 20-node solid element (SOLID186) that exhibits quadratic displacement behaviour. The element is defined by 20 nodes having three translational degrees of freedom per node. The element supports plasticity, hyperelasticity, creep, stress stiffening, large deflection, and large strain capabilities. It also has mixed formulation capability for simulating deformations of nearly incompressible elastoplastic materials, and fully incompressible hyperelastic materials. The acoustic bodies are then meshed using 3D 20-nodes FLUID220 type element which exhibits quadratic pressure behaviour and it is suitable fluid-structure interaction problems.

The structural element size is chosen to accurately describe the high order mode shapes of the excited membrane. In order to get a regular and symmetric mesh distribution the same number of elements is applied on the edge of the membrane. Because of the analysis type is a harmonic analysis, a mesh convergence check is performed at the maximum frequency of the working frequency range (800 Hz) using the average membrane displacement in the out of plane direction as reference function. In Figure 7.1 the out of plane displacement as a function of the number of elements on the membrane edge. According with Figure 7.1, the structural element size is defined as 1.2mm (35 elements per edge).

Regarding the acoustic body, the limitation of 12 elements pre wavelenght need to be guaranteed for the acoustic meshing in order to define a mesh grid enough to capture the acoustic mode shapes and guarantee a plane wave condition. In this case two different mesh convergence analyis are performed to define the element size on the sound wave propagation direction and on the cross section of the acoustic bodies respectivelly. As for the structural convergecne check, the maximum frequency on the considered frequency range is used and the average upstream and downstram pressure are used as reference function. Figure 7.2 shows the pressures as a function of the element number along the sound wave propagation direction. According with Figure 7.2 30 element on the sound propagation direction are considered with an equivalet element size of 16mm foe the upstream acoustic body and 0.6mm for the resonator chamber. Figure 7.3 shows the pressure upstream and downstream as a function of the element number in the cross section of the acoustic body. Also in this case 35 element per edge (1.2mm) are defined on the acoustic bodies cross section. such simmetric and fine mesh allows to pick up all the higher order acoustic modes in the frequency range of interest.

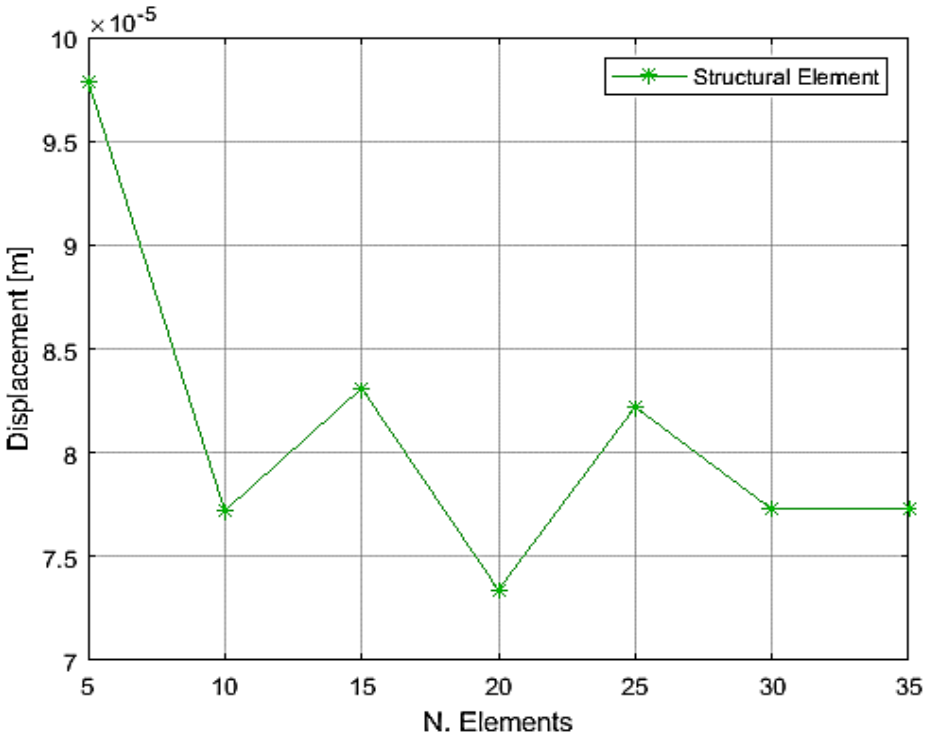

Figure 7.1. Structural element mesh convergence analysis

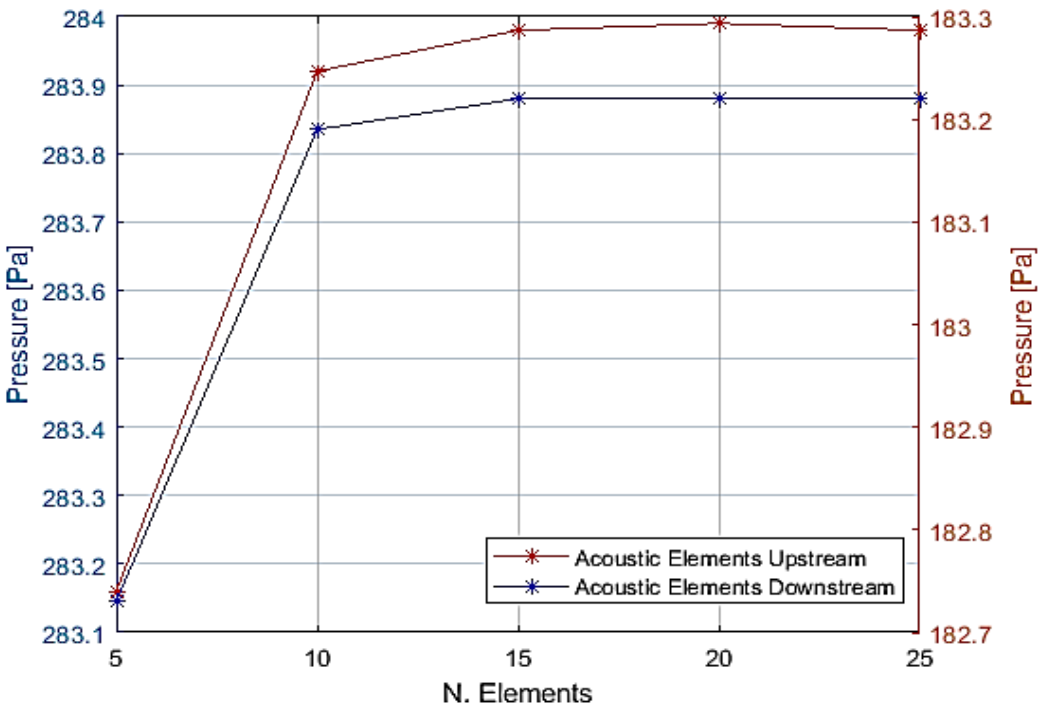

Figure 7.2. Acoustic element mesh convergence analysis along the sound wave direction

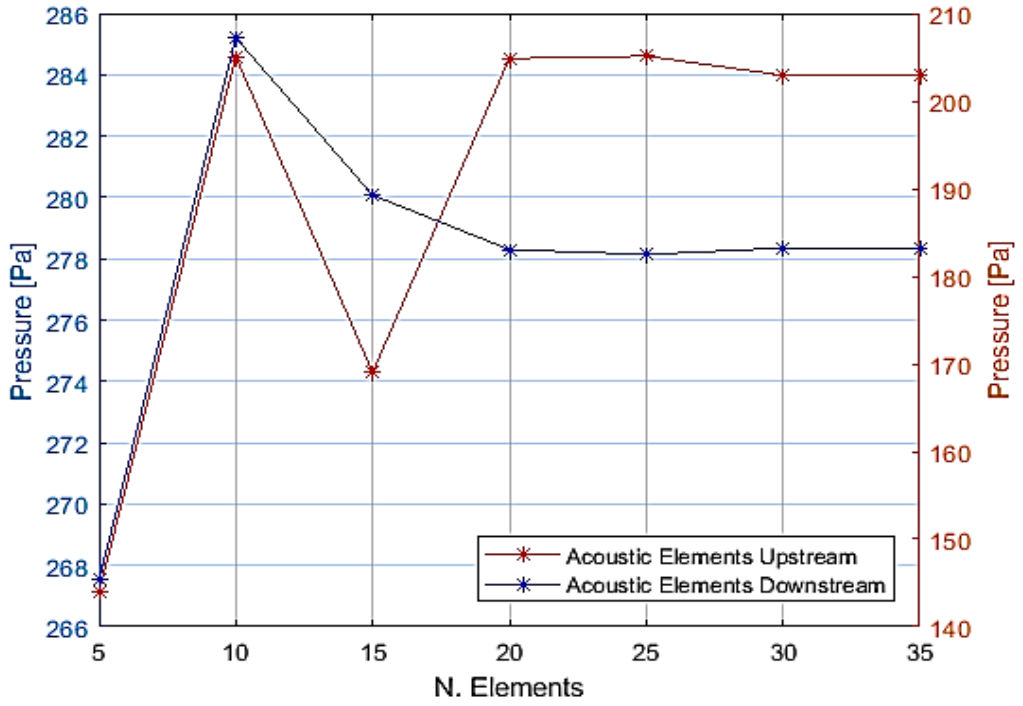

Figure 7.3. Acoustic element mesh convergence analysis on the acoustic bodies cross section

An optimized unit cell prototype is then presented and tested in an impedance test rig. This represent a deeply subwavelength structure of 23mm thickness ($^1/_{58}$ λ) which show two main absorption peaks at 268Hz and 369 Hz with the 80% of sound absorbed and an averaged broadband absorption over 50% of absorption between 250Hz and 400Hz.

7.1 List of Symbols

The symbols and their explanation used in Chapter 7 for the mathematical notation are reported below:

Symbol	Description
[M], [C], [K]	Structural Mass, Damping and Stiffness Matrix
[Q], [D], [H]	Acoustic Inertia, Damping and Stiffness Matrix
{w},{p}	Nodal Displacement and Pressure vector
{f}	Structural Nodal Load vector
{q}	Acoustic Volumetric Load vector
[S]	Acoustic-Structural Coupling Matrix
H_i	Acoustic Transfer Function of incident pressure component
H_r	Acoustic Transfer Function of reflected pressure component
H_{12}	Acoustic Transfer Function of combined incident-reflected component
k_0	Wave number
s	Microphone Spacing
L	Distance between sample and 2nd Microphone
c	Speed of sound in air
R	Reflection Coefficient
α	Absorption Coefficient
E	Elastic Modulus of Material
ρ_p	Density of membrane
ρ	Density of air
t	Thickness of membrane
D	Length of air cavity
Δp	Difference between membrane upstream and downstream pressure
m	Mass density per unit area of the membrane

7.2 Journal Paper Reference Details

The research work presented in this chapter is part of published journal paper which the reference details are as follow:

"Broadening sound absorption coefficient with hybrid resonances"

Authors:
Fabrizio Bucciarelli - Department of Mechanical Engineering, University of Bath, Bath, UK.
Michele Meo - Department of Mechanical Engineering, University of Bath, Bath, UK.

Corresponding Authors: Michele Meo – m.meo@bath.ac.uk
Journal: Applied Acoustics, Volume 160, pages 1-11,(2020) - DOI: 10.1016/j.apacoust.2019.107136

The Statement of Authorship From and the paper a reported next.

This declaration concerns the article entitled:	
Broadening sound absorption coefficient with Hybrid Resonances	
Publication status (tick one)	
Draft manuscript	
Submitted	
In review	
Accepted	
Published	✓

Candidate's contribution to the paper (detailed, and also given as a percentage).	
The candidate contributed to/ considerably contributed to/predominantly executed the…	
Formulation of ideas:	80% I proposed the initial and the methodology and the experimental/manufacturing approach. The idea was discussed and supported by Prof. Meo.
Design of methodology:	100% I designed and developed the numerical model used in this research work and the experimental tested.
Experimental work:	100% I worked in the manufacturing of the prototype. I designed and machined the test rig used in all the test campaigns. I performed the tests, collected and post processed the data reported in the paper.
Presentation of data in journal format:	80% I worked on the paper structure, figures and plots. I wrote the paper drafts and provided the answers to the reviewer's comments. Prof. Meo provided the first review of the paper and he supported in the submission and publication process.
Statement from Candidate	
This paper reports on original research I conducted during the period of my Higher Degree by Research candidature.	

Signed		**Date**	05/01/2020

Broadening Sound Absorption Coefficient with Hybrid Resonances

F. Bucciarelli[1], M. MEO[1,a]

[1] Department of Mechanical Engineering, University of Bath, Bath, UK

[a] m.meo@bath.ac.uk

Abstract

In the last years, a great research effort has been focused on the noise mitigation at low frequencies. Membrane-type acoustic metamaterials (AMM) are one of the most promising solutions to meet the growing demand for low frequency sound absorbers. Typically, acoustic membrane absorbers require large back cavities to achieve low frequency sound absorption, which is usually categorised by a single narrow absorption peak. This paper presents an acoustic resonator unit cell, comprising of a thin elastic silicone plate with an air gap cavity with broadband absorption in a frequency range between 250-400Hz. The broadband and multiple peak sound absorption showed by the proposed resonator is due to hybrid resonances which occur in the frequency range due to coupling of the structural dynamic response of the plate with the acoustic response of the air cavity. A numerical model based on acoustic-structural interaction, validated for experimental data, has been used to explain how the broadening gain in the sound absorption level is strictly related to the hybrid resonances of the unit cell resonator. We demonstrated that hybrid resonances are a function of the geometrical parameters and the ratio between the Young's modulus and the density of the material plate, thus the proposed resonators absorption frequency range is tuneable at low frequencies allowing a wider broadband not achievable with acoustic membrane absorbers.

1. Introduction

Noise control and reduction has become an important factor in many fields, along with an increased focus on sound absorption and sound absorbing materials. In particular, researchers have concentrated on improving the performance of acoustic metamaterial at low frequencies. Usually sound absorption is the result of the dissipation of sound energy through different physical mechanisms, such as viscous dissipation. Sound is associated with small air displacement velocities and thus sound dissipation can be expressed as a quadratic function of the frequency [1]. As a consequence, absorption at low frequencies is considerable weaker compared to higher frequencies; this highlight one of the main limitations of porous absorbers. Another important parameter associated to the dissipated energy is the impedance mismatch between the air and the solid, as the total sound absorption is low if most of the incident sound wave is reflected at the solid-air interface. To diminish effects of impedance mismatch many researchers propose microperfored panels (MPP), which use both; the concept of resonance to dissipated the sound energy and designed back-cavities to better impedance match with air over a desired frequency range. MPPs are generally tuned around a resonance frequency, so they are characterized by a single narrow absorption peak around such frequency [2-3]. In order to overcome single absorption peaks, many approaches have been presented. Parallel or series arrangement of multiple MPP absorbers with different cavity depths shows better absorption properties when compared with single MPP absorber [4-5-6]. Different research work tried to combine MPPs with honeycomb structures [7-8] or with elastic membranes [9-10] which showed absorption increases over larger frequency ranges. In any case, the absorption performance of MPP absorbers are strictly related to the geometrical properties and broadband absorption at low frequencies can only be achieved with high absorber thickness which represents a considerable engineering constrain. This has led the researchers to develop new acoustic metamaterials (AMM) [11] with the aim of achieving negative effective modulus and/or negative effective density. A particular type of AMMs membranes and plate type acoustic metamaterial which have relatively

simple geometry and are generally light-weight and smaller compared with other absorbers [12]. Yang [13] first proposed a membrane-type AMM composed by a pre-stressed membrane decorated with an attached mass which allowed for double peaks in the transmission curve, related to the eigenmodes frequencies, and one dip in between due to the anti-resonance because the two eigenmodes were excited with opposite phase. . The effect of the pretension, the mass, the geometry and the number of the attached masses has also been investigated by Naify [14-15]. Mei proposed a fixed rectangular membrane decorated with semi-circular iron platelets backed with an aluminium reflector which could yield almost 100% absorption at low frequencies within a narrow band. This so called "dark AMM" [16] converts the sound energy into elastic energy through a flapping motion of the platelets, while resonance frequencies where peak absorption occurs can be tuned by adjusting the weight of platelets. Ma [17] presented a membrane –type metasurface comprised of a circular membrane with a circular attached mass with sealed gas behind. In this case, a narrow peak with 50% absorption was achieved at low frequencies because the resonator surface became impedance-matched to air at certain frequencies, (due to hybrid resonances). Whilst these AMM induce negative effective density, Yang [18] proposed a new concept which showed both negative effective density and negative effective bulk modulus. When two membranes (top and bottom) each decorated with a mass are connected to a ring and fixed to a sidewall, two main resonances are identified: monopolar and dipolar resonances. In the frequency range where monopolar and dipolar resonances overlap double negativity can be achieved with consequent narrow absorption peaks at the resonance peaks.

Membrane or plate type unit cells proposed until now allow good sound absorption at low frequencies, however broadband absorption cannot be achieved because the narrow absorption peaks which characterized such absorber occurs around the resonance of the resonator itself.

In this paper, a membrane-type unit cell acoustic metamaterial is proposed which guarantees a low frequency broadband absorption in the frequency range 250-400 Hz with two main absorption peaks of 80% at 268Hz and 369 Hz. The unit cell

includes a silicone membrane fixed on a rigid frame with an air cavity behind. A prototype has been manufactured and tested in an impedance tube test rig. Also, a numerical model is presented based on the acoustic-structure response in terms of the combination of structural and acoustic mode shapes. The numerical model was validated through experimental data and used to understand the reasons behind the multiple peaks and broadband absorption of the AMM unit cell.

2. Theoretical Framework

Considering an elastic and flexible plate with an enclosed cavity, then the vibration of plate is perturbed by the fluid pressure loading and the acoustic filed in the cavity is influenced by the dynamic response of the plate. The coupled structural-acoustic response of the system can be explained in terms of a combination of structural and acoustic mode shapes.

The structural flexural vibration of flat thin plate can be described in the finite element matrix formulation, by the *n* ordinary differential equations [19-20-21]

$$[\boldsymbol{M}]\{\ddot{\boldsymbol{w}}(t)\} + [\boldsymbol{C}]\{\dot{\boldsymbol{w}}(t)\} + [\boldsymbol{K}]\{\boldsymbol{w}(t)\} = \{\boldsymbol{f}(t)\} \quad (1)$$

where $[\boldsymbol{M}], [\boldsymbol{C}], [\boldsymbol{K}]$ are respectively the global mass, damping and stiffness matrices, while $\boldsymbol{w}(t), \boldsymbol{f}(t)$ are the column vectors with the nodal degrees of freedom and the nodal excitations generated by the transverse forces acting on surface elements.

$$[\boldsymbol{Q}]\{\ddot{\boldsymbol{p}}(t)\} + [\boldsymbol{D}]\{\dot{\boldsymbol{p}}(t)\} + [\boldsymbol{H}]\{\boldsymbol{p}(t)\} = \{\boldsymbol{q}(t)\} \quad (2)$$

where $[\boldsymbol{Q}]$, $[\boldsymbol{D}]$, $[\boldsymbol{H}]$, are the global acoustic inertia, damping and stiffness matrices, while $\boldsymbol{p}(t)$ is the column vector of the nodal pressure ($\{\boldsymbol{p}\} = -\rho\left\{\frac{\partial \Phi}{\partial t}\right\}$, with Φ the velocity potential function, ρ the fluid density) and $\boldsymbol{q}(t)$ is the column vector of nodal excitations generated by the volumetric sound sources into the cavity.

However, in order to model the response of a structural-acoustic coupled system, two additional terms must be added to equations (1) and (2) which take into account

the acoustic-structural interaction. First, the transverse displacement of the plate produces volumetric acoustic excitation acting on the acoustic cavity, while the sound pressure represents the distributed force acting on the plate. So, considering the virtual work done by the plate displacement on the acoustic cavity and the virtual work done by the acoustic pressure on the plate, equations (1) and (2) can be written as

$$[\boldsymbol{M}]\{\ddot{\boldsymbol{w}}(t)\} + [\boldsymbol{C}]\{\dot{\boldsymbol{w}}(t)\} + [\boldsymbol{K}]\{\boldsymbol{w}(t)\} + [\boldsymbol{S}]\{\boldsymbol{p}(t)\} = \{\boldsymbol{f}(t)\} \tag{3}$$

$$[\boldsymbol{Q}]\{\ddot{\boldsymbol{p}}(t)\} + [\boldsymbol{D}]\{\dot{\boldsymbol{p}}(t)\} + [\boldsymbol{H}]\{\boldsymbol{p}(t)\} + [\boldsymbol{R}]\{\ddot{\boldsymbol{w}}(t)\} = \{\boldsymbol{q}(t)\} \tag{4}$$

where $[\boldsymbol{S}]$ is the global acoustic-structural coupling matrix, while $[\boldsymbol{R}]$ is the structural-acoustic coupling matrix. Since the reciprocity [23], the two coupling matrices are related such that $[\boldsymbol{S}] = [\boldsymbol{R}]^T$ and the dynamic response of the structural-acoustic coupled system can be described solving the system equations

$$\begin{bmatrix} [\boldsymbol{M}] & [\boldsymbol{0}] \\ -[\boldsymbol{S}]^T & [\boldsymbol{Q}] \end{bmatrix} \begin{Bmatrix} \{\ddot{\boldsymbol{w}}(t)\} \\ \{\ddot{\boldsymbol{p}}(t)\} \end{Bmatrix} + \begin{bmatrix} [\boldsymbol{C}] & [\boldsymbol{0}] \\ [\boldsymbol{0}] & [\boldsymbol{D}] \end{bmatrix} \begin{Bmatrix} \{\dot{\boldsymbol{w}}(t)\} \\ \{\dot{\boldsymbol{p}}(t)\} \end{Bmatrix} + \begin{bmatrix} [\boldsymbol{K}] & [\boldsymbol{S}] \\ [\boldsymbol{0}] & [\boldsymbol{H}] \end{bmatrix} \begin{Bmatrix} \{\boldsymbol{w}(t)\} \\ \{\boldsymbol{p}(t)\} \end{Bmatrix} = \begin{Bmatrix} \{\boldsymbol{f}(t)\} \\ \{\boldsymbol{q}(t)\} \end{Bmatrix} \tag{5}$$

Solving the system of equations (5), the pressure field due to the dynamic response of a structural-acoustic system when an external load excites the system, can be completely estimated.

3. Numerical Model

The developed numerical FE model includes two acoustic bodies upstream and downstream of the structural body, which represent the flexible plate. At the interface of the structural-acoustic bodies, fluid-structural boundary conditions are applied in order to define the system of equations described in equation (5). The downstream acoustic body is the air cavity enclosed, meanwhile the upstream acoustic body is included in order to apply an acoustic plane wave as the loading

condition. In particular, an acoustic source is applied in the input plane of the upstream acoustic body, which is long enough so that a plane wave is fully developed before reaching the structural body. In the same input plane, radiation boundary conditions are applied, therefore acoustic waves normal to the boundary will be absorbed and not reflected back into the acoustic domain. Fixed structural boundary conditions are applied on the edges of the elastic plate in order to avoid any relative translational and rotational modes of the plate into the acoustic domain. Sound excitation was modelled as a plane wave from 100Hz to 800Hz, which yields a maximum and minimum wavelength of 1.37m and of 0.43m, respectively. Since the mesh should be fine enough to capture the acoustic and structural mode shapes, 6 elements per wavelength were used according to the high frequency.

An example of the FE model is shown in Figure 7.4.

Harmonic analysis is set on the frequency range of interest (100Hz - 800Hz) and equation (5) is solved estimating the pressure field of the acoustic bodies and the displacement-velocity of the structural elements. In order to characterize the acoustic performance of the acoustic resonator, the Transfer Function Method (24-25-26) is applied. When the pressure field is completely estimated in the upstream acoustic body, the sound pressures (p_1 and p_2) (equation (5)) at two microphone locations can be acquired, where the spacing between the two microphones (s) is defined to be less than 80% of shortest half wave length of interest (24) ($s < 0.4\frac{c}{f_u}$, with f_u is the upper frequency in the frequency range of interest). The reflection coefficient (R) is expressed through the transfer function between the complex pressures measured at two microphone positions ($H_{12} = \frac{fft(p_2)}{fft(p_1)}$) and the transfer function of the incident (H_i) and the reflecting (H_r) plane sound wave

$$R = \frac{H_{12} - H_i}{H_r - H_{12}} e^{[2jk_0(L+s)]} \quad (6)$$

where s is the microphones spacing, L is the distance between the plate of the acoustic resonator and the closer microphone location and k_0 is wave number. The

transfer function of the incident and reflecting sound waves at the two microphone locations are expressed as

$$H_i = e^{(jk_0 s)} \tag{7}$$

$$H_r = e^{-(jk_0 s)} \tag{8}$$

So the sound absorption coefficient of the acoustic resonator can be the estimated by [29]

$$\alpha = 1 - |R|^2 \tag{9}$$

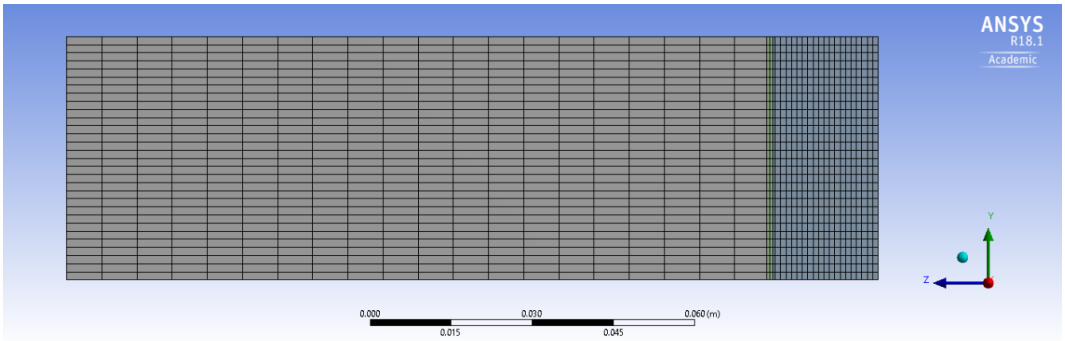

Figure 7.4. FE model the acoustic resonator for the acoustic performance evaluation

3.1 Parametric Analysis

The proposed membrane-type unit cell includes a square elastic plate (45x45mm) of certain thickness (t) with an enclosed cavity of certain depth (D).

The proposed numerical FE model is used to perform a parametric analysis in order to understand the effect of the geometrical parameters of the resonator (t, D) and the material properties of the membrane (ρ_p, E) on the absorption performance of the resonator.

The effect of the plate thickness is studied in a frequency range between 100-800Hz 800Hz keeping constant the cavity depth (D = 20mm), the plate size (45x45mm) and the material properties (E = 1.65MPa and ρ_p = 1200 Kg/m^3).

The effect of the plate resonator thickness on the sound absorption is shown in Figure 7.5.

For thin membrane (t = 0.5mm), the resonator behaves as a common membrane-type resonator showing a single high peak in the absorption coefficient. Small thickness variations induce considerable changes in the absorption properties. Increasing the membrane thickness the frequency range where the maximum resonator absorption properties may be noticed is shifting at lower frequencies. However, the absorption frequency range is not the only parameter which is affected by the membrane thickness. For membrane of thickness between 1 and 2 mm, the normal absorption coefficient shows not 1 peak anymore, but two considerable peaks close in frequency. Further increasing the thickness, the two absorption peaks start to move away to each other, and the absorption of the second peak starts to reduce in amplitude, until only the first peak becomes relevant.

The effect of the membrane thickness can be summarized as follow. Increasing such parameter, a main shift at lower frequencies can be observed for the absorption working frequency range, and three limit cases can be identified. For thin membrane (t=0. 5mm) only one absorption peak is relevant at high frequencies, for thicker membranes (t=3.0mm) only one peaks is dominant at lower frequencies, while for intermediated values 1.0mm<t< 2mm) two absorption peaks can be observed very close in frequencies which provide a quite broadband absorption.

After evaluating the effects of the membrane thickness, the effect of cavity depth is investigated for a membrane of 1.2mm thickness (size of 45x45mm, E = 1.65MPa and ρ_p = 1200 Kg/m^3), since this thickness provide a double peak and broadband absorption. Increasing the depth of the enclosed cavity, the absorption peaks are shifting at lower frequencies on average (Figure 7.6). Also, in this case three main cases can be identified. For high values of cavity depth (D=40mm) the absorption is dominated by the first peak at lower frequency, while there is drop in amplitude of the second peaks. On the other hand, the second absorption peak at higher frequencies is dominant with small cavity depth (D=15mm). Resonators with cavity depth around 20mm keep the double peak and guarantee a broadband absorption.

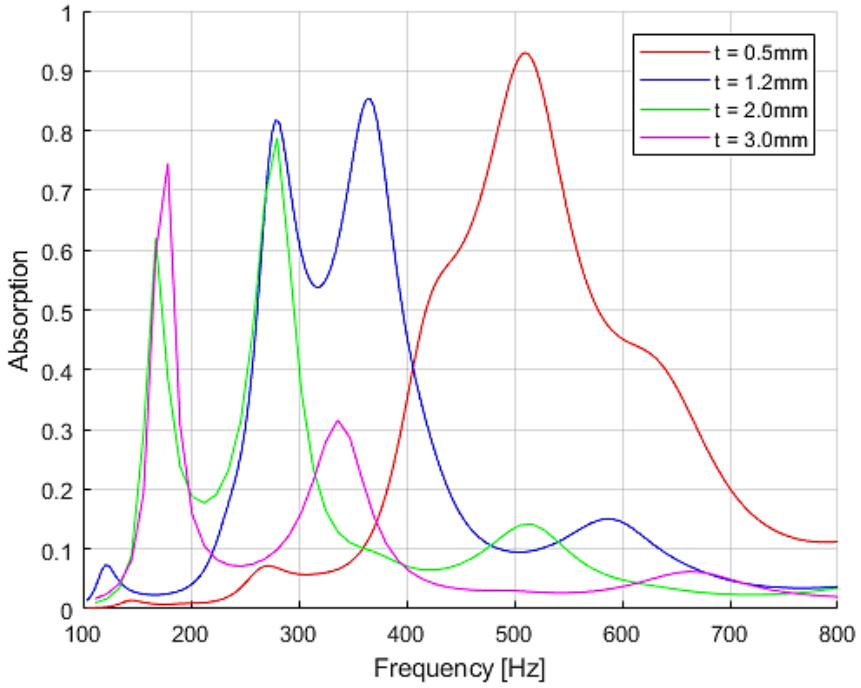

Figure 7.5. Parametric study of the resonator absorption coefficient varying the plate thickness (E = 1.65MPa and ρ = 1200 Kg/m3, d = 20mm)

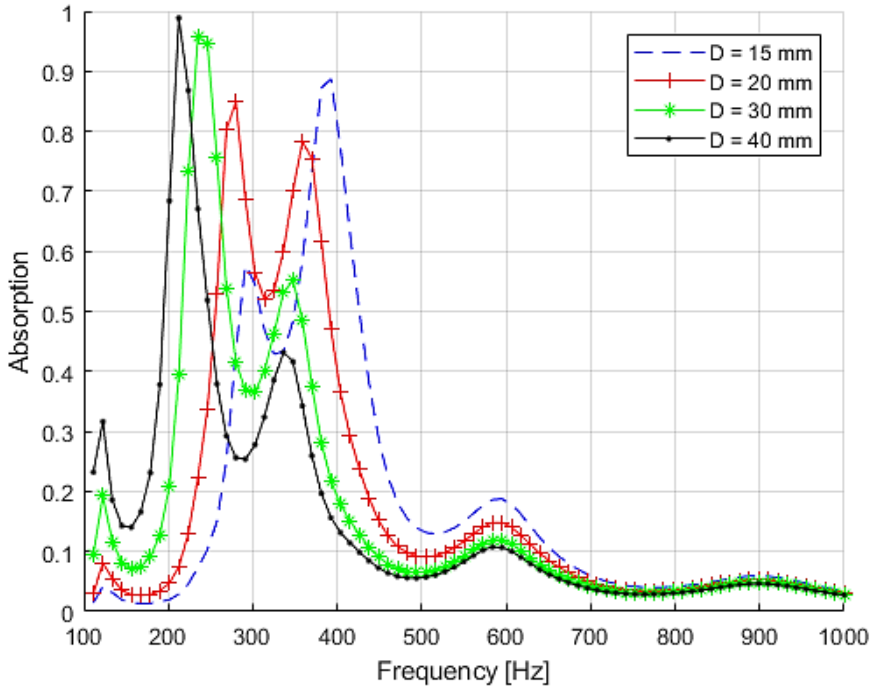

Figure 7.6. Parametric study of the resonator absorption coefficient varying the cavity depth (E = 1.65MPa and ρ = 1200 Kg/m3, t = 1.2mm)

At this stage, the plate material properties effect on the sound absorption is investigated, keeping constant the geometrical parameters (*t = 1.2mm, D=20mm*). The material density doesn't affect the global shape of the absorption profile, but increasing the density of the resonator plate, the absorption coefficient peaks shift at lower frequencies with a reduction of the absorption level (Figure 7.7). In particular increasing the density from 500 Kg/m^3 to 2000 Kg/m^3 the main absorption peak move from 430 Hz to 210 Hz with a drop-in amplitude of 15%.

When the density increases the out of plane membrane displacement will be lower when excited by a plane sound wave. It means the absorption level will be lower because less sound energy will be dissipated through the resonators vibration.

Not only the materials density plays a key role on the sound absorption of the acoustic resonator. As long as the ration E/ρ_p is kept constant, the acoustic properties of the resonator do not change, in the other cases, the effect of the E/ρ_p will affect the acoustic absorption of the resonator.

Figure 7.8 shows the parametric analysis of the sound absorption coefficient with different values of E/ρ_p, while keeping the resonator geometrical parameters constant (*t = 1.2mm, D=20mm*). An optimal value of E/ρ_p = 1.4e3 m^2/s^2 can be identified where the resonator shows a broadband absorption between 240 Hz -400 Hz with a sound absorption level all over 50% and two different peaks at 268 Hz and 369 Hz with 82% and 85% absorption. Moreover E/ρ_p = 1.0e5 m^2/s^2 represents a limit value which results in only a single absorption peak.

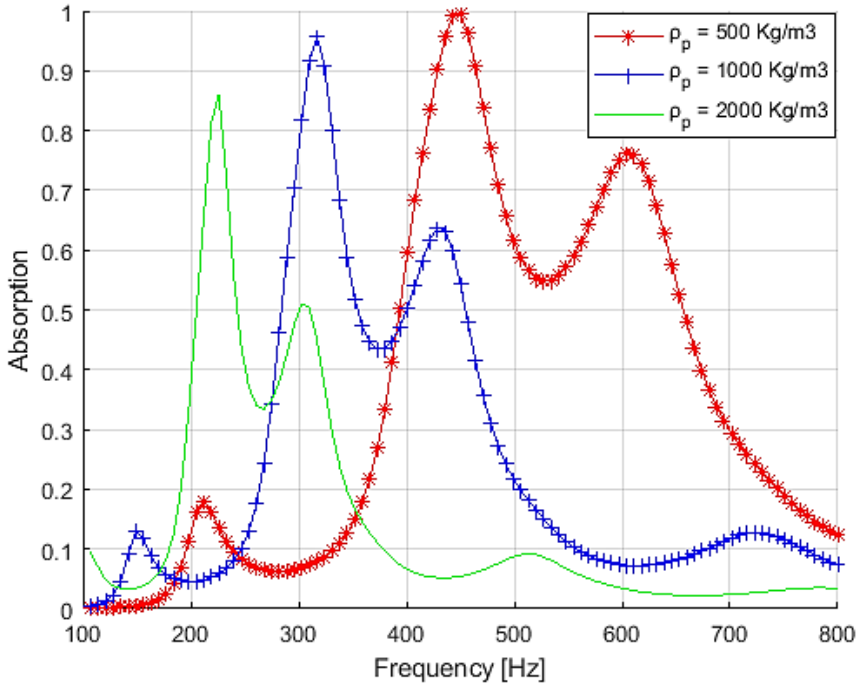

Figure 7.7. The absorption coefficient of the resonator absorber varying with the plate density (45x45mm plate, t = 1.2mm, D=20mm, E=1.9MPa)

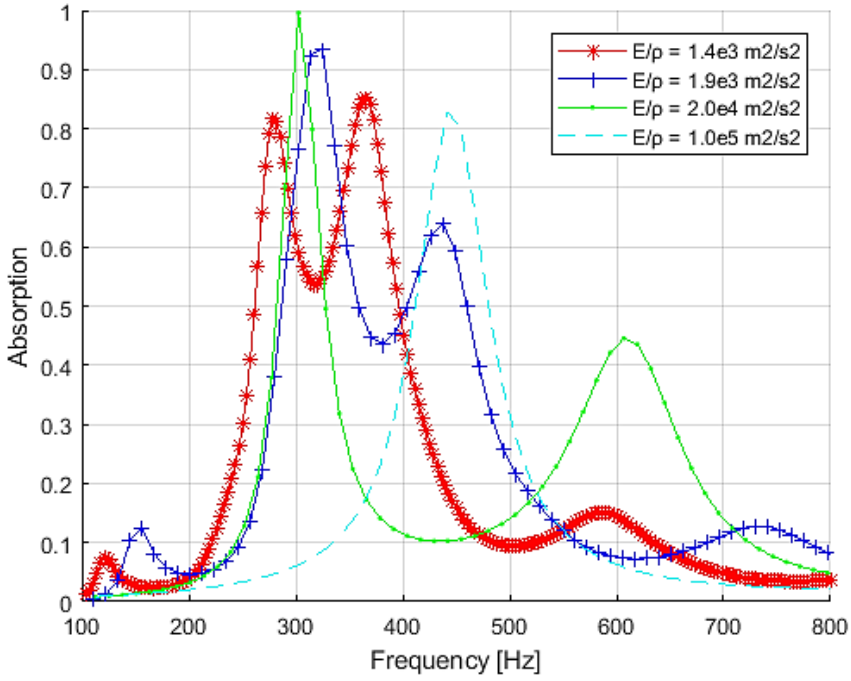

Figure 7.8. The absorption coefficient of the resonator absorber varying with the ratio E/ρ (45x45mm plate, t = 1.2mm, D=20mm)

3.2 Numerical Model Validation

The parametric analysis results are used to identify the optimized configuration for the resonator. This optimum configuration is chosen to validate the proposed FE numerical model.

The resonator unit cell is machined and tested in an impedance tube test ring in order to measure the normal sound absorption which will be compared with the numerical one.

The considered acoustic resonator unit cell (Figure 7.9) consists of a square elastic plate (45x45mm) of 1.2mm thickness with an enclosed cavity of 22mm depth. The plate is made of silicone by casting process and the elastic properties of the material is measured through tensile testing. According with ISO 527 – 1:1996 (27) dog bone shape samples are tested with a test speed of 1 mm/min and the stress-strain curve is shown in Figure 7.5. The Silicone shows an elastic modulus of 1.65MPa and a density of 1200 Kg/m^3.

The material is tested also through Dynamic Mechanical Analysis (DMA) in order to measure the damping properties of the used silicone. DMA results show a constant trend of the tanδ over the frequency which can give us an indication about the damping coefficient ($\tan\delta \approx 2\xi$ [30-31]). From such result a constant structural damping of 0.1 is applied on the material properties definition of the FE model.

These experimental results are used as input data in the numerical simulation.

The unit cell is tested in a two microphones impedance tube test rig, according with the ASTM E 1050 (24), for which the working frequency range (interval where plane-standing wave conditions are guaranteed) is 250-3000 Hz. However, at this stage, the normal incident sound absorption coefficient is measured in a sub-frequency range between the 250Hz to 800 Hz in order to validate the numerical results.

The measured and numerical sound absorption coefficient are plotted in Figure 7.10 which shows a good agreement between the experimental and numerical result, and small differences in terms of amplitude is due to the assumption of a constant damping ratio in the numerical model.

In conclusion, the proposed FE numerical model is a usefulness approach to predict the acoustic properties of the proposed membrane-type acoustic resonator and can be used to better understand the absorption mechanism. Moreover, the experimental measurement demonstrates that the proposed unit cell acoustic resonator provides subwavelength absorption with two considerable absorption peaks at 268 Hz and 369 Hz. Unlike usual membrane-type metamaterial or resonator absorbers, the absorption performances of the proposed resonator is not identified by a single narrow peak. Optimizing the physical properties of the resonator, in terms of geometry and material properties, a double absorption peak is generated broadening the frequency range in which the sound absorption is considerable high (over 50%).

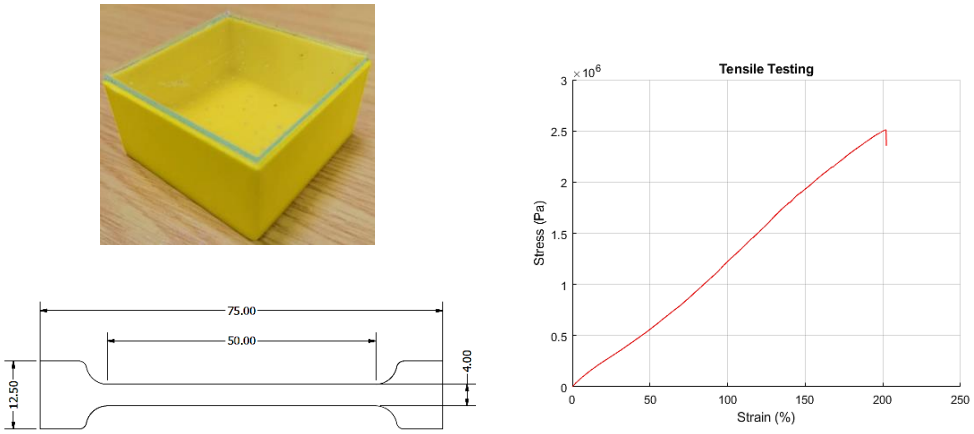

Figure 7.9. (Left-Up) Acoustic resonator unit cell; (Left-Bottom) Dog bone shape sample for tensile testing; (Right) Stress-Strain curve for Silicone measured by tensile testing

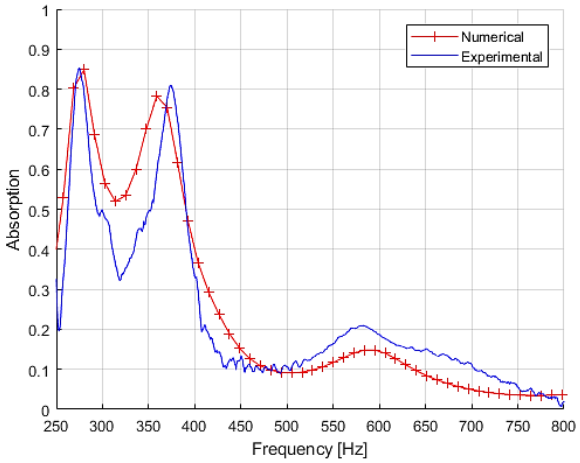

Figure 7.10. Comparison between the experimental sound absorption coefficient (blue line) and the numerical one (red line) estimated with FE model

4. Results and Discussion

In this section the validated numerical model is used to better understand the absorption mechanism of the proposed resonator.

The optimized unit cell resonator shows an extended low frequency response in the sound absorption coefficient which is characterized by two main absorption peaks.

In this section the optimized unit cell acoustic performances are compared with a non-optimized one in order to study the reasons behind such broadband and mutli-peaks absorption which is unusual for a membrane-type metamaterial.

In particular, keeping constant the material properties (elastic modulus of 1.65MPa and a density of 1200 Kg/m^3), the unit cell size (45x45mm) and the enclosed cavity depth (D=22mm), two membrane thickness are investigated: the optimized t=1.2mm and the non-optimized t=0.5mm one.

In order to investigate the actual acoustic-structural interaction for the unit cell resonator when it is excited by an acoustic sound wave, the acoustic response of the enclosed cavity and the structural response of the membrane of the two considered case studies are deeply analysed further in this section. The acoustic response of the resonator is studied in terms of difference (Δp) between the pressure into the unit cell chamber and the upstream sound pressure (Figure 7.12), while the structural response is expressed in terms of Frequency Response Function (*FRF*) estimated using the out of plane velocity response of the resonator membrane (Figure 7.13).

The Δp and the *FRF* are estimated according with the proposed FE modal in a frequency range between 100Hz and 800Hz.

The two case studies are discussed individually below.

4.1 Non-optimized unit cell resonator (t=0.5mm)

The absorption coefficient (Figure 7.11 (a)) for the unit cell resonator with a membrane of 0.5mm thickness presents only one peak at 513 Hz.

First of all the membrane structural dynamic response is discussed.

Taking into account the structural response of the membrane described by the FRF, as well-known at that frequency where the membrane presents a structural resonance the FRF show a peak in modulus, a phase shifting, a relative maximum/minimum in the imaginary part zero value in the real part.

In this case of membrane with 0.5mm thickness, it clear that the membrane presents a structural resonance at 515 Hz (Figure 7.13 – Red line). To confirm such result extracted from the FRF, a modal analysis is performed on a fixed-supported membrane with the same geometry and material properties of the unit cell resonator membrane. The modal analysis demonstrate that a symmetric bending mode appears at the resonance frequency of 515Hz (Figure 7.11 (b)). Comparing now the structural response of the membrane itself with the unit cell resonator acoustic performances, we can notice a perfect match between the structural resonance frequency (515 Hz) and the absorption peak (513 Hz), which suggests that the absorption mechanism is related to the sound energy dissipation due to the resonance phenomena of the membrane resonator.

Consider now the acoustic response.

According with the general formulation of the acoustic resonator which could be the membrane type resonator, the acoustic resonance frequency is related to the mass density per unit area of the membrane (m) and the cavity depth (D) [28]

$$f_r = \frac{c}{2\pi}\sqrt{\frac{\rho}{mD}} \tag{10}$$

where c is the sound speed in air and ρ is the air density. Applying this formula to the unit cell resonator, the acoustic resonance can be identified at 516 Hz, which is basically the acoustic resonance of the resonator chamber. There is perfect match in frequency between the structural resonance (515 Hz) of the plate and the acoustic resonance of the chamber (516Hz). So, the sound absorption is not only related to the structural resonance of the membrane itself but it is rather due to resonance of the global resonator. In other words, the mass of the plate is being treated as single

lump mass and therefore the plate should vibrate as a piston and the effect of the cavity is only a lump stiffness of the system.

The Δp between the chamber pressure and incoming sound pressure and the isosurface for the pressure distribution in the chamber and in the upstream acoustic body are used to support that thesis.

From the real part of the Δp plotted in Figure 7.12 – red line, a positive peak is picked up at the max absorption frequency, which means that a such frequency the air mass into the resonator chamber is moving in-phase with the sound wave excitation.

In Figure 7.11 (c-d) the isosurface are plotted. For each section the pressure, both into the resonator chamber and in the upstream acoustic body, is constant. Moreover, focusing on the isosurface at the upstream and downstream membrane interface, we can see how a constant pressure distribution is distributed at upstream and downstream membrane interface. The small proximity pressure changing at the downstream interface are due to the membrane resonance at that frequency, however these changing are ±2% around the mean pressure value on average. So, we can assume constant pressure distribution. Also, the constant pressure distribution upstream and downstream the membrane present the same sign which confirm that the membrane-chamber system is vibrating as a single degree of freedom piston.

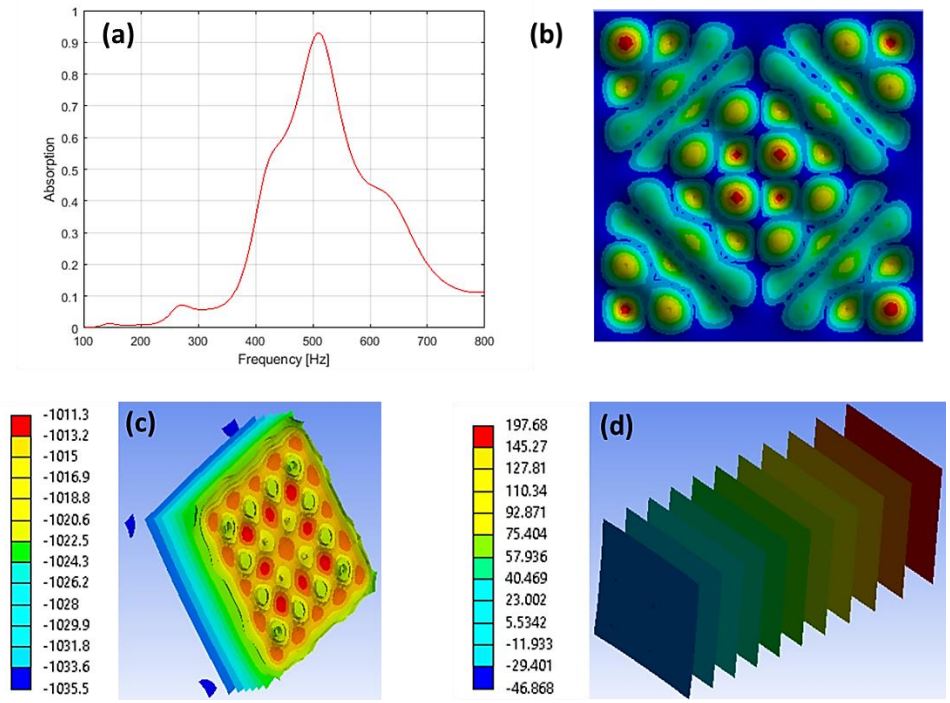

Figure 7.11. Unit cell resonator t=0.5mm (45x45mm, D = 22mm, E = 1.65MPa and ρ = 1200 Kg/m3): (a) Absorption coefficient; (b) Modal Analysis: membrane mode shape at 515Hz; (c) Isosurface downstream the membrane; (d) Isosurface upstream the membrane.

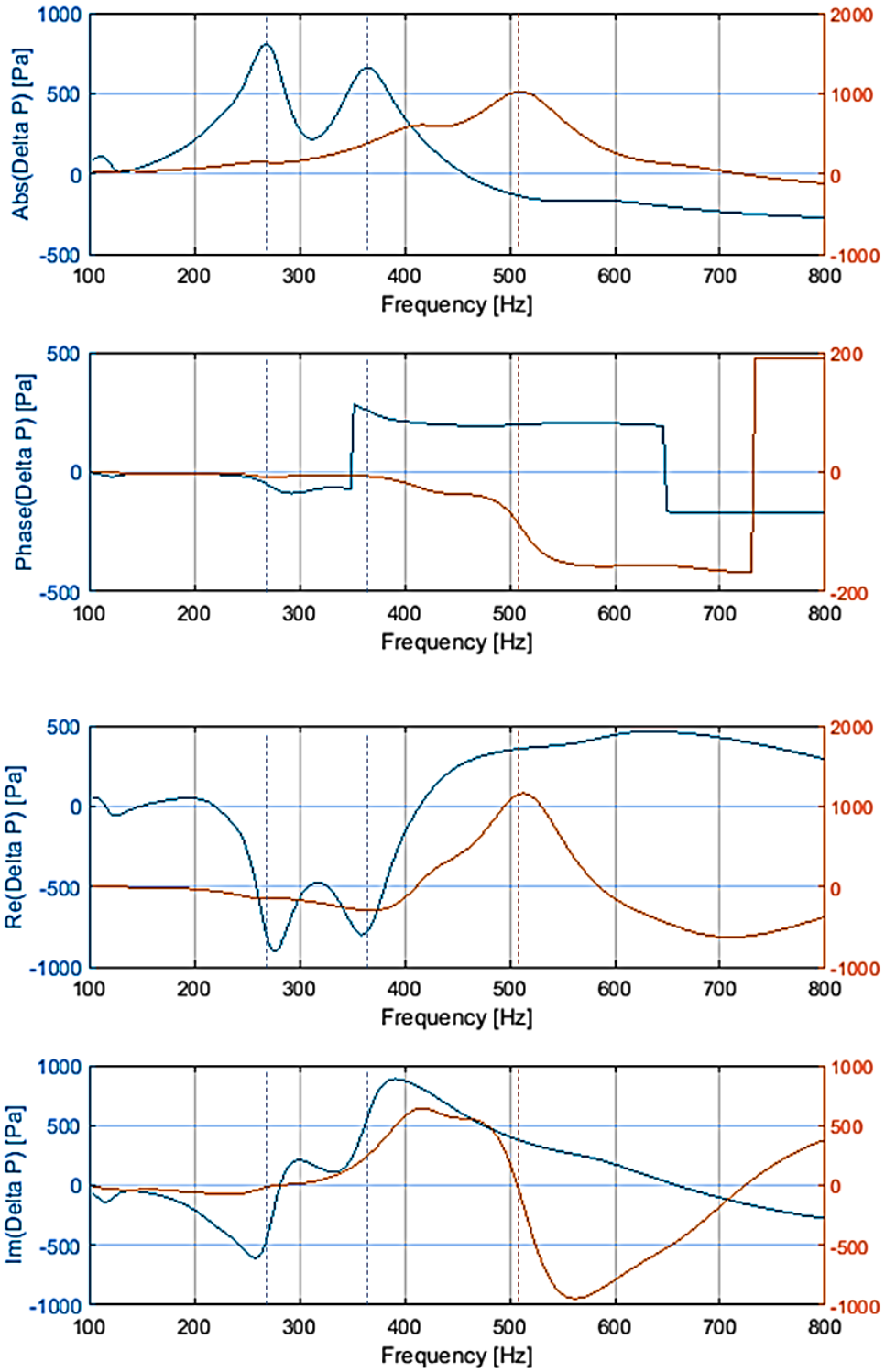

Figure 7.12. Modulus and Phase (upper plots) and Real and Imaginary part (lower plots): resonator with 1.2mm membrane thickness – Blue line; resonator with 0.5mm membrane thickness – Red line.

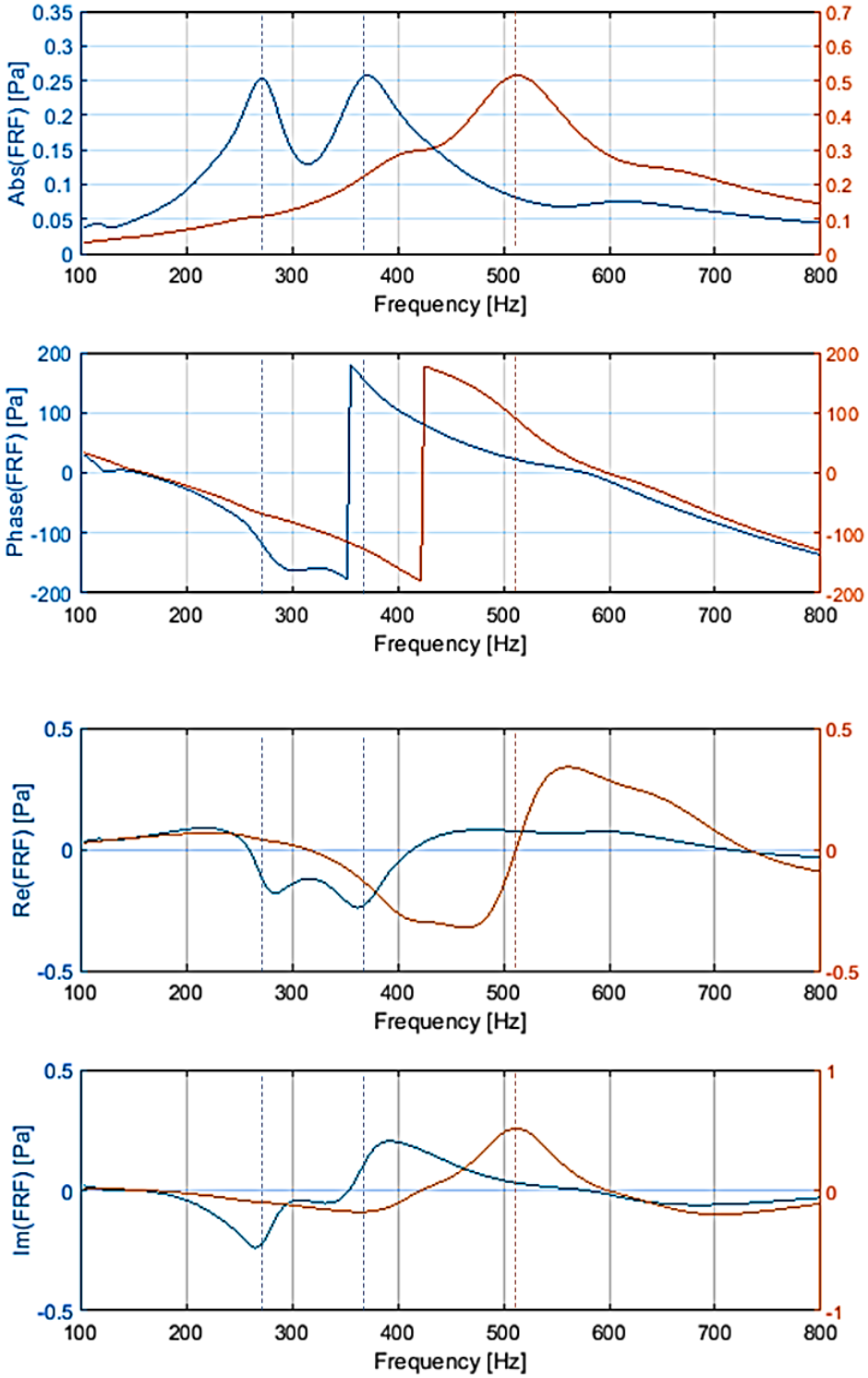

Figure 7.13. Modulus-Phase (upper plots) and Real-Imaginary Part (lower plots) of Velocity Frequency Response Function: resonator with 1.2mm membrane thickness – Blue line; resonator with 0.5mm membrane thickness – Red line.

4.2 Optimized unit cell resonator (t=1.2mm)

The absorption coefficient (Figure 7.14 (a)) for the optimized unit cell resonator (membrane of 1.2mm thickness) presents two peaks at 268 Hz and 369 Hz.

As we discuss for the non-optimized unit cell resonator, first of all we take into account the structural response of the only membrane when it is excited by an acoustic sound wave.

As we describe above for the non-optimized resonator, the FRF measured on the membrane give us an indication about the structural resonance frequency of the membrane itself.

The FRF for the optimized membrane is plotted (Modulus-Phase and Real-Imaginary Part) in Figure 7.13 – Blue line. In this case, the FRF show peaks in the modulus and a phase changing at the maximum absorption frequencies: 268Hz and 369 Hz. However, at these frequencies the real part is not zero and the relative maximum/minimum in the imaginary part, which is usually associated to a structural resonance, are shifted at different frequencies with respect to the absorption peak frequencies.

Also in this case, we run a numerical modal analysis on an equivalent membrane applying the equivalent boundary conditions, to verify the actual structural resonance frequencies and the relative mode shapes. Since a plane wave can excite only the symmetric bending modes of the membrane, only these modes have been taken into account from the modal analysis in the frequency range of interest (100Hz-800 Hz). Three main structural resonance frequencies are picked up in that frequency range respectively at 231 Hz, 323 Hz and 406 Hz, and the relative mode shapes are plotted in Figure 7.14 (b1-2-3), which are close to the absorption peak frequencies but don’t match them. In other words, the absorption peaks in this case is not associated to pure structural resonances of the resonator membrane.

If we consider now the acoustic response contribution, according with equation (10) an acoustic resonance can be identified at 356 Hz which is in between the absorption peaks frequencies. So, the absorption mechanism behind the optimized resonator is not strictly related to the structural resonance of the membrane and it is not even

strictly related to the acoustic resonance of the air into the enclosed cavity. Moreover, while the numerical model presented by equation (10) leads to an acoustic resonance of 356 H, the resonator does not behave like a single degree of freedom piston which is instead the main reason behind the single absorption peak of the commonly used membrane-type metamaterial.

In Figure 7.12 – Blue line, we plot the upstream-downstream Δp for the optimized resonator. Focusing on the real part, we can see how at the absorption peak frequencies the real part of Δp shows two negative peaks which means that the air mass into the resonator chamber is moving out of phase with the incoming sound wave excitation. In other word, on the contrary to the non-optimized unit cell resonator, the enclosed air mass reacts out of phase with the incoming sound wave which excite the unit cell resonator. This is confirmed by the pressure isorsurface plotted in Figure 7.14 (d1-2) respectively for the maximum absorption frequencies (268Hz and 369 Hz). For both the frequencies 268Hz and 369Hz, the mean value of the incoming pressure wave is positive while mean value of the reaction pressure in the enclosed cavity is negative, so the pressure field of the incoming pressure wave and the resonator's chamber are opposite in sign. Looking at the isosurface at upstream and downstream interface of the membrane, the pressure distribution at the interface is not constant which means that the resonator is not behave as a piston. Moreover, the isosurface in the chamber show how the higher acoustic modes of the mass air in the chamber are excited at the absorption peak frequencies. The non-uniform pressure distribution due to higher acoustic modes of the chamber will act on the membrane which, on the other hand will react according with its intrinsic mode shapes related to its structural resonances excited by the incoming sound wave excitation. This interaction between the higher acoustic modes and structural modes generated a hybrid resonance of the resonator assembly which dissipate the sound energy associated to the incoming sound wave.

So, for the optimized resonator, the high absorption is still related to sound energy dissipation resonance phenomena of the resonator, but in this case the resonances are not pure structural membrane resonance or pure acoustic resonance of the enclosed cavity. The mutual interaction of structural dynamic of the membrane and

the acoustic dynamic response of the air into the cavity must be taken into account as a combination of the higher structural and acoustic modes. As a consequence, the maximum absorption, is related to the hybrid resonances of the coupled structural-acoustic system due to non-uniformly distributed pressure acting on the membrane, which is not behave as piston anymore.

The proposed optimized resonator is designed to move close the structural-acoustic hybrid resonances in order to broaden the absorption at low frequencies.

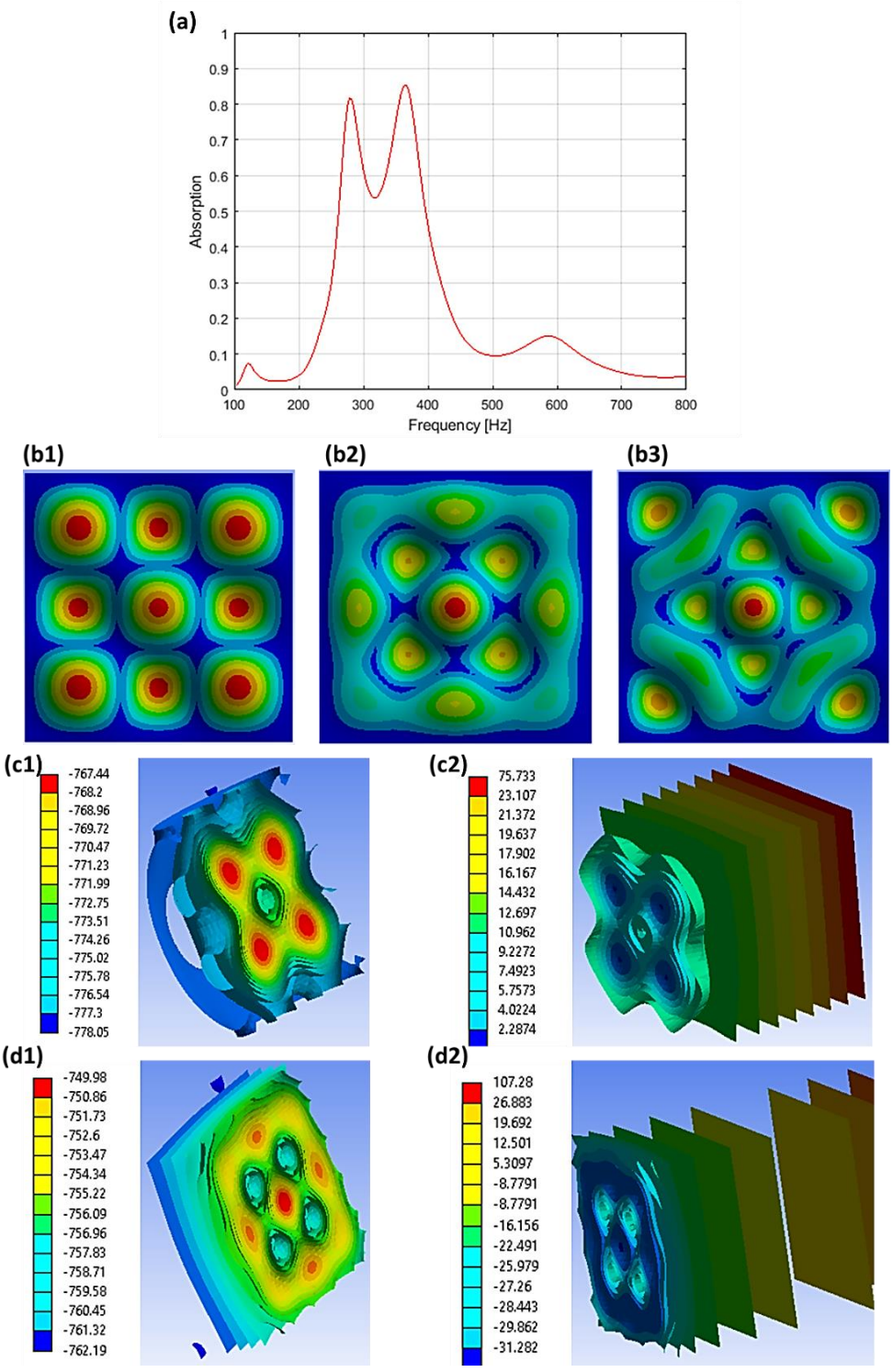

Figure 7.14. Unit cell resonator t=1.2mm (45x45mm, D = 22mm, E = 1.65MPa and ρ = 1200 Kg/m3): (a) Absorption coefficient; (b) Modal Analysis: membrane mode shape at 231 Hz (b1), 323 Hz (b2) and 406 Hz (b3); (c) Isosurface downstream (c1)-upstream (c2) the membrane at268 Hz ; (d) Isosurface downstream (d1)-upstream (d2) the membrane at 369Hz.

4.3 Effect of the geometrical parameters and material properties on the absorption

Now that absorption mechanism of the proposed membrane type unit cell has been deeply discussed and the reasons behind the improvement of the absorption properties with respect to the common membrane type resonator has been demonstrated, it is easy to understand the effect of the geometrical parameters which are presented in previous parametric analysis.

Considering first of all the membrane thickness effect (Figure 7.5).
Changing the thickness of the membrane, the entity of the interaction between the structural dynamic response and the acoustic response of the resonator will change as consequence. For small thickness the structural dynamic response of the membrane does not have a great effect. In this case the effect of the membrane is a lump mass which reacts in phase with the mass air in the enclose cavity where the higher acoustic modes are not excited. So, the structural-acoustic interaction can be described as a single degree of freedom mass spring system. Increasing the thickness of the plate, the vibration of the plate itself will be not neglectable. Moreover, the mutual interaction between the membrane and enclose air mass lead to a non-uniform upstream-downstream pressure with consequent excitation of the higher acoustic modes in the chamber. Hybrid structure-acoustic resonance come out due to the coupling of higher structural modes of the plate and acoustic modes of the chamber; thus, leading to multiple absorption peaks.

The main effect of the cavity depth is on the acoustic response of the unit cell.
Considering the simple case of piston behaviour (single degree of freedom) of the unit cell, the acoustic resonance of the enclosed cavity is described by equation (10). According with such equation, increasing the depth, the acoustic resonance moves towards lower frequencies.
Considering now the optimized unit cell which provides multiple absorption peaks, the cavity depth changing will affect the mutual acoustic-structural interaction. In

particular, since the acoustic cavity mode moves towards lower frequencies (according to equation (10)) as the cavity depth is increased, the coupling with the structural modes will change and will be stronger at lower frequencies for bigger cavity depth. So for bigger cavity depth, the sound absorption (Figure 7.6) will be dominated by the coupling between the acoustic modes shifted at lower frequencies and the relative structural modes at lower frequencies; while reducing the cavity depth the acoustic modes will move at higher frequencies and they will couple with the structural modes at higher frequencies increasing the global absorption performance of the unit cell resonator at higher frequencies.

The material density for the resonator membrane affects both the structural dynamic response of the membrane and the acoustic one of the cavities. Both the acoustic resonance (equation (10)) and the structural resonance are inversely proportional ($\sim 1/\rho_p$) to the material density, so hybrid structural-acoustic resonances at lower frequencies of the acoustic resonator can be expected because of density increases. Considering the optimized unit cell resonator, the main effect of the density increasing is the translation of the absorption peaks at lower frequencies. However, when density increases the response displacement of the membrane will be lower when excited by an incoming sound wave. It means the absorption level will be lower because less sound energy will be dissipated through the resonators vibration. More than the material density, the ratio E/ρ_p plays a key role on the sound absorption of the proposed acoustic resonator. As long as the ration E/ρ_p is kept constant, the acoustic properties of the resonator do not change, in the other cases, the effect of the E/ρ_p will affect the acoustic-structure interaction between the resonator plate and the resonator chamber as well as we discussed for the membrane thickness variations. In particular the proposed resonator presents an optimal value of E/ρ_p = 1.4e3 m^2/s^2 where the structural-acoustic coupling results in broadband absorption between 240 Hz -400 Hz with a sound absorption level all over 50% and two different peaks at 268 Hz and 369 Hz with 82% and 85% absorption. Increasing the ratio results in a reduction in the hybrid resonances due to structural acoustic interaction. A limiting value of E/ρ_p = 1.0e5 m^2/s^2 was determined, which results in

only a single absorption peak due to the plate vibrating as a piston and thus the effect of the cavity is only a lump stiffness of the system.

5. Conclusion

Membrane-type metamaterials provide good sound absorption at low-frequencies, however wide band absorption is difficult to achieve in one device, as they are categorised by a single narrow absorption peak. Therefore, the frequent challenges in the design of membrane-type and resonator absorbers is to extend the frequency bandwidth. A subwavelength acoustic resonator unit cell was proposed in this paper which included an elastic silicone plate of 1.2mm thickness with an enclosed air cavity of 22mm depth. The results showed that it was possible to achieve two high and broadening absorption peaks over 80% at 268Hz and 369Hz, which provided broadband absorption in the frequency range between 250Hz and 400Hz. Using an acoustic-structural interaction based numerical model, it was demonstrated that the absorption of the resonator was associated to hybrid resonances which occur when high order structural modes of the elastic plate are coupled with the acoustic modes of the cavity. Furthermore, the sound absorption performance is related to the geometry and material (inertia and elastic properties) characteristics of the resonator absorber. Thus, it was shown that by optimisation of these parameters, the membrane absorber can be tuned to achieve the best performances in the specified frequency range using very cheap materials.

6. References

1. Yang M., Sheng P., Sound Absorption Structures: from porous media to acoustic metamaterials, Annual Review of Material Research, Vol 47:83-114 (2017).
2. Maa D.Y., Theory and design of microperforated panel sound absorbing construction, Sci Sin, 18:55-71 (1975).
3. Maa D. Y., Potential of microperforated panel absorber, Journal Acoust Soc A, 29:77-84 (1987).
4. Wang C., Huang L., On the acoustic properties of parallel arrangement of multiple micro-perforated panel absorbers with different cavity depths, Journal Acoust. Soc. Am, Vol.130, No1, (2011).
5. Guo W., Min H., A compound micro-perforated panel sound absorber with partitioned cavities of different depths, IBPC, 78: 1617-1622, (2015).
6. Bucciarelli F., Malfiense F., Meo M., A multilayer microperforated panel prototype for broadband sound absorption at low frequencies, Applied Acoustics, 146: 134-144 (2019).
7. Pan J., Guo J., Ayres C., Improvement of Sound Absorption of Honeycomb panels, Proceeding of Acoustics 2005.
8. Sakagami K., Yamashita I., Yairi M., Morimoto M., Effect of honeycomb on the absorption characteristics of double-leaf microperforated panel (MPP) space sound absorbers, Noise Control Eng. J. 59.4:363 (2011).
9. Sakagami K., Fukutani Y., Yairi, Morimoto M., Sound absorption characteristics of double-leaf structure with an MPP and a permeable membrane, Applied Acoustics, 76: 28-34, (2014).
10. Sakagami K., Morimoto M., Yairi M., A note on the relationship between the sound absorption by microperforated panels and panel/membrane type absorbers, Applied Acoustics, 70: 1131-1136, (2009).
11. Ma G., Sheng P., Acoustic metamaterial: From local resonators to broad horizons, Sci. Adv. 2(2), el1501595 (2006).
12. Huang T.-Y., Shen C., Jing Y., Membrane-and plate-type acoustic metamaterials, J. Acoust. Soc. Am., 139 (6) (2016).
13. Yang Z., Mei J., Yang M., Chan N. H., Sheng P., Membrane-type acoustic metamaterial with negative dynamic mass, Phys. Rev. Lett. 101(20), 204301 (2008).
14. Naify C. J., Chang C. M., McKnight G., Nutt S., Transmission Loss and dynamic response of membrane-type locally resonant acoustic metamaterial, J. Appl., Phys. 108 (11), 114905 (2010).

15. Naify C. J., Chang C. M., McKnight G., Nutt S., Transmission loss of multi-celled arrays, J. Appl. Phys., 109(10), 104902 (2011).
16. Mei J., Ma G., Yang M., Yang Z., Wen W., Sheng P., Dark acoustic metamaterials as super absorber for low-frequency sound, Nat. Commun. 3, 756 (2012).
17. Ma G., Yang M., Xiao S., Yang Z., Sheng P., Acoustic metasurface with hybrid resonances, Nat. Matt. 3:873-878 (2014).
18. Yang M., Ma G., Yang Z., Sheng P., Coupled membranes with doubly negative mass density and bulk modulus, Phys. Rev. Lett. 110(13), 134301 (2013).
19. Zienkiewicz O. C., Taylor R. L., The finite element method for solid and structural mechanics, Butterworth-Heinemann (2013).
20. Petyt M., Introduction to finite element vibration analysis, Cambridge University Press (2010).
21. Reddy J. N., Mechanics of laminated composite plates and shells, CRC (2004).
22. Glandwell G.M.I., Zimmermann G., On energy and complementary energy formulations of acoustic and structural vibration problems, J. Sound Vib., 1996.
23. Fahy F., Gardonio P., Sound and structural vibration: Radiation, Transmission and Response, Technology & Industrial Arts 1985.
24. ASTM E 1050, Standard test method for impedance and absorption of acoustical materials using a tube, two microphones and a digital frequency analysis system, ASTM INTERNATIONAL (2012).
25. Seybert A. F., Ross D. F., Experimental determination of acoustic properties using a two-microphone random-excitation technique, J. Acoust. Soc. Am. 61, 1362-1370 (1977).
26. Chu W. T., Extension of two-microphone transfer function method for impedance tube measurement, J. Acoust. Soc. Am. 80, 347 (1986).
27. ISO 527 – 1 : 1996, Plastic – Determination of tensile properties, British Standard Institution (1996).
28. Cox T. J., D' Antonio P., Acoustic Absorption and Diffusers: Theory, Design and Application, Spon Press (2004).
29. D.T. Blackstock, Fundamentals of Physical Acoustics, JOHN WILEY & SONS, 2000.
30. Lenk P., Coult G., Damping of glass structures and components, Challenging Glass 2, Vol 2, 2010.
31. Carfagni M., Lenzi E., Pierini M., "The Loss Factor as a Measure of Mechanical Damping," Atti del 16th International Modal Analysis Conference, Santa Barbara, CA (USA), 2-5 febbraio 1998, Vol. 1, pp. 580-584

Chapter 8

Sub-Wavelength Metamaterial for perfect broadband sound absorption

In the previous Chapter we proposed a new concept of membrane-type metamaterial unit cell which behaves as multi degree of freedom system (MODF). With a global thickness of 23mm, the unit cell arises multiple resonance frequency, due to the mutual interaction between the structural dynamic response of the membrane and acoustic dynamic response of the resonating chamber, in a frequency range of 250Hz-400Hz. In particular, two coupled hybrid resonance frequencies are generated in the considered frequency range which lead to broadband absorption level over 50% between 250-400 Hz with two main absorption peaks over 80%.

Referring to the automotive NVH, the interior noise spectrum is extended from 100Hz to 4000Hz, since it includes different contributions coming from different noise sources.

So, the MDOF membrane-type unit cell is a powerful solution of sound mitigation at low frequencies but it is weak for the high frequency contributions.

In order to broadening the absorption profile a new concept of MDOF hybrid absorber is proposed in this Chapter. The proposed MDOF hybrid absorber combines the concept of MDOF membrane-type unit cell, deeply investigated in

the previous Chapter, with the materials properties of Graphene Oxide (GO). The absorber includes a unit cell which behaves as MDOF membrane-type, where a GO micro-foil acts as a membrane and the unit core cell of a Honeycomb (HC) structure acts as resonating acoustic chamber. Two different configurations are discussed. The standard configuration includes a micro foil of GO embedded in HC core structure and a second GO micro foil as external skin. Since not only the acoustic properties need to be guaranteed but also the mechanical strength of the device, a second configuration is also proposed. The MPP configuration includes the same unit call, GO micro foil embedded in HC structure, with an external skin of MPP (Microperforated pane). We demonstrate how the standard and MPP configurations are characterized by the same absorption properties, since the absorption is mainly related to the common membrane-type unit cell. The absorption mechanism is associated to the multiple resonance frequencies generated by the membrane-type unit cell, due to the mutual interaction between the higher order structural modes of the membrane and higher order acoustic modes of the acoustic chamber. The Graphene Oxide shows high damping properties, inducing a distortion on the resonance peaks which become broader in frequency. Then, if the resonance frequencies are close to each other, the resonance peaks start to collapse on each other. As consequence, the absorption profile will be flat in all the frequency range of interest. Moreover, we demonstrate that high perforation ration of the MPP external skin allows the same absorption profile for the standard configuration with GO as external skin. Otherwise, for low perforation ratio the amount of air passing through the MPP external skin is not enough to excite the dynamic response of the membra-type unit cell and the absorption profile will be characterized by a single absorption peak related to the MPP acoustic properties.

In conclusion the proposed MDOF Hybrid absorber is a subwavelength structure with a global thickness of 70mm which allows a flat absorption over 90% in a frequency range of 300Hz-2500Hz.

The advantages in terms of NVH applications are clear. For example, if we compare the absorber acoustic performances with the commonly used porous materials (Figure 1.3, Figure 1.4), we are able to cut off the low frequencies contributions

(below 500Hz) in the vehicle interior noise spectrum reducing considerable the structure thickness.

In this Chapter we present the both MDOF Hybrid absorber configuration: GO external skin and MPP external skin, investigating the mechanisms behind the absorption properties and the effects of the MPP as external skin.
We developed a manufacturing process to manufacture micrometric GO foils starting from Graphite Oxide (GtO) powder through sonication treatments.
Analytical models are proposed and use to study the absorption mechanism for the proposed metamaterial. For the GO external skin configuration, the GO foil is considered as a vibrating plate and the HC core as an acoustic resonator chamber developing a coupled modal-acoustic model. While for the MPP external skin, the membrane-type effect is combined with the MPP properties absorber combining the modal-acoustic model for the GO foil with the equivalent electric circuit analysis for the MPP.

The Statement of Authorship From and the paper a reported next.

This declaration concerns the article entitled:	
Graphite-Oxide hybrid multi-degree of freedom resonator metamaterial for broadband sound absorption	
Publication status (tick one)	
Draft manuscript	✓
Submitted	
In review	
Accepted	

Published	

Candidate's contribution to the paper (detailed, and also given as a percentage).

The candidate contributed to/ considerably contributed to/predominantly executed the…

Formulation of ideas:	80% I proposed the initial and the methodology and the experimental/manufacturing approach. The idea was discussed and supported by Prof. Meo.
Design of methodology:	70% I designed and developed the analytical model used in this research work and the experimental tested. G.P. Malfense Fierro help me with the analytical model implementation.
Experimental work:	60% I performed the experimental test for the acoustic performance of the prototypes. G.P. Malfense Fierro help me with the HC core design and 3D manufacturing. M. Rapisarda worked on the GO foil production and microscopic characterization
Presentation of data in journal format:	80% I worked on the paper structure, figures and plots, writing the paper drafts. Prof. Meo provided the first review of the paper and he supported in the submission process.

Statement from Candidate

This paper reports on original research I conducted during the period of my Higher Degree by Research candidature.

Signed		**Date**	05/01/2020

8.1 List of Symbols

The symbols and their explanation used in Chapter 8 for the mathematical notation are reported below:

Symbol	Description
Λ_m	Modal Mass
Λ_n	Modal Volume
w_m	Structural modal participation factor
p_n	Acoustical modal participation factor
C_{mn}	Acoustic-Structural coupling matrix
F_m	Force vector acting to the structure
Q_n	Modal Volume acceleration
ρ_0	Density of air
c_0	Speed of sound in air
P	Uniform Pressure acting to the structure
v	Panel out of plane velocity
D	Length of unit cell cavity
Z_{MPP}	Impedance of microperforated panel
Z_{HC}	Impedance to the enclosed cavity
R_1	Acoustic Resistance of microperforated panel
M_1	Acoustic Reactance of microperforated panel
p	MPP perforation ratio
k	Wave number
$Z_{MPP\text{-}HC}$	Impedance of MPP with cavity
$Z_{GO\text{-}HC}$	Impedance of GO foil with cavity
Z_T	Total impedance of combined configurations
α	Absorption Coefficient
l_1, l_2	Dimension of unit cell cavity
t_{GO}	Thickness of GO foil
t_{MPP}	Thickness of Microperforated panel
V	Cavity Volume
S	Perforation area
λ_{ij}	Dimensionless function of the mode index
E	Membrane Elastic Modulus
a	Characteristic dimension of the membrane
γ	Membrane mass per unit area
υ	Poisson Ratio

Graphite-Oxide hybrid multi-degree of freedom resonator metamaterial for broadband sound absorption

F. Bucciarelli[(1)], G.P. Malfense Fierro[(1)], M. Rapisarda[(1)], M. Meo[(1)]*

[1] Department of Mechanical Engineering, University of Bath, Claverton Down, Bath, United Kingdom, BA2 7AY

* Michele Meo: m.meo@bath.ac.uk

Abstract

Low frequency broadband sound absorption for thin structures is still a great challenge. A new concept of a stackable hybrid resonator metamaterial is proposed which exhibits super broadband low-frequency sound absorption. The proposed metamaterial is based on micrometric scale thickness Graphene Oxide (GO) embedded in a stacked structure or used as external skin in a designed honeycomb (HC) structure. The stackable nature of the proposed structure allows the GO-HC cores to be embedded within micro-perforated panels (MPP) providing enhanced stiffness/strength to the structure and high absorption characteristics. We demonstrate how the exploitation of the GO elastic and mass properties result in multiple hybrid structural-acoustic resonances. These resonances are tailored to occur in a frequency range of interest by the theoretical calculation of the sound absorption coefficient. The theoretical model combines the mutual interaction between the structural dynamic of the GO foil and acoustic higher modes of the HC core cell as well as stacked MPP-HC/GO-HC cores. The result is a multi-degree of freedom hybrid resonator which provides subwavelength scale perfect sound absorption in broadband low frequency range between 300Hz to 2500Hz.

Introduction

Acoustic metamaterials are engineered materials with periodic structure which have wide range of capabilities in sound wave manipulations, enabling phenomena such as acoustic cloaking [1], sound insulation [2-3] and sound absorption[5-6-37]. This new class of materials are designed most of the time to show unusual physical behaviours such as negative effective, modulus [7-8], negative effective density [9-10] and both the negative effects simultaneously [11]. Focusing on the sound absorption, the development of acoustic metamaterials are trying to meet the growing and challenging need for broadband sound absorption at low frequencies while maintaining sub-wavelength thickness. Porous absorbers need considerable thickness to maximize the absorption performance at low frequencies since the minimum thickness required is usually one order of magnitude smaller than the incident wavelength [12-13]. Based on localised resonances [4-9-14-15] and monopolar/dipolar resonances [16-17], several membrane-type metamaterials have been proposed in last few years which can fully absorb low frequency sound waves with a deep subwavelength. However, most of these devices behave as a single degree of freedom resonator, thus as the wavelength increases relative to the size of the absorber, the narrower the frequency band [18]. Metamaterials based on the space-coiling approach [19] are suitable for full low frequency absorption. This class of metamaterial allow for the design of ultrathin structures and overcome the ¼ wavelength (λ) limitation of resonators using coplanar coiled chambers [20-21-22]. The effective absorption frequency band of metamaterials can be increased by combining multiple single resonators or multiple Fabry-Perot channels in series or parallel [23-24]. An effective approach for reducing the size of the structure and ensuring broadband absorption is by combining the effect of a miroperforated panel (MPP) with a coiled up Fabry-Perot channels [25] or honeycomb structure [26]. In particular, Tang [27] proposed a hybrid metamaterial where a MPP was combined with a perforated honeycomb-corrugation hybrid core achieving an absorption level over 50% in a frequency range between 290Hz to 1000Hz with a structural thickness of 60mm.

However, the problem of expanding the low frequency band of subwavelength metamaterial absorber remains relevant and crucial for acoustic engineering.
In the last few years there is a strong ongoing interest for Graphene-derived materials such as the Graphene Oxide (GO). Since GO can be easily functionalised via chemical, thermal or mechanical routes, it has several applications such as water treatment, energy storage, and composite reinforcements, among others [28-29-30-31-32]. However, only recently, GO has started to be of interest in acoustic engineering for sound absorption applications. Nine et al. [33] used a melamine foam as structural support to create a lamella network of self-assembled GO micro-sheets obtained by dipping the support foam in an aqueous GO solution. This 26mm GO lamella network increased the air-flow resistance and tortuosity consequently enhancing sound absorption coefficient resulting in 60% absorption over 800Hz. Good sound absorption performance was achieved by Oh et al. [34-35] who proposed a periodically self-aligned and hierarchically porous graphene-polyurethane foam. The 3D graphene microstructure into the open cell of existing polyurethane foam was achieved by hybrid physical-chemical crosslinking of graphene oxide liquid crystal-like structure. The result is a broadband absorption over 60% between 1000Hz to 6300Hz. Recently, Lu et al. [36] developed a 60mm thickness bubbled graphene monolith, obtained via the freeze-casting of a GO dispersion, with a normalized absorption coefficient of 0.9 from about 60 Hz to 6300 Hz.

In this report GO foil is used to realise a subwavelength hybrid metamaterial suitable for low frequencies broadband sound absorption. Starting from designed and machined Honeycomb core structure (HC) with millimetre scale square unit cells; two main configurations are presented. The first one includes micrometric thickness GO foil embedded on the HC core and used also as external skin (GOHCGOHC). The second is still considering the embedded GO foil but the external skin is changed with a millimetric Microperforated Panel (MPPHCGOHC). The first configuration define a plate-type resonator metamaterial, where the GO foil is studied as a vibrating plate and the HC core unit

cell represents the acoustic resonator chamber. While in the second configuration the plate-type effect of the GO-HC structure is combined with the MPP absorber properties where the HC core unit cell is still the resonator chamber of the MPP absorber. We demonstrate how the proposed GO based metamaterials behave as a multi degree of freedom resonator, generating hybrid structural-acoustic resonances due to the mutual interaction of GO foil vibration resonances and higher acoustic resonance modes which contribute to the dissipation energy of the incoming sound wave.

As a results the proposed hybrid metamaterial provide a perfect sound absorption in a frequency range 300Hz to 2500Hz.

Theoretical Framework

Based on 3D geometrical model of one unit cell, an analytical model is developed and experimental validated to describe the acoustic performances in terms of sound absorption for the different proposed configurations of the GO hybrid resonator metamaterial.

The proposed hybrid metamaterial is a periodic structure defined by its unit cell shown in Figure 8.1. The normal sound absorption is calculated by the acoustic impedance definition of the single unit cell. Regarding the plate covered cavity configuration (GOHC structure), the acoustic impedance is estimated solving coupled acoustic-structural problem, while the MPP absorber configuration (MPPHC structure) is described by the equivalent electric circuit approach.

The GOHC structure can be considered a plate covered cavity. A modal coupling theory based on fluid-structure interaction was used to calculate the coupled vibro-acoustic response. This information was then used to determine the absorption of the evaluated system. Membrane sound absorbers generally consist of rigid sides and back, covered with limp lightweight fronts and are used for low frequency absorption applications (but not limited to this). Predicting the response of these structures provides a quick tool to evaluate and design for specific acoustic conditions. In this case, the model was used to provide a quick analytical solution

which was validated by the experimental results. The analytical model used in this work follows that outlined in [39], where equations for determining the coupled structural-acoustic displacement response of a system are described [40]:

$$\begin{bmatrix} \Lambda_m(\omega_m^2 - \omega^2) & -S[C_{nm}]^T \\ (-\omega^2)S[C_{nm}] & \frac{\Lambda_n}{\rho_0 c_0^2}(\omega_n^2 - \omega^2) \end{bmatrix} \begin{bmatrix} w_m \\ p_n \end{bmatrix} = \begin{bmatrix} F_m \\ Q_n \end{bmatrix} \quad (1)$$

where: m and n are the structural and acoustic modes, w_m is a vector of all structural modal participation factors, p_n is a vector of all the acoustic modal participation factors. Q_n is the modal volume acceleration, S is the total surface area of the structure in contact with the acoustic fluid, C_{nm} is the dimensionless coupling coefficient, F_m is the force acting on the structure, Λ_m is the modal mass and Λ_n the modal volume, ω is the structural displacement at a given frequency, ω_m structural modal participation factor, ω_n natural frequencies of the cavity, ρ_0 density of the fliud, c_0 speed of sound of sound in the fluid.

The acoustic impedance of the membrane covered cavity (Z_{GO-HC}) can be calculated as follows:

$$Z_{GO-HC} = \frac{P}{\rho_0 c_0 v} \quad (2)$$

Where P is the external uniformly distributed sound pressure acting on the panel, v velocity at depth of D.

The acoustic impedance of the MPPHC structure is calculated according with electric equivalent model proposed by Maa [44]. In this model the acoustic impedance for an MPP absorber is expressed as a series of the acoustic impedance related to the panel (Z_{MPP}) and the acoustic impedance related to the enclosed cavity (Z_{HC}). Moreover, the complex impedance for the MPP can be expressed in terms of real and imaginary part. The real part, named acoustic resistance (R_1) represent the energy radiation and the viscous loses of the acoustic wave propagating through the perforations. The imaginary part, named acoustic reactance (M_1) refers the mass of the air moving inside the perforation.

$$Z_{MPP} = \frac{Z_1}{p\rho_0 c} = R_1 - i\omega M_1 \quad (3)$$

where p is the panel perforation ratio.

The acoustic impedance associated to the honeycomb core cell, which represents the enclosed cavity for the MPP absorber, depends on the mass of air behind the panel which is a function of the cavity depth

$$Z_{HC} = i\cot(Dk) \quad (4)$$

With k the wavenumber.

Then the acoustic impedance for the MPP absorber is expressed as follow:

$$Z_{MPP-HC} = \left(\frac{1}{R_1 - i\omega M_1}\right)^{-1} + Z_{HC} \quad (5)$$

The sound absorption of the hybrid structure, considering a normal incidence plane wave, can be calculated theoretically by determining the total acoustic impedance (Z_T) of the structure. The hybrid MPPHC and GOHC structures require two separate approaches in order to calculate the total acoustic impedance. The structure can be considered a series-parallel connection system when considered in the format: MPPHCGOHC or GOHCGOHC [41-42]. The absorption coefficient (α) [43] can then be calculated from the equations below:

$$\begin{aligned} Z_T &= Z_{MPP-HC} + Z_{GO-HC} \\ Z_T &= Z_{GO-HC} + Z_{GO-HC} \end{aligned} \quad (6)$$

$$\alpha = \frac{4\mathrm{Re}(Z_T)}{(1+\mathrm{Re}(Z_T))^2 + (1+\mathrm{Im}(Z_T))^2} \quad (7)$$

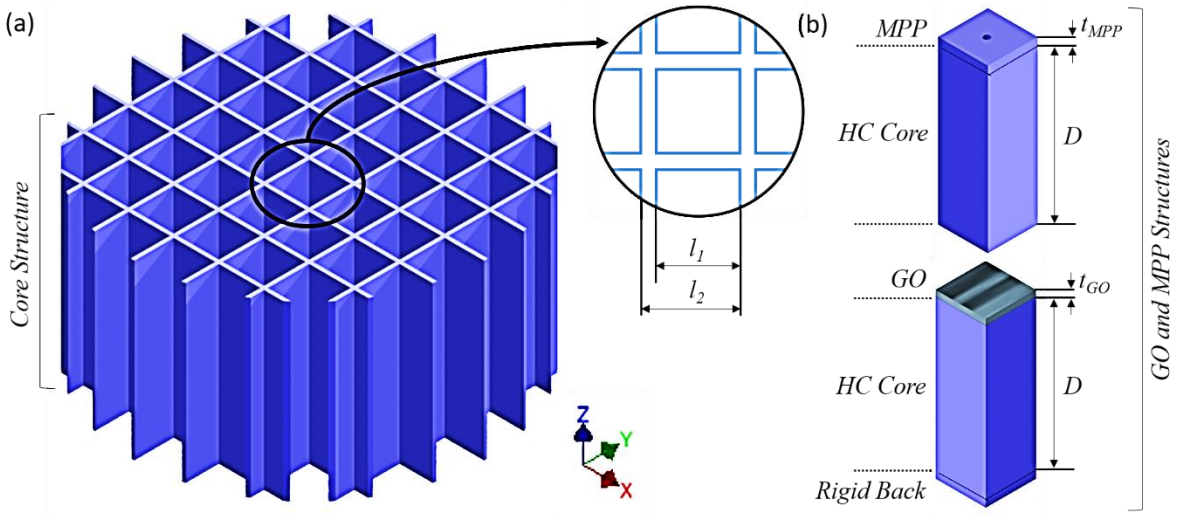

Figure 8.1. (a) Schematic of honeycomb (HC) structure which is either composed of a micro-perforated panel (MPP) as a top facesheet or a graphite oxide (GO) layer, (b) Unit cell of MPP-HC and GO-HC. Sound absorption of the metamaterial is investigated from a plane acoustic wave normally incident to the top facesheet.

Results and Comments

Broadband sound absorption at low frequencies for proposed HGO

In order to achieve perfect sound absorption at low frequencies different thicknesses of GOHCGOHC and MPPHCGOHC structures are investigated. Keeping constant the geometry of the HC unit cell (l_1 and l_2), the GO foil thickness and the geometrical characteristic of the MPP (panel thickness, perforation ratio and perforation diameters), the proposed hybrid structures behave different varying the HC core thickness. In particular we compared the absorption properties of hybrid structures with three different global thickness 30mm, 50mm and 70mm with the design parameters summarized in Table1.

A good agreement between the experimental results and the analytical ones is shown in Figure 8.2 except for the boundary frequency regions of the plot where the discrepancies are mainly due to the limit working frequency range of the experimental test rig. A perfect broadband sound absorption is achieved with all the different thickness configurations.

Sample	*Structure*	*GO Foil Thickness (μm)*	*HC core Thickness (mm)*	*MPP thickness (mm)*	*MPP perforation ratio (%)*	*Total thickness (mm)*
GOHCGOHC-30	GO Foil + HC + GO Foil + HC	30	15			30
MPPHCGOHC-30	MPP + HC core + GO Foil + HC core	30	15	1.5	6.0	30
GOHCGOHC-50	GO Foil + HC + GO Foil + HC	30	25			50
MPPHCGOHC-50	MPP + HC core + GO Foil + HC core	30	25	1.5	6.0	50
GOHCGOHC-70	GO Foil + HC + GO Foil + HC	30	35			70
MPPHCGOHC-70	MPP + HC core + GO Foil + HC core	30	35	1.5	6.0	70

Table 1. Design parameters of proposed GOHCGOHC and MPPHCGOHC structures with different HC thickness

However, increasing the core HC thickness and as a consequence the global structure thickness, the broad absorption is shifting at lower frequencies because the acoustic resonances of the single HC core cavity is proportional to the acoustic volume of the cavity itself. In particular 15mm thickness of the single HC core and 30mm global structure thickness allows a broadband absorption from 550Hz with global sound absorption over 50% and over 90% from 1400Hz. 50mm global thickness result the best configuration in terms of broadening sound absorption with absorption properties over 50% from 300Hz and over 90% from 700Hz. Increasing the global thickness to 70mm, the maximum absorption is moving at lower frequencies but with a reduction of the broadening properties compared with the 50mm thickness. In this case we can guarantee a sound absorption over 90% from

400Hz but we reduce the capability of perfect sound absorption over 1500Hz. Moreover, we demonstrate how, keeping constant the thickness and all the other geometrical parameters, using an MPP with high perforation ratio as external skin for the hybrid resonator the same sound absorption properties are guaranteed compared with a GO foil as external skin. To investigate the effect of the perforation ratio on the sound absorption properties, two different perforation ratios are compared in Figure 8.3. In particular the MPPHOGOHC structure with 2% and 6% of MPP perforation ratio are compared with equivalent GOHCGOHC with 50mm thickness.

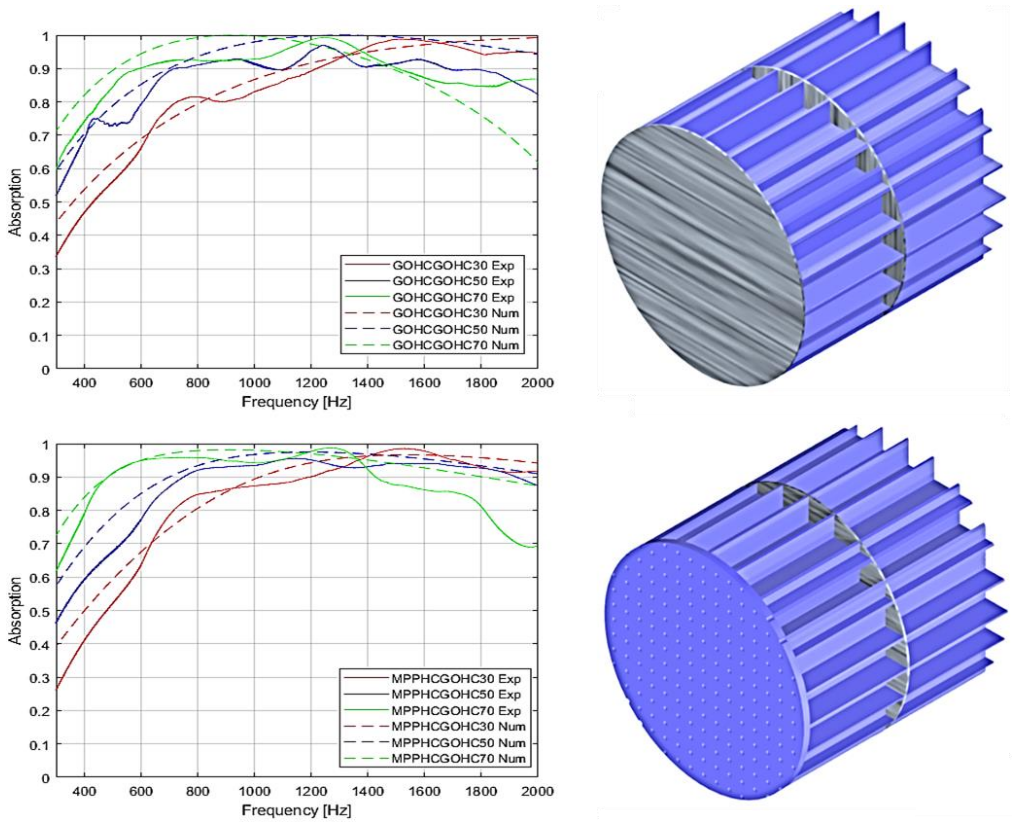

Figure 8.2. Absorption coefficient for the proposed MPPHCGOHC and GOHCGOHC structures with different thickness compared with the analytical results

As shown in Figure 8.3 the sound absorption properties of the MPPGOHCGO structure is strictly related to the entity of perforation because depending on the perforation ratio the effect of GO embedded foil will be considerable or not. For small grade of perforation, the absorption profile shows a unitary peak at 620Hz which is due to the main resonance of the preceding MPP absorber. In fact

comparing the absorption profile of the MPPHCGOHC and the equivalent MPPHC structure with same perforation ratio, we can identify the same trend with single absorption peaks at same frequency 620Hz. In other words, the effect of the GO embedded foil is negligible for low perforation ratio. So for the MPPHCGOHC structure with 2% of perforation, the GO induce a small contribution to increase the absorption level at higher frequencies, but the absorption properties are mainly dominated by the preceding MPP structure because the dynamic of the GO is not excite by the incoming sound wave due to the low porosity. However, increasing the perforation ratio to 6%, there is a complete superposition principle, so the net absorption performances of MPPHCHOHC structure is the combination result between the low frequency absorption due the resonance plus the viscous loss of the preceding MPP and the broadening effect associated to the to the embedded GO foil.

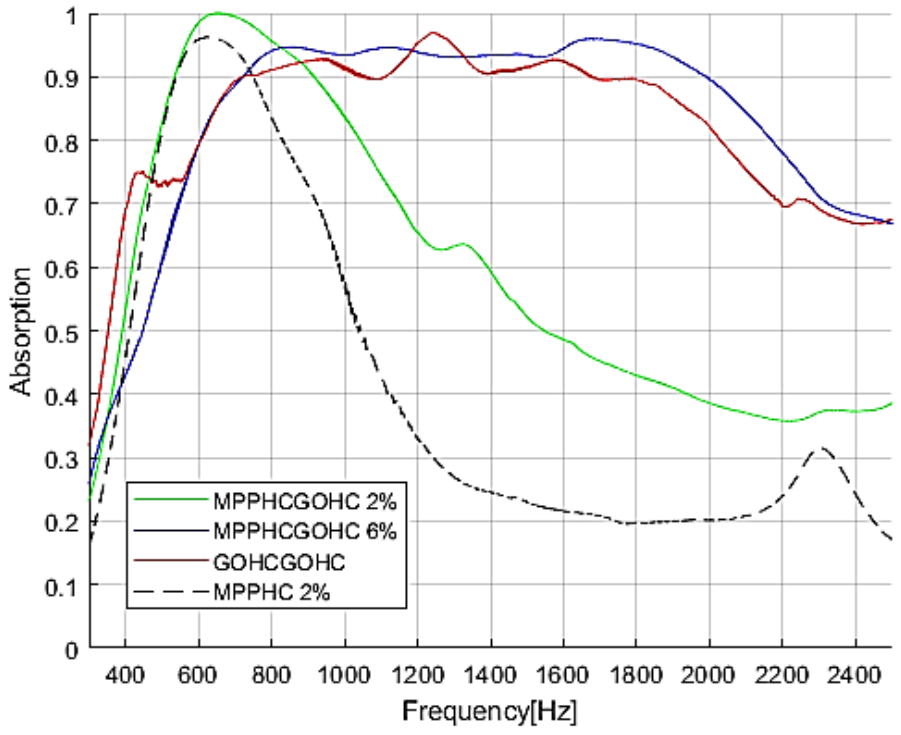

Figure 8.3. Comparison of GOHCGOHC structure with the MPPHCGOHC structure with different perforation ratio (2% and 6%) and the MPPHC structure. The global thickness of the structures is 50mm

To demonstrate the advantages induced by the GO on the absorption performances, the proposed GOHCGOHC and MPPHCGOHC with the equivalent commonly used MPP absorber backed by air cavity and MPP backed by HC core. The compared structures, reported in Table 2, are tested keeping constant the global thickness of the structure 50mm. The compared structure present the same HC core unit cell geometry and the same geometrical parameter for the MPP.

Sample	***Structure***	***GO Foil Thickness (μm)***	***HC core Thickness (mm)***	***MPP thickness (mm)***	***MPP perforation ratio (%)***	***Air-Gap (mm)***
GOHCGOHC-50	GO Foil + HC + GO Foil + HC	30	25			
MPPHCGOHC-50	MPP + HC core + GO Foil + HC core	30	25	1.5	6.0	
MPP	MPP + Air-Gap			1.5	6.0	50
MPPHC	MPP + HC core		50	1.5	6.0	
MPPHCMPPHC	MPP + HC core + MPP + HC core		25	1.5	6.0	

Table 2. Design parameters for the proposed metamaterial structure and the equivalent commonly used absorber based on MPP. The global thickness for all the tested structure is 50mm.

In Figure 8.4 are plotted the absorption coefficient measured for the 5 tested structures. As expected the MPP absorber realized by micro perforated panel with submillimetre perforation comparable with the boundary layer thickness and a resonant enclosed air cavity, is characterized by a single absorption peak around the resonance frequency $f = \frac{c_0}{2\pi}\sqrt{\frac{S}{VL}}$ [38], where c_0 is the speed of sound, S is the perforation area and V is the cavity volume. In fact the MPP absorber behave as a

mass spring single degree of freedom system where the mass is the mass moving into the perforation and the stiffness is related to volume of air in the resonant cavity, so the absorption present only one peaks related to the system resonance around 1100Hz. The designed honeycomb core doesn't affect the absorption performances of the MPP in terms of broadening or shifting in frequency the absorption peak. Because of the regularity of the core size, no fluctuation or changes in the perforation ratio between the core unit cells could affect the sound absorption. As a result, the single core cell of the MPPHC structure acts as a single MPP absorber with the same perforation ratio and an equivalent cavity volume, which is characterized by the same resonance frequency. However, a small enhancement in the absorption level is measured due to the contribution of all the core cell to the sound absorption. Considering now the MPPHCMPPHC where the embedded Go foil is replaced by a second MPP. As demonstrated in previous work [49], the effect on the sound absorption of a MPP series is to sum the single MPP contribution. Then the absorption profile is characterized by two main absorption peaks, the first one at same frequency of the MPPHC structure associated to the first MPP backed by 50mm thickness of acoustic resonant volume, and the second one related to second MPP which is backed by a smaller resonator acoustic volume (25mm).

Therefore, the proposed GOHCGOHC and MPPHCGOHC metamaterial resonator show the best low-frequency and broadband sound absorption properties. Such metamaterials represent a powerful subwavelength ($^{1}/_{14}\,\lambda$) solution for broadband sound absorption at low frequencies.

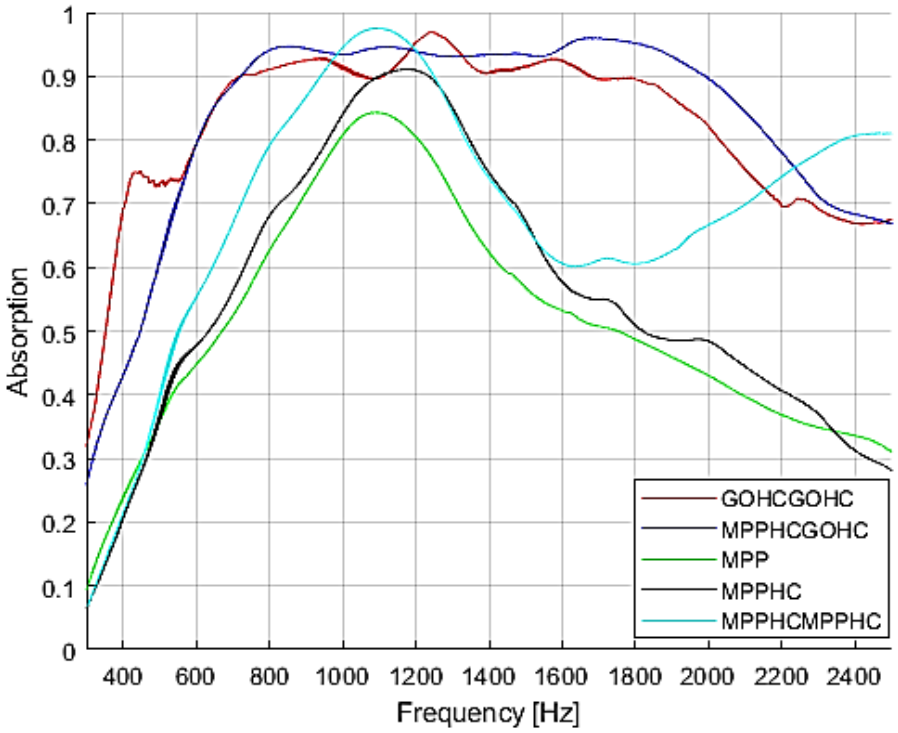

Figure 8.4. Comparison between the proposed metamaterial structure GOHCGOHC and MPPHCGPHC, the MPP absorber, the MPPHC structure and MPPHCMPPHC structure. All the tested structure present the same global thickness (50mmm) and the same geometrical parameter (MPP thickness 1.5mm, perforation ratio 6% GO foil thickness 30 μm)

GO based metamaterial as multi degree of freedom hybrid resonator

In Figure 8.2 we saw how there is a perfect match between the experimental results and the analytical results for the proposed GOHCGOHC structure metamaterial, which means that the coupled acoustic-structural dynamic model used to describe the metamaterial structure is accurate. In fact the impressive results in terms of absorption are due to the fact that the unit cell of the proposed metamaterial doesn't behave as single degree of freedom resonator, as the common MPP absorbers of the membrane-type metamaterial, but as multi degree of freedom resonator and the absorption broadening characteristics are then associated to multiple hybrid resonances. We demonstrated in a previous work [48] how considering thin plate with enclosed airgap, because of the fluid-structure interaction, the plate doesn't

behave as a piston system as the other membrane-type acoustic metamaterials [9-14-17]. Considering the single HC core unit cell, it acts as a senator acoustic cavity covered by the GO foil which acts as plate fixed supported on the HC cell edges. There is a mutual interaction between the GO foil and the HC core cavity. The vibration of GO foil is perturbed by the fluid pressure loading and the acoustic filed in the cavity is influenced by the dynamic response of the foil itself. In particular, the non-uniform pressure distribution due to higher acoustic modes of the HC core cavity will act on the GO foil which, on the other hand will react according with its intrinsic mode shapes related to its structural resonances excited by the incoming sound wave excitation. This interaction between the higher acoustic modes and structural modes generated multiple hybrid resonances which dissipate the sound energy associated to the incoming sound wave. As a consequence, the multiple hybrid resonances coming out from the interaction between the high orders vibration modes of the GO foil and the non-uniform pressure distribution on the HC cavity due to the higher acoustic modes, guarantee a broadband sound absorption. To achieve a higher absorption at lower frequencies two GOHC structures are stuck together forming the GOHCGOHC structure. In this case, the interaction between the high order structural modes of the GO foil and the higher acoustic modes of the cavity are still on introducing multiple hybrid resonances and ensuring a broadband absorption. Moreover, for the GOHCGOHC the first GO layer sees a global acoustic volume of 50mm thickness due to the two stuck HC core which means moving a lower frequency the acoustic mode of the HC cavity.

The absorption performances of metamaterial are usually strictly related to the acoustic impedance and acoustic reactance in order to achieve an impedance matching. The class of resonator metamaterial in particular are characterize by zero acoustic reactance ($Im(Z_T)=0$) which indicates the resonance frequency of the acoustic chamber and unitary acoustic resistance ($Re(Z_T)=1$) which indicates impedance matching with the impedance of air [21-27]. In Figure 8.5 we plot the acoustic reactance and the acoustic resistance for the proposed hybrid metamaterial structure. Starting from the MPPHCGOHC with 2% of perforation ratio structure (green line), the acoustic resistance cross 1 at 600Hz and at same frequency the

acoustic reactance is zero. The combination of zero reactance and unitary resistance confirms that for this structure the GO effect is negligible and the perfect absorption at 600Hz is due to the acoustic resonance of the HC core cell ($Im(Z_T)=0$) and impedance matching ($Re(Z_T)=1$) due to the MPP as for other resonator metamaterials. Increasing the perforation ratio, the effect of the GO becomes important on the absorption characteristic. In fact, for the MPPHCGOHC structure with 6% of perforation ratio, the reactance is zero around 1600Hz which the frequency where the preceding MPPHC structure presents the main acoustic resonance of the HC core cell, but the acoustic resistance is never equal 1 in the frequency range of interest. Together with GOHCGOHC structure is analysed also the single GOHC structure which show, and completely different behaviour compared with the usual resonator metamaterials. The acoustic resistance never assumes unitary value but is constant around zero which means that the great absorption properties of this structure are not related to impedance matching with the incoming sound wave. However, the acoustic reactance is always positive and assume an asymptotic behaviour to zero but it is never zero in the frequency range of interest. This confirm the hypothesis that the broadband absorption for the GOHC structures is associated to the multiple hybrid resonances not only associated to the acoustic resonance of the HC cavity but to the mutual interaction between the structural dynamic response for the GO foil and the higher acoustic modes of the HC cell, as discussed above. The better acoustic performances are also confirmed from the acoustic reactance plot, where moving from GOHC to GOHCGOHC structure the reactance is more important because it has a larger quantity in the low frequency range.

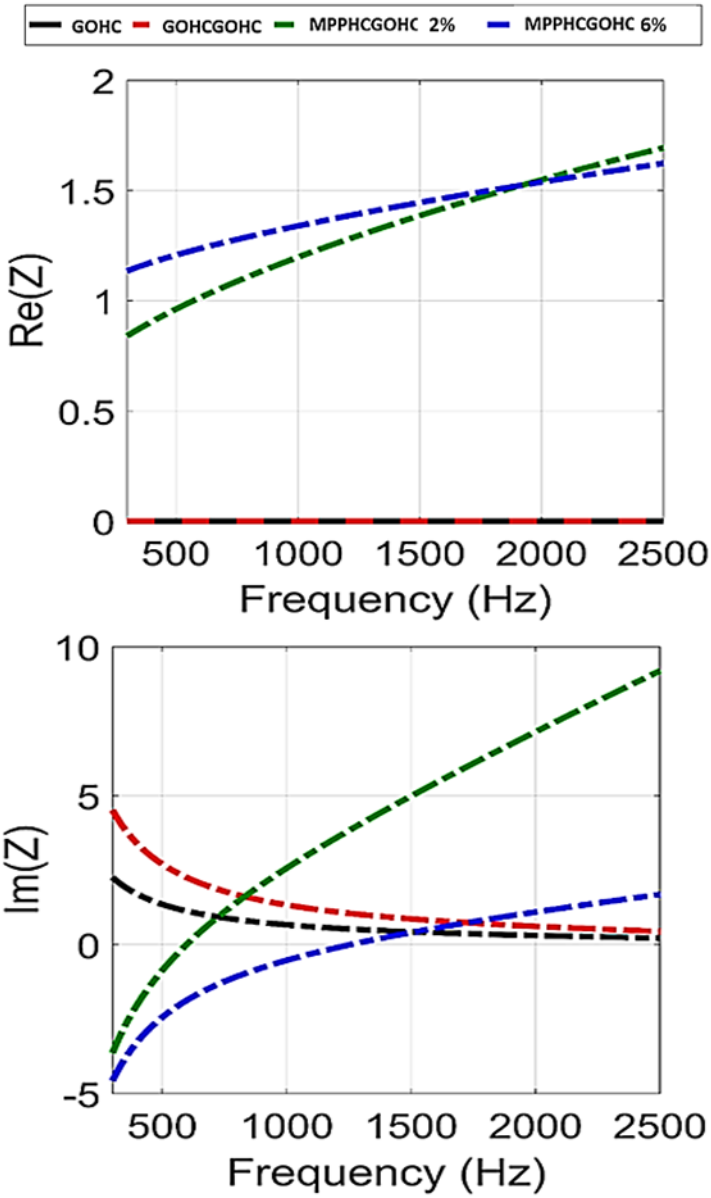

Figure 8.5. Acoustic Reactance (Im(ZT)) and Acoustic Resistance (Re(ZT)) for the proposed Hybrid metamaterial structures: GOHC, GOHCGOHC, MPPHCGOHC with 2% of perforation ratio and MPPHCGOHC with 6% of perforation ratio

Methods

GO Hybrid Metamaterial Manufacturing

The proposed metamaterial consisted of various combinations of MPP-HC and GO-HC as outlined in Figure 8.1. The HC core structure was 3d printed using stereolithographic technology using Formlabs Tough Resin (refer to Method for detail) which has good mechanical stiffness and strength, thus it is considered acoustically rigid in the theoretical model. An aluminium facesheet was used as the backing of the structure when tested in an Impedance Tube test rig. The HC core has a square cross-section with an inner side length l_1 (6mm) and a unit cell side length l_2 (6.5mm, refer to Figure 8.1 (a)). The thickness of the MPP and GO top facesheets are t_{MPP} (t_{MPP} = 1.5mm) and t_{GO} (t_{GO} = 30μm). The depth of the HC core is D (25mm, if not otherwise specified), with multiple cores stacked to increase this depth. This design of the metamaterial combines the effects of the MPP resonator with that of a membrane covered cavity.

The GO micro-sheets were manufactured starting from Graphite Oxide (GtO) powder through sonication treatments (Figure 8.6). GtO powder (TOB-2430, Xiamen TOB New Energy Co., LTD) was added to distilled water and gently stirred for 30 min to obtain a dispersion with a concentration of 8 mg ml-1. The GtO dispersion was then exfoliated to GO thanks to the mechanical excitation provided by a probe sonicator (UP100H, Dr. Hielscher GmbH) for 1 h with 100 % amplitude and continuous power discharge, under an ice bath to prevent the temperature to raise and with gentle stirring to ensure a homogeneous exfoliation process. The obtained slurry was then casted in PTFE moulds, exploiting its low surface free energy for an easy release of the foils, with a circular shape of 8 cm diameter. The thickness of each sample was controlled by adjusting the volume of the GO suspension poured inside the mould. The GO Foils were finally obtained, peeling them off the PTFE moulds after 24 hours of oven drying at 40 °C, and cut to the desired size.

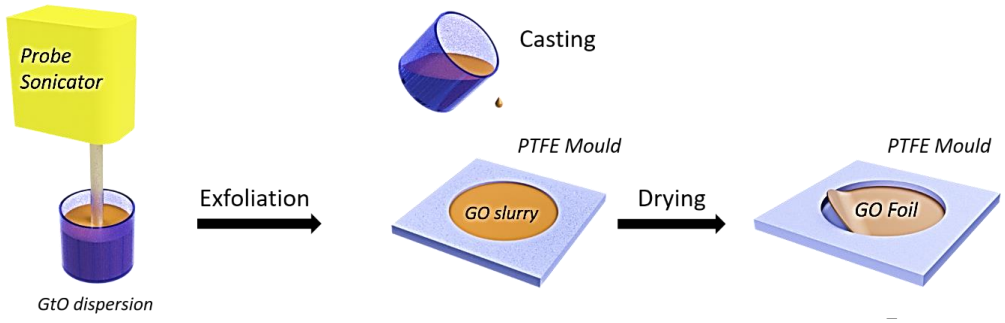

Figure 8.6. Manufacturing process scheme of GO micro-sheets

Graphite-Oxide characterization

First microscopic characterization of GO foil was performed through scanning electron microscopy (SEM) analysis and X-Ray diffraction analysis.

The surface of a GO Foil specimen imaged via scanning electron microscopy (SEM) shows a distinctive chain-like pattern in the low magnification image, attributable to the stress induced by the surface tension between the liquid suspension and the sides of the mould during the drying process (Figure 8.7-a). In the high magnification image, it's worth noting that during the self-assembly of the foil a wrinkled morphology is obtained (Figure 8.7-b), made by the non-ordered overlapping of GO layers. The cross-section images of a cryogenically fractured GO Foil confirmed the non-ordered overlapping of GO layers and revealed a nanolayered structure where each layer, having a thickness of few nanometres, is well distinguishable (Figure 8.7-c).

The X-Ray diffraction patterns of the pristine GtO powder and GO Foil are shown in Figure 8.8-a. The (001) reflection peak, typical in GtO and useful to characterize the interplanar spacing (d-spacing) between the oxidised graphene layers [45], is found at $2\theta = 11.20°$ with its amplitude strongly reduced and its position slightly shifted to $2\theta = 11.59°$ after the exfoliation and casting process. The application of Bragg's law allowed the calculation of d-spacings in in GtO powder and GO Foil, with results of respectively $d = 7.89$ Å and $d = 7.63$ Å. These findings confirm a

successful exfoliation of GtO in GO and that no restacking happened during the foil manufacturing process, in accordance with Kashayap et al. work [46].

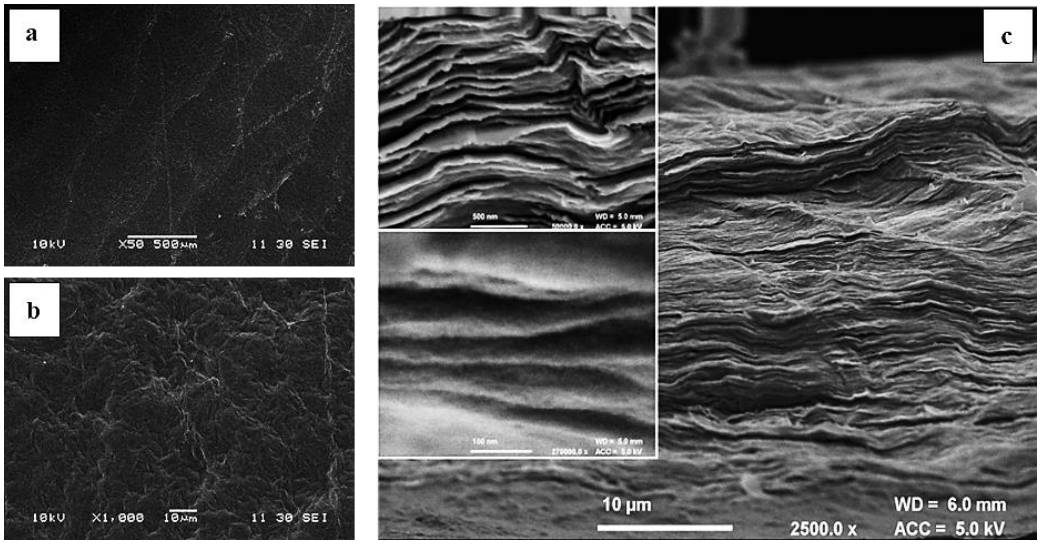

Figure 8.7. (a) Low-magnification SEM image of GO foil. (b) High magnification (10000x) SEM image of GO foil. (c) Cross section SEM image of GO foil with onset at higher magnification (top100k, bottom 270k)

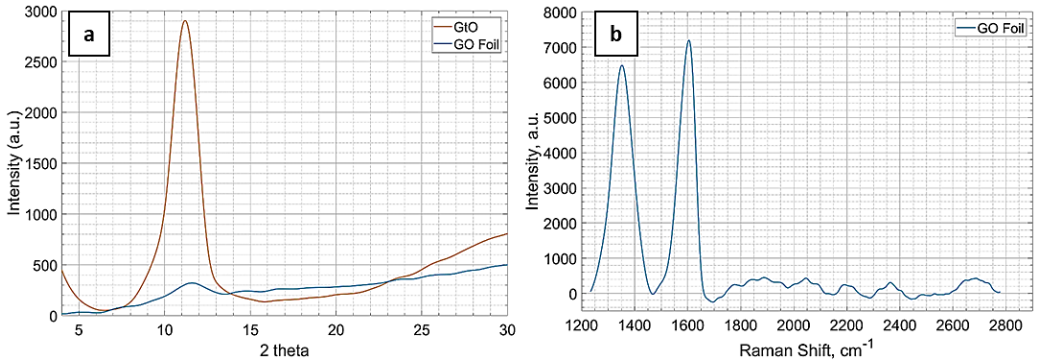

Figure 8.8. (a) XRD patterns of GtO powder and GO Foil. (b) Raman spectra of the GO Foil

The Raman spectra in Figure 8.8-b presents the typical D and G bands of carbon materials at respectively 1352 cm-1 and 1604 cm-1. The first arises from breathing modes of sp2 atoms in rings while the second is characteristic of primary in plane vibrations mode, their intensity ratio (D/G ratio) can be used to describe the order of the system: in single layer graphene it approaches zero while higher values are associated to more disordered structures [47].A D/G ratio of 0.88 was found for the

GO Foil, confirming the existence of structural defects introduced after the oxidation of Graphite.

Macroscopic characterization was also performed to investigate the elastic properties of the GO foil. In particular the Elastic Modulus of manufactured GO foil was measured using a non-destructive approach based on the resonances of the foil. The used non-destructive approach is based on the plate's theory. According with [37] the natural frequencies are function of the indices associated with the number of flexural half-waves in the two plate dimensions. Moreover, they are related to the material properties following the equation

$$f_{ij} = \frac{\lambda_{IJ}^2}{2\pi a^2}\left[\frac{E {t_{GO}}^3}{12\gamma(1-\nu^2)}\right]^2 \qquad \begin{cases} i = 1,2,3,\dots \\ j = 1,2,3,\dots \end{cases} \tag{8}$$

where λ_{ij} is a dimensionless which is function of the mode indices, a is the characteristic dimension of the plate, h is the plate thickness, ν is the Poisson's ration, E the Young modulus and γ is the mass per unit area of the plate. So the equation (8) can be solved in term of E when the i-j-th natural frequency is known. So the GO foil of 35μm thickness (h) and 0.0254m radius (a) is placed in one end of an impedance tube and a plane wave generated into the tube is used to excite the foil. The structural dynamic response of the plate is measured focusing a laser-vibrometer on a grid of points on the downstream surface of the foil. Since a plane wave can excite only the symmetric bending modes of the foil, from the measured frequency response function, the frequencies of i-j-th bending mode can be estimated.

Considering a circular plate under clamped edges boundary conditions and normal distributed load, the dimensionless parameter $\lambda_{01} = 39.77$ for i=0 and j=1 (according with [37]), and the natural frequency for such mode is 160Hz (according with equation (8)). So for the proposed GO foil the elastic modulus is E =2.9 e+09 Pa. This result was confirmed by Dynamic Mechanical Analysis (DMA, Tritec 2000 DMA, Tryton Technology Ltd) in tension mode with ramp loading of 0.02 N min-1 applied on GO specimen cut in stripes (20mm x 5mm). The Elastic Modulus extracted from the measured stress-strain curve was 3.1 GPa.

This result was confirmed by Dynamic Mechanical Analysis (DMA, Tritec 2000 DMA, Tryton Technology Ltd).

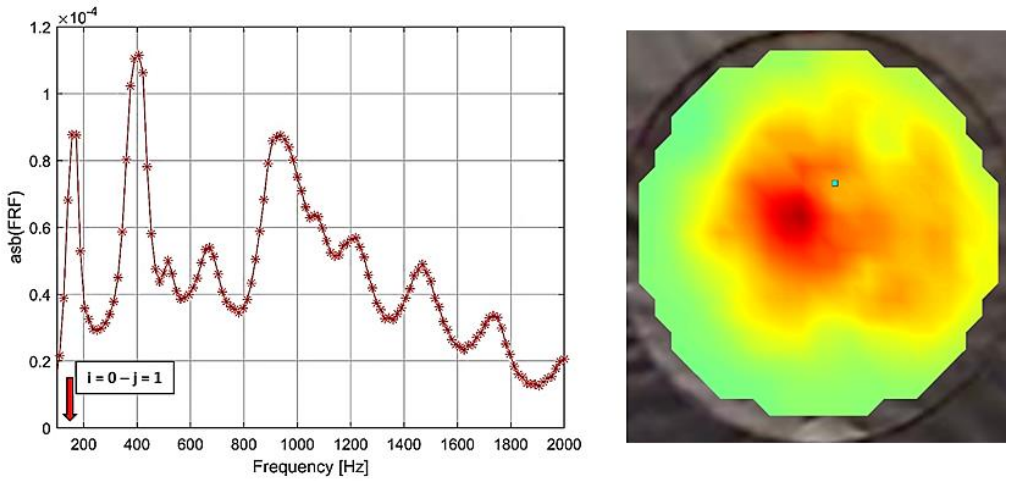

Figure 8.9. Frequency response function of Graphene-Oxide foil (h = 35 μm, a = 0.0254 m, ρ=1800Kg/m3), and mode shape (i = 0, j = 1) measured by laser-vibrometer rig.

Acoustic properties measurement test rig

The acoustic performance in terms of normal sound absorption was characterized with an in-house impedance tube test rig, consisting of an aluminium impedance tube with circular cross section and internal dimeter of 50.8mm, a full range speaker (2", BMS 4592 Compression Driver), pressure-field microphones (1/4", 10mV/Pa, GRAS 40PL-CCP Free-field Array Microphones), audio power amplifier (model: Behringer: NU1000, High-Density 1000-Watt Power Amplifier), data acquisition device (24-bit, 105.4 kS/s/ch, model: DT9837C Dynamic Signal Analyser, Data Translation)**.** The standardized Transfer Function Method was used to measure the normal sound absorption coefficient staring from the standing wave pressure measured at two microphone stations. The measured pressure signals were processed with LabView user interface implemented in the test rig.

Honeycomb structures were printed with Formlabs Form 3 (XY resolution 25µm, layer thickness 25µm, 250mW Laser Power) using Formlabs Tough Resin (https://formlabs-media.formlabs.com/datasheets/Tough_Technical.pdf).

Conclusion

Recently introduced and studied acoustic metamaterials, such as membrane-type metamaterials, Helmholtz's resonator-type metamaterials and MPP-type metamaterials allow good sound absorption properties at low frequencies, but the main goal of broadband sound absorption at low frequencies with relative thin structure is still challenging. In this report, we proposed a novel acoustic Hybrid Multi-Degree of Freedom resonator Metamaterial based on a lightweight honeycomb core structure (HC) with skin and embedded submillimetre Graphite Oxide (GO) foils. Two main configurations are proposed; GOHCGOHC and MPPHCGOHC, which provide perfect sound absorption while maintaining excellent mechanical stiffness/strength properties related to the HC core structure. Making use of the electro-acoustical equivalent circuit theory for the MPP and the coupled acoustic-structural motion equation for the GO and HC structure, we developed an analytical model to compute the absorption properties through the evaluation and combination of the acoustic impedance. The analytical and experimental results show good agreement, demonstrating that the proposed matematerial with GOHCGOHC and MPPHCGOHC structures achieve a nearly perfect broadband absorption at low frequencies. We demonstrated how the broadband characteristic is mainly due to multiple hybrid structural-acoustic resonances that arise because of mutual interaction between the high order structural and acoustic vibration modes. The proposed Hybrid GO based metamaterial with a structure of 50mm thickness represents a subwavelength acoustic metamaterial with outstanding nearly perfect absorption over a broadband low frequency range from 300Hz to 2500Hz.

References

1. B.-I Popa, L- Zigoneanu, S. A Cummer, Experimental Acoustic Ground Cloak in Air. Phys. Rev. Lett. 106, 253901 (2011).
2. G. D'Aguanno, K. Q. Le, R. Trimm, A. Alu, N. Mattiucci, A.D. Mathias, N. Akozbek, M. J. Bloemer, Broadband metamaterial for nonresonant matching of acoustic waves. Sci. Rep. 2, 340 (2012).
3. L. Fan, Z. Chen, S-Y Zhang, J. Ding, X-J Li, H. Zhang, An acoustic metamaterial composed of multi-layer membrane-coated perforated plates for low-frequency sound insulation. Appl. Phys. Lett. 106, 151908 (2015).
4. J. Mei, G. Ma, M. Yang, Z. Yang, W. Wen, P. Sheng, Dark acoustic metamaterials as super absorbers for low-frequency sound. Nat. Commun. 3, 756 (2012).
5. Y.Duan, J. Luo, G. Wang, Z. Hong Hang, B. Hou, J. Li, P. Sheng, Y. Lai, Theoretical requirements for broadband perfect absorption of acoustic waves by ultra-thin elastic meta-films. Sci. Rep. 5, 12139 (2015).
6. J. Christensen, V. Romero-Garcia, R. Pico, A. Cebrecos, F. J. Garcia de Abajo, N. A. Mortensen, M. Willatzen, V. J. Sanchez-Morcillo, Extraordinary absorption of sound in porous lamella-crystals. Sci. Rep. 4, 4674 (2014).
7. S. H. Lee, C. M. Park, Y. M. Seo, Z. G. Wang, C. K. Kim, Acoustic metamaterial with negative modulus, J. Phys.: Condens. Matter 21 175704, 2009.
8. C. Shen, Y. Jing, Side branch-based acoustic metamaterials with a broad-band negative bulk modulus, Appl. Phys. A (2014) 117:1885–1891, 2014.
9. Z. Yang, J. Mei, M. Yang, N. H. Chan, P. Sheng, Membrane-Type Acoustic Metamaterial with Negative Dynamic Mass. Phys. Rev. Lett. 101, 204301 (2008).
10. S. H. Lee, C. M. Park, Y. M. Seo, Z. G. Wang, C. K. Kim, Acoustic metamaterial with negative density. Phys. Lett. A. 373, 4464–4469 (2009).
11. S. H. Lee, C. M. Park, Y. M. Seo, Z. G. Wang, C. K. Kim, Composite Acoustic Medium with Simultaneously Negative Density and Modulus, Physical Review Letters, 104, 2010.
12. T.J. Lu, F. Xin, Vibro-acoustics of Lightweight Sandwich Structures, Springer, (2014).
13. M. Yang, P. Sheng, Sound Absorption Structures: From Porous Media to Acoustic Metamaterials, Ann. Rev. Mater. Res. 47:83-114, (2017).
14. G. Ma, M. Yang, S. Xiao, Z. Yang, P Sheng, Acoustic metasurface with hybrid resonances, Nat Mater.13, 873-878, (2014).
15. M. Yang, C. Meng, C. Fu, Y. Li, Z. Yang, P. Sheng, Subwavelength total acoustic absorption with degenerate resonators, Appl. Phys. Lett. 107(10), 104104 (2015).

16. M. Yang, G. Ma, Z. Yang, P. Sheng, Coupled membranes with doubly negative mass density and bulk modulus, Phys. Rev. Lett. 110(13), 134301, (2013).
17. J. Li, C. T. Chan, Double-negative acoustic metamaterial, Phys. Rev. E 70, 055602, (2004).
18. Y. Auregan, M. Farooqui, In-parallel resonators to increase the absorption of subwavelength acoustic absorbers in the mid-frequency range, Scientific Reports 9:11140(1), 2019.
19. Z. Liang, J. Li, Extreme Acoustic Metamaterial by coiling up space, Phys. Rev. Lett. 108, 114301, (2012).
20. X. Cai, Q. Guo, G. Hu, J. Yang, Ultrathin low-frequency sound absorbing panels based on coplanar spiral tubes or coplanar Helmholtz resonators, Applied Physics Letters 105, 121901, (2014).
21. Y. Li, B. M. Assouar, Acoustic metasurface-based perfect absorber with deep subwavelength thickness, Appl. Phys. Lett., 108, 063502, (2016).
22. C. Chen, Z. Du, G. Hu, J. Yang, A low-frequency sound absorbing material with subwavelength thickness, Appl. Phys. Lett. 110, 221903, (2017).
23. N. Jiménez, V. Romero-García, V. Pagneux, J-P. Groby, J.-P. Quasiperfect absorption by subwavelength acoustic panels in transmission using accumulation of resonances due to slow sound. Phys. Rev. B 95, 014205 (2017).
24. M. Yang, S. Chen, C. Fu, P. Sheng, P. Optimal sound-absorbing structures. Mater. Horizons 4, 673–680 (2017).
25. F. Wu, Y. Xiao, D. Yu, H. Zhao, Y. Wang, J. Wen, Low-frequency sound absorption of hybrid absorber based on micro-perforated panel and coiled-up channels, Appl. Phys. Lett. 114, 1581901, (2019).
26. X. Peng, J. Ji, Y. Jing, Composite honeycomb metasurface panel for broadband sound absorption, The Journal of the Acoustical Society of America 144, EL255 (2018).
27. Y. Tang, S. Ren, H. Meng, F. Xin, L. Huang, T. Chen, C. Zhang, T-J. Lu, Hybrid acoustic metamaterial as super absorber for broadband low-frequency sound, Scientific Reports, 7, 43340 (2017).
28. L. Cui,Y. Wang, L. Gao, L. Hu, L. Yan, Q. Wei, B. Du EDTA functionalized magnetic graphene oxide for removal of Pb(II), Hg(II) and Cu(II) in water treatment: Adsorption mechanism and separation property, Chemical Engineering Journal, 281: 1-10, (2015).
29. V. Chandra, J. Park, Y. Chun, J. W. Lee, In-C. Hwang, K. Kim, Water-dispersible magnetite-reduced graphene oxide composites for arsenic removal. ACS Nano, 4(7), 3979-3986, (2010).
30. D. Chen, H. Feng, and J. Li, Graphene Oxide: Preparation, Functionalization, and Electrochemical Applications. Chemical Reviews, 112(11), 6027-6053, (2012).

31. M.F. El-Kady, V. Strong, S. Dubin, R. B. Kaner, Laser Scribing of High-Performance and Flexible Graphene-Based Electrochemical Capacitors. Science, 335(6074), 1326-1330, (2012).
32. H. Kim, A.A. Abdala, C.W. Macosko, Graphene/Polymer Nanocomposites. Macromolecules, 43(16): 6515-6530, (2010).
33. Md. J. Nine, Md. Ayub, A. C. Zander, D. N. H. Tran, B. S. Cazzolato, D. Losic, Graphene Oxide-Based Lamella Network for Enhanced Sound Absorption. Advanced Functional Materials, 27(46): 1703820, (2017).
34. J-H. Oh, J. Kim, H. Lee, Y. Kang, I-K. Oh, Directionally Antagonistic Graphene Oxide-Polyurethane Hybrid Aerogel as a Sound Absorber. ACS Applied Materials & Interfaces, 10(26): 22650-22660, (2018).
35. J-H. Oh, H. R. Lee, S. Umrao, Y. J. Kang, I-K. Oh, Self-aligned and hierarchically porous graphene-polyurethane foams for acoustic wave absorption. Carbon, 147: 510-518, (2019).
36. B. Lu, L. Lv, H. Yang, J. Gao, T. Xu, G. Sun, X. Jin, C. Shao, L. Qu, J. Yang, High performance broadband acoustic absorption and sound sensing of a bubbled graphene monolith, Journal of Materials Chemistry A, 7(18): 11423-11429, (2019).
37. D. Blevins, R. Formulas for natural frequency and mode shape. Van Nostrand Reinhold company (1979).
38. T. J.Cox, P. D' Antonio, Acoustic Absorbers and Diffusers: Theory, Design and Application, CRC Press, 3th Edition, 2016.
39. C. Howard, B. Cazzolato, Acoustic analyses using MATLAB and ANSYS, CRC press, (2014).
40. F. J. Fahy, P. Gardonio, Sound and structural vibration: radiation, transmission and response, Elsevier, (2007).
41. H. Ruiz, P. Cobo, F. Jacobsen, Optimization of multiple-layer microperforated panels by simulated annealing, Applied Acoustics 72, pp. 772-776 (2011).
42. L. Brekhovskikh, Waves in layered media, Elsevier 16, (2012).
43. D. Takahashi, A new method for predicting the sound absorption of perforated absorber systems, Applied Acoustics 51, pp. 71-84 (1997).
44. D.Y. Maa. "Theory and design of microperforated panel sound absorbing construction". Sci Sin, 18:55-71 (1975).
45. L. Stobinski, N. Lesiak, A. Malolepszy, M. Mazurkiewicz, B. Mierzwa, J. Zemek, P. Jiricek, I. Bieloshapka, Graphene oxide and reduced graphene oxide studied by the XRD, TEM and electron spectroscopy methods. Journal of Electron Spectroscopy and Related Phenomena, 195: 145-154, (2014).
46. S. Kashyap, S. Mishra, S.K. Behera, Aqueous Colloidal Stability of Graphene Oxide and Chemically Converted Graphene. Journal of Nanoparticles, 2014: p. 6, (2014).

47. Ferrari, A.C., Raman spectroscopy of graphene and graphite: Disorder, electron–phonon coupling, doping and nonadiabatic effects. Solid State Communications, 143(1): 47-57, (2017).
48. F. Bucciarelli, M. Meo, Broadening sound absorption coefficient with hybrid resonances, Applied Acoustics, 160,107136, (2020).
49. F. Bucciarelli, G. P. Malfense Fierro, M. Meo, A multilayer microperforated panel prototype for broadband sound absorption at low frequencies, Applied Acoustics 146: 134-144, (2019).

Chapter 9

Conclusions and Future Works

Nowadays the sound wave manipulations are involved in many researches in order to achieved extraordinary and uncommon behaviours and properties which cannot be found in the natural materials/structural properties. This is the reason why this topic found interest and applicability in many engineering fields.
The research work presented in this thesis is based on the study of the sound wave manipulation and the mutual interaction between the sound wave and materials/structure in order to develop new engineered materials/structure which represent a solution to two main engineering challenging objectives: the material elastic properties evaluation using non-destructive approach and the broadband sound absorption at low frequencies through subwavelength structures.
Regarding the first object, we propose a new non-destructive method for the out-of-plane elastic properties evaluation for composite and porous materials. Based on acoustic measurements, the method represents an innovative approach where for the first time an impedance tube test rig is used to estimate not only the acoustic properties but also the elastic properties of the tested materials. The novelty of this research work can be identified in two main aspects. We proposed and validated the novel idea to estimate the material elastic properties starting from acoustic measurements, using a device which is commonly used only for the acoustic properties measurement. The proposed method finds applicability in particular in

the out-of-plane elastic properties measurement which is crucial for the composite materials characterization. Moreover, compared with other non-destructive approach, the proposed method overcome the limitations associated to the ultrasound time of flight approach. The method can be then applied also to porous materials where the applicability of the time of flight is limited to the scattering of the propagating ultrasound pulse through the net structure of such materials.

The second objective try to cover the need of noise mitigation and noise cancellation in automotive NVH applications.

The interior vehicle noise spectrum is spread on a broad frequency range from 100 Hz to 4000Hz since it is a sum of different noise contributions. The main solution adopted by the automotive industries is to use porous absorbers to reduce the noise into the vehicle cabin. However, porous absorbers are completely inefficient for the low frequencies noise contributions since the absorption properties are related to the thickness of the porous material which is typically one order of magnitude smaller than the wavelength. One of the main engineering constrain for automotive application is the size of the absorber. This is the reason why the porous absorbers are unsuitable for application at low frequencies. Usually they are inefficient below 1000 KHz where a minimum thickness of 100mm is required.

Many new absorber concepts have been proposed in the last years with the main goal to increase the absorption properties in the frequency range below the 1000Hz, keeping the global size of the device small. An example are the acoustic membrane-type metamaterials. Such devices represent mostly subwavelength resonator which can guarantee high absorption performance below 500Hz with a thickness of 30-50mm. However, they cannot provide a broadband absorption property since they behave as single degree of freedom resonator and the absorption is related to the resonance phenomena.

In this research work we designed and validated novel resonator absorbers based on different approaches suitable for low frequencies noise absorption. The proposed resonators are subwavelength resonators which provide almost perfect broadband sound absorption in a frequency range between 300Hz to 2000Hz with a global thickness of 50mm. The proposed devices represent a promising alternative to the

porous material for NVH applications which guarantee a broader absorption profile keeping smaller the size and provide low frequencies cancellation for the interior noise spectrum.

9.1 Conclusion

To cover the first objective, a new non-destructive approach is presented to estimate the out of plane elastic modulus for porous, polymeric and composite material. The method is based on impedance tube test rig measurement and the application of the Transfer Function Method that derives information about the sound reflection coefficient and the acoustic impedance as consequence. Under the hypothesis of plane standing wave, the reflection coefficient is a function of the longitudinal sound speed, so the elastic modulus of the material can be extracted exciting the material by a plane standing sound wave in a non-destructive way. The proposed method is first tested in-silico using a Representative Volume Element (RVE) approach and then experimental verified trough several experimental measurement campaign on different materials. In conclusion, using sound wave the out of plane elastic properties of polymeric and composite materials can be evaluated where no standard tests are available, with a discrepancy less than 10% with respect to ultrasonic test. The limitation of the proposed method is associated to high sound reflective materials, where the elastic modulus estimation is particularly sensitive to small variations in the reflection coefficient measurements. So in this case, high accuracy in reflection coefficient measurement is required.

As introduced before, the second object of the thesis is the broadband sound absorption at low frequencies provided by subwavelength structures for NVH applications in automotive field. In this case, the mutual interaction between resonator structures and the sound wave is used to manipulate the incoming sound wave and achieve the prescribed objectives. It leads to new prototypes of acoustic metamaterials proposed in this research work. It is well known how the acoustic metamaterial are playing a key role in acoustic engineering field with the goal of achieve perfect sound absorption. However, it is still a challenging objective the

achievement of perfect broadband sound absorption at low frequencies keeping the metamaterial thickness of subwavelength size. In this thesis three different new concept of acoustic resonator metamaterials are presented.

Looking for an efficient sound absorbing structure, the first device is based on the Microperforated Panel (MPP) resonator absorber. In particular an optimized prototype is designed and manufactured consisting of multiple MPP in series with different and optimized geometrical parameters which guarantee a sound absorption over 90% in a frequency range between 400Hz and 2000Hz

To optimize the design parameters an analytical model based on the Equivalent Electric Circuit approach is proposed and used for the parametric analysis.

The second proposed device is a subwavelength membrane-type unit cell metamaterial which shows broadband absorption in the frequency range between 250Hz and 400Hz with two main peaks at 268Hz and 369Hz with over 80% sound absorption. A numerical model based on fluid-structure interaction is used to study the acoustic performances of the unit cell, and the results demonstrated that the absorption is associated to hybrid resonances which occur when high order structural modes of the membrane couple with the acoustic modes of the resonance cavity. The common membrane-type metamaterials allow only one narrow absorption peaks, while the proposed resonator proposed multiple peaks and broad absorption at very low frequencies keeping the thickness of subwavelength size.

A third acoustic metamaterials resonator is proposed in the thesis, combing the effect of the honeycomb core structure, the membrane and micro perforated panel resonances. The proposed metamaterial results a novel acoustic Hybrid Multi-Degree of Freedom resonator Metamaterial based on a lightweight honeycomb core structure (HC) with skin and embedded submillimetre Graphite Oxide (GO) foils. Two main configurations are proposed; GOHCGOHC and MPPHCGOHC which include a GO foil and a MPP as external skin respectively. This is a subwavelength structure with outstanding perfect absorption over a broadband low frequency range from 300Hz to 2500Hz. An analytical model is proposed and implemented to investigate the reasons behind such impressive absorption performance which is also validate through experimental measurement.

9.2 Future Works

The presented research work exposes several sound absorber and acoustic metamaterial with the common objective to achieve broadband sound absorption at low frequency which is of interest for many engineering applications: automotive, aerospace, etc.

One of the further goals is to use the knowledge developed in the here presented research works to design a passive absorber device to use in a specific application in automotive field. With the support of my supervisor we are working on a new passive resonator absorber to be use in well define application in automotive field to reduce the noise and increase the car cabin acoustic performances. At this point the mentioned device is at design status, so the next step would be the manufacturing of first prototype and consequently test qualification.

Moreover, in Chapter 7 we highlighted the potential of Graphite Oxide for acoustic and noise reduction applications. At this stage we are working on new metamaterials based on GO structures, not only GO foils but also GO foams. Numerical and analytical modelling of these new metamaterials is required, as well the experimental acoustic properties characterization.

Appendix. A1

Two Microphone Impedance Tube Drawings

A1.1. Tube Supports

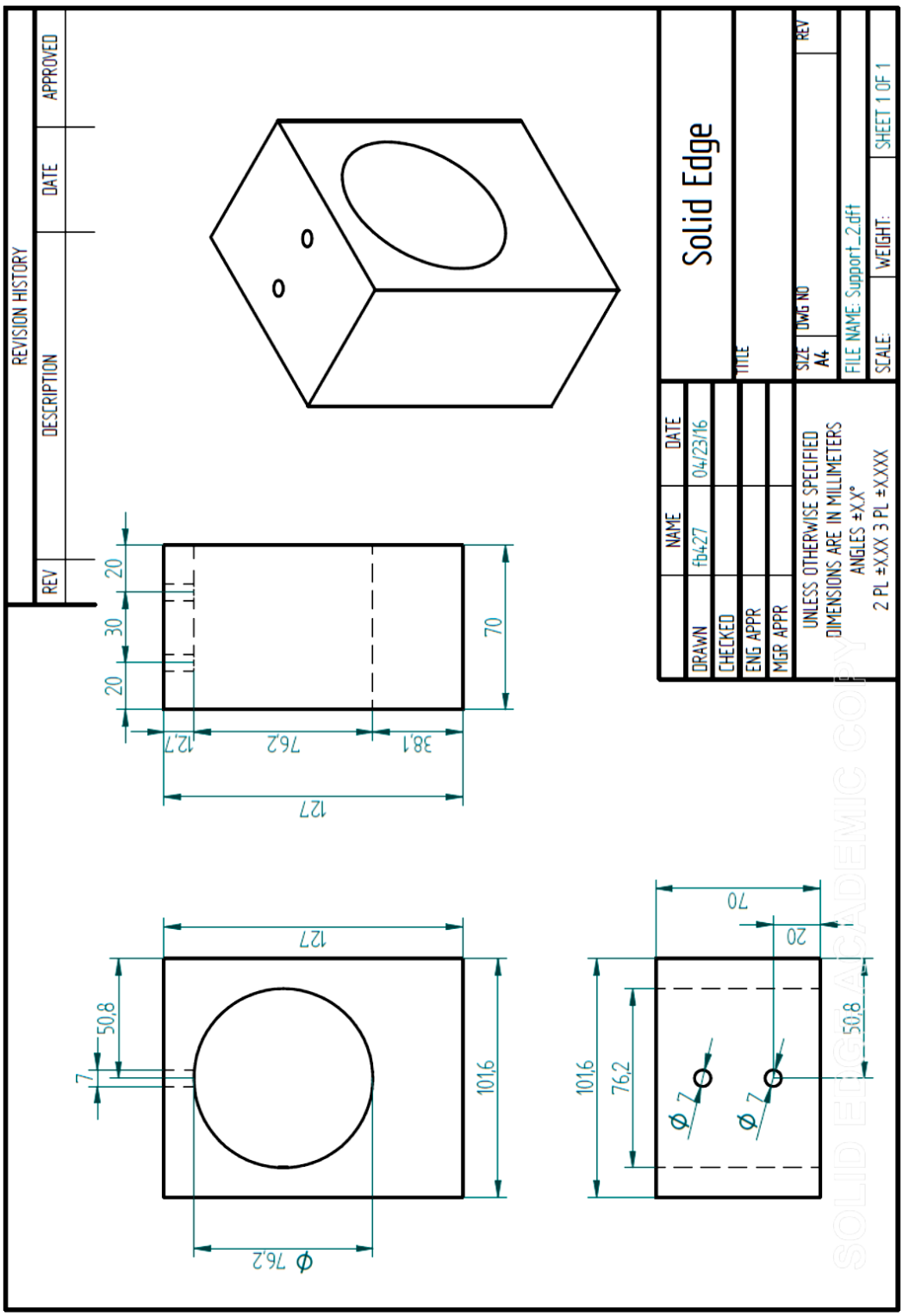

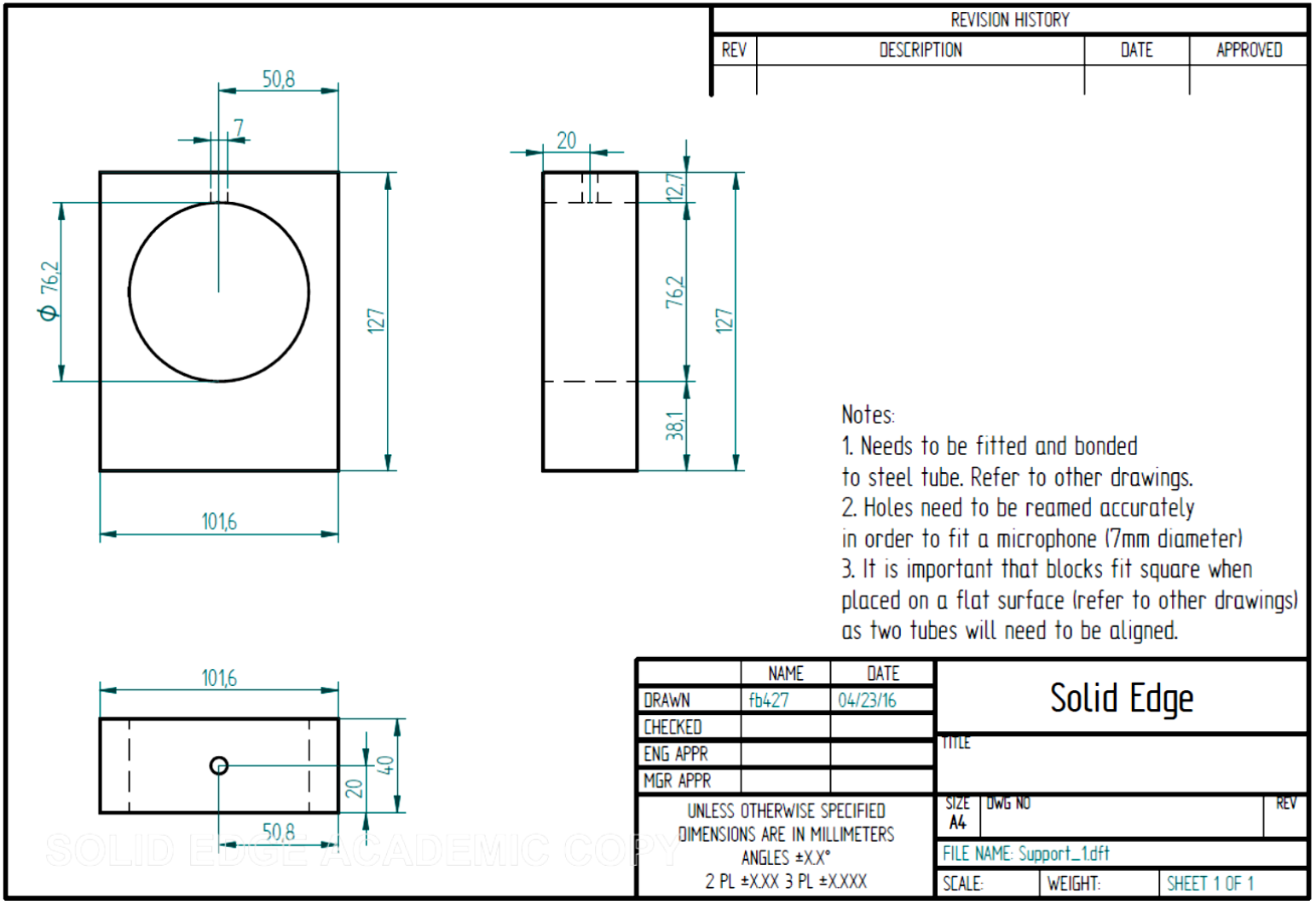
REVISION HISTORY
REV
DESCRIPTION
DATE
APPROVED
50,8
7
20
12,7
Φ 76,2
76,2
127
127
38,1
101,6
Notes:
1. Needs to be fitted and bonded
to steel tube. Refer to other drawings.
2. Holes need to be reamed accurately
in order to fit a microphone (7mm diameter)
3. It is important that blocks fit square when
placed on a flat surface (refer to other drawings)
as two tubes will need to be aligned.
101,6
40
20
50,8
NAME
DATE
DRAWN
fb427
04/23/16
CHECKED
ENG APPR
MGR APPR
UNLESS OTHERWISE SPECIFIED
DIMENSIONS ARE IN MILLIMETERS
ANGLES ±X.X°
2 PL ±X.XX 3 PL ±X.XXX
Solid Edge
TITLE
SIZE
A4
DWG NO
REV
FILE NAME: Support_1.dft
SCALE:
WEIGHT:
SHEET 1 OF 1
SOLID EDGE ACADEMIC COPY

A1.2. Specimen Holder – Tube Termination

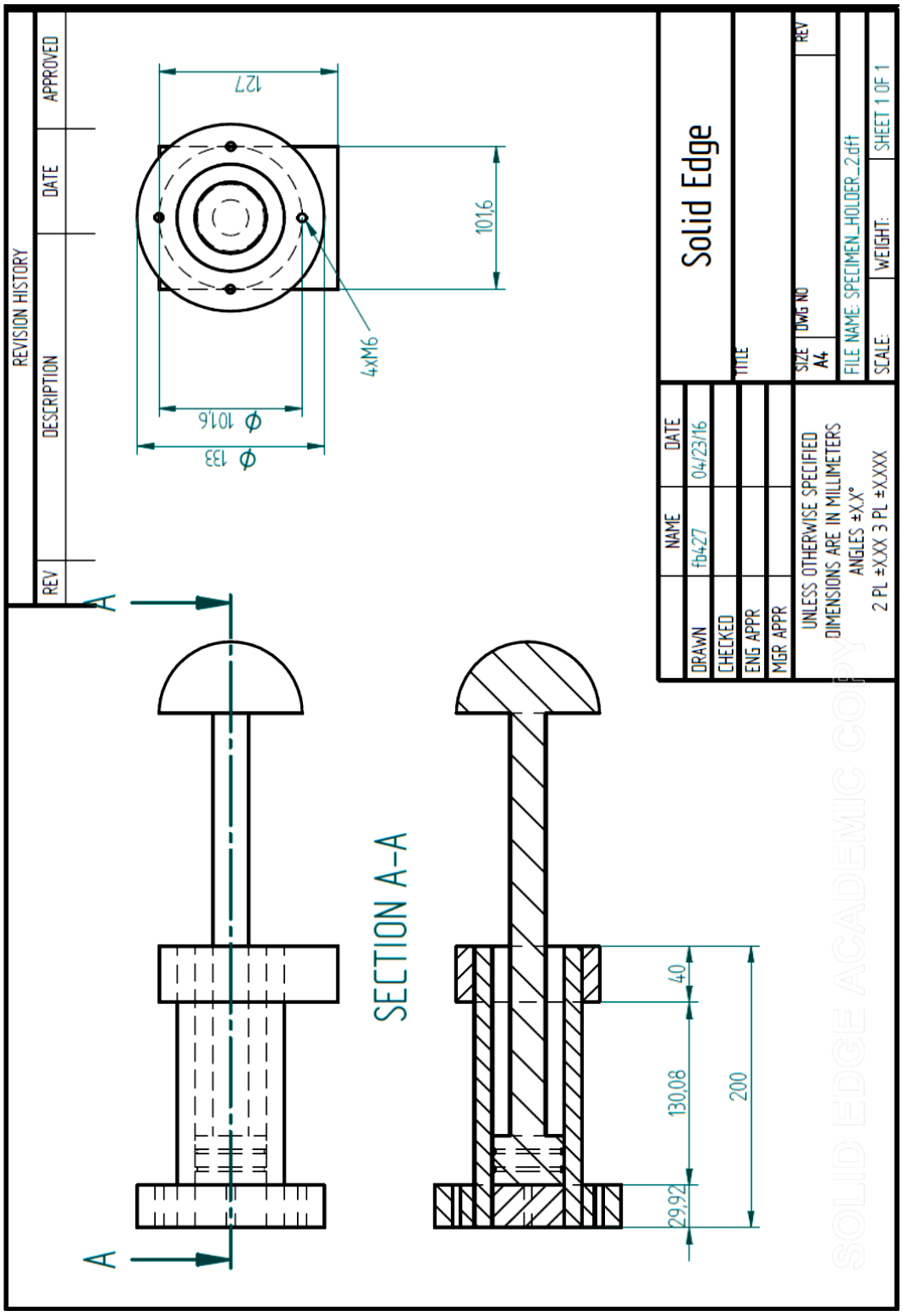

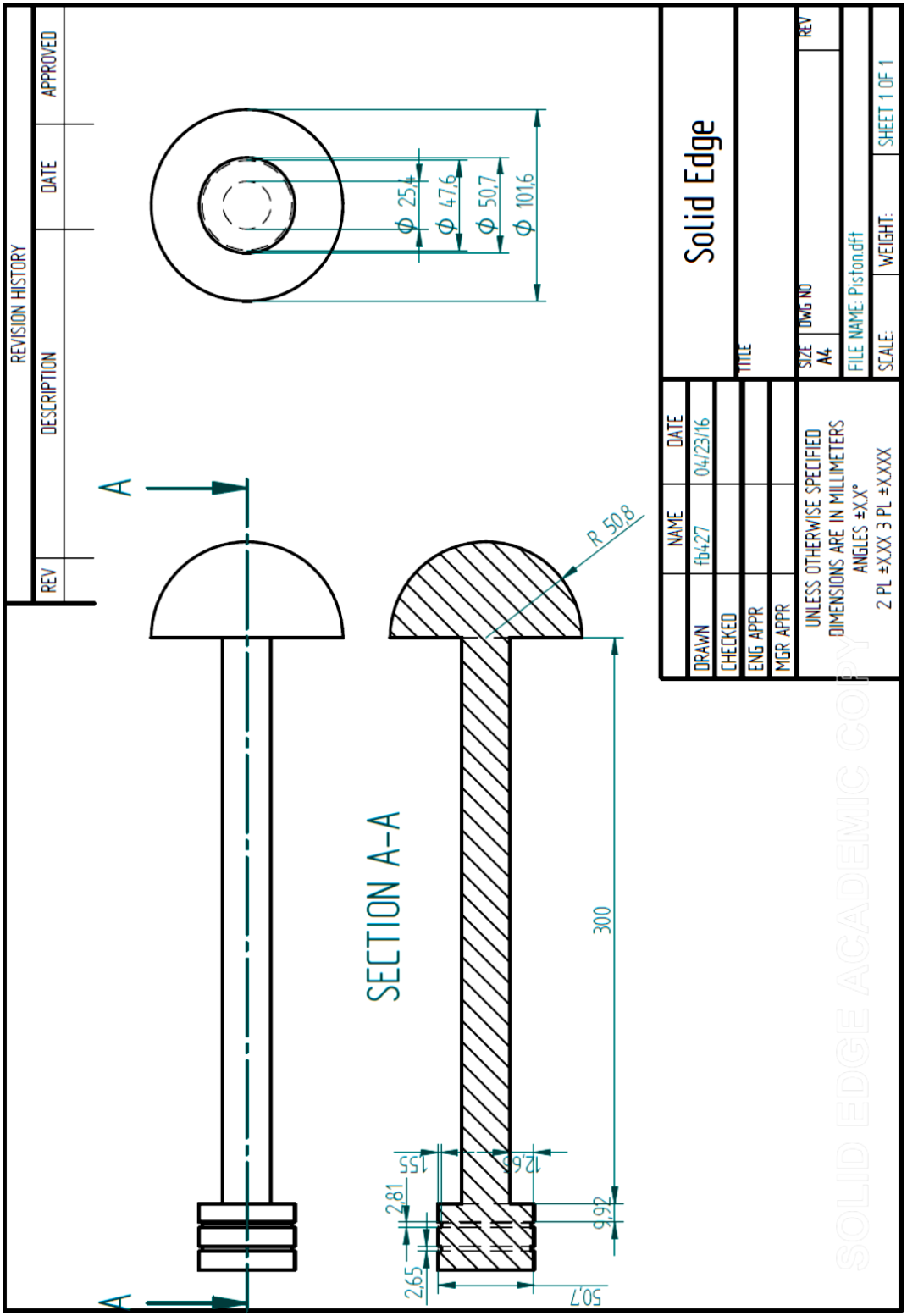
REVISION HISTORY
REV
DESCRIPTION
DATE
APPROVED
Φ 25,4
Φ 47,6
Φ 50,7
Φ 101,6
A
A
SECTION A-A
R 50,8
300
2,81
2,65
9,92
50,7
NAME
DATE
DRAWN
fb427
04/23/16
CHECKED
ENG APPR
MGR APPR
UNLESS OTHERWISE SPECIFIED
DIMENSIONS ARE IN MILLIMETERS
ANGLES ±X.X°
2 PL ±.XXX 3 PL ±.XXXX
Solid Edge
TITLE
SIZE
A4
DWG NO
REV
FILE NAME: Piston.dft
SCALE:
WEIGHT:
SHEET 1 OF 1
SOLID EDGE ACADEMIC COPY

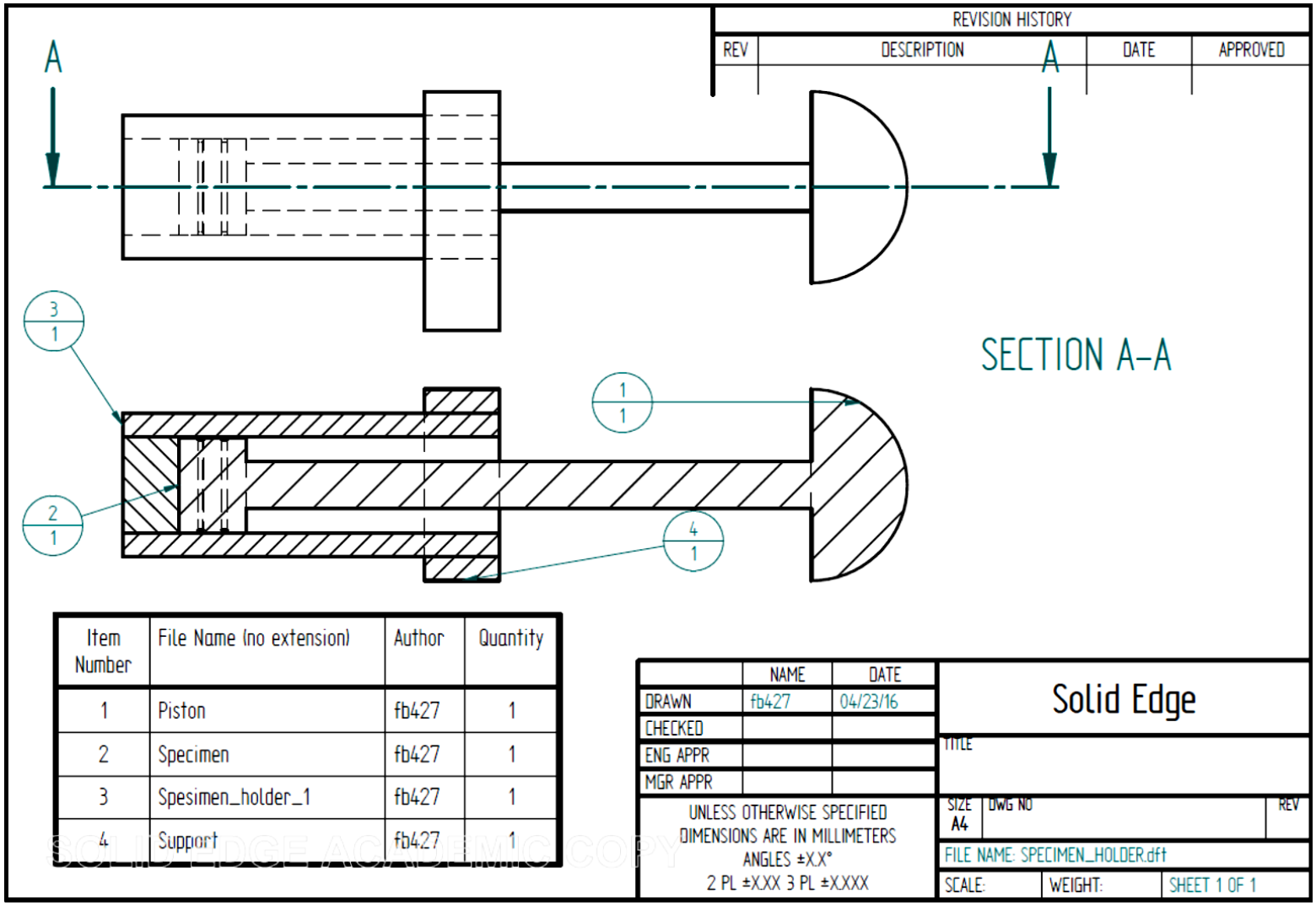

SOLIDEDGE ACADEMIC COPY

A1.3. Tube – Impedance Tube Assembly

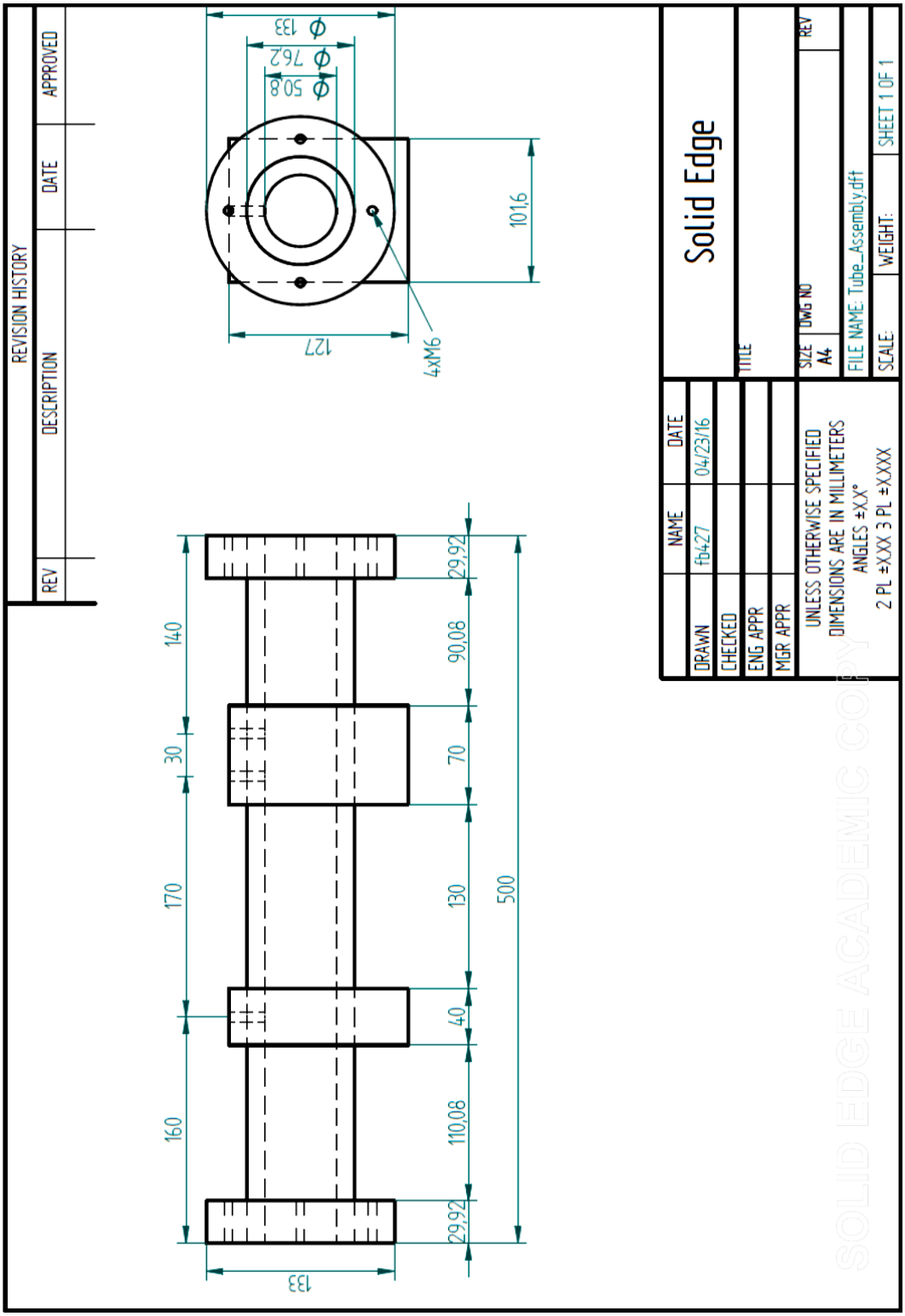

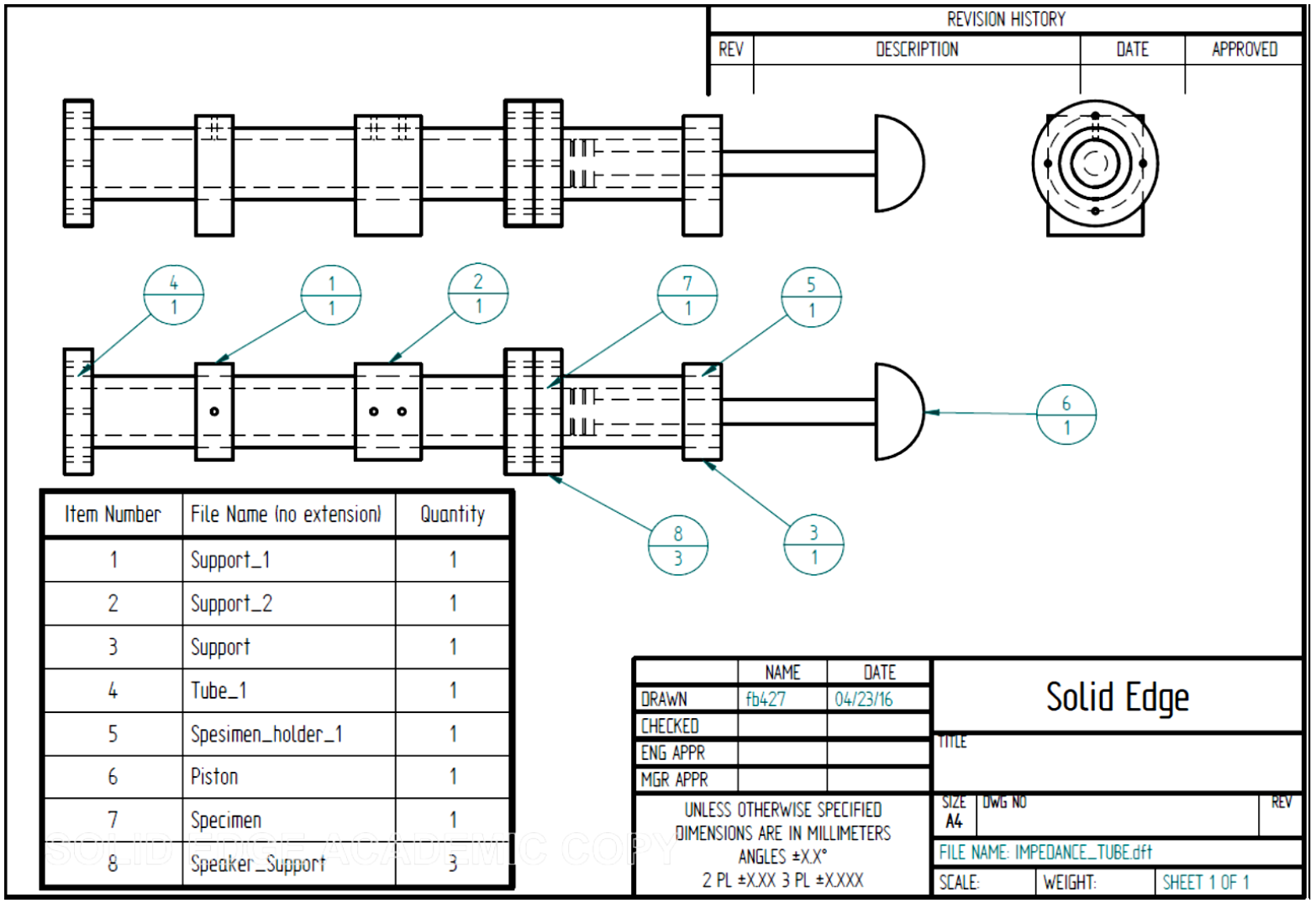
REVISION HISTORY
REV
DESCRIPTION
DATE
APPROVED
4 1
1 1
2 1
7 1
5 1
6 1
8 3
3 1
Item Number | File Name (no extension) | Quantity
1 | Support_1 | 1
2 | Support_2 | 1
3 | Support | 1
4 | Tube_1 | 1
5 | Spesimen_holder_1 | 1
6 | Piston | 1
7 | Specimen | 1
8 | Speaker_Support | 3
NAME
DATE
DRAWN
fb427
04/23/16
CHECKED
ENG APPR
MGR APPR
UNLESS OTHERWISE SPECIFIED
DIMENSIONS ARE IN MILLIMETERS
ANGLES ±X.X°
2 PL ±X.XX 3 PL ±X.XXX
Solid Edge
TITLE
SIZE
A4
DWG NO
REV
FILE NAME: IMPEDANCE_TUBE.dft
SCALE:
WEIGHT:
SHEET 1 OF 1

Appendix. A2

Four Microphone Impedance Tube Drawings

A2.1. Anechoic Termination

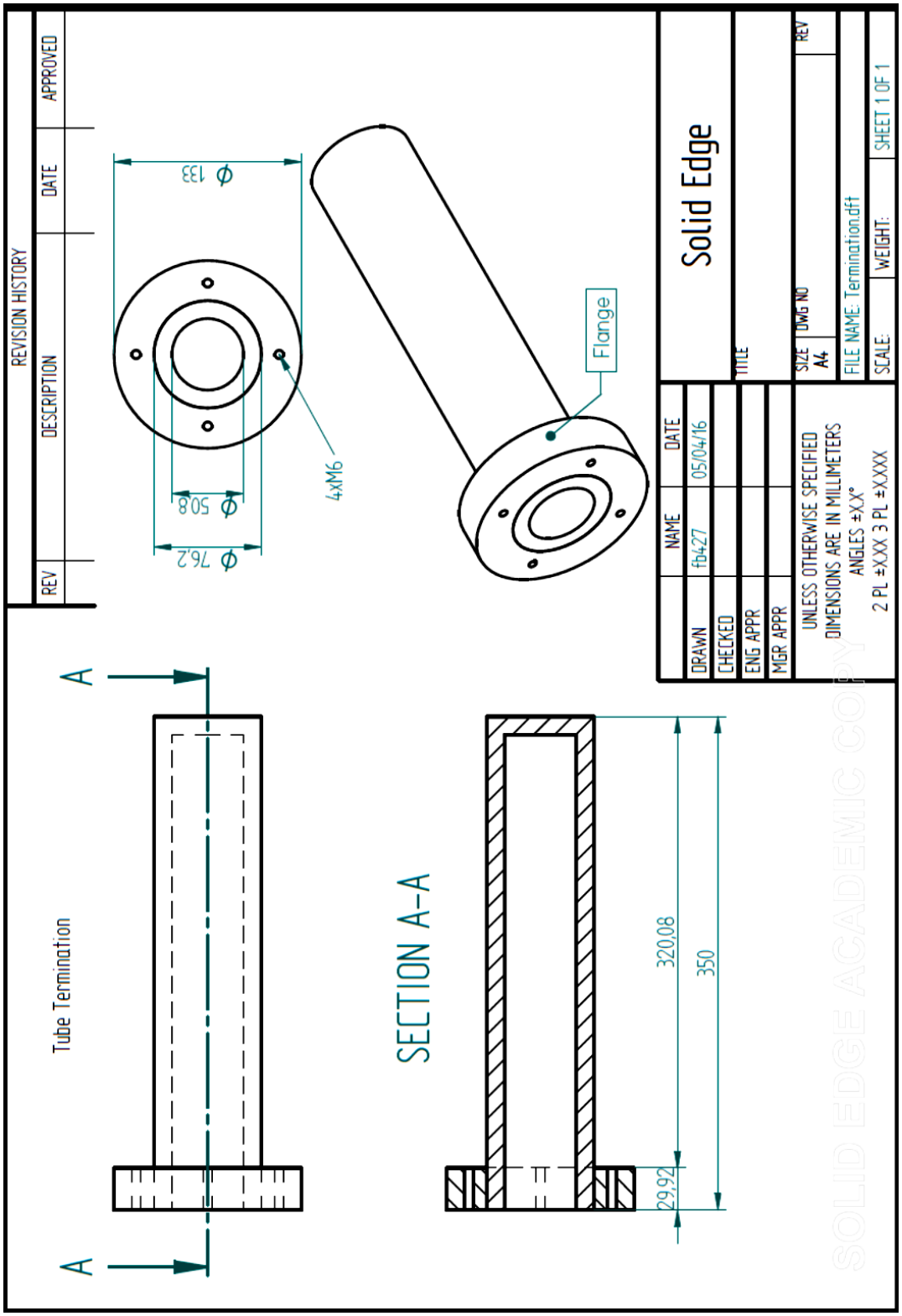

A2.2. Microphones Plugs

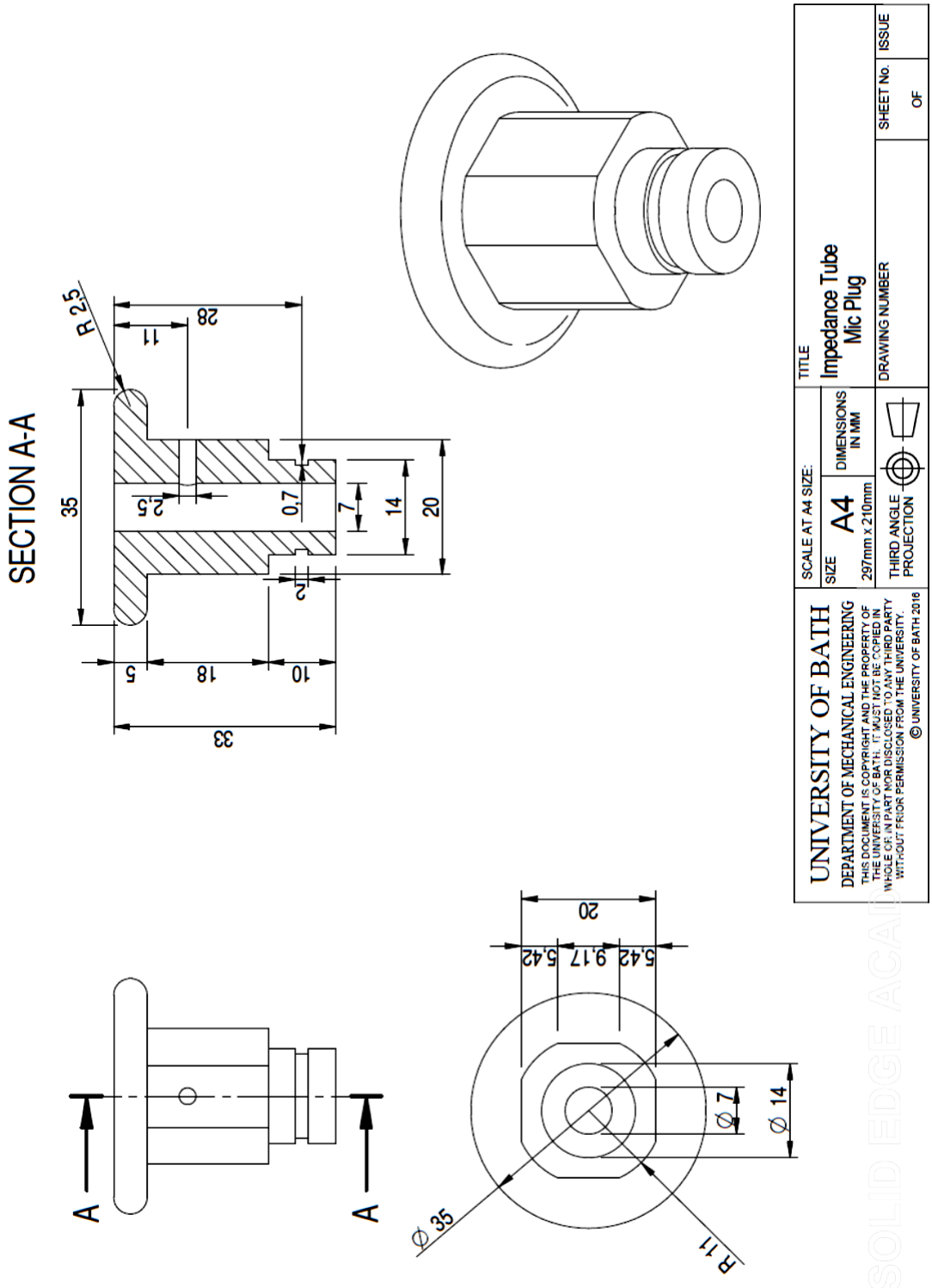

SOLID EDGE ACA

Appendix. A3

Transfer Function – Two Loads Method: Four Microphones Configuration

The Two Loads Method for the acoustic transmission loss evaluation was introduce in the 1979 by To and Doige [8-9] and standardized in ASTM E-2611 [2].
This method is based on the solving of the four-pole equations associated to the sound field into a plane wave standing wave tube.
Assuming a plane wave distribution into the tube, the sound field can expressed by the wave equation [5-7]

$$c^2\psi_{xx} = \psi_{tt} \tag{a.1}$$

where ψ is the velocity potential, and the subscript *x* and *t* denoting respectively differentiation of the velocity potential to the x (spatial coordinate along the tube) and t (time variable), while *c* is the speed of sound in air.
Solving equation (a.1) between two station of the tube *x1* and *x2*, it is possible define the four-pole matrix for the acoustic system, which is a transfer matrix between the sound pressure (*p*) and the normal acoustic particle velocities (*u*) at two stations

$$\begin{bmatrix} p_{x1} \\ u_{x1} \end{bmatrix} = \begin{bmatrix} T_{11} & T_{12} \\ T_{21} & T_{22} \end{bmatrix} \begin{bmatrix} p_{x2} \\ u_{x2} \end{bmatrix} \tag{a.2}$$

Considering the sound transmission in a layer, the acoustic pressure components and the normal velocity components in the layer can be expressed as (referring to ***Figure a.***)

$$p_1 = P_1 e^{j(\omega t - kx)} \tag{a.3}$$

$$u_1 = \frac{U_1}{\rho c} e^{j(\omega t - kx)} \tag{a.4}$$

$$p_2 = P_2 e^{j(\omega t - kx)} \tag{a.5}$$

$$u_2 = -\frac{P_2}{\rho c} e^{j(\omega t + kx)} \tag{a.6}$$

Assuming that only plane waves exist within the layers with normal incidence, and that the propagation is entirely contained in the x-y plane, then considering the continuity of pressure and velocity at the boundaries [10] it is possible to relate the surface pressure and the velocity of one layer to the next one combining the previous equations:

$$\begin{bmatrix} p_{x1} \\ u_{x1} \end{bmatrix} = \begin{bmatrix} T_{11} & T_{12} \\ T_{21} & T_{22} \end{bmatrix} \begin{bmatrix} p_{x2} \\ u_{x2} \end{bmatrix} = \begin{bmatrix} cos(kd) & j\rho c\, sin(kd) \\ \frac{j}{\rho c} sin(kd) & cos(kd) \end{bmatrix} \begin{bmatrix} p_{x2} \\ u_{x2} \end{bmatrix} \tag{a.7}$$

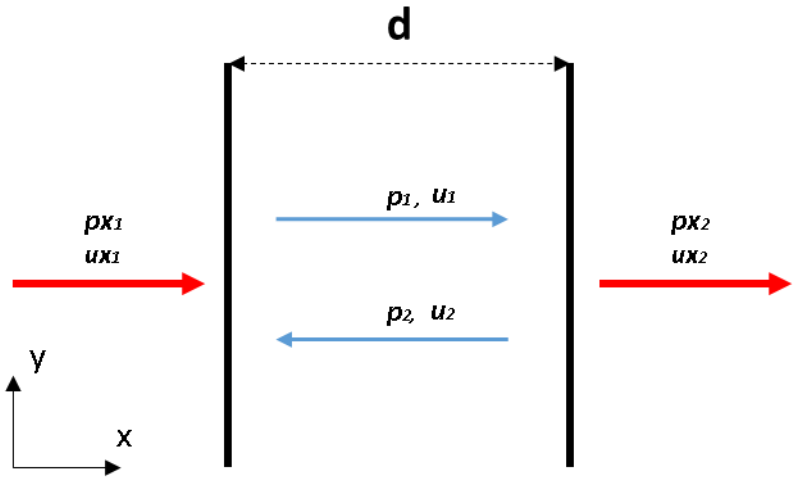

Figure a.1. Geometry for transfer matrix model of multi-layers

The four-pole transfer matrix approach can be applied on the 4 microphones configuration impedance tube to estate the sound transmission loss coefficient.

According with the reference system shows in ***Figure 4.4***, the sound filed into the impedance tube generated be the plane wave propagation can be described by the

superposition of the incident and reflected plane wave upstream and the transmitted and reflected plane wave downstream:

$$p(x,t) = \begin{cases} \left(A(\omega)e^{-jkx} + B(\omega)e^{jkx}\right)e^{j\omega t}, & x \le 0 \\ \left(C(\omega)e^{-jkx} + D(\omega)e^{jkx}\right)e^{j\omega t}, & x \ge d \end{cases} \quad \text{(a.8)}$$

$$v(x,t) = \begin{cases} \dfrac{\left(A(\omega)e^{-jkx} - B(\omega)e^{jkx}\right)}{\rho c}e^{j\omega t}, & x \le 0 \\ \dfrac{\left(C(\omega)e^{-jkx} + D(\omega)e^{jkx}\right)}{\rho c}e^{j\omega t}, & x \ge d \end{cases} \quad \text{(a.9)}$$

where *p(x,t)* and *v(x,t)* are the complex sound pressure and the complex particle velocity, while the coefficients *A, B,C* and *D* are the complex amplitude of the plane wave components.

Then the complex sound pressures at the four microphone stations can be writes as

$$p_{m1}(t) = \left(A(\omega)e^{-jk(l+s)} - B(\omega)e^{jk(l+s)}\right)e^{j\omega t} \quad \text{(a.10)}$$

$$p_{m2}(t) = \left(A(\omega)e^{-jkl} - B(\omega)e^{jkl}\right)e^{j\omega t} \quad \text{(a.11)}$$

$$p_{m3}(t) = \left(C(\omega)e^{-jkl} - D(\omega)e^{jkl}\right)e^{j\omega t} \quad \text{(a.12)}$$

$$p_{m4}(t) = \left(C(\omega)e^{-jk(l+s)} - D(\omega)e^{jk(l+s)}\right)e^{j\omega t} \quad \text{(a.13)}$$

Combining the equations (a.10 - a.13), the complex coefficients can be estimated as a function of the complex pressure at the microphone stations and the relative distances of the microphones from the sample

$$A = j\frac{(p_{m1}e^{jkl} - p_{m2}e^{jk(l+s)})}{2sin\,(ks)} \quad \text{(a.14)}$$

$$B = j\frac{(p_{m2}e^{-jk(l+s)} - p_{m1}e^{-jkl})}{2sin\,(ks)} \quad \text{(3.15)}$$

$$C = j\frac{(p_{m3}e^{jk(l+s)} - p_{m4}e^{jkl})}{2sin\,(ks)} \quad \text{(a.16)}$$

$$D = j\frac{(p_{m4}e^{-jkl} - p_{m3}e^{-jk(l+s))})}{2sin\,(ks)} \quad \text{(a. 17)}$$

Assuming the assumption of plane standing wave upstream/downstream the tube, the complex coefficients, can be expressed in terms of transfer functions instead of the complex pressures at the microphones locations.

Assuming for example the microphone in station *1* as reference, we can define the complex acoustic transfer functions between the reference and the remaining microphones:

$$H_{n,1} = \frac{G_{n,1}}{G_{1,1}} \quad \text{(a.18)}$$

where the equation (a.18) defines the transfer function by taking the ratio between the cross power spectrum with the reference auto spectrum. Taking into account equation (3.47), equations (3.43-3.46) can be rewritten:

$$A = j\frac{(H_{1,1}e^{jkl} - H_{2,1}e^{jk(l+s)})}{2sin\,(ks)} \quad \text{(a.19)}$$

$$B = j\frac{(H_{2,1}e^{-jk(l+s)} - H_{1,1}e^{-jkl)})}{2sin\,(ks)} \quad \text{(a.20)}$$

$$C = j\frac{(H_{3,1}e^{jk(l+s)} - H_{4,1}e^{jkl})}{2sin\,(ks)} \quad \text{(a.21)}$$

$$D = j\frac{(H_{4,1}e^{-jkl} - H_{3,1}e^{-jk(l+s))})}{2sin\,(ks)} \quad \text{(a.22)}$$

These coefficients expressed in equations (a.19 - a.22) are required for determining the elements of the four-pole transfer matrix applied to the two surface of the tested sample at x=0 and x=d. Applying the boundary conditions on both faces of the

specimen, the acoustic pressure and the velocity can be estimated using the equations (a.10 – a.13):

$$p_0 = A + B, \;\; v_0 = \frac{A - B}{\rho c} \tag{a.23}$$

$$p_d = Ce^{-jkd} + De^{jkd}, \;\; v_d = \frac{Ce^{-jkd} - De^{jkd}}{\rho c} \tag{a.24}$$

So the four-pole transfer matrix can be rewritten as

$$\begin{bmatrix} p_0 \\ v_0 \end{bmatrix} = \begin{bmatrix} T_{11} & T_{12} \\ T_{21} & T_{22} \end{bmatrix} \begin{bmatrix} p_d \\ v_d \end{bmatrix} \tag{a.25}$$

In order to solve the four-pole transfer matrix the four complex coefficients must be determined. But from equations (a.25), it is clear how a system of two equations with four unknown parameters need to be solved. So the tube must be configured with two different terminations, and the four-pole matrix approach applied to both the configurations in order to define four linear equations that can be used to solve for the four unknown matrix elements. For example, an open end tube termination, identified by the subscript "*op*" and an anechoic termination, identified by the subscript "*an*", can be considered.

Hence the elements of the transfer matrix can be easily calculated as:

$$T_{11} = \frac{p_{0\,op} v_{d\,an} - p_{0\,an} v_{d\,op}}{p_{d\,op} v_{d\,an} - p_{d\,an} v_{d\,op}} \tag{a.26}$$

$$T_{12} = \frac{p_{0\,an} p_{d\,op} - p_{0\,op} v_{d\,an}}{p_{d\,op} v_{d\,an} - p_{d\,an} v_{d\,op}} \tag{a.27}$$

$$T_{21} = \frac{v_{0\,op} v_{d\,an} - v_{0\,an} v_{d\,op}}{p_{d\,op} v_{d\,an} - p_{d\,an} v_{d\,op}} \tag{a.28}$$

$$T_{22} = \frac{p_{d\,op} v_{0\,an} - p_{d\,an} v_{0\,op}}{p_{d\,op} v_{d\,an} - p_{d\,an} v_{d\,op}} \tag{a.29}$$

Assuming the specimen backed by a perfectly anechoic termination, the complex coefficient *D* is identically zero in the downstream tube section. Then, assuming the incident plane wave has a unit amplitude, the sound pressure and the particle velocity on both specimen surface

$$p_0 = 1 + R, \;\; v_0 = \frac{1 - R}{\rho c} \tag{a.30}$$

$$p_d = Te^{-jkd}, \;\; v_d = \frac{Te^{-jkd}}{\rho c} \tag{a.31}$$

where $R=B/A$ is the complex reflection coefficient and $T=C/A$ is the transmission coefficient for the anechoic-backed sample.

Combining the equations (a.30) and (a.31) with equation (a.25), the normal incident transmission coefficient is found to be

$$T = \frac{2e^{jkd}}{T_{11} + \frac{T_{12}}{\rho c} + \rho T_{21} + T_{22}} \tag{a.32}$$

Then the normal incident transmission loss of a specimen can be calculated

$$TL_n = 20log_{10}\left|\frac{1}{T}\right| \tag{a.33}$$

References

1. ASTM E-1050, Standard Test Method for Impedance and Absorption of Acoustical Materials Using a Tube, Two Microphones and a Digital Frequency Analysis System. American Society for Testing of Materials, (2008).
2. ASTM E-2611, Standard Test Method for Measurement of Normal Incident Sound Transmission of Acoustical Materials Based on the Transfer Matrix Method, (2008).
3. Chung J. Y., Blaser D. A., Transfer function method of measuring in-duct acoustic properties. I. Theory, The Journal of the Acoustical Society of America 68, 907, (1980).
4. Chung J. Y., Blaser D. A., Transfer function method of measuring in-duct acoustic properties. II. Experiment, The Journal of the Acoustical Society of America 68, 914, (1980).
5. J. David, N. Cheeke, Fundamentals and Applications of Ultrasonic Wave, CR PRESS, 2002.
6. A.B. Wood, A Textbook of Sound, G. BELLAND SONS LTD, 1964.
7. D.T. Blackstock, Fundamentals of Physical Acoustics, JOHN WILEY & SONS, 2000.
8. C.W.S. To, A.G. Doige, A transient testing technique for the determination of matrix parameters of acoustic system, I: Theory and Principles, Journal of Sound and Vibration, 62(2), 207-222, 1979.

9. .W.S. To, A.G. Doige, A transient testing technique for the determination of matrix parameters of acoustic system, II: Experimental Procedures and Results, Journal of Sound and Vibration, 62(2), 223-233, 1979.

10. J.C. Trevor, P. D Antonio, Acoustic Absorbers and Diffusers: Theory, Design and Application, SPON PRESS, 2004.

11. A.F. Seybert, D.F. Ross, Experimental determination of acoustic properties using a two-microphone random excitation technique, J. Acoust. Soc. Am., 68, 907-913, 1980.

12. W. T. Chu, Further experimental studies on transfer-function technique for impedance tube measurements, J. Acoust. Soc. Am., 83, 2255, 1988.

13. D. Maa, Theoty and Design of Microperforated panel sound absorbing contractions, Scientia Sinica, 18, 1, 55-71, 1975.

14. D. Maa, Microperforated-Panel wideband Absorbers, Noise Control Eng. J., 29,77-84, 1987.

15. D.Maa, Potential of microperforated panel absorber, J. Acoust. Soc. Am, 104, 2861-2866, 1988.

16. U. Ingard, On the theory and design of acoustic resonators, J. Acoust. Soc. Am, 25, 1037-1061, 1953.

17. P.M. Morse, U. Ingard, Theoretical Acoustic, McGraw-Hill, 1968.

18. J. Liu, X. Hua, D. W. Herrin, Estimation of effective parameters for microperforated panel absorbers and applications, Appl. Acoust, 75, 86-93, 2014.

19. K. Sakagami, M. orimoto, M. Yairi, A note on the effect of vibration of microperforated panel on its sound absorption characteristic, Acoust. Sci. & Tech, 2, 2005.

20. K. Sakagami, M. Morimoto, M. Yairi, A note on the relationship between the sound absorption by microperforated panels and panel/membrane-type absorbers, Applied Acoustics, 70, 1131-1136, 2009.

21. Z. Liu, J. Zhan, M. Fard, J. L. Davy, Acoustic measurement of a 3D printed micro-perforated panel combined with porous material, Meas. J. Int. Confed, 104, 233-236, 2017.

22. Z. Liu, J. Zhan, M. Fard, J. L Davy, Acoustic properties of multilayer sound absorber with 3D printed micro-perforated panel, Appl. Acoust., 121, 25-32, 2017.

23. K. Sakagami, S. Kobatake, K. Kano, M. Morimoto, M. Yairi, Sound Absorption characteristics of a single microperforated panel absorber backed by a porous absorbent layer, Acoustic Australia, 39, 2011.

24. I. Falsafi, A. Ohadi, Design guide of single layer micro perforated panel absorber with uniform air gap, Applied Acoustic, 126, 48-57, 2017.

25. C. Wang, L. Cheng, J. Pan, G. Yu, Sound absorption of a micro-perforated panel backed by an irregular-shaped cavity, J. Acoust. Soc. Am, 127, 2010.

26. X. L. Gai, T. Xing, X. H. Li, B. Zhang, F. Wang, Z.N. Cai, Y. Han, Sound absorption of microperforated panel with L shape division cavity structure, Applied Acoustics, 122, 41-50, 2017.

27. C. Wang, L. Huang, KVH, On the acoustic properties of parallel arrangement of multiple micro-perforated panel absorbers with different cavity depths, J. Acoust. Soc. Am., 130, 1, 2011.

28. W. Wang, Improving the performance of microperforated panel absorbers using designed backings, ICSV22, 2015.

29. W. Guo, H. Min, A compound micro-perforated panel sound absorber with partitioned cavities of different depths, IBPC, Energy Procedia 78, 1617-1622, 2015.

30. K. Sakagami, M. Morimoto, W. Koike, A numerical study of double-leaf microperforated panel absorbers, Applied Acoustics, 67, 609-616, 2006.

31. K. Sakagami, K. Matsutani, M. Morimoto, Sound absorption of double-leaf micro-perforated panel with air-back cavity and a rigid-back wall: Detailed

analysis with a Helmholtz-Kirchhoff integral formulation, Applied Acoustics, 71, 411-417, 2010.

32. P. Cobo, H. Ruiz, J. Alvarez, Double-layer microperforated panel/porous absorber as liner for anechoic closing of test section in wind tunnels, Acta Acust. United with Acust., 96, 5, 914-922, 2010.

33. Y. J. Qian, J. Zhang, N. Sun, D. Y. Kong, X. X. Zhang, Pilot study on wideband sound absorber obtained by adopting a serial-parallel coupling manner, Appl. Acoust. 124, 48-51, 2017.

34. K. Sakagami, Y. Nagayama, M. Morimoto, M. Yairi, Pilot study on wideband sound absorber obtained by combination of two different microperforated panel (MPP) absorbers, Acoust. Sci. & Tech. 30, 2, 2009.

35. Y,J. Qian, K. Cui, S.M. Liu, Z.B. Li, D.S. Shao, D. Y. Kong, S.M. Sun, Optimization of multi-size micro-perforated panel absorber using multi-population genetic algorithm, Noise Control Engr J., 62, 2014.

36. I. Prasetiyo, J. Sarwono, I. Sihar, Study on inhomogeneous perforation thick micro-perforated panel sound absorbers, Journal of Mechanical Engineering and Sciences, 10, 3, 2350-2362, 2016.

37. A. I. Mosa, A. Putra, R. Ramlan, I. Prasetiyo, A. A. Esraa, Theoretical model of absorption coefficient of an inhomogeneous MPP absorber with multi-cavity depths, Applied Acoustics, 146, 409-419, 2019.

38. Y. Y. Lee, E. W. M., Lee, C. F., Ng, Sound absorption of a finite flexible micro-perforated panel backed by an air cavity, Journal of Sound and Vibration, 287, 227-243, 2005.

39. J. Kang, H. V. Fuchs, Predicting the absorption of open weave textiles and micro-perforated membranes backed by an air space, Journal of Sound and Vibration, 2250, 908-920, 1999.

40. K Sakagami, M. Morimoto, D. Takahashi, A note on the acoustic reflection of an infinite membrane, Acustica, 80, 1994.

41. D. Takahashi, K Sakagami, M. Morimoto, Acoustic properties of permeable membrane, J. Acoust. Soc. Am, 99, 1996.

42. K Sakagami, M. Kiyama, M. Morimoto, D. Takahashi, Details analysis of acoustic properties of a permeable membrane, Applied Acoustics, 54, 93-111, 1998.

43. K. Sakagami, Y. Fukutani, M. Yairi, M. Morimoto, Sound absorption characteristics of a double-leaf structure with an MPP and a permeable membrane, Applied Acoustics, 76, 28-34, 2014.

44. X. L. Gai, X. H. Li, B. Zhang, T. Xing, J. J. Zhao, Z. H. Ma, Experiential study on sound absorption performance of microperforated panel with membrane cell, Applied Acoustics, 110, 241-247, 2016.

45. X. L. Gai, T. Xing, X. H. Li, B. Zhang, Z.N. Cai, F. Wang, Sound absorption properties of microperforated panel with membrane cell and mass blocks composite structure, Applied Acoustics, 137, 98-107, 2018.

46. J. Pan, J. Guo, C. Ayres, Improvement of sound absorption of honeycomb panels, Proc Acoustics, 2005.

47. K. Sakagami, M. Morimoto, M. Yairi, Application of microperforated panel absorbers to room interior surfaces, Int J. Acoust Vib, 13, 120-4, 2008

48. K Sakagami, I. Yamashita, M. Morimoto, Sound absorption characteristics of a honeycomb-backed microperfoated panel absorber: revised theory and experimental validation, Noise Control Eng J, 58:157-62, 2010.

49. T.Y. Huang, C. Shen, Y. Jing, Membrane-and plate-type acoustic metamaterials, J. Acoust. Soc. Am., 139, 6, 2016.

50. S. H. Lee, C. M. Park, Y. M. Seo, Z. G. Wang, C. K. Kim, Acoustic metamaterial with negative density, Phys. Lett. A, 373, 48, 4464-4469, 2009.

51. N. Sui, X. Yan, T. Y. Huang, J. Xu, F. G. Yuan, Y. Jing, A light-weight yet sound-proof honeycomb acoustic metamaterial, Appl. Phys. Lett. 160, 17, 171905, 2015.

52. S. Yao, X. Zhou, G. Hu, Investigation of the negative-mass behaviours occurring below a cut-off frequency, New J. Phys. 12, 103025, 2010.

53. P. Li, X. Chen, X. Zhou, G. Hu, P. Xiang, Acoustic cloak constructed with thin-plate metamaterials, Int. J. Smart Nano Mater, 6, 1, 73-83, 2015.

54. Y. Jing, J. Xu, N. X. Fang, Numerical study of a near-zero-index acoustic metamaterials, Phys. Lett A 376, 45, 2834-2837, 2012.

55. H.H. Huang, C.T. Sun, G.L. Huang, On the negative effective mass density in acoustic metamaterials, In: International Journal of Engineering Science, 47, 4, 610-617, 2009.

56. F. Bongard, H. Lissek, J.R. Mosig, Acoustic transmission line metamaterial with negative/zero/positive refractive index, Phys Rev. B, 82, 9, 094306, 2010.

57. C. Shen, Design of Acoustic Metamaterials and Metasurfaces, North Carolina State University, 2016.

58. S. H. Lee, C. M. Park, Y. M. Seo, Z. G. Wang, C. K. Kim, Composite Acoustic Medium with Simultaneously Negative Density and Modulus, Physical Review Letters, 104, 2010.

59. C. Shen, Y. Jing, Side branch-based acoustic metamaterials with a broad-band negative bulk modulus, Appl. Phys. A (2014) 117:1885–1891, 2014.

60. S. H. Lee, C. M. Park, Y. M. Seo, Z. G. Wang, C. K. Kim, Acoustic metamaterial with negative modulus, J. Phys.: Condens. Matter 21 175704, 2009.

61. S. H. Lee, C. M. Park, Y. M. Seo, Z. G. Wang, C. K. Kim, Reversed Doppler effect in double negative metamaterials, Physical Review B 81, 241102R, 2010.

62. Z. Yang, J. Mei, M. Yang, N. H. Chan, P. Sheng, Membrane-type metamaterial with negative dynamic mass, Physical Review Letters, 101, 204301, 2008.

63. Z. Yang, H. M. Dai, N. H. Chan, G. C. Ma, P. Sheng, Acoustic metamaterial panels for sound attenuation in the 50-1000 Hz regime, Appl. Phys. Lett. 96, 041906 (2010).

64. C.J. Naify, S. R. Nutt, Scaling of membrane-type locally resonant acoustic metamaterial arrays, J. Acoust. Soc. Am. 132, 2784-2792, (2012).

65. C.J. Naify, C. M. Chang, G. McKnight, S. Nutt, Transmission loss and dynamic response of membrane-type locally resonant acoustic metamaterial, J. Appl. Phys, 108(11), 114905, (2010).

66. C.J. Naify, C. M. Chang, G. McKnight, S. Nutt, Transmission loss of membrane-type acoustic metamaterials with coaxial ring masses, J. Appl. Phys., 109(10) 124903, (2011).

67. Y. Zhang, J. Wen, Y. Xiao, X. Wen, J. Wang, Theoretical investigation of the sound attenuation of membrane-type acoustic metamaterials, Physics Letter A 376, 1489-1494, (2012).

68. H. Tian, X. Wang, Y. Zhou, Theoretical model and analytical approach for a circular membrane-type structure of locally resonant acoustic metamaterial, Appl. Phys. A 114(3), 985-990, (2014).

69. J. Mei, G. Ma, M. Yang, Z. Yang, W. Wen, P. Sheng, Dark acoustic metamatrials as super absorber for low-frequencies sound, Nat. Commun. 3, 756, (2012).

70. E. Ventsel, T. Krauthammer, Thin Plates and Shells: Theory and Applications, Marcel Dekker, (2001).

71. L. D. Landau, E. M Lifshitz, Theory of Elasticity, 3rd edn, Pergamon, (1986).

72. B. A. Auld, Acoustic Fields and Waves in Solid, John Wiley & Sons, (1973).

73. Y. Chen, G. Huang, X. Zhou, G. Hu, C. T. Sun, Analytical coupled vibroacoustic modelling of membrane-type acoustic metamaterials: Plate Model, J. Acoust. Soc. Am. 136(6), 2926-2934, (2014).

74. Y. Chen, G. Huang, X. Zhou, G. Hu, C. T. Sun, Analytical coupled vibroacoustic modelling of membrane-type acoustic metamaterials: Membrane model, J. Acoust. Soc. Am. 136(6), 969-979, (2014).

75. G. Ma, M. Yang, S. Xiao, Z. Yang, P Sheng, Acoustic metasurface with hybrid resonances, Nat Mater.13, 873-878, (2014).

76. M. Yang, C. Meng, C. Fu, Y. Li, Z. Yang, P. Sheng, Subwavelength total acoustic absorption with degenerate resonators, Appl. Phys. Lett. 107(10), 104104 (2015).

77. M. Yang, G. Ma, Z. Yang, P. Sheng, Coupled membranes with doubly negative mass density and bulk modulus, Phys. Rev. Lett. 110(13), 134301, (2013).

78. J. Li, C. T. Chan, Double-negative acoustic metamaterial, Phys. Rev. E 70, 055602, (2004).

79. M. P. Norton, D. G. Karczub, Fundamentals of Noise and Vibration Analysis for Engineers, 2nd Ed., Cambridge University Press., (2003).

80. S.R. Kim, Y. H. Kim, J. H. Jang, A theoretical model to predict the low-frequency sound absorption of Helmholtz resonator array, The Journal of Acoustical Society of America 119, 1933, (2006).

81. S.H. Park, Acoustic properties of micro-perforated panel absorbers backed by Helmholtz resonators for the improvement of low-frequency sound absorption, Journal Of Sound and Vibration, Vol.332, Issue 20, 4895-4911,(2013).

82. S.K. Tang, C. H. Ng, E.Y.L. Lam, Experimental investigation of the sound absorption performance of compartmented Helmholtz resonators, Applied Acoustics, Vol 73, Issue 9, 969-976, (2012).

83. A. Sanada, N. Tanaka, Extension of the frequency range of resonant sound absorbers using two-degree of freedom Helmholtz based resonators with flexible panel, Volume 74, Issue 4, 509-516, (2013).

84. X. Cai, Q. Guo, G. Hu, J. Yang, Ultrathin low-frequency sound absorbing panels based on coplanar spiral tubes or coplanar Helmholtz resonators, Applied Physics Letters 105, 121901, (2014).

85. Z. Liang, J. Li, Extreme Acoustic Metamaterial by coiling up space, Phys. Rev. Lett. 108, 114301, (2012).

86. M. R. Stinson, The propagation of plane sound waves in narrow and wide circular tubes, and generalization to uniform tubes of arbitrary cross-sectional shapes, J. Acoust. Soc. Am. 89(2), 550-558, (1991).

87. Y. Li, B. M. Assouar, Acoustic metasurface-based perfect absorber with deep subwavelength thickness, Appl. Phys. Lett., 108, 063502, (2016).

88. C. Chen, Z. Du, G. Hu, J. Yang, A low-frequency sound absorbing material with subwavelength thickness, Appl. Phys. Lett. 110, 221903, (2017).

89. D. L. Johnson, J. Koplik, R. Dashen, Theory of dynamic permeability and tortuosity in fluid-saturated porous media, J. Fluid Mech. 176, 379-402, (1987).

90. J.P. Groby, R. Pommier, Y. Auregan, Use of slow sound to design perfect and broadband passive absorbing materials, The Journal of the Acoustical Society of America 139, 1660, (2016).

91. X. Jiang, B. Liang, R. qi Li, X. ye Zou, L. lei Yin, J. chun Cheng, Ultra-broadband absorption by acoustic metamaterials, Appl. Phys. Lett. 105, 243505, (2014).

92. V. Kadam, R. Nayak, Basic of Acoustic Science, In: Acoustic Texiles, Ed. By Padhye R. and Nayak R., Springer, (2016).

93. C. Foreman, Acoustical Fundamentals, URL: http://proaudioencyclopedia.com/acoustical-foundamentals, (2019).

94. S. Amares, E. Sujatmika, T. W. Hong, R. Durairaj, H. S. H. B. Hamid, A Review: Characteristics of Noise Absorption Material, Journal of Physics: Conference Series 908.1, (2017).

95. M. Yang, P. Sheng, Sound Absorption Structures: From Porous Media to Acoustic Metamaterials, Ann. Rev. Mater. Res. 47:83-114, (2017).

96. T.J. Lu, F. Xin, Vibro-acoustics of Lightweight Sandwich Structures, Springer, (2014).

97. C.D. Field, F.R. Fricke, Theory and Application of Quarter-wave Resonators: A Prelude to their use for attenuating Noise Entering Buildings through ventilation opening, Applied Acoustics, Vol. 53, No. 1-3,pp. 117-132, (1998).

98. L. Billings, Exotic optics: Metamaterial world, Nature 500.7461, (2013).

99. G. Ma, P. Sheng, Acoustic metamaterials: From local resonances to broad horizons, Sci. Adv. 2:e1501595, (2016).

100. J.J. Park, C. M. Park, K. J.B. Lee, S.B. Lee, Acoustic superlens using membrane-based metamaterials, Applied Physics Letters, 106.5, (2015).

101. M.R. Haberman, M.D. Guild, Acoustic metamaterials, Physics Today, 69.6, (2016).

102. K. J. Bathe, Finite Element Procedures, PRENTICE-HALL, (1996).

103. O.C. Zienkiewicz, R. E. Newton, Coupled Vibrations of a Structure Submerged in a Compressible Flui, PROCEDINGS OF THE SYMPOSIUM ON FINITE ELEMENT TECHNIQUES, (1969).

104. I. B. Crandall, Theory of Vibrating and Sound, Van Nostrand, (1926).

105. C. Zwikker, C. W. Kosten, Sound Absorbing Materials, Elvisier, (1949).

106. Rayleigh, Theory of Sound (1929 ed.), II, 323, 487, MacMillan, (1978).

107. Y. Liu, Y. Jia, X. Zhang, Z. Liu, Y. Ren, B. Yang, Noise test and analysis of automobile engine, Applied Mechanics and Materials, 307, 196-199, (2013).

108. M. Harrison, Vehicle refinement: Controlling Noise and Vibration in Road Vehicles, Elsevier, (2004).

109. D. Siano, M. Viscardi, M. A. Panza, Automotive materials: an experimental investigation of an engine bay acoustic performances, Energy Procedia 101, 598-605, (2016).

110. H. Boden, M. Abom, Influence of errors on the two-microphone method for measuring acoustic properties in ducts, The Journal of the Acoustical Society of America 79, 541, (1986).